

RF PHOTONIC APERTURES

by

Dylan D. Ross

A dissertation submitted to the Faculty of the University of Delaware in partial fulfillment of the requirements for the degree of Doctor of Philosophy in Electrical and Computer Engineering

Spring 2018

© 2018 Dylan D. Ross
All Rights Reserved

RF PHOTONIC APERTURES

by

Dylan D. Ross

Approved: _____
Kenneth E. Barner, Ph.D.
Chair of the Department of Electrical and Computer Engineering

Approved: _____
Babatunde A. Ogunnaike, Ph.D.
Dean of the College of Engineering

Approved: _____
Ann L. Ardis, Ph.D.
Senior Vice Provost for Graduate and Professional Education

I certify that I have read this dissertation and that in my opinion it meets the academic and professional standard required by the University as a dissertation for the degree of Doctor of Philosophy.

Signed:

Dennis W. Prather, Ph.D.
Professor in charge of dissertation

I certify that I have read this dissertation and that in my opinion it meets the academic and professional standard required by the University as a dissertation for the degree of Doctor of Philosophy.

Signed:

Richard D. Martin, Ph.D.
Member of dissertation committee

I certify that I have read this dissertation and that in my opinion it meets the academic and professional standard required by the University as a dissertation for the degree of Doctor of Philosophy.

Signed:

Daniel S. Weile, Ph.D.
Member of dissertation committee

I certify that I have read this dissertation and that in my opinion it meets the academic and professional standard required by the University as a dissertation for the degree of Doctor of Philosophy.

Signed:

Joseph C. Deroba, Ph.D.
Member of dissertation committee

ACKNOWLEDGMENTS

I would like to take a moment to express my gratitude to all colleagues and mentors who have had an impact on me throughout these past years, and the scattering of topics I have been fortunate enough to explore, from EO polymers to RF photonic imaging systems.

“But with diffractive optics, you can have multiple focuses.”

– Dr. Christopher Schuetz

First, I would like to thank my advisor, Dr. Dennis Prather, for all his support and guidance throughout my time in his lab. I entered his lab as a sophomore without a true appreciation of the RF photonics field and very little electrical engineering experience in general; nevertheless, he immediately provided encouragement and all the resources necessary to become, and grow as a researcher. His enthusiasm, motivation, and persistence in exceeding general expectations have not just made me a better researcher, but an overall better person.

I want to separately thank colleagues who have played a large role in the development of this research. On the transmit side, I owe an unmeasurable amount of thanks to Dr. Shouyuan Shi. His gift of patience and profound aptitude to transfer complex concepts into simple, clear explanations are unmatched, and I am extremely grateful to have had the opportunity to have him as a mentor. Additionally, I would like to thank my research partner during the transmit aperture development, Dr. Matthew

Konkol, who was vital in all aspects leading to the successes of this research. Furthermore, the shared capability to find humor within the challenges endured throughout this work has made the process much more enjoyable.

I also would like to specifically thank the members of the k-team. Most specifically, Drs. Janusz Murakowski and Garrett Schneider without whom none of the k-space tomography work would have been possible. I thank you both for patiently answering the hundreds and hundreds of theoretical and experimental questions I have asked throughout the past few years. I have thoroughly enjoyed all of our conversations, your insight and openness to use creativity and unconventional ideas to help solve problems (and create more areas of exploration than we know what to do with) have been, and will continue to be greatly appreciated. I also thank Dr. Christopher Schuetz, who took time out of his schedule to discuss aspects of the system development, and offer advice on valuable considerations throughout the process. Additionally, I would like to thank my partner in the receive aperture work, Conor Ryan, who has been extremely helpful throughout the past year in, not only bringing this work to where it is today, but keeping the lab environment fun and interesting.

It goes without saying that this experience was also positively impacted by all of the graduate students and researchers associated with Dr. Prather's research. I thank everyone, past and present, whom I had a chance to meet and work with, not limited to: Dr. David Eng, Dr. Benjamin Olbricht, Dr. Joseph Deroba, Dr. Tom Dillon, Dr. Mathew Zablocki, Dr. Tim Creazzo, Dr. Jian Bai, Dr. Peng Yao, Stephen Kozacik, Andrew Mercante, Chris Cullen, Charles Harrity, Andrew Wright, and James Bonnett. Each person has contributed to an enjoyable work environment that is much appreciated.

Finally, I would like to thank my parents, Ann and Duane, who always inspire and support me through all my endeavors. Last, but not least, I am overly grateful for my girlfriend, Logan, for her continual encouragement throughout lows, and celebration of each accomplishment, no matter how small.

TABLE OF CONTENTS

LIST OF TABLES	xi
LIST OF FIGURES	xii
ABSTRACT	xxi

Chapter

1	INTRODUCTION	1
1.1	Phased Array Background	1
1.2	Considerations for 5G Wireless Communications	2
1.3	Spatial Beamforming	3
1.4	Microwave Photonics for 5G Wireless Communications	8
1.5	Dissertation Outline and Original Contributions	11
2	RF PHOTONIC TRANSMIT APERTURE FUNDAMENTALS	14
2.1	UWB Phased Array Antenna	14
2.1.1	Current Sheet Arrays	16
2.1.2	Current Sheet Array Feeding	23
2.2	High Power Photodiodes	30
2.3	Photodiode-Coupled Antennas	35
2.3.1	RF Output Power	36
2.3.2	Bandwidth	36
2.3.3	Power Conversion Efficiency	39
2.4	Photonic Feed Network	40
2.4.1	UWB Tunable Photonic RF Signal Generation	40
2.4.2	Phase Control Network	42
2.5	Conclusion	45
3	PHOTONIC PHASED ARRAY ANTENNA DESIGN AND FABRICATION	46

3.1	Photonic Array Antenna Simulation	46
3.1.1	Infinite Array Model.....	47
3.1.2	Substrate	50
3.1.3	Bias Line Circuitry	53
3.1.4	Inductive Peaking	55
3.1.5	Optical Alignment Components	58
3.1.6	Beam Steering	61
3.1.7	Discrete Array Modeling.....	62
3.2	Fabrication.....	66
3.2.1	Antenna.....	68
3.2.2	Optical Integration.....	68
3.2.2.1	Orthonormal Optical Fiber Configuration.....	70
3.2.2.2	Parallel Optical Integration Configuration	74
3.2.3	Packaging	75
4	TX SYSTEM CHARACTERIZATION.....	77
4.1	Experimental Setup	77
4.2	Characterization and Results	81
4.2.1	1 × 4 Connected Array Antenna	82
4.2.2	1 × 8 Connected Array Antenna	86
4.3	Conclusion.....	92
5	K-SPACE TOMOGRAPHY FUNDAMENTALS.....	94
5.1	k-Space Fundamentals.....	94
5.1.1	Defining k-Space	94
5.1.2	Practical System Considerations	96
5.2	RF Photonic Spatial-Spectral Processing	102
5.2.1	Spatial Processing.....	103
5.2.1.1	Optical Up-Conversion Process	104
5.2.1.2	RF Image Reconstruction	107
5.2.2	Temporal Processing	114

5.3	k-Space Tomography.....	122
5.4	Conclusion.....	127
6	K-SPACE RF IMAGING RECEIVER DESIGN AND FABRICATION	129
6.1	Distributed-Aperture Imaging Receiver Design.....	129
6.1.1	System Architecture	133
6.2	k-Space Imaging Receiver Design	136
6.2.1	Spatial Aperture.....	137
6.2.2	Temporal Aperture	142
6.3	Numerical Analysis	144
6.3.1	Weight-Matrix Formulation	147
6.3.2	k-Space Reconstruction Process.....	150
6.3.3	Numerical Model Characterization	152
6.3.3.1	Two-Dimensional k-Space Reconstructions	153
6.3.3.2	Three-Dimensional k-Space Reconstructions	157
6.4	k-Space Imaging Receiver Fabrication	159
6.4.1	Spatial Aperture.....	159
6.4.1.1	RF Frontend.....	160
6.4.1.2	Mechanical Components	164
6.4.2	Temporal Aperture	168
6.4.3	k-Space Imaging Receiver System.....	170
7	EXPERIMENTAL SPATIAL-SPECTRAL MAPPING.....	174
7.1	System Calibration and Experimental Setup.....	174
7.2	Characterization and Results	177
8	COMPRESSIVE K-SPACE TOMOGRAPHY	186
8.1	Compressive Sensing.....	186
8.2	Compressive k-Space Tomography.....	189
8.3	Numerical Analysis	191
8.4	Experimental Results.....	198
8.5	Conclusion.....	203

9	CONCLUSION	205
9.1	Summary.....	205
9.2	Future Work.....	210
9.2.1	RF Photonic Transmit Apertures.....	210
9.2.1.1	mmW Photonic Phased Arrays.....	210
9.2.1.2	Scalable Integration	211
9.2.1.3	Photonic Feed Network	212
9.2.2	RF Photonic Receive Apertures	213
9.2.2.1	Sparse Calibration	213
9.2.2.2	Accelerated Processing Hardware	213
	REFERENCES	215

LIST OF TABLES

Table 3.1: Comparison of 1×4 CA antenna's photodiode responsivity before and after optical alignment.....	73
Table 6.1: Simulated 3D k-space reconstruction results for the 5-source scene. Measured frequency and AoA positions are in plain text and expected positions are in parenthesis.....	158
Table 6.2: Simulated 3D k-space reconstruction results for the 10-source scene. Measured frequency and AoA positions are in plain text and expected positions are in parenthesis.....	159
Table 7.1: Experimental k-space reconstruction results. Measured values are presented in plain text, and expected values are presented within parenthesis.	184
Table 7.2: Weight-matrix size in terms of k-points, total numerical values, and required memory for three k-space regions. Each value was calculated based on the presented k-space imager resolutions and Nyquist sampling.	185

LIST OF FIGURES

Figure 2.1: Overview of UWB antenna elemental radiator categories.	15
Figure 2.2: Uniform current sheet of current density \mathbf{J} , phase shifting of the current density results in radiation beam steering in the (θ, ϕ) direction.	17
Figure 2.3: Conceptual CSA of adjacent connected-dipole arrays (left) with dipole spatial periods dx and dy , and it's equivalent circuit model (right).	18
Figure 2.4: Equivalent circuit model for TCA of dipoles positioned above a PEC.	21
Figure 2.5: Feed organizer used to route coaxial feed to dual-polarization CSA antenna, from [94], [110].	24
Figure 2.6: Common-, TE ₁₀ - mode resonance introduced by unbalanced feeding (solid arrows mimic current flow, dotted lines depict electric field associated with common-mode resonance.	26
Figure 2.7: (a) External balun linking 50Ω CPW electrical feed and 200Ω CPS of dipole TCA [98], © 2013 IEEE; (b) schematic of 50Ω CPW/coaxial cable connection [98], © 2013 IEEE; (c) UWB balun with microstrip-stripline transition [117], © 2009 IEEE; and (d) Hybrid integrated balun [111] © 2013 IEEE.....	28
Figure 2.8: 28 μm diameter MUTC photodiode fabricated at University of Delaware.	32
Figure 2.9: (a) Bandwidth performance of 28 μm diameter photodiode, and (b) power output of approximately 24.8 dBm at 25 GHz.	33
Figure 2.10: Equivalent circuit representation of photodiode-coupled CA antenna.	35
Figure 2.11: Schematic of photonic radiofrequency signal generation system [130]. Image courtesy of Dr. Garrett J. Schneider.	41
Figure 2.12: UWB phase control optical feed network.	42
Figure 3.1: Infinite array model of photodiode-coupled hybrid bowtie/dipole antenna.....	48

Figure 3.2: Simulated active resistance and reactance results of infinite CA. Solid lines represent resistance and dotted represent reactance.	49
Figure 3.3: Simulated substrate effect in terms of (a) dielectric constant and (b) AlN thickness on active radiation impedance at 20 mA photocurrent. Solid lines represent resistance and dotted represent reactance.	52
Figure 3.4: Bias line network for photodiode-coupled CA antenna, g is the capacitive coupling gap between dipole edges, s_b is the spacing of the bias line from the edge of the dipole, and w_b is the bias line width.	53
Figure 3.5: Active impedance response to s_b sweep, solid lines represent resistance and dotted represent reactance, and surface current distributions at the resonant 23 GHz.	54
Figure 3.6: Effects of inductive peaking on active impedance, solid lines represent resistance and dotted represent reactance, and total radiate power at 20 mA photocurrent.	57
Figure 3.7: Proposed optical feed integration techniques for photodiode-coupled CA antennas. (a) Orthogonal GRIN lens, fiber ferrule, and fiber mating sleeve configuration, and (b) Low profile, parallel prism, GRIN lens, fiber ferrule, and fiber mating sleeve configuration.	58
Figure 3.8: Comparison of RF response of an infinite array element fed by a normally incident optical integration and a prism based integration at 20 mA photocurrent. The 50 Ω ideal output power is 10 dBm, indicated by the dotted line.	61
Figure 3.9: Simulated CA beam steering results at 20 mA photocurrent.	62
Figure 3.10: (a) 1×4 photodiode-coupled CA antenna with optical integration components, and (b) boundary conditions applied for finite modeling. .	63
Figure 3.11: Surface current distribution for a discrete 1×4 photodiode CA antenna model at (a) 5 GHz without flanking resistors (FR), (b) 5 GHz with surrounding 75 Ω FR, (c) 12 GHz w/o, (d) 12 GHz w/ 75 Ω FR, (e) 15 GHz w/o FR, and (f) 15 GHz w/ 75 Ω FR.	65
Figure 3.12: Overview of 1×8 photodiode-coupled CA antenna with integration of low profile optical components linked to feed network.	67
Figure 3.13: Photodiodes thermally and electrically connected to CA antenna.	69

Figure 3.14: Optical alignment setup of the (a) orthonormal optical integration configuration used for the 1×4 CA antenna, and (b) parallel optical integration configuration consisting of a single prism-included GRIN lens assembly and optical fiber through the optical coupling slot of the glass-topped ABS mount. The current supplied by the photodiode is read through probing the white surface mounted flex cable edge of each array.	72
Figure 3.15: (a) 1×4 CA antenna, and (b) low profile 1×8 CA antenna after completing the optical alignment process.	75
Figure 3.16: Packaged (a) 1×4 CA, and (b) low profile 1×8 CA connected to biasing control boards via FFC cables, and the optical inputs to the feed network.	76
Figure 4.1: Schematic of experimental setup. The schematic includes the two-tone input from the TOPS system, optical phase feed network, PD-coupled CA, and photonic receiver unit. Note that the TOPS input does not include the sideband injection process for generation of the RF frequency offset optical signals.	79
Figure 4.2: Image of experimental setup during 1×8 CA antenna characterization. The packaged 1×8 CA antenna is connected to optical fiber inputs from the phase feed network, and an RS-232 cable for photodiode (PD) biasing before being mounted on a rotation stage. Positioned 1 m away from the 1×8 CA antenna in the broadside direction is the horn-coupled photonic receiver.	80
Figure 4.3 Normalization of measured far-field response of the 1×4 photonic CA antenna at various frequencies during electronic steering of a beam -60° to $+60^\circ$ with stationary receiver at 0° [141] © 2017 IEEE.	83
Figure 4.4 Frequency response of the 1×4 photonic CA antenna at 30 mA photocurrent per CC-MUTC photodiode. The ideal 50Ω RF transmitted power at this photocurrent is approximately 18.3 dBm.	85
Figure 4.5: Normalization of measured far-field response at various frequencies during electronic steering of a beam -90° to $+90^\circ$ with stationary receiver at 0° . The angle is representative of the directional setting of the phase shifters in the phase feed network, i.e. the angular offset between the electrically steered main lobe position and the stationary receiver horn.	87

Figure 4.6:	Bandwidth characterization of the array at approximately 8 mA photocurrent per diode (45mA total photocurrent). The ideal 50 Ω RF transmitted power at this photocurrent is approximately 8 dBm.	89
Figure 4.7:	EIRP comparison of ideal 50 Ω array output and measured 1x8 CA antenna output for photocurrents of 8 mA, 20 mA, and 40 mA per photodiode at 13 GHz. Measured values approach the ideal as photocurrent is increased.	89
Figure 4.8:	Normalization of the measured radiation patterns at various frequencies ranging from 5-20 GHz. The dotted lines represent the simulated results; measured results are overlaid with solid lines of the same color. The angle is representative of the broadside position of the physically rotated phased array transmitter relative to the stationary receiver.	90
Figure 4.9:	Low profile optically addressed 1x8 CA antenna beam steering at 16 GHz as it is excited with a total array photocurrent of 45 mA. Measured transmitted RF powers recorded during -90° to $+90^\circ$ broadside rotational scans with concurrent, increment electrical scans to $\pm 30^\circ$ in 10° increments.	91
Figure 5.1:	Mergence physical space and k-space, as a base station senses the k-space representation of the RF environment.	97
Figure 5.2:	Two dimensional k-space representation.	99
Figure 5.3:	Truncated k-space representations for (a) an omnidirectional antenna, (b) a constant gain antenna, and (c) an antenna with a constant effective size.	100
Figure 5.4:	Distinguishable k-space regions based on constant lines of projection for (a) a channelized receiver coupled to a constant gain antenna, (b) an achromatic imaging system, and (c) a hypothetical system comprised of an ideal camera coupled to a channelized receiver.	101
Figure 5.5:	Conceptual representation of an imaging receiver.	104
Figure 5.6:	Optical up-conversion link and the frequency spectrum through the process.	108
Figure 5.7:	Geometrical setup and mapping of RF-encoded optical beam projections between the optical fiber array and CCD camera.	109

Figure 5.8: Squint effects from the phased array antenna effectively appear as chromatic aberration in the imaging receiver, where incident RF waves with same AoA, but different frequency are reconstructed at different positions in the image plane.	115
Figure 5.9: Incident RF waves are imaged in k-space by the imaging receiver as projections of 3D wave-vectors onto a 2D image plane of the lens. The chromatic aberration is realized through the scalar projection of each k-vector onto the RF imaging axis.....	117
Figure 5.10: (a) The view of k-space from an imaging receiver is based on the system's ability to only sense projections onto the RF imaging axis, collapsing incident RF waves along lines of constant k_x . (b) At the image plane, each pixel corresponds to a particular line of constant k_x projection.....	118
Figure 5.11: Introduction of a linear optical fiber length progression across the array steers the achromatic axis of the imaging receiver.....	119
Figure 5.12: (a) The view of k-space from an imaging receiver with a linear optical fiber length distribution distorts projection lines based on achromatic axis tilt. (b) At the image plane, each pixel corresponds to a particular line of constant projection comprised of mixed k_x and k_z values.....	119
Figure 5.13: (a) Stereoscopic imaging of k-space is created by splitting output from EO modulator into two opposing linear optical fiber length progressions across the array, effectively forming two non-parallel achromatic axes. (b) As a result the distorted projection lines created by each linear progression are combined as one set of non-parallel lines of constant projection.....	121
Figure 5.14: Introduction of an arbitrary optical fiber length distribution behind the RF frontend creates a different projection of k-space at each pixel in the CCD camera at the image plane.	125
Figure 6.1: Distributed-aperture configurations (left) and corresponding PSF (right) for the (a) concentric hexagonal pattern, and (b) five-arm spiral pattern.	133
Figure 6.2: Schematic of original 35 GHz passive mmW imager. Blue lines indicate optical signal paths, red lines indicate RF signal paths, thin green lines indicate singular electrical signal paths, thick green lines indicate electrical signal array paths, and red blocks indicate free-space paths.	135

Figure 6.3: ALTS antenna S11 measurements over operational bandwidth.	138
Figure 6.4: Measured RF Lambda LNA (a) gain, (b), noise figure, (c) flat phase response calibrated at 33 GHz, and (d) flat phase response of a single LNA over a time period of 45 min.	139
Figure 6.5: Measured Covega, Inc. EO phase modulator (a) conversion efficiency, and converted to (b) half-wave voltage assuming 50 Ω impedance.....	140
Figure 6.6: Component configuration within the distributed-aperture for (a) LNA gain, (b) LNA NF, and (c) modulator conversion efficiency. The color bar in these three panes represent the measured value for the respective figure of merit. (d) Simulated PSF, and a (e) PSF comparison for the k-space imaging receiver and original passive mmW imager.	142
Figure 6.7: Component configuration and PSF response.....	145
Figure 6.8: Spatio-temporal aperture with arbitrary optical fiber lengths coupled to each receiver channel in the distributed-aperture array.....	146
Figure 6.9: Node-based k-space scene used for calibration. Each discrete point represents an AoA/frequency pair that is projected onto the image plane, from which the inteferogram is compiled into the weigh-matrix.....	149
Figure 6.10: Kaczmarz algorithm convergence with respect to signal density in the k-space visible by the receiver. The black dotted line, representing a 1% change between iterations, serves as an empirically defined cut-off for a well reconstructed scene [171] © 2018 IEEE.....	152
Figure 6.11: Simulated 2D k-space amplitude distribution reconstructions for a (a) 10-source scene, (b) 25-source scene, (c) 50-source scene, and their respective peak detection results in (d-e). Each scene is reconstructed using the required number of iterations.....	155
Figure 6.12: Simulated 2D k-space amplitude distribution reconstructions for a (a) 10-source scene, (b) 25-source scene, (c) 50-source scene, and their respective peak detection results in (d-e). Each scene is reconstructed using the required number of iterations for a 25-source scene.....	156
Figure 6.13: Simulated 3D k-space amplitude distribution reconstructions for a (a) 5-source scene, (b) 10-source scene. Each scene is reconstructed using the required number of iterations.	157

Figure 6.14: (a) Comparison of old and new RF frontend components, and the complete up-conversion module shown in (c) with optical and electrical input highlighted in (b).....	161
Figure 6.15: Distributed-aperture RF frontend for the (a) original 35 GHz passive mmW imager, and (b) upgraded 26 – 40 GHz k-space imaging receiver.	162
Figure 6.16: (a) Side view of the distributed-aperture, with a white arrow indicating the direction that the up-conversion modules are physically moved, and (b) an example fringe interference pattern produced when two channels are on, the black arrows indicate the fringe drift direction, if the path lengths are not equal.....	163
Figure 6.17: (a) Original motion controller and driver setup with a National Instruments NI UMI-7774 Universal Motion Interface and Aries AR-02AE drivers. (b) Updated motion controller and driver setup with a Galil DMC-2030 motion controller and Aries AR-02AE drivers.....	165
Figure 6.18: (a) Initial distributed-aperture steel framing, and (b) new, lighter, aluminum framing.	166
Figure 6.19: Example positions of the mechanically steered distributed-aperture. ..	167
Figure 6.20: Finalized spatial aperture for the Ka-band distributed-aperture k-space imaging receiver.	167
Figure 6.21: One of the four housing populated with temporal aperture channels. ..	168
Figure 6.22: Complete temporal aperture, installed into the imaging receiver, with optical fiber inputs from the up-conversion modules and outputs to the optical fiber array.	169
Figure 6.23: (a) 19” equipment rack housing the control CPU (top), DFB laser, power supply, two EDFAs, splitter network, and rotation stage control components (bottom). (b) Distributed-aperture k-space imaging receiver spatio-temporal aperture.....	171
Figure 6.24: Distributed-aperture k-space imaging receiver optical processor.....	172
Figure 6.25: (a) Phase alignment FPA board, (b) FPGA used for controlling phase feedback and component biasing, and (c) bias distribution board coupled to each LNA and EO modulator.	172

Figure 7.1:	(a) Isometric view of \mathbf{k} -space cross configuration. (b) Side view of elevation and frequency sampling points. (c) Top-down view of azimuthal and frequency sampling points.	175
Figure 7.2:	Calibration scene depicting broadside positioning of the calibration source at 2 m from the five-spiral distributed-aperture.	176
Figure 7.3:	Experiment RF scenes consisting of (a) azimuthal only, (b) elevation only, and (c) both angular direction emitter locations.	177
Figure 7.4:	Camera responses (left) corresponding to reconstructed amplitude distributions (right) for two emitters in the azimuthal plane.	180
Figure 7.5:	Camera responses (left) corresponding to reconstructed amplitude distributions (right) for two emitters in the elevation plane.	181
Figure 7.6:	(a) Camera response from a source scene comprised of two emitters, one in the azimuthal plane, and one in the elevation plane, with both emitters transmitting at 28 GHz. Corresponding reconstructions for (b) azimuthal plane cross-section, (c) emitter plane cross-section, and (d) elevation plane cross-section.	182
Figure 7.7:	(a) Camera response from a source scene comprised of two emitters, one in the azimuthal plane, and one in the elevation plane, with both emitters transmitting at 39 GHz. Corresponding reconstructions for (b) azimuthal plane cross-section, (c) emitter plane cross-section, and (d) elevation plane cross-section.	183
Figure 8.1:	Numerical analysis results for compressive \mathbf{k} -space tomography in terms of (a) reconstruction time as a function of compression ratio for different algorithm iteration counts, and reconstruction error as a function of compression ratio at different levels of sparsity for algorithm iteration counts of (b) 10 iterations, (c) 25 iterations, and (d) 50 iterations [171] © 2018 IEEE.	194
Figure 8.2:	Numerical simulation reconstruction for a scene of sparsity $S = 1$, completed with 5 iterations of the Kaczmarz algorithm under different levels of compression. (a) Ideal non-compressed scene reconstruction completed with error = 0, and $t \approx 1.8$ s, (b) compressed scene with $M/N = 0.1$, error = 0, and $t \approx 195$ ms, (c) compressed scene with $M/N = 0.01$, error = 0, and $t \approx 22$ ms, and (d) compressed scene with $M/N = 0.005$, error = 0, and $t \approx 12$ ms. The colorbar in each pane corresponds to the intensity of a resolved source in arbitrary units [171] © 2018 IEEE. ...	196

Figure 8.3: Numerical simulation reconstruction for a scene of sparsity $S = 5$, completed with 10 iterations of the Kaczmarz algorithm under different levels of compression. (a) Ideal non-compressed scene reconstruction completed with error = 0, and $t \approx 3.5$ s, (b) compressed scene with $M/N = 0.1$, error = 0, and $t \approx 350$ ms, (c) compressed scene with $M/N = 0.05$, error = 0, and $t \approx 180$ ms, and (d) compressed scene with $M/N = 0.01$, error = 0.5, and $t \approx 40$ ms. The colorbar in each pane corresponds to the intensity of a resolved source in arbitrary units [171] © 2018 IEEE. ... 197

Figure 8.4: Experiment simulation reconstruction for a scene of sparsity, $S = 2$, with two 28 GHz sources positioned along the azimuthal plane at 0° elevation, with one at -2.5° and the other at 4.0° . (a) Ideal non-compressed scene reconstruction with sources at detected 28 GHz, -2.4° and 28 GHz, 4.0° in 17.06 s, (b) compressed scene with $M/N = 0.1$, and sources detected at 28 GHz, -2.4° and 28 GHz, 4.0° in 1.71 s, (c) compressed scene with $M/N = 0.01$, and sources detected at 28 GHz, -2.4° and 28 GHz, 4.0° in 185 ms, and (d) compressed scene with $M/N = 0.005$, and sources detected at 28 GHz, -2.4° and 28 GHz, 4.0° in 99 ms. Black dots are the reconstructed source in k-space, and circle centers indicate actual position of the emitter. The colorbar in each pane corresponds to the intensity of a resolved source in arbitrary units [171] © 2018 IEEE. 201

Figure 8.5: Experiment simulation reconstruction for a scene of sparsity, $S = 2$, with one 39.5 GHz source positioned at -2.5° along the elevation plane at 0° azimuth, and one 28 GHz source positioned at 4.0° along the elevation plane at 0° azimuth. (a) Ideal non-compressed scene reconstruction with sources at detected 39.5 GHz, -2.4° and 28 GHz, 4.0° in 17.62 s, (b) compressed scene with $M/N = 0.1$, and sources detected at 39.5 GHz, -2.4° and 28 GHz, 4.0° in 1.91 s, (c) compressed scene with $M/N = 0.01$, and sources detected at 39.5 GHz, -2.4° and 28 GHz, 4.0° in 181 ms, and (d) compressed scene with $M/N = 0.005$, and sources detected at 39.5 GHz, -2.4° and 28 GHz, 4.0° in 105 ms. Black dots are the reconstructed source in k-space, and circle centers indicate actual position of the emitter. The colorbar in each pane corresponds to the intensity of a resolved source in arbitrary units [171] © 2018 IEEE. ... 202

ABSTRACT

For decades, phased array antenna technology has served as the main platform for controlling the directionality and shape of electromagnetic energy in accordance to application specific tasks. Modern development of these systems has shifted focus towards phased arrays that perform all operations through multifunctional apertures, which simultaneously support radar, RF sensing, imaging, and ultra-fast wireless communication links. While technological research and development efforts pertaining to this goal has mostly manifested within military applications, the advent of 5G deployment has spurred recent interest in adopting comparable functionality requirements, and phased array configurations, to satisfy the needs these of next generation wireless communications networks. In particular, the transition to mmW frequency operation in multiple-input multiple-output (MIMO) networks, at a massive scale, drives new systems to be highly integrated, fast scanning apertures, with low size, weight and power (SWaP), to dynamically support multiple users with low latency and fine phase resolution. Unfortunately, the design requirements concomitant with this paradigm shift in commercial wireless communications have exposed many difficulties inherent to the deployment of traditional electronic systems.

In this work, two novel RF photonic aperture designs are proposed for integration into spatially-coherent phased array architectures to facilitate 5G wireless networking. One RF photonic aperture comprises a highly integrated photodiode-coupled phased array transmit antenna which transfers the optical-to-electrical

conversion process directly to the antenna's radiating elements. By directly coupling high-power charge-compensated modified uni-traveling carrier (CC-MUTC) photodiodes at each antenna element, bulky and expensive RF cables, which are fundamentally limited at mmW frequencies by loss, can be replaced with light weight, low-loss, and electromagnetic interference immune optical fibers. As a result, remote deployment of phased array antennas with sufficient RF output powers and beamsteering capability, over multiple 5G spectral bands, is realizable. The efficacy of this approach is presented through low SWaP photonic connected array antennas designed for wide scan operation over 5 – 20 GHz.

The second RF photonic aperture consists of a Ka-band phased array receive antenna coupled to a temporal aperture. By integrating this spatio-temporal aperture into an imaging system, the simultaneous detection of radio waves' frequency and angle of arrival is enabled through coherent optical processing. This newly developed imaging modality, referred to as k-space tomography, uses fiber-length dispersion in conjunction with a distributed antenna array to provide unique spatio-temporally encoded CCD-captured interferograms, from which a computational tomographic reconstruction of the RF signal environment can be obtained for newly allocated 5G bands. A key aspect of this work is using the sparsity of RF spatial and spectral distributions in the electromagnetic environment to merge this imaging modality with established compressive sensing techniques. By adapting specific characteristics of this methodology, and applying them to k-space tomography, compressive k-space tomography is developed. As a result, reconstruction data size and processing time are reduced significantly, without loss of information, for low latency spatial-spectral utilization mapping.

Chapter 1

INTRODUCTION

1.1 Phased Array Background

In RF wireless technology it has become progressively more desirable to control the directionality and shape of electromagnetic (EM) energy in accordance to application specific tasks. Efforts to attain these capabilities relate back to early array beam steering concepts proposed between 1899 and 1903 [1], where specific time delays were introduced at elements within an antenna array for coherent summation at a desired angle. These ideas remained in their original conceptual form until early development of radar technology in the 1930s and 1940s, where mechanically tuned phase shifters enabled re-steerable configurations to replace large, heavy reflector systems [2], [3]. Further advancement in phased array technology, through military applications, occurred throughout the 1950s and 1960s at MIT Lincoln Labs, and led to the development of non-mechanical beamsteering through ferrite phase shifters [4], [5]. Electronically steerable antenna technology formulated from these discoveries, combined with cost effective integrated solutions developed under the MMIC program at the Defense Advanced Research Projects Agency (DARPA) in the 1980s and 1990s, have since become a foundation of modern RF remote sensing and communications.

More recently, this evolution of phased array technology has driven concomitant next generation system demands to include a multitude of goals. Generally, such requirements are compressed into three primary groups [6]. The first desirable feature is multi-functional operation, meaning the phased array aperture is capable of

supporting simultaneous operations in radar, RF sensing, imaging, and communication through independent beams across several octaves of frequency. Secondly, the technology must adapt extensions in operational bandwidths toward the millimeter wave (mmW) regime as applications expand out of congested frequency space below 6 GHz. Lastly, phased array systems are required to consistently improve size, weight, power, and cost (C-SWaP) to meet a new multitude of deployment scenarios that may require small form-factor, conformality, and high element counts. While technological research and development efforts pertaining to the above trends have mostly manifested within military applications, the advent of 5G deployment has generated interest in adopting comparable functionality requirements, and phased array configurations, to satisfy the needs of next generation wireless communications networks [7].

1.2 Considerations for 5G Wireless Communications

Similar to phased array technology, commercial wireless communications have experienced a substantial evolution since inception [8], [9]. Since the 1980s, each decade has comprised foundational expansion to continually adapt to growing data traffic, which is projected to surpass wired connection transfers within the current year [10]. Accordingly, wireless communication networks are set to undergo a new phase of transformation during the deployment of 5G wireless technology, which is expected to push metrics far beyond those seen in 4G systems. These include gigabit per second data rates, ubiquitous access with a connection density of 1 million users per square kilometer, low latencies extending to the millisecond range, and improvements in spectral and energy efficiencies [11]. To achieve such demands, several disruptive technologies have been selected as focus points: small-cell architectures constructed in the form of ultra-dense networks (UDNs), spectrum access extension into the mmW

regime, and integration of massive multiple-input, multiple-output (MIMO) into base station (BS) systems.

Recently, the Federal Communications Commission (FCC) opened up licensed spectrum from 27.5 – 28.35 GHz, 37 – 38.6 GHz, and 38.6 – 40 GHz, and an unlicensed band at 64 – 71 GHz for 5G [12]. In addition to these, seven additional bands ranging from 24 – 86 GHz have been proposed for consideration [12]. By introducing high-dimensional MIMO at these frequencies, the short wavelengths enable formation of dense, spatially isolated data channels spanning large volumes for simultaneous non-interfering communication links [13], [14]. As a result, the spatial orthogonality of sector-defined narrow, high-gain beams affords substantial improvements in energy efficiency and spectral utilization, in addition to data capacity.

Based on this desirable functionality, it is evident that phased array antennas must play a crucial role in this wireless communications paradigm shift. As with the network level deployment, these apertures need to satisfy their own set of requirements for deployment in ultra-dense mmW massive MIMO networks [15]: 1) highly integrated, with low C-SWaP; 2) fast scanning apertures must be capable of dynamically monitoring user-space to optimize beam channel configurations; 3) fine phase resolution; 4) back end processors will utilize pre-stored algorithms to meet low latency requirements; and 5) each phased array needs to be able to provide support to multiple users.

1.3 Spatial Beamforming

In general, multi-beamforming architectures can be categorized as either analog or digital. Analog multi-beam phased array antennas are simply an expansion of early phased array antennas designed to form and steer a single beam [16], and operate

through either RF phase shifting, intermediate frequency (IF) phase shifting, or baseband phase shifting. Of the three techniques, RF phase shifting is the most common method implemented, and consists of phase shifting or transmission path length tuning for spatial beam forming at carrier frequencies. A conventional RF analog beamforming network consists of N antenna elements, and M RF channels, where each antenna is coupled to each RF channel through a phase-shifter channel. With the shift towards the mmW regime, it has been shown that RF analog beamforming circuitry can be integrated onto a single chip, provided the number of beams is limited [17]. Furthermore, it has been demonstrated that this integrated circuitry is capable of dynamically controlling the directionality and number of beams, and supports up to four simultaneous beams [18]. To improve performance at the element-level, a wide variety of variable phase shifting components have been designed based on CMOS and GaAs platforms [19]. However, one common disadvantage with these phase-shifting components, and variable attenuators often included for amplitude control, is that each device experiences poor isolation, inaccuracies in beam generation due to temperature-related phase drift, and insertion loss, which increases when operating frequencies progress into the mmW regime.

To improve upon particular aspects of analog beamforming, IF and baseband phase shifting have been investigated [20]–[22]. Each method allows for the use of cheaper phase-shifting components, and results in a reduction in insertion losses; however, wideband true-time delay circuits demonstrated in RF phase shifting [23], are not realizable at baseband. Consequently, IF and baseband phase shifting circuitry typically induces phase offsets in antenna distributed local oscillators (LO) [24]–[26]. Similar to the RF phase shifting case, a conventional IF/baseband analog beamforming

network consists of N antenna elements, and M LO channels, where each antenna is coupled to each LO through mixers. This common theme stands as an overarching limitation within analog beamforming. For the RF phase shifting case, the number of beams generated are limited based on the fact that the number of required phase shifters is equal to the product of the number of antenna elements and RF channels, or $M \times N$. In the case of IF or baseband phase shifting, the number of beams is limited since the number of required mixers is equal to twice the product of number of antenna elements and LO channels, due to mixing of both in-phase and quadrature components. Thus, while integrated analog approaches enable the capability to dynamically control the directivity and form of beams, practical implementation into large dense arrays for massive MIMO creates overly expensive and bulky systems.

Digital beamforming (DBF) stands as the alternative method with improved flexibility and agile beamforming, which reduces the required number of mixers to be equivalent to the number of RF channels, and operational capability during low-count channel failure [27]–[29]. With the recent advancements in integrated circuitry for digital signal processing, such as FPGAs, DBF systems have become the leading candidate for multi-beam generation in massive MIMO [30], [31]. However, full DBF systems quickly encounter limitations with respect to analog-to-digital converters (ADCs) and digital-to-analog converters (DACs) and digital signal processing (DSP) for the desired channels counts in massive MIMO base station antennas [29]. In addition to this, if ADCs and DACs are placed at each channel, DBF systems will become cost-prohibitive and require an immense amount of power. Further disadvantages in DBF become apparent when analyzing transmit and receive portions of the system separately.

On the transmit side, a DAC supplies I/Q information to each channel within the DBF network of LOs, mixers, amplifiers, and antenna elements. The first issue in this configuration stems from the LOs. In order to form multiple beams with minimal imperfections, LO amplitude and phase needs to be synchronized across each channel; however, non-idealities in the components routinely leads to phase drifting that causes degradation in beam shape and directionality accuracy. Similar errors are also commonly experienced with the DAC from nonlinearities in the form of clock jitter, or quantization error. It is possible to improve channel synchronization, and mitigate the aforementioned issue; however, synchronization circuitry increases the signal routing intricacy, and may require additional amplifiers, which risk the introduction of nonlinearities that affect other performance metrics, such as adjacent channel leakage ratio.

On the receive side, the RF frontend, consisting of antennas and low-noise amplifiers (LNAs), captures signals that are subsequently conveyed through filters, and depending on the processing method, undergo a down-conversion process prior to being input to an ADC. Integrated circuitry for digital signal processing, subsequently analyzes the digitized channel signals for reconstruction of spatial-spectral channel information. The primary difficulty with digital beamforming stems from data transfer limitations as channel counts and receive bandwidth increase, where the upper bound of the number of beams that can be simultaneously processed by the digital beamformer is computationally confined based on the beam bandwidth product. Furthermore, assuming the ADC and digital signal processing circuitry are even capable of managing 5G data rates and bandwidth, quantization errors in the ADC introduce a lower bound on the noise floor in each mmW communication channel. This fundamental limitation

places more stress on development of efficient algorithms to maximize the remaining SNR [32], in addition to algorithms already required for high phase resolution multi-user direction finding and complex weighting matrix formulation.

At this point, it is apparent that neither analog nor digital beamforming currently serve as the sole technological solution to mmW massive MIMO requirements. For this reason, many have proposed to merge them into a hybrid beamforming configuration with reduced system complexity [33]–[35]. In these beamforming architectures, the nature of the beamspace is either static, or dynamic, i.e., the feed network is either fixed phase or has tunable phase. For the latter case, the beamforming network limitations are the same as mentioned above for active analog beamforming with discrete tunable phase shifter components. Contrarily, passive, static beamforming networks eliminate the need for active phase-shifting devices by utilizing time-delay-based lens apertures, where a set of isolated, transceiver-coupled input ports control predetermined directional beams. Collectively, the beams generated from each port concurrently radiate out of a continuous aperture in a multi-beam configuration.

Initial development of these passive beamforming apertures started with basic concave, bifocal, and spherical lens configurations [36]–[40]. Later on, designs became more complex with graded-index geodesic lenses, such as the Luneberg lens and half Maxwell fish-eye lens [41], [42]. In these designs, 2D beam forming is achieved by conforming antennas directly to the lens surface. Using this technique, the Luneberg lens has already been implemented into beamspace MIMO applications [43]. An alternative lens-based passive beamformer configuration comprises integrated input/output ports on opposite sides of the lens for improvements in antenna and feed network integration. Rotman lenses are the most well studied of this type [44], [45], and

have already been introduced into hybrid beamforming architectures for 5G massive MIMO [46], [47].

While coupling lens-based passive analog beamformers to a digital transceiver architecture has arisen as a viable option for massive MIMO, the shared lens apertures introduce several detrimental factors, many of which stem from large number of beams required within 5G networks. More specifically, generating hundreds of beams over a broad angular range, where desired coverage is as high as 120° , is not practical for lens-base systems, as this would require compact installment of antennas within an extraordinarily large aperture. In addition to poor SWaP, this configuration is also prone to mutual coupling and phase error that will significantly degrade beamforming. Furthermore, these techniques do not necessarily relieve the burdens of ADC and DSP processing performance at the backend, which are a common component set in high phase resolution, multi-user direction finding [48]–[52].

1.4 Microwave Photonics for 5G Wireless Communications

Collective consideration of the 5G network and mmW massive MIMO phase array antenna requirements, along with existing multi-beamforming methods, depicts current technological developments is lacking the capability to satisfy the versatile requirements of next generation wireless networks. This, combined with the fact that the disruptive technology proposed is completely unprecedented, creates an opportunity to introduce an entirely new paradigm for solutions. One particularly well-suited for this application is microwave photonics.

The field of microwave photonics has now progressed through over three decades of research focused on leveraging optical fiber transmission's superior loss, bandwidth, and immunity to EM interference for improvements in microwave

technology [53]–[60]. In general, microwave photonics comprises analog system operation; therefore, much of the development has revolved around component and link linearization [55], [61]–[67] for efficient wideband signal distribution [68]–[70]. Conveniently, these demonstrations, which are well understood by the microwave photonics community, align with requirements for high-fidelity 5G wireless network formulation, and serve as a natural fit for the aforementioned deployment of ultra-dense MIMO networks operating at mmW frequencies.

RF-over-fiber is commonly used for broadband data distribution, and currently exists as a core component in small-cell networks. These networks have been demonstrated with information transmitted through RF-, IF-, and digital-over-fiber [59], [71], [72], allowing simple integration with existing beamforming methodology. Microwave photonic architectures also naturally accommodate the expansion to mmW frequencies, as the complete mmW regime is a small fractional bandwidth of standard telecomm laser sources, i.e., a conceptual data bandwidth residing between 30 – 300 GHz is $< 0.2\%$ of the 1550 nm optical carrier signal. As a result, there have been several demonstrations of optical-fiber based signal distribution systems operating within the mmW regime [73]–[75].

While significant progress has been made with respect to mmW signal distribution in small-cell networks, the beamforming architecture still remains as one of the bottlenecks in massive MIMO deployment. Most demonstrations of beamforming at mmW frequencies for microwave photonic platforms have relied on passive beamforming elements like reflector antennas and lenses [76]–[78], or optical fiber true-time delay (TTD) methods [79]–[81]. In the previous sections, the implications of using passive beamforming elements have been discussed, and reflector arrays carry similar

limitations as lenses, in addition to potential blind spots from the device structure. As for optical fiber TTDs, this method is most likely counterproductive for 5G wireless communications, as the large beam numbers required would necessitate complicated routing circuitry for a fractional data bandwidth small enough for simple, tunable phase shifters not limited by beam squint.

In addition to these beamforming considerations, RF photonic antennas have generally been limited to low-power applications. This is a consequence of particular designs attempting to compensate for low-power photodetectors with RF amplifiers at mmW frequencies [82]. Implementation of RF amplifiers prior to the antenna feed also introduces complications in phased array feeding at higher allocated 5G frequencies around 60 GHz, especially if these antennas are to efficiently cover multiple bands. However, through recent developments in high-power photodiode research, charge-compensated uni-traveling carrier (CC-MUTC) photodiodes have demonstrated output powers over 1 W at 10 GHz under continuous wave operation [83], 10 W at 10 GHz under pulsed power [84], and 100 mW at 60 GHz [85]. Given the significant RF output power enabled by these photodiode, and superior bandwidth, conversion efficiency, and linearity with respect to standard RF amplifiers [86], it is possible to completely eliminate the amplifier stage of previous designs.

Provided the same can be accomplished with an electro-optic modulator, extremely dense, high element-count RF photonic phased array antennas can be designed due to the fact that array feeds solely consist of small, light, and low cost optical fiber. As a result, highly integrated mmW phased arrays can be remotely deployed into small-cell networks at a massive scale with hybrid beamforming feed networks installed far away from BS towers. Additionally, by designing the network

around microwave photonics, spatial imaging techniques, well-known within the optical community, can be opportunistically integrated into the hybrid beamforming system.

1.5 Dissertation Outline and Original Contributions

The work within this dissertation concentrates on two separate RF photonic aperture designs pertinent in facilitating 5G wireless network demands, and collectively satisfying the aforementioned phased array antenna requirements. One RF photonic aperture comprises a highly integrated photodiode-coupled phased array transmit antenna to transfer the optical-to-electrical conversion proximal to the antenna input. The other RF photonic aperture consists of a distributed-aperture phased array receiver coupled to an optical fiber, temporal aperture for accurate spatial-spectral utilization mapping of user-space through simple computational reconstruction free of ADCs. Realization of beamforming in these apertures comes from the ability to up-convert all transmitted and received RF signals using an analog process that preserves spatial coherence across the entire array and over a broad bandwidth, where subsequent pairing with lens based processing techniques effectively enables a continuum of spatial beams at the system output. The culmination of each aperture with this processing method sets the foundation for a new RF photonic discipline – spatially-coherent phased array antennas.

The presented work is divided into two parts. The first part focuses on an RF photonic transmit aperture, where much of the novel design work was developed as part of a M.S. Thesis. The second part focuses on an RF photonic receive aperture, and introduces a new imaging modality, referred to as k-space tomography. Accordingly, organization of the Chapters is as follows:

Chapter 2 discusses the fundamental components relating to the RF photonic transmit aperture, and corresponding analog beamforming network. This begins with a discussion of ultra-wideband (UWB) antenna arrays, namely connected array (CA) and tightly coupled array (TCA) antennas, and high-power CC-MUTC photodiodes. The formulation of a photodiode-coupled CA antenna, and figures of merit are subsequently presented. Lastly, the optical RF source, and phase feed network used throughout this work are described.

Chapter 3 describes the process of designing UWB CC-MUTC photodiode-coupled CA antennas, which is exemplified for a 5-20 GHz operational bandwidth design. The presented design is then fabricated in two separate transmit phased array configurations: one 4-element array with normally incident optical coupling, and one low-profile 8-element array with parallel optical coupling.

Chapter 4 describes the experimental setup and processes utilized in characterization and analysis of each fabricated photonic CA antenna. Performance metrics analyzed throughout experimental testing include operational bandwidth, maximum effective isotropic radiated power, radiation patterns, and steering range.

Chapter 5 discusses the fundamentals of k-space tomography, where an RF photonic receive aperture is used for spatial-spectral utilization mapping of RF signals. This begins with a mathematical formulation of time- and space-varying field representations, along with an introduction to k-space. The techniques for spatial processing are described through a proposed imaging receiver architecture, and methods for inclusion of simultaneous spatial and spectral processing is elaborated on. From the spatial-spectral processing basis, the technique of coupling a spatial aperture to a unique

temporal aperture and utilizing computational methods to reconstruct the RF signal environment is presented.

Chapter 6 includes the process of designing and fabricating a Ka-band distributed-aperture k-space imaging receiver. The configuration of the RF photonic spatial-spectral receive aperture is described in detail, and performance metrics associated with design parameters are discussed. A numerical model of the system is constructed, and used to analyze the efficacy of the proposed imaging system for spatial-spectral sensing. The system architecture, components and operational flow of the experimental system are also presented in detail.

Chapter 7 comprises the calibration routine, experimental setup, and test scenes used to characterize the Ka-band distributed-aperture k-space imaging receiver. Various RF signal distributions, with emitters operating within newly allocated 5G frequency bands, are reconstructed to provide spatial and spectral aspects of each source. Methods for quantifying the new system's reconstruction performance are included as well.

Chapter 8 includes a novel adaptation of k-space tomography through integration of compressive sensing techniques into the reconstruction process. The general methodology of compressive sensing is presented to aid in the formulation of compressive k-space tomography. Numerical analysis of the adaptation is discussed, and the performance metrics created are analyzed for various signal distributions. The learnings in the numerical simulation study are subsequently applied to experimental demonstrations.

Lastly, Chapter 9 summarizes the key contributions presented throughout this dissertation, and future research opportunities and suggestions are discussed.

Chapter 2

RF PHOTONIC TRANSMIT APERTURE FUNDAMENTALS

2.1 UWB Phased Array Antenna

For modern RF antenna systems, it is desired to replace overabundant narrowband devices, commonly grouped into overly complicated, large, heavy, and costly systems and networks, with a singular UWB, low profile, wide-scanning aperture. As mentioned recent development of such arrays encompasses several trends and requirements [6]: 1) multi-functionality, i.e., supporting various applications through multiple radiating elements with polarization flexibility over independently steerable beams; 2) bandwidth extension towards operating frequencies into the mm-wave regime to escape congested bands (<6 GHz), affording improved data rates due to relative bandwidth scaling, i.e., 5% relative bandwidth at 60 GHz is much greater than 5% relative bandwidth at 5 GHz; 3) emphasis on size, weight, power, and cost (C-SWaP).

Substantial efforts to satisfy these requirements through UWB array antennas have been demonstrated by Vivaldi or tapered-slot antennas arrays (TSA) [87]–[89], bunny-ear antennas [90]–[92], fragmented antennas [93], and dipole connected and tightly coupled arrays (CA) (TCA) [94]–[98]. Overall performance and characteristics of each of these arrays as a whole are a function of the selected elemental radiator. Thus, it is important to understand the unique advantages afforded by the presented elemental radiating elements, a collective categorization is displayed in Figure 2.1.

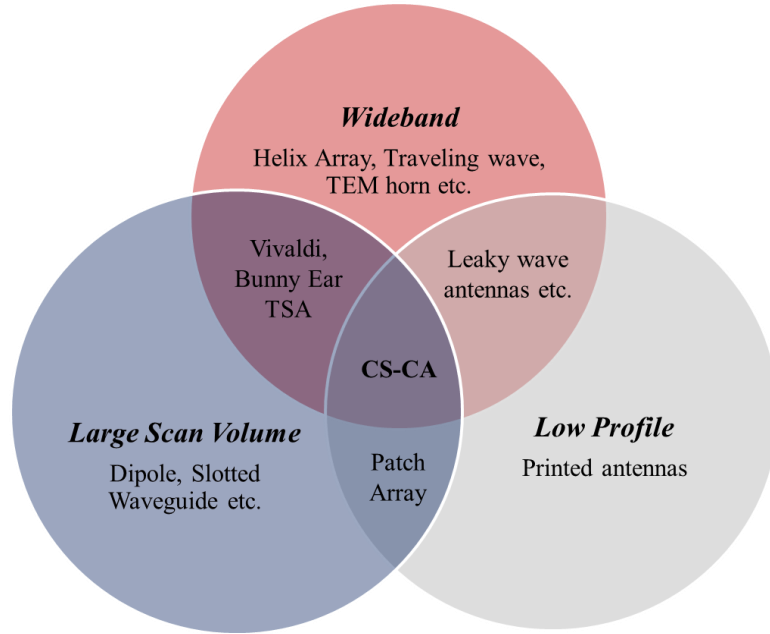


Figure 2.1: Overview of UWB antenna elemental radiator categories.

The first generation of these designs primarily consisted of TSAs and bunny-ear antennas integrated into traditional phased array antennas. This type of phased array configuration employs weakly coupled elements, acting as independently isolated elements in the near-field with superposition contribution to the array's far-field radiation pattern. At higher frequencies, these weakly coupled arrays endure bandwidth degradation due to grating lobes. In an effort to prevent these grating lobes and extend operational bandwidth, elemental radiator spacing can be reduced; however, this introduces detrimental mutual coupling at lower frequencies. Furthermore, coaxial cable based feeding often limits the reduction in elemental radiator spacing unless complex feed network components are introduced. In addition to these cumulative phased array effects, each elemental radiator from this first generation of design introduces additional factors which reduce particular performance metrics. For example TSA arrays typically

suffer from high profile, high-order resonance induced modes, and high cross-polarization in the E- and H-planes. Mitigation of scan blindness while maintaining a comparable operational bandwidth can be achieved with the bunny-ear antenna. Unfortunately, while these types of antennas address the UWB problem, each is limited by the inherent size necessary to achieve high gain. Not only does this characteristic restrict low profile design architectures, scanning ranges are still limited in comparison to other antennas, such as inherently low profile planar dipoles. Furthermore, the feeding system of these antennas, specifically the bunny-ear array, requires baluns, *i.e.*, balanced to unbalanced transformers, for connection of coaxial cables to a parallel strip-line input. Consequently, the operation bandwidth and SWaP becomes constrained by balun functionality, a problem common with electrically fed UWB array antennas.

2.1.1 Current Sheet Arrays

In an effort to improve phased array antenna performance of the next generation of UWB phased arrays, Wheeler systematically studied electronically scanned arrays via infinite array models [99], [100]. In 1948, Wheeler proposed that an infinite array, shown in Figure 2.2, formulated as a sheet of uniformly polarized current, J , with constant phase, will produce identical bidirectional broadside radiation of two TEM-mode plane waves across all frequencies. Through phasing the lines of current, the broadside radiation can be steered in two principle planes, *i.e.*, the x,z and y,z planes.

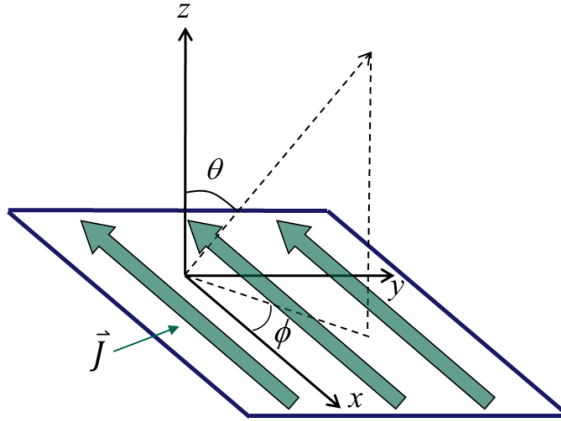


Figure 2.2: Uniform current sheet of current density \mathbf{J} , phase shifting of the current density results in radiation beam steering in the (θ, ϕ) direction.

This current sheet array (CSA) was viewed by Wheeler as the space limit of closely spaced dipole elements, popularly used for their low cross-polarization and profile properties, into parallel conductive strips. Modeling of this effect into the CSA concept was initially accomplished through infinite parallel plate waveguides, with PEC walls defining the dipole array unit cells' boundaries. The active impedance of these waveguides was determined to be equal to the ratio of the effective height of the antenna over the physical rectangular cross-sectional area, multiplied by the intrinsic impedance of free-space [99]. By designing equivalent square unit cells, and factoring in the CSA's inherent bidirectional radiation, the input impedance becomes half of the plane-wave impedance of free space ($R_o = 188 \Omega$). As the current is phased, the radiation impedance of the TE- and TM-modes become $R_o \cos\theta$ and $R_o / \cos\theta$, respectively, resulting in an antenna impedance proportional to beam direction and not operational frequency, *i.e.*, a theoretically infinite relative bandwidth [100]. This scan angle dependent impedance

can be interpreted as the effective waveguide dimensions being changed as the beam is directed away from broadside.

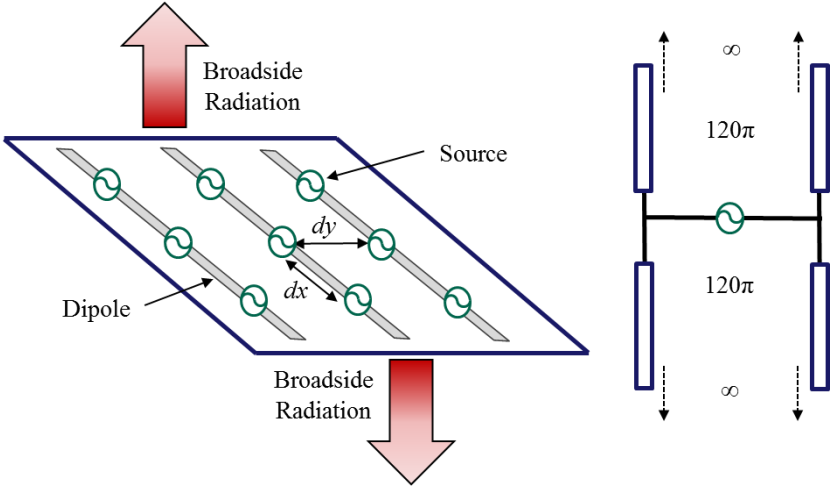


Figure 2.3: Conceptual CSA of adjacent connected-dipole arrays (left) with dipole spatial periods dx and dy , and its equivalent circuit model (right).

In practice, a CSA can be realized by populating an array of equally spaced adjacent infinitely-connected dipole elements, referred to as a CA, as illustrated in Figure 2.3. It is important to note that the terminology, “connected,” is indicative of the spacing between elements being small enough to consider a short at RF frequencies. This dipole array’s input impedance is formulated to [96]

$$Z_{in} = \frac{d_x}{d_y} \frac{k_0 \eta_0}{2} \sum_{m_x=-\infty}^{+\infty} \frac{\text{sinc}^2\left(\frac{k_{xm} t}{2}\right)}{(k_0^2 - k_{xm}^2) \sum_{m_y=-\infty}^{+\infty} \frac{J_0\left(k_{ym} \frac{w_s}{2}\right)}{\sqrt{k_0^2 - k_{xm}^2 - k_{ym}^2}}}, \quad (2.1)$$

where d_x and d_y represent the dipole spatial periods along the x and y axis, k_0 is the wavenumber in free space, η_0 is the impedance of free space, J_0 is the Bessel function of the zeroth order, k_{xm} and k_{ym} are the x - and y - wavenumber components of the m^{th} order spatial harmonic or Floquet mode, and t and w_s are the thickness and width of the infinitely long dipoles. By fundamental mode approximation, *i.e.*, $m_{x,y} = 0$, which becomes dominant at lower frequencies, *i.e.*, $k_0 \rightarrow 0$, the sinc and Bessel functions can be simplified to an approximate value of 1. Combining this fundamental mode approximation with the scanning angle relations of the x - and y - wavenumber components, the input impedance of the dipole array is represented as [96]

$$Z_{in} \approx \frac{d_x}{d_y} \frac{\eta_0}{2} \frac{\cos \theta}{1 - \sin^2 \theta \sin^2 \phi}, \quad (2.2)$$

eliminating frequency dependence, and confirming the CSA's relative theoretical infinite bandwidth, while approaching a more realizable design. It is important to note, that when the dipoles approach lengths proportional to the operating wavelength, this approximation of Equation 2.1 no longer holds, and the CSA inherits a frequency dependent impedance bandwidth. Based on this, dipoles are commonly designed at half-wavelength spacing at the highest desired operating frequency to preserve this infinite CSA approximation through an ultra-wideband that is cut-off at a low frequency response determined by the size of the aperture.

Further advancement of the CSA into real-world applications as a CA of dipoles involves implementation of a ground plane to focus radiation into one of the two bidirectional radiation directions, improving power efficiency and reducing interference from feed network components. However, introduction of a ground plane into the CA antenna significantly changes the input impedance by introducing a strong frequency dependence, consequently reducing bandwidth capabilities. When a PEC is placed below a CA of dipoles, the input impedance's reactance becomes strongly inductive, and the radiation resistance approaches zero toward lower frequencies, *i.e.*, since the distance to the ground plane becomes electrically smaller, the array eventually becomes short circuited to the ground plane. Therefore, the reduced bandwidth capability is primarily a product of these low frequency effects. In order to accurately and efficiently analyze these effects for future design considerations a more thorough model is required.

Equivalent circuit modeling of dipole array antennas began with CSA antenna circuit analyses done by Munk [101]. Figure 2.4 illustrates an updated equivalent circuit model for the infinite array of dipoles backed by a ground plane, where C_{cp} is the capacitance between adjacent dipoles and L_{dp} is the self-inductance of the dipoles [102]. In the original equivalent circuit model, Munk did not account for the effects of the dipole feed. Therefore, shunt capacitance, C_{dp} , and inductance, L_f , were introduced to account for dipole feed coupling. By incorporating these circuit model properties, the antenna impedance can be derived using Equations 2.3-2.7:

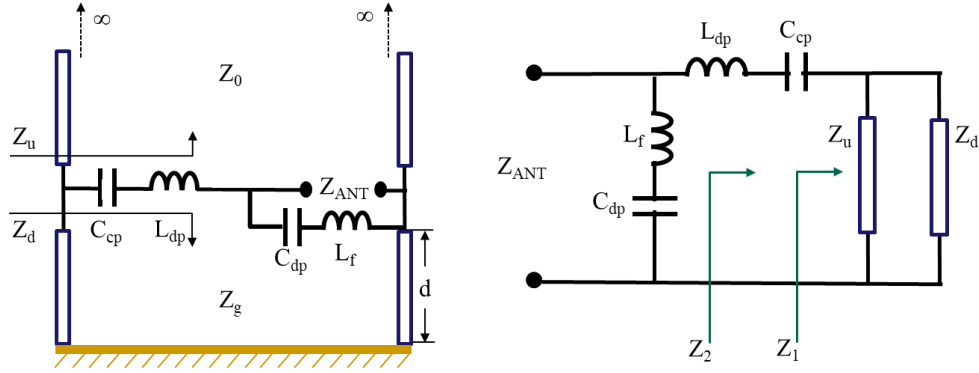


Figure 2.4: Equivalent circuit model for TCA of dipoles positioned above a PEC.

$$Z_u = Z_0 \quad (2.3)$$

$$Z_d = jZ_g \tan(\beta_g d) \quad (2.4)$$

$$Z_1 = Z_u \parallel Z_d \quad (2.5)$$

$$Z_2 = Z_1 + j\omega L_{dp} + \frac{1}{j\omega C_{cp}} \quad (2.6)$$

$$Z_{ANT} = \left(j\omega L_f + \frac{1}{j\omega C_{dp}} \right) \parallel Z_2 . \quad (2.7)$$

The introduced frequency dependent impedance can now be realized by the relation of Equation 2.4, *i.e.*, the input impedance of transmission line (TL) traveling through a medium of impedance Z_g shorted at a distance d away from the input. As the frequency is shifted towards DC, the ground plane distance becomes electrically smaller until the array of dipoles becomes shorted. In addition to this, once the ground plane distance is effectively less than $\lambda/4$, the impedance becomes inductively dominant due to the tangent function in (2.4). Ideally, this strongly inductive reactance added into the antenna circuit would be cancelled out by introducing a negative inductance [103].

However, Munk refrained from increasing the complexity of the dipole feed to obtain negative impedance through active elements, instead proposing a coupling capacitance between the dipole ends to counteract the ground plane inductance at a targeted frequency within the operational bandwidth [104], [105]. By designing the coupling-ends as interdigital capacitors, the added capacitance could be greatly increased, and precisely controlled to cancel out the ground plane inductance at low frequency. Use of this circuit model analysis and the dipole coupling capacitance introduced by Munk has afforded an increase in the previous 2.5:1 bandwidth limit to 4.5:1 [94]. It is important to note that this capacitive technique is responsible for the separation of the terms *connected array* and *tightly coupled array*.

Since the initial development of the bandwidth broadening capacitive coupling technique, additional modern TCA design features have been proposed for further extension of operational bandwidth, as well as other phased array metrics, such as steering range and polarization flexibility. To accomplish these goals, impedance halving methods, such as oversampling the unit cells in the array to reduce antenna impedance towards a standard $50\ \Omega$ input, have been utilized [94], [106]. This technique not only produces improvements in bandwidth, but adds potential for polarization flexibility [95], [107], [108]. Another method is to introduce additional components, e.g. “R-cards” or frequency selective surfaces, to shield ground plane effects, and add a superstrate layer in front of the array to direct radiation away from the ground plane.

Incorporation of these components has enabled increases in beam steering range up to 70° [109], and the combination of the two afforded bandwidths up to 21:1 [95].

2.1.2 Current Sheet Array Feeding

Although the advantages seen in demonstrations of the CA and TCA are superior in terms of bandwidth, scan volume, and profile to other UWB antenna array designs, multiple challenges are faced to efficiently excite of the radiating elements. The primary difficulty with array feeding is the fact that a standard $50\ \Omega$ coaxial cable is not suitable. The dipole elements within CA and TCA antennas are referred to as “balanced antennas” due to their symmetric geometry. Thus, a balanced feed, *i.e.*, symmetric transmission lines supplying dipole arms with current of equal magnitude and opposing phase, is necessary to match the balanced nature of the dipoles in order to maintain a uniform current distribution. Traditional power sources driving RF antennas employ coaxial cable RF feeding links with components designed at a standard $50\ \Omega$ impedance. Unfortunately, coaxial transmission lines are inherently unbalanced resulting in a non-zero net current flow on the outer conductor, which may produce undesired common-mode radiation.

One of the earlier techniques of suppressing these undesirable common mode currents from the coax feed was integrating a “feed organizer” to route $50\ \Omega$ coaxial cables to the radiating elements [94], [110]. The feed organizer, displayed in Figure 2.5, was fed with two pairs of cables, where outer conductors were grounded to the metal structure while inner conductors were directly connected to the dipole. On the back-end of the cables, $0/180^\circ$ hybrid circuits enable a method for supplying the correct phase to each dipole arm [94]. Although this device is able to suppress common mode radiation that degrades array radiation, its physical structure degrades the low profile properties

of dipole-based CSA antennas. Additionally, mechanical tolerances limit use of feed organizers to lower-frequencies [111].

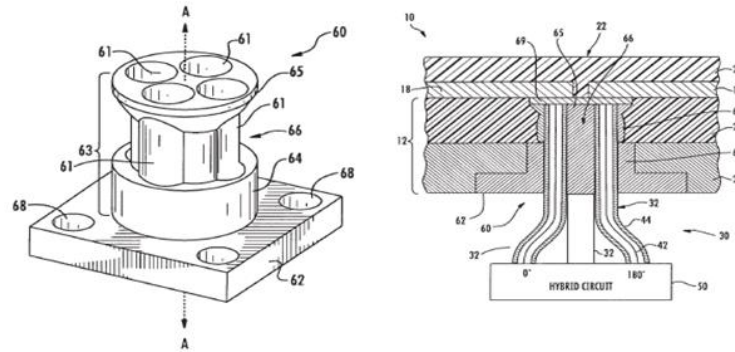


Figure 2.5: Feed organizer used to route coaxial feed to dual-polarization CSA antenna, from [94], [110].

A different method of introducing a balanced feed directly with a coaxial cable without the bulky feed organizer and external hybrid circuit is presented in [112]. In this design, the dipole array is directly connected to a coaxial cable whose outer conductor is soldered to the ground plane, while the inner signal conductor is connected to a coplanar strip (CPS) feeding one of the dipole arms. Coupling the unbalanced coaxial cable to the balanced CPS/dipole produces a radiating TE_{10} -mode resonance (common-mode) via a non-zero net current in the CPS lines, as displayed in Figure 2.6. The solid lines represent the current flow through the CPS and dipoles, and the dotted lines represent the electric field distribution in the mode whose resonant frequency can be formulated as [112]

$$f_{cm} = \frac{c_o}{2\sqrt{\epsilon_{eff}} \sqrt{D_x^2 + D_y^2}}, \quad (2.8)$$

where D_x and D_y is the spacing between coaxial feed points, and the ϵ_{eff} is the effective dielectric constant between the planes.

Calculation of the fundamental common-mode resonant frequency results in a frequency component located within the desired operational bandwidth. To circumvent this issue, shorting posts were introduced next to the coaxial cable signal feeds between the dipole and ground plane, enabling a shift of the resonance to higher frequencies by decreasing D_x and D_y [112]. Utilizing this method has afforded a 6:1 bandwidth [113]; however, in conjunction with higher bandwidth array antennas this method becomes a limiting factor of the antenna unit, leading to restrictions in application. More prevalent is the issue of scalability towards high frequency operation, due to the tight fabrication tolerances. Additionally, this method does not inherently include any impedance transformation techniques to match the 50Ω coaxial cables. Thus, necessary integration of a dielectric substrate thickened the array by a factor of two, reducing the attractive low profile nature of the original CSA-based design. Moreover, if this dielectric substrate does not possess a low dielectric constant, resonances can be reintroduced into the operational bandwidth.

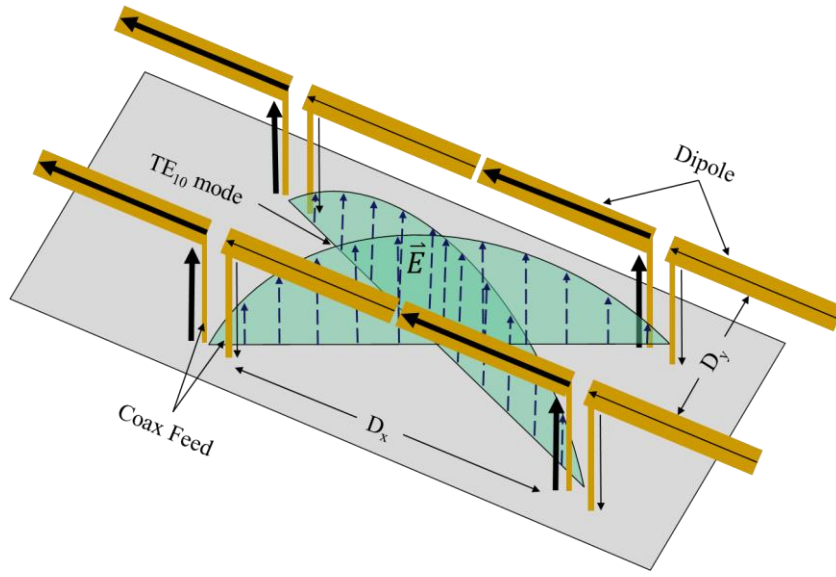


Figure 2.6: Common-, TE_{10} - mode resonance introduced by unbalanced feeding (solid arrows mimic current flow, dotted lines depict electric field associated with common-mode resonance).

Thus far, electrical feeding techniques discussed have primarily focused on introducing components to compensate, or control the spurious monopole radiation stemming from a directly integrated unbalanced coaxial cable. One detail neglected by these methods is the approximate 4:1 impedance mismatch between CA/TCA antennas and coaxial cables. In order to satisfy both impedance matching and balanced feed requirements balanced-to-unbalanced transformers, or “baluns”, can be implemented between each coax/antenna element link.

Even though a balun resolves two inceptive difficulties, it is a simplistic solution for a challenging problem and tends to introduce trade-offs between operational frequency, bandwidth, profile, and weight. External baluns have proven capable of performing coplanar waveguide (CPW)/coplanar stripline (CPS), 200Ω to 50Ω transitions; however, this accomplishment comes paired with insertion losses up to 3

dB and operational frequency restrictions (< 600 MHz) [98]. In contrast, integrated baluns, such as ones based off the coupled ring hybrid design [114]–[116], provide a planar balanced feed with low insertion loss and high operational frequencies. Precise engineering of the paired feed wires, designed in sync with dipole elements, allows for these advantages, but also introduces limited bandwidth due to the strict dimensional requirements of the ring-hybrid. Lastly, UWB Marchand baluns have been developed for high operational frequencies and bandwidth through tapering a microstrip to CPS [117]. Unfortunately, the tapered feed length necessary for operation is proportional to multiple wavelengths of the bandwidth ceiling frequency, making this approach unsuitable for operation in the mm-wave regime.

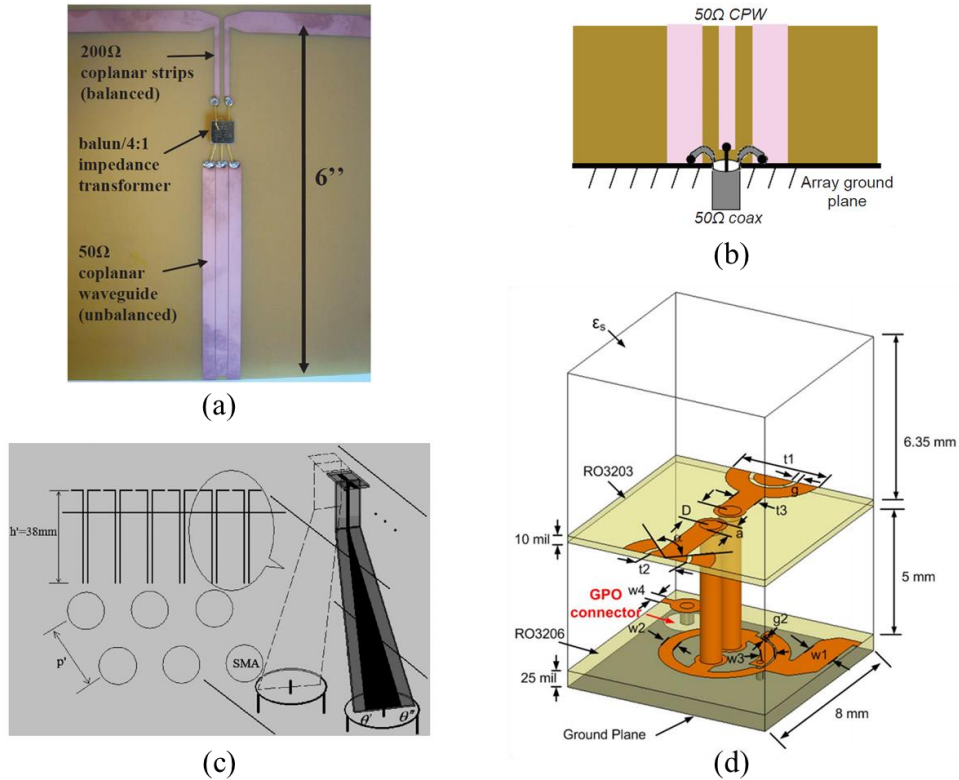


Figure 2.7: (a) External balun linking 50Ω CPW electrical feed and 200Ω CPS of dipole TCA [98], © 2013 IEEE; (b) schematic of 50Ω CPW/coaxial cable connection [98], © 2013 IEEE; (c) UWB balun with microstrip-stripline transition [117], © 2009 IEEE; and (d) Hybrid integrated balun [111] © 2013 IEEE.

Optical excitation of antenna arrays serves as an alternative to conventional electrically addressed arrays, as recent advances in microwave electronics corresponding to progressions in communication applications have drastically increased system complexity. Eventually increases in application needs will push microwave electronics towards limitations in multiple areas. First, source tunable range of voltage controlled oscillators are restricted primarily to narrowband ranges. Next, data capacity controlled by Nyquist-Shannon sampling theorem shows data rates are set by carrier

frequencies which is a primary bottleneck for microwave electronic communications. Lastly, these rapidly growing systems quickly exceed minimum SWaP requirements due to bulky, expensive RF cables yielding a substantial 360 dB/km propagation loss factor [53].

Lasers, low loss silica fibers, and low noise optical amplifiers promise capabilities of THz regime data transmission with propagation losses <0.5 dB/km, presenting a theoretically frequency independent platform for high-speed communications [118]–[120]. Lasers' bandwidth enabling tuning capabilities alone categorize photonics as a “natural fit” for high frequency/data rate applications with a common comparison of 1 nm tuning being equivalent to 125 GHz bandwidth at 1550 nm. Furthermore, optical fibers light weight and immunity to EMI aid in improving SWaP and efficiency in future systems. Additionally, leveraging these point-to-point advantages of optical fiber communications in conjunction with microwave frequency range atmospheric attenuation properties permits advancement of microwave systems without the same limitations previously mentioned. This interplay between optical and microwave frequency regimes is the basis of the rapidly growing microwave photonics discipline.

These advantages can be leveraged by directly integrating a photodiode into each antenna element, eliminating the need for any RF feed network. Thus, bulky and expensive RF cables can be replaced with optical fibers. Furthermore, maintaining a balanced signal towards each antenna is straightforward by using a photodiode integrated proximal to each radiating element. This eliminates common-mode resonance, which typically disrupts electrically fed array operation, thereby making bandwidth-limiting baluns unnecessary.

Furthermore, tightly spaced photodiodes provide a nearly ideal current source, allowing close approximation to Wheeler’s theoretical current sheet, which would otherwise not be possible using conventional electrical feeding at high frequencies and operational bandwidths. However, the introduction of an optical feed network does not eliminate the difficulties in designing wideband antenna arrays, it only shifts them from the RF circuitry to the photodiode. Robust and efficient alignment of high-power optical inputs to high frequency, micron-scale photodiodes can be challenging without introducing some loss into the system. Notably, introducing a ground plane behind the array while maintaining a fiber-feed to the photodiodes is a concern. Each photodiode also requires a carefully applied bias across their junctions for efficient high power operation. If the bias lines are not designed appropriately they can introduce resonances of their own into the RF system, limiting array bandwidth analogous to the common-mode resonances seen with electrical feeding. Fortunately, while these problems are non-trivial, solutions have been proposed in the literature [121]–[123], and appropriate design and fabrication techniques, presented in the subsequent sections, can effectively deal with these issues.

2.2 High Power Photodiodes

Historically, the biggest deterrent in the adoption of optically fed arrays has been the low RF power output per antenna element, *i.e.*, the power handling of the photodiodes. While commercial photodiodes can achieve bandwidths between 50 and 100 GHz, frequency regimes that would make for impressive arrays, their output powers are typically limited to less than 10 dBm. For optically fed arrays to be routinely integrated into functioning systems, high-power photodiodes are a necessity for solving

this fundamental power output problem of transmit antennas. To this end, state of the art high-power, charge-compensated uni-travelling carrier (CC-MUTC) photodiodes have recently been designed by the University of Virginia [124], [125] to enable output powers over 1 W at 10 GHz under continuous wave operation [83] and 10 W at 10 GHz under pulsed power [84].

In order to achieve these high RF output powers, the CC-MUTC photodiode InP/InGaAs epitaxial structure was strategically designed [124]. By configuring the epitaxy as that of a uni-traveling carrier device [126], a fast diode response is afforded through the high saturation velocity of electrons in InP, which act as the sole active carriers in the drift/collection region. In addition to the inherent high-frequency nature of the UTC structure, high RF power operation at these frequencies is realized by introducing a “charge-compensation” layer. This layer predistorts the electric field within the junction to prevent collapse of the photodiode bias at high photocurrents. Lastly, inclusion of a “cliff-layer” reduces heterojunction field breakdown at the InGaAs/InP interface. Due to this epitaxial design, RF output power is primarily limited by thermal burnout of the device, *i.e.*, the photodiode overheats at high photocurrents, rather than space-charge effects; hence the aforementioned power handling improvements through time-multiplexing the optical input to the photodiode using pulsed power modulation [84].

In order to leverage the exceptional power handling of the MUTC photodiodes for array excitation, the transmitting aperture must be designed with thermal management in mind. This requirement can be satisfied, while retaining an adequate platform for integration into a phased array antenna, through flip-chip bonding the photodiodes to high-thermal conductivity substrates. Implementation of a gold-gold

thermo-compression bonding technique has been routinely demonstrated as an optimal process for mitigation of thermal effects in solo photodiode devices with materials such as aluminum nitride (AlN) (190 W/(m·K)) and diamond (2200 W/(m·K)).

One more key thing to address with respect to thermal device effects is the tradeoff between maximum RF output power and operational bandwidth. The tradeoff stems from thermal dissipation and capacitive characteristics attributed to photodiode diameters [83]. Optimal thermal dissipation occurs in devices fabricated with large diameters; however, increasing this design parameter results in larger capacitance in the device circuit, and consequently reduces the operational bandwidth. Based on this tradeoff, photodiode diameter needs to be carefully selected to maximize RF output at the specific operating frequencies of the antenna array.

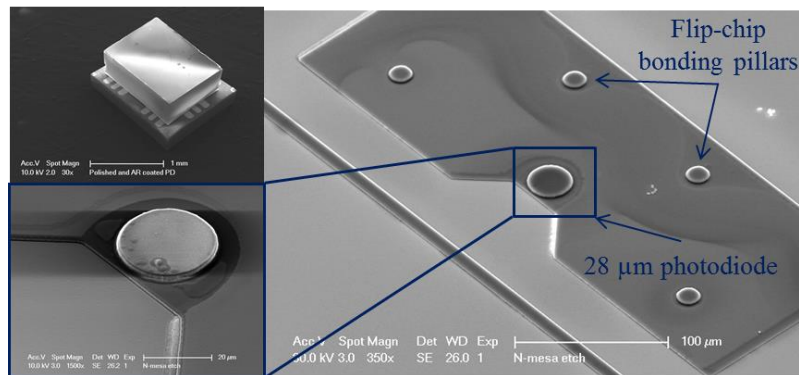


Figure 2.8: 28 μm diameter MUTC photodiode fabricated at University of Delaware.

While taking into account these design considerations, CC-MUTC photodiodes and flip-chip bond pads were fabricated at the University of Delaware, in collaboration with UVA [127], to facilitate integration of the devices onto a phased array antenna platform. Figure 2.8 illustrates a fabricated 28 μm diameter photodiode both before and

after gold-gold thermo-compression bonding onto AlN bond pads. AlN was selected as the focus for the presented RF photonic transmitting aperture development due to the fact that diamond is significantly more expensive, and difficult to process for antenna fabrication and photodiode integration.

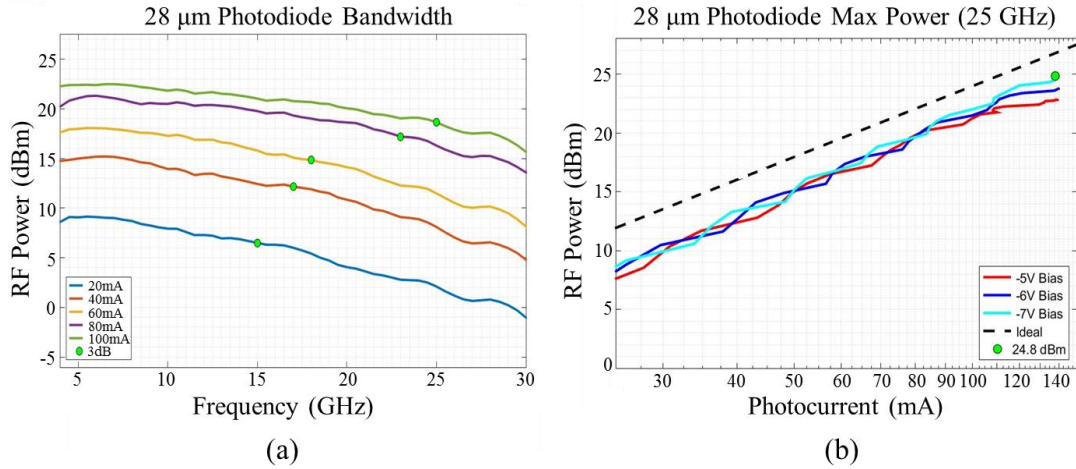


Figure 2.9: (a) Bandwidth performance of 28 μm diameter photodiode, and (b) power output of approximately 24.8 dBm at 25 GHz.

Upon completion of the fabrication process, the unpackaged photodiodes are characterized to ensure adequate operation prior to antenna integration. In the bandwidth characterization of the 28 μm diameter photodiode presented in Figure 2.9 (a), it is important to emphasize two points about the operation. First, at low frequencies the RF output power is approximately the ideal RF power,

$$P_{RFideal} = (m_{\omega} I_{PD})^2 R_{LOAD}, \quad (2.9)$$

where m_ω is the modulation depth, I_{PD} is the DC photocurrent, and R_{LOAD} is the load resistance. In the case presented here, $m_\omega = 1$, and $R_{LOAD} = 50 \Omega$ based on the equal power of the heterodyning laser sources, and the RF power meter's standard input impedance, respectively. Second, the bandwidth of the photodiode increases with photocurrent. This relationship arises due to increased electron carrier velocity induced through an induced electric field formed within the photodiode absorption region during high photocurrent operation. Quantification of this effect can be realized through the relation of high-frequency photocurrent with carrier transit time as a function of frequency [128]:

$$i_{PD}(f) = I_{PD} \frac{1 - e^{j2\pi f \tau_r}}{j2\pi f \tau_r}, \quad (2.10)$$

where I_{PD} is the low-frequency photocurrent, f is the frequency, and τ_r is the carrier transit time.

After characterizing the bandwidth performance of the CC-MUTC device, the maximum RF output power is characterized at the 3-dB bandwidth of the specific diameter photodiode. As displayed in Figure 2.9 (b), the RF output power of the 28 μm diameter photodiodes were tested at a constant frequency of 25 GHz, with an increasing optical input. This process is repeated at several reverse-bias voltages up for peak unsaturated power output until thermal failure due to the product of DC photocurrent and bias voltage. The maximum RF power measured for the 28 μm diameter devices, flip-chip bonded to AlN, at the University of Delaware was 24.8 dBm at 25 GHz under a 7 V bias, while the maximum recorded value for this device is 25.0 dBm under a 7.5 V bias [129].

2.3 Photodiode-Coupled Antennas

Utilizing CSA concepts and MUTC photodiodes presented in the previous section, a photodiode-coupled CA antenna can be realized through the conceptual CSA design illustrated in Figure 2.2, where the current sources exciting the dipole elements are photodiodes. Each photodiode is modeled as a parallel ideal current source and capacitor circuit. The CA antenna is represented by the impedance relation derived in the previous section, and changing Equation 2.4 to $Z_d = Z_o$ due to the absence of a ground plane. Connecting each of these equivalent circuits in parallel affords a representation of the photodiode-coupled CA antenna, as shown in Figure 2.10. Analysis of this equivalent circuit model provides the necessary terms to evaluate the performance of the photodiode-coupled antenna, namely radiated power, bandwidth, and power efficiency.

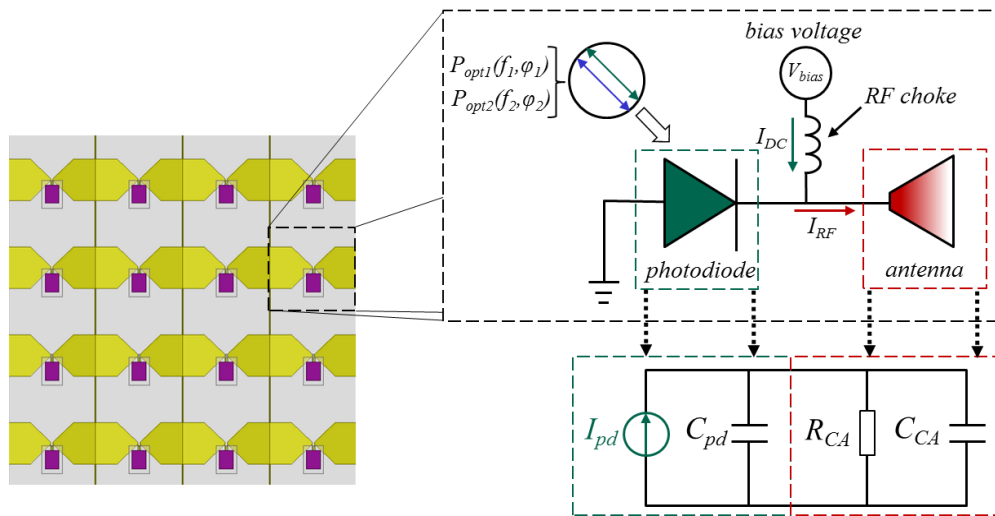


Figure 2.10: Equivalent circuit representation of photodiode-coupled CA antenna.

2.3.1 RF Output Power

Further illustration in Figure 2.10 shows the photodiode provided concurrently with reverse biased through an inductor, *i.e.*, rf choke, and an incident two-tone optical signal to generate photocurrent given by

$$I_{pd}(f_{RF}) = \Re \sqrt{2P_{opt1}P_{opt2}} H(f_{RF}) e^{j(2\pi f_{RF}t + \varphi_{RF})}, \quad (2.11)$$

where $f_{RF} = f_{opt1} - f_{opt2}$ is the frequency and $\varphi_{RF} = \varphi_{opt1} - \varphi_{opt2}$ is the phase of the RF photocurrent, while \Re and $H(f_{RF})$ represents the photodiode responsivity and frequency response, respectively. This current will subsequently drive the CA antenna element to radiate RF power, represented as

$$P_r(f_{RF}) = \frac{\frac{1}{2} I_{pd}^2 R_{CA}}{1 + (2\pi f_{RF} R_{CA} (C_{pd} + C_{CA}))^2}. \quad (2.12)$$

Both circuit terms, R_{CA} and C_{CA} , for the CA antenna can be extracted from infinite array simulation results. The maximum radiated power can be realized by shifting operational frequency toward DC:

$$P_{r\max}(f_{RF}) = \frac{1}{2} I_{pd}^2 R_{CA}. \quad (2.13)$$

2.3.2 Bandwidth

The frequency response, $H(f_{RF})$, enables the photodiode capacitance to be estimated as:

$$C_{pd} = \frac{1}{100\pi B_{pd}}, \quad (2.14)$$

where the term B_{pd} represents the 3-dB bandwidth of the photodiode loaded with a load of 50Ω , $R_L = 50 \Omega$:

$$B_{pd} = \frac{1}{2\pi R_L C_{pd}}. \quad (2.15)$$

Next, the operational frequency range of the photodiode-coupled CA antenna is determined by the cutoff frequency, f_c , marking 3-dB roll off of radiated power. This operational bandwidth is conveyed as

$$BW = f_c = \frac{1}{2\pi R_{CA} (C_{pd} + C_{CA})}. \quad (2.16)$$

From these expressions, it is apparent that there is a trade-off between radiated power and bandwidth in relation to impedance. In a practical sense, this trade-off will be balanced by selecting the largest photodiode capable of satisfying antenna bandwidth requirements for maximized radiated power within that band. Furthermore, the bandwidth and radiation power per photocurrent squared can conveniently be used as a figure of merit for both photodiode-coupled CA antenna performance and transmission information capacity [123]:

$$\frac{BW \cdot P_{r\max}}{I_{pd}^2} = \frac{1}{2\pi(C_{pd} + C_{CA})}. \quad (2.17)$$

Although the theoretical basis of bandwidth as a figure of merit is, in a general sense, uniformly used to characterize phased array antenna operation, a fundamental difference between photonic and purely electronic antennas creates a divide in measurement and analysis methodology. Since the photonic CA antenna is designed to be excited by an integrated photodiode, the standard method of measuring and characterizing the bandwidth based on the voltage standing wave ratio (VSWR), or S_{11} , is not realistic. While the CA antenna itself could be probed to obtain these parameters,

the response would provide an inaccurate representation of the photonic CA antenna's bandwidth performance, as it neglects effects from the internal circuit of the photodiode.

As an alternative, the photonic CA antenna bandwidth is characterized by a continuous frequency region with a transmitted RF power variation limited to 3-dB, which is analogous to 3-dB impedance bandwidth. Quantifying bandwidth in this way provides a more instructive representation of the photonic CA antenna's frequency-dependent RF power output responses at different photocurrent values. Furthermore, bandwidth measurements at discrete photocurrent excitation levels are more practical, as any significant variation in antenna impedance bandwidth would require adjustments in photodiode bias voltages to avoid photodiode saturation. It is important to note that the RF output power can be greater than the upper limit of the 3-dB bandwidth range; a distinct difference from a standard 3-dB roll-off response, e.g. CC-MUTC bandwidth response. This is in fact the case for the CA antennas discussed here, where radiation resistance at low frequencies approaches the theoretical value of 188Ω , while high-frequency responses are design to be lower in resistance for efficient radiated power.

Since this specific method of defining operational bandwidth is different than the metrics commonly seen in literature, it is important to compare the photonic CA antenna figure of merit with the standard VSWR metric. The baseline value set for electrically excited antenna bandwidth is a 2:1 VSWR, with UWB antennas often being characterized to 3:1, or greater. These VSWR values scale to a RF power variation limited to ranges of 6-dB and 9-dB, respectively. Thus, a direct comparison to electrically fed antennas can be made through extending the 3-dB range to either value;

however, in the work presented throughout this dissertation, each photonic CA antenna is characterized to the originally stated 3-dB range.

2.3.3 Power Conversion Efficiency

Another figure of merit for the antenna is the ratio of radiated RF power, P_r , to total power consumption, referred to as power conversion efficiency (PCE):

$$\eta = \frac{P_r}{P_{opt1} + P_{opt2} + P_{dc}} . \quad (2.18)$$

The total power consumed by the photodiode-coupled CA antenna consists of total incident optical power, $P_{opt1} + P_{opt2}$, and DC power product of the reverse bias voltage and DC photodiode current, P_{dc} . In order to maximize radiated power, each two-tone signal optical power component should have equal power, *i.e.*, $P_{opt} = P_{opt1} = P_{opt2}$, and the photodiode should be supplied with a minimum bias voltage, $V_{minbias} \approx \sqrt{2}I_{ph}R_{CA}$, to minimize the DC power consumption to:

$$P_{DC} \approx \sqrt{2}\mathfrak{R}P_{opt}I_{pd}R_{CA} . \quad (2.19)$$

Using these conditions, the maximum RF PCE is equated to:

$$P_r(f_{RF}) = \frac{\Re^2 H^2(f_{RF}) I_{opt} R_{CA}}{1 + 2\Re^2 H^2(f_{RF}) I_{opt} R_{CA}}, \quad (2.20)$$

resulting in a theoretical PCE limit of 0.5.

2.4 Photonic Feed Network

2.4.1 UWB Tunable Photonic RF Signal Generation

In order for the MUTC photodiodes to provide optically fed arrays with the RF power output to be competitive with conventional electrically fed systems, the diodes need to be excited using a low-noise RF source. Simple heterodyning of 2 lasers onto the photodiodes would result in excess system noise and spurious beam generation that would limit system performance at high-output powers. Therefore, an injection-seeding based source to correlate phase noise between the feed lasers, and greatly suppress spurious noise, developed at the University of Delaware has been selected for microwave photonic signal generation. This tunable optical paired source (TOPS) is capable of providing signals from 0.5 to 110 GHz with a linewidth <1 Hz, indicating ultra-low phase noise [130].

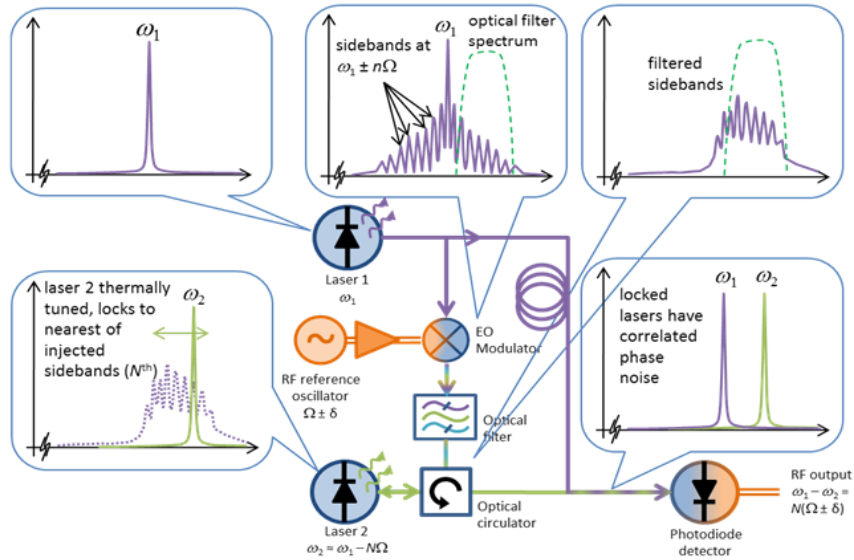


Figure 2.11: Schematic of photonic radiofrequency signal generation system [130]. Image courtesy of Dr. Garrett J. Schneider.

As illustrated in Figure 2.11, the TOPS system utilizes two semiconductor lasers capable of being thermally tuned over THz ranges for necessary wide tuning abilities in heterodyne detection on the photodiodes. However, for high-purity signal generation, the heterodyne process needs to incorporate two coherent optical signals. This can be accomplished by modulating a local oscillator (LO) reference signal onto a master laser, filtering out the carrier and lower modulation-sideband comb, and injecting the upper modulation-sideband comb into the slave laser. The slave laser is tuned to within locking range of one of these sidebands, which correlates the phase noise between the 2 lasers. If equal channel path length is assumed, it is possible for the optical phase noise produced through the spontaneous emission process to be cancelled when the lasers interfere at the photodiode. By using this technique, precise tuning of the reference oscillator and rough thermal tuning of the slave laser affords selection of modulation-

sideband harmonics, which results in widely tunable, spectrally pure, low-noise RF carriers that form the basis for the phase control network discussed in the next section.

2.4.2 Phase Control Network

This low-noise TOPS can be used in conjunction with a dual-polarization, optical interleaving feed network to provide the MUTC photodiodes with a clean RF signal [20]. The network exploits polarization maintaining (PM) fiber, and polarization dependent phase modulators, to mitigate the effects of acoustic vibration on the incident fiber-optic signals. Additionally, the photocurrent from the MUTC diodes can be monitored to provide feedback to the feed network's polarization controllers in order to suppress phase drift. This novel feed architecture [131] combined with the practically unlimited bandwidth of optical fiber can be used to simultaneously drive multiple high-fidelity beams over a wide operational bandwidth.

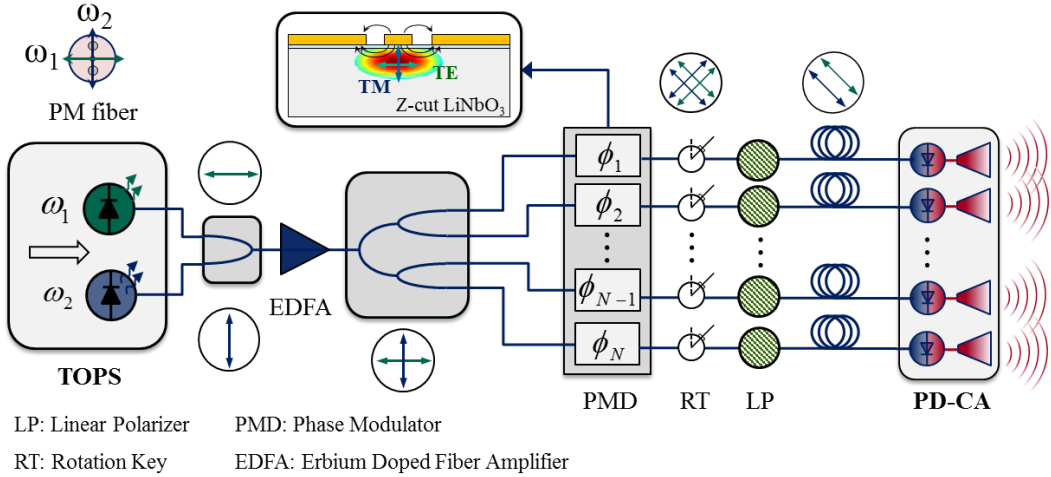


Figure 2.12: UWB phase control optical feed network.

The optical phase feed network, displayed in Figure 2.12, begins with two coherent optically paired sources of frequency ω_1 and ω_2 launched orthogonally on the fast and slow axes of a single PM fiber, yielding the following optical signal:

$$E_0 = \hat{x}E_x e^{j(\omega_1 t + \varphi_1(t))} + \hat{y}E_y e^{j(\omega_2 t + \varphi_2(t))}, \quad (2.21)$$

where E_x and E_y are the electric field magnitudes located in the slow and fast axes of the PM fiber, and $\varphi_1(t)$ and $\varphi_2(t)$ represent corresponding phase fluctuations. This combined optical signal is then amplified, and split into N channels before being fed into an EO phase modulator. Coupling of the PM fiber and EO phase modulator is accomplished by aligning *fast* and *slow* axes to TE and TM modes experienced in a LiNbO₃ waveguide [132]. A representation of the axes/mode alignment can be seen in the inset of Figure 2.12.

Each modulator will subsequently be fed a modulation bias voltage, V_m , to induce EO modulation on each polarized axis. For z -cut LiNbO₃, TE and TM modulation is unequal due to EO coefficient offsets between the r_{33} and r_{13} tensors causing a phase difference between the two optical modes. This effect can be realized as

$$E_{PM} = \hat{x}E_x e^{j\left(\omega_1 t + \varphi_1(t) + \frac{\pi V_m}{V_\pi}\right)} + \hat{y}E_y e^{j\left(\omega_2 t + \varphi_2(t) + \frac{\pi V_m}{3V_\pi}\right)}, \quad (2.22)$$

where V_π is the voltage necessary to induce a π phase shift on the optical signal, *i.e.*, the half-wave voltage. This difference in modulation efficiency between the 2 polarizations, allows for a tunable phase shift of the heterodyning signal.

Next, the combined phase modulated signals transmit through a 45° rotational key for projection of each signal onto both the fast and slow axes of the PM fiber before filtering out one overlapped pair by a linear polarizer. This deliberate rotation of both

optical signals eliminates orthogonality cancellation while the linear polarization filter sets both signals for interference on the photodiode fed by a single-mode fiber. A representation of the rotated, linear polarization filtered field can be expressed as the following:

$$E_{LP} = \frac{\sqrt{2}}{2} \left(E_x e^{j\left(\omega_1 t + \phi_1(t) + \frac{\pi V_m}{V_\pi}\right)} + E_y e^{j\left(\omega_2 t + \phi_2(t) + \frac{\pi V_m}{3V_\pi}\right)} \right). \quad (2.23)$$

A $\sqrt{2}/2$ factor is added into the expression to account for 3-dB polarizer loss. Lastly, the signal is photomixed onto the photodiodes to generate an RF photocurrent,

$$I_{RF} = \frac{1}{2} \Re E_x^2 E_y^2 \cos \left((\omega_1 - \omega_2)t + \phi_1(t) - \phi_2(t) + \frac{2\pi V_m}{3V_\pi} + \frac{\omega_1 - \omega_2}{c} n_o L \right), \quad (2.24)$$

where \Re represents the responsivity of the photodiode, $\omega_1 - \omega_2$ is the RF angular frequency, c is the speed of light, and n_o and L are index and length of single-mode fiber, respectively.

A clear advantage of this system is the fact that the phase change effect occurring within a single fiber so that noise due to vibration and thermal variations is minimized. Since both signals detected at each photodiode are combined then split into channels of equal length, phase noise experienced by each signal will cancel out at the photodiodes, *i.e.*, $\phi_1(t) = \phi_2(t)$. Also, additional noise contributed by the single-mode fiber, $[(\omega_1 - \omega_2)/c] n_o L$, can be significantly reduced, by again, keeping the L of each channel equivalent, as well as bundling fibers together to experience similar acoustic and thermal variation [131]. Furthermore, residual path length mismatch can be accounted for by tuning the phase shifters in a calibration process. The last remaining phase term relates to the phase modulators used to control the beam steering. By biasing the

modulators, a progressive phase is projected across array antenna elements to shift beam directionality at angle, θ . Beam steering can be control based on the relation:

$$\Delta\varphi = k_{RF}d \sin \theta = \frac{2\pi V_m}{3V_\pi}, \quad (2.25)$$

where d is the array antenna element separation and k_{RF} is the wave-vector of the RF signal.

2.5 Conclusion

By pairing the University of Delaware's RF source capable of providing low-noise, high purity signals from 0.5 to 110 GHz with the phase control network, UWB steering capabilities are enabled. Addition of MUTC photodiodes, extends system performance to encompass high power and linearity while maintaining bandwidth applicable to desired communication systems. In order to fully maximize the Tx system, a photonic CA antenna should be designed to balance performance previously demonstrated by CSA arrays while incorporating coupling of optical phase feeding components.

Chapter 3

PHOTONIC PHASED ARRAY ANTENNA DESIGN AND FABRICATION

3.1 Photonic Array Antenna Simulation

Creation of a theory-matched CA antenna and reliable photodiode model sets a foundational starting point for designing a photodiode-coupled CA antenna complete with all necessary optical excitation components. Formulation of the 3D antenna model and associated operating principles including antenna structure, optical integration components, BCs, and beam steering parameters is completed in MATLAB (Mathworks). Design parameters were input and swept for substrate characteristics, photodiode biasing circuitry, optical excitation components, and photodiode electrical connection placement. Execution of the MATLAB parametric analysis control script generates a visual basic script to interface with the High Frequency Structure Simulator (HFSS) 3D full-wave EM field solver (ANSYS) to solve for the antenna's active S-parameters. These real and imaginary S-parameters are exported, and imported back into MATLAB where they merge with the photodiode model to calculate active input impedance, far-field and gain profiles, and radiated power.

Four main design characteristics were taken into consideration: substrate material and thickness, bias circuitry dimensions and position, photodiode electrical feeding of the dipoles, and optical excitation method/components. Each design factor was implemented in sequential series, as listed, to study the effects on active input impedance, far-field and gain profiles, and radiated power. All components added into the model must be characterized in this manner due to the introduction of parasitic

reactance. A few parasitic reactance examples are: 1) adding the photodiode will likely introduce a height offset from the dipole leading to parasitic capacitance, 2) electrical connection of the photodiode through either wirebonds or flip-chip bonding produces inductance, and 3) optical alignment components, *i.e.*, GRIN lens, optical fiber ferrules, and ferrule mounts, will affect near-field distribution, which manifests as changes to antenna impedance. Optimization of each design characteristic was complete before addition of the next variable. Focus of results was placed on reduction of the photodiode capacitance and CA resistance and capacitance, $R_{CA}(C_{pd} + C_{CA})$, while limiting parasitic reactance until the desired operational bandwidth of 5-20 GHz (4:1) was achieved over a significant steering range.

3.1.1 Infinite Array Model

Replication of Wheeler's CSA impedance characteristics began by designing a hybrid bowtie/dipole antenna unit cell and duplicating it along the x - and y -axis to construct a CA. Each unit cell radiator carries a dynamic load factor associated with the excitation sources which determines the overall CA performance, making large arrays computationally intensive. In order to simplify and accelerate computation of the array properties, uniformity in excitation sources for both amplitude and phase is applied through a unit cell expansion into a 2D infinite array. Implementation of this infinite array model provides an accurate approximation for larger arrays, *i.e.*, 10×10 and greater.

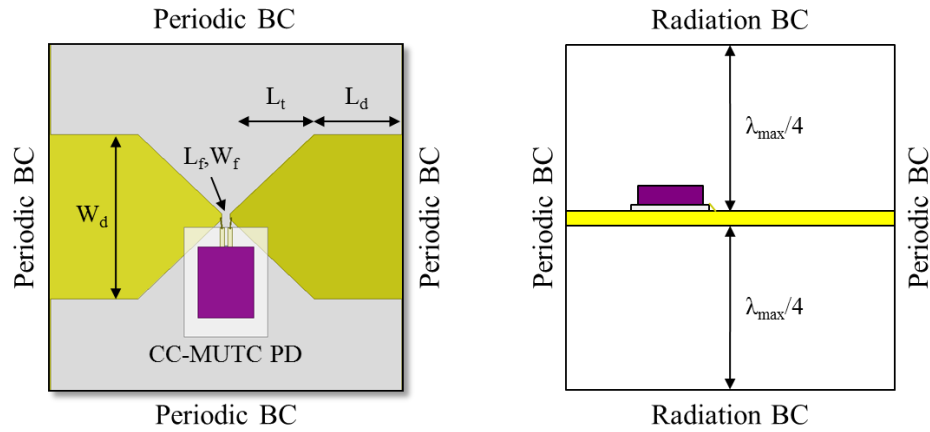


Figure 3.1: Infinite array model of photodiode-coupled hybrid bowtie/dipole antenna.

A top- (left) and side-profile (right) view of the photodiode-coupled hybrid bowtie/dipole antenna unit cell can be seen in Figure 3.1. Periodic boundary conditions (PBCs) surround the outer edges for planar replication of the unit cell, and are capable of simulating beam steering operation through phasing adjacent walls (left-right wall pair and top-bottom wall pair). Radiation BC are set $\lambda/4$ at the longest desired operating wavelength away for emulation of free-space radiation in the \pm broadside directions. Selection of the radiation BC is dependent on the direction of radiation investigated at each component design step. While investigating the effects of the design characteristics at broadside, absorbing boundary conditions (ABCs) enable accurate solutions with reduced computation time [133]. In this case phase delay between PBCs walls is set to zero, inducing maximized broadside radiation due to no scanning. As the design process progresses towards characterization of beam steering range, the compatibility of absorbing boundary conditions is reduced, leading to degradation in modeling performance. To circumvent this issue, perfectly matched layer (PML) BCs are used as a substitute for accurate scan angle and radiation pattern analysis. During the change in

radiation BCs, the proximal location of the boundary needs to satisfy respective requirements of each boundary type. Therefore, ABCs are positioned at $\lambda/4$, shown in Figure 3.1, and PMLs are placed at $\lambda/10$ of the lowest frequency.

Another effect linked to BC selection for this model is the type of excitation port introduced. With the PBCs integrated around the unit cell in HFSS, and a photodiode modeled as an ideal current source, a lumped port is utilized as an excitation source. The lumped ports excite the hybrid bowtie/dipole radiating element with a constant, uniform current at the inner ports of each arm until the photodiode is added, in this case the lumped port is shifted to the photodiode CPS input. Note, this excitation method is adequate for the specific antenna geometry used here, but other excitation methods, such as wave ports, i.e., a modal source, will provide a more accurate source for other photodiode-coupled antenna designs.

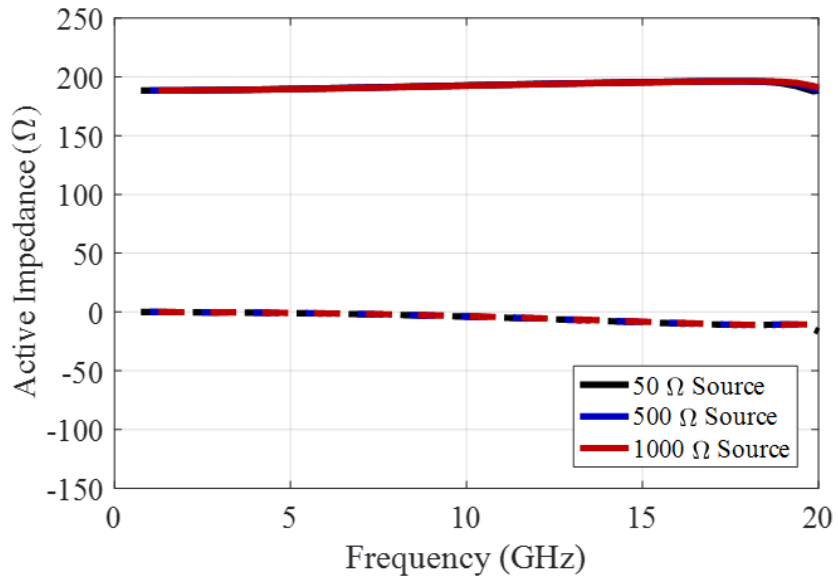


Figure 3.2: Simulated active resistance and reactance results of infinite CA. Solid lines represent resistance and dotted represent reactance.

With proper configuration of the BCs and excitation method, the geometry parameters of the hybrid bowtie CA, absent of a substrate, can be tuned to replicate CSA impedance characteristics. First, the unit cell size of the radiating element was set to 6.35 mm for a $\lambda/2$ resonance response slightly above the 5-20 GHz design bandwidth. Second, the dipole length (L_d) and width (W_d), taper length (L_t), and feed length (L_f) and width (W_f) are tuned to provide a flat real impedance of 188 Ω , i.e. one-half of the free-space impedance due to bidirectional radiation, and an imaginary impedance of zero. The final values for these parameters are as follows: $L_d = 1.6$ mm, $W_d = 3.0$ mm, $L_t = 1.5$ mm, $L_f = 0.15$ mm, and $W_f = 0.1$ mm. The impedance of the lumped port was subsequently varied from 50 – 1000 Ω , and the frequency was swept from 1 – 20 GHz at each port impedance. Results for the active resistance and reactance both converge to the theoretically predicted values at low frequencies, as shown in Figure 3.2. At the higher frequencies resistance increases to 200 Ω and the antenna becomes slightly capacitive. Notably, active impedance properties remained independent of all lumped port impedances to verify expectations of non-source impedance susceptibility. Overall, based on these results, the design satisfies all anticipated properties of the CSA model.

3.1.2 Substrate

Up to this point the antenna model provides an ideal response; however, when a photodiode is coupled to the current CA antenna the photodiode, which has a bandwidth characterized based on a 50 Ω load, the device will exhibit a 4 fold decrease in operational bandwidth. Attempting to counteract this fundamental effect with further tuning of the radiating element's geometrical values will not yield sufficient antenna impedance reduction across the band. Therefore, use of substrate design is introduced to decrease the real part of the antenna impedance.

As previously mentioned, the photodiode epitaxial structure is designed so that the RF output power is primarily limited by thermal burnout. Ideally, the antenna substrate would operate on a TEC ground plane; however, as compensation balance between high photodiode output power and high antenna radiated power, a largely thermally conductive material is used as the antenna substrate. Additionally, the substrate should have a relatively low permittivity to reduce defects in radiation. AlN was selected, remaining consistent with the heatsinking strategy described earlier, for the photodiode flip-chip bonding sub-mounts. Although AlN's dielectric constant is not significantly large, $\epsilon_{r,AlN} \approx 9$ [134], any permittivity-related radiation effects from the material are able to be minimized by controlling substrate thickness.

Simulation of AlN effects on active impedance and radiated power were accomplished by adding a substrate to the infinite array model presented in the previous section. Influence of the dielectric properties of the substrate are highlighted in Figure 3.3 (a), where AlN is represented by the red trace. The thickness of the AlN substrate was subsequently swept in thickness from 0.2 mm to 0.8 mm. The relation of substrate thickness and impedance can be realized by adding an AlN slab between the antenna and infinite free space in the CA dipole antenna circuit model, Figure 2.3, then adjusting the transmission line impedance equation, i.e. setting $d = \infty$, to yield

$$Z = Z_{AlN} \frac{Z_0 + jZ_{AlN} \tan(\beta_1 d_{AlN})}{Z_{AlN} + jZ_0 \tan(\beta_1 d_{AlN})}, \quad (3.1)$$

where Z_{AlN} is the impedance of AlN ($Z_{AlN} = Z_0/\epsilon_{r,AlN}$), Z_0 is the impedance of free space, β_1 is the wavenumber in the AlN slab, and d_{AlN} is the thickness of AlN.

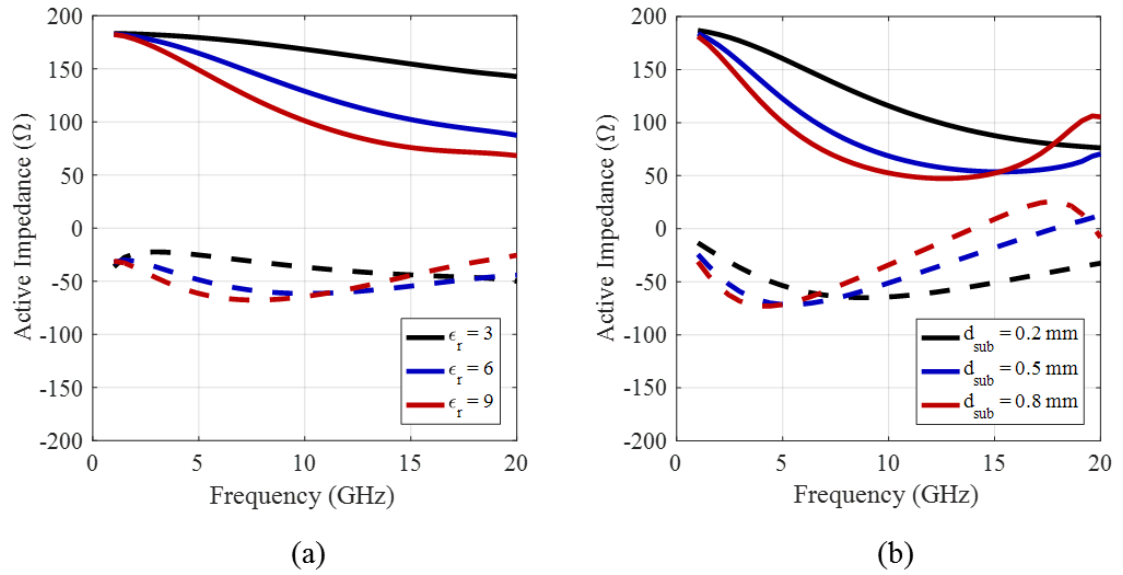


Figure 3.3: Simulated substrate effect in terms of (a) dielectric constant and (b) AlN thickness on active radiation impedance at 20 mA photocurrent. Solid lines represent resistance and dotted represent reactance.

As shown in Figure 3.3, and verified in equation 3.1, increasing substrate thickness reduces the radiation resistance significantly at frequencies greater than 5 GHz while the reactance increases, becoming more inductive. Initially it appears as if thicker substrates are the best option due to the lower radiation impedances necessary for extension towards high frequency operation; however, potential introduction of substrate modes risk degradation of beam steering range and radiation efficiency [135]. Contrarily, AlN is brittle and is difficult to produce at extremely thin substrates ($< 200 \mu\text{m}$), and its thermal sinking abilities also decrease. Thus, a substrate thickness of 250

μm was selected to balance these negative effects while affording relatively flat radiated power over a wide frequency band.

3.1.3 Bias Line Circuitry

Unsaturated photodiode operation requires a DC biasing network to supply a reverse bias to each active photodiode-coupled CA antenna element. Ideally, the biasing circuitry should remain simple and introduce negligible effects on antenna radiation. To accomplish these goals, bias lines were designed orthogonal to the dipole arm length direction, creating cascaded biasing of multiple adjacent antenna elements at once, as shown in Figure 3.4. Additionally, bias line position and width were carefully selected to ensure only DC current flow, and minimal scan blindness from resonances.

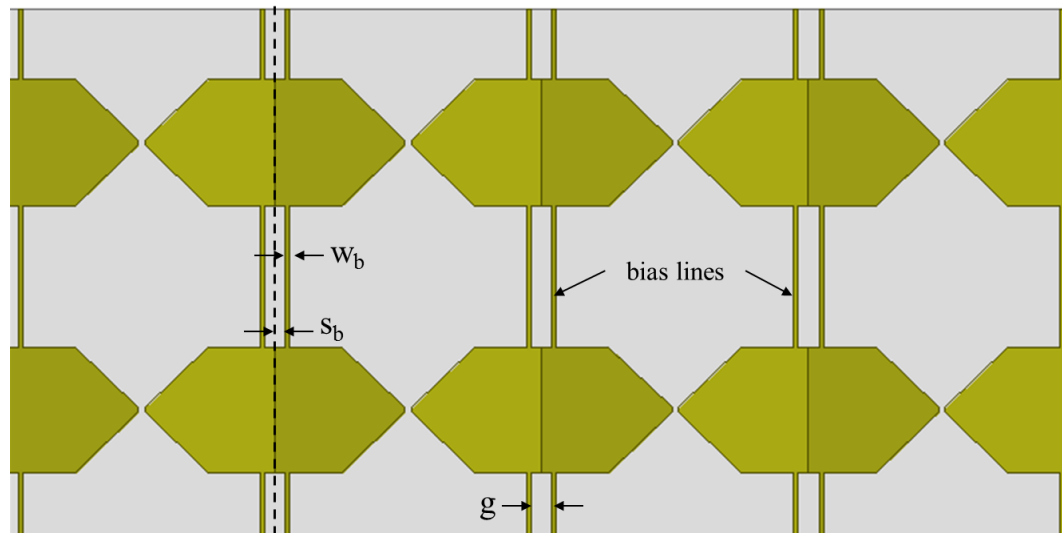


Figure 3.4: Bias line network for photodiode-coupled CA antenna, g is the capacitive coupling gap between dipole edges, s_b is the spacing of the bias line from the edge of the dipole, and w_b is the bias line width.

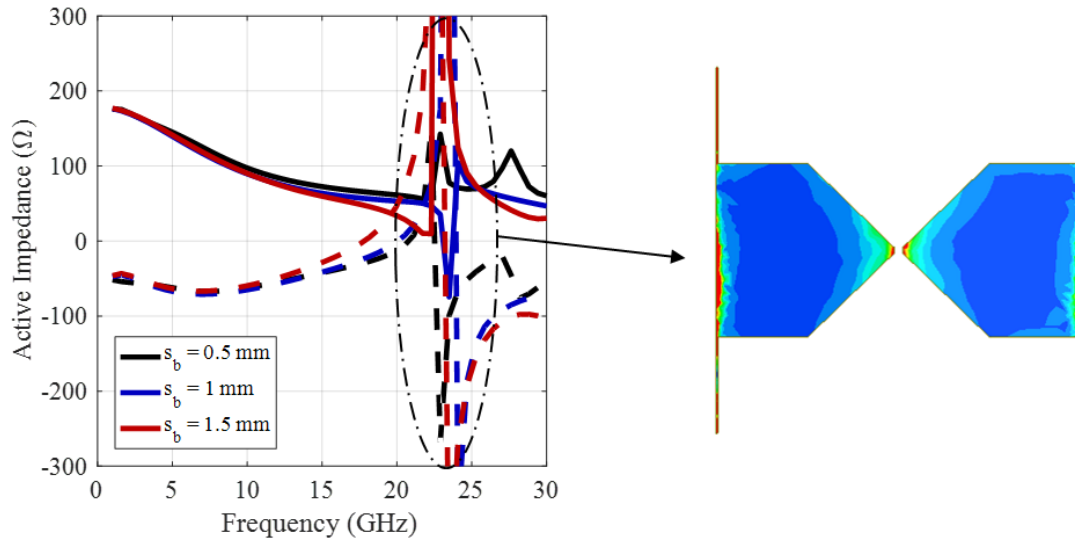


Figure 3.5: Active impedance response to s_b sweep, solid lines represent resistance and dotted represent reactance, and surface current distributions at the resonant 23 GHz.

To guarantee the bias lines do not degrade antenna performance, each bias line should be positioned away from strong RF current distribution. Thus, DC bias lines were set flush with the outer edge of the dipoles, $s_b = 0$, due to RF current being applied at the inner feed points. Sweeping the bias line position verifies that at $s_b = 0$ shifts resonance induced by bias lines to a higher frequency, *i.e.*, decreases the capacitance created between bias lines, leading to an increased resonance frequency. The resonance effects related to the offset of the bias lines from the edge are illustrated in Figure 3.5, where a greater offset causes the resonance intensity to increase, and the resonance position is moves slightly more towards the desired operation band. By implementing outer edge positioning of the DC feed, direct connection of the dipoles is not achievable due to opposing bias on connected arms. Therefore, a small gap of $5 \mu\text{m}$ was introduced

to act as a DC current block while still appearing electrically connected at microwave frequencies.

Although positioning of the bias line aids in reducing resonances detrimental to radiation and beam steering, dimensional parameters, namely length and width, still pose risks associated with antenna impedance and scan blindness. For length, the bias lines in each dipole unit cell need to be designed less than half a wavelength at highest operating frequency. Taking into account the antenna substrate yields the following bias line design length relation,

$$L_b \leq \frac{\frac{1}{2} \lambda_{\min}}{\sqrt{\frac{1}{2}(\varepsilon_r + 1)}} , \quad (3.2)$$

in which L_b , λ_{\min} , and ε_r are the bias line length, wavelength at highest operating frequency, and dielectric constant of the substrate, respectively. Note that in this case the antenna's near field was approximated to be equally distributed between the AlN substrate and free space. Selecting a width requires balancing a size trade-off; too large of a bias line width will increase cross polarization and eventually distort the flat frequency response at high frequencies, too small of a width will drastically increase electrode resistance in the line and potentially lead to thermal burnout. Final length and width dimensions satisfying all requirements are $L_b = 6.35$ mm and $w_b = 30$ μm , both of which are incorporated into the results shown in Figure 3.5.

3.1.4 Inductive Peaking

Incorporating all the fundamental operation components for an optically-excited CA antenna has resulted in a 2:1 bandwidth, *i.e.*, 10-20 GHz, not even matching up with the now far surpassed initial 2.5:1 TCA bandwidth limit. However, to improve on this

operational bandwidth, a series inductance circuit can be introduced into the photodiode-to-antenna feed. By adding this extra circuitry, inductive lines enable implementation of a technique referred to as inductive peaking [136], [137]. Inductive peaking allows the antenna impedance to overcome the inherent capacitive nature of the CC-MUTC photodiodes, flattening out the radiated power decay with a peak at a particular frequency where the added inductance exactly cancels the photodiode's internal capacitance.

The new RF current feed design consists of the photodiode bond pad CPS with wirebonds connecting the end of each CPS to the internal feed points of the antenna arms. These loop wirebond connections were introduced as a simple addition to the CPS lines to allow for maximization of inductance without changing the antenna unit cell size or shape. Sweeping different lengths of wirebonds yielded a 5 GHz extension on the low end of the previous results to obtain a 4:1 (5-20 GHz) bandwidth by raising the high frequency response into a constant 3-dB radiated power band, displayed in Figure 3.6 (a).

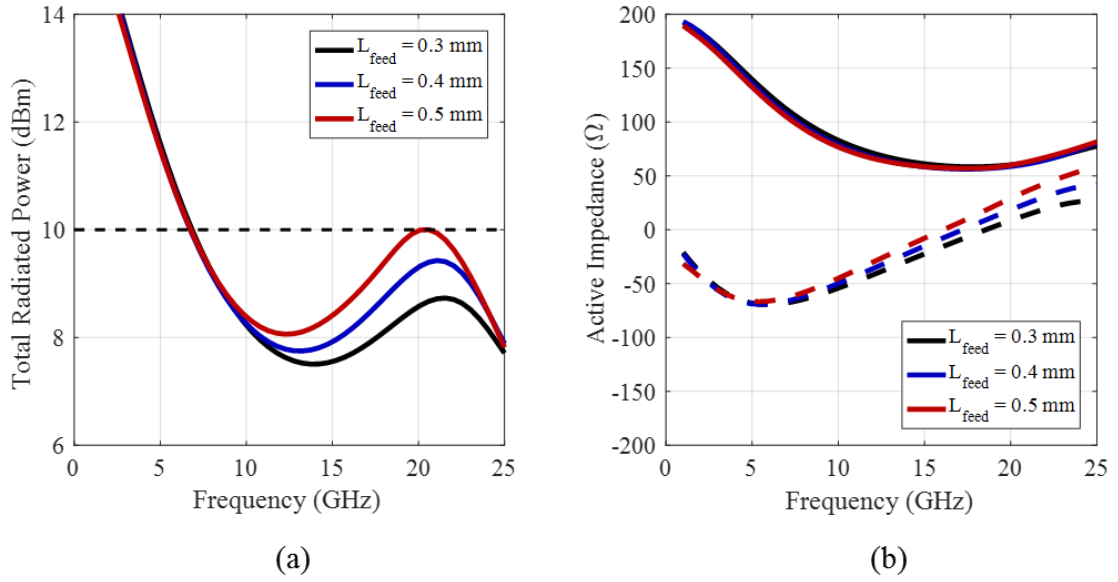


Figure 3.6: Effects of inductive peaking on active impedance, solid lines represent resistance and dotted represent reactance, and total radiate power at 20 mA photocurrent.

At low frequencies the substrate is electrically thin, causing the radiated power corresponding to the antenna impedance to become high. However, during operation it is expected the photodiode will readily saturate at these higher impedances due to the minimum biasing condition mentioned in Section 3.2. Throughout mid-band operation, the inductive peaking adjusted impedance remains constant, with the photodiode responding accordingly, for a flat radiated response. Lastly, as higher frequencies are approached, integrated photodiodes are not able to output sufficient RF power causing a sharp drop-off in antenna output power despite increasing antenna impedances.

3.1.5 Optical Alignment Components

Completion of the electrical component design allows for expansion into optical components necessary for implementation of the optical phase feed network. Since the photodiode will be fed a two-tone optical signal through a single-mode fiber, a small optical alignment system needs to be designed to focus the optical power from the single-mode fiber to the photodiode. Uniform illumination of the photodiode junction requires a lens for controlled focusing of light; therefore, the alignment system will consist of an optical fiber ferrule for robust alignment with a graded-index (GRIN) lens to focus the light, and a mount to secure the focusing components to the antenna. Two examples of how this can be accomplished are illustrated in Figure 3.7.

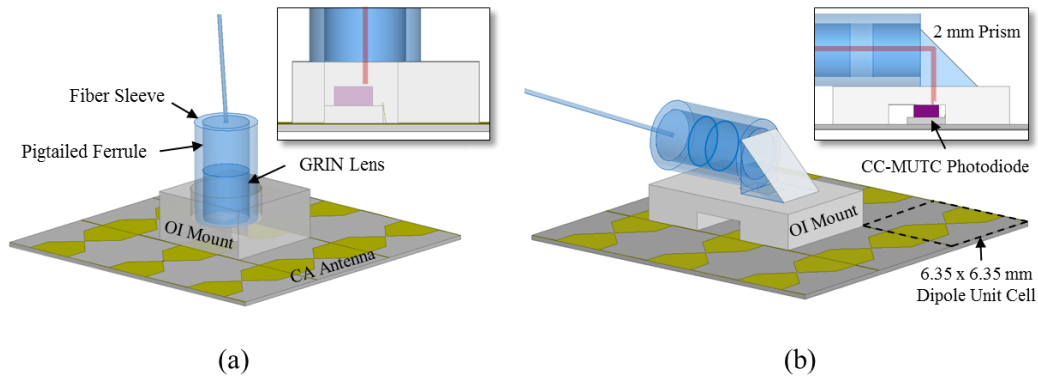


Figure 3.7: Proposed optical feed integration techniques for photodiode-coupled CA antennas. (a) Orthogonal GRIN lens, fiber ferrule, and fiber mating sleeve configuration, and (b) Low profile, parallel prism, GRIN lens, fiber ferrule, and fiber mating sleeve configuration.

Dimensions and positioning of the GRIN lens and single-mode pig-tailed fiber ferrule were based off of components purchased from Thorlabs, Inc. Both the GRIN lens and fiber ferrule are made from oxide glass with a diameter of 1.8 mm and length

of 5.6 mm. The mating sleeve has an inner diameter of 1.818 mm, outer diameter of 2.8 mm, length of 10 mm, and is made out of borosilicate glass. Additionally, a fiber spacer/mount was designed to position the GRIN lens, or 2 mm prism, output approximately 2 mm away from the photodiode, matching its effective focal length.

Since the GRIN lens, mating sleeve, and pig-tailed fiber ferrule are all components purchased from Thorlabs, Inc. their physical properties are fixed; therefore, direct input of the dimensions and material properties is all that can be done for modeling. On the other hand, the fiber mount allows for flexible design in order to optimize antenna performance. A good spacer/mount should provide exceptional stability to maintain light-to-photodiode coupling, in addition to being low-dielectric for minimizing back-radiation towards the feed network, and low loss [138]. Based on this criteria, it was determined that these spacer/mounts could be 3D printed, with low fill-factor acrylonitrile butadiene styrene (ABS) material, for increased structural design flexibility and the capability of minimizing dielectric-induced radiation effects. First, the spacer/mount was designed structurally to support the optical alignment components since material properties are more flexible to implement. Once a reliable structure for holding the sleeve was finalized, different forms of the spacer body needed to be considered to minimize dielectric effects. If not properly constructed, either through a low fill factor ABS print, or utilizing an aerated design, resonance can be introduced into the operational bandwidth. These resonance effects seen with fuller spacer/mounts are introduced through the interaction between the bias line circuitry and the spacer material. Essentially, the added spacer sandwiches the bias line between ABS and AlN media, increasing the effective bias line length to

$$L_{eff} \approx \sqrt{\frac{\epsilon_{r,AIN} + \epsilon_{reff,ABS}}{2}} L_b \quad (3.3)$$

where $\epsilon_{r,AIN}$ is the permittivity of AlN, $\epsilon_{reff,ABS}$ is the effective permittivity of ABS, and L_b is the physical bias line length. As the effective length increases, it begins to violate the relation in Equation 3.2, therefore introducing a resonance at lower frequencies. Based on this relation, and improvements in 3D printed technology, a low fill factor optical alignment mount was printed to afford a dielectric constant close to 1.

The selected optical alignment mount, and both proposed optical alignment configurations were added into the photodiode-coupled CA antenna model, separately, for full-wave simulation. Of the two optical coupling techniques, the major design component at risk of degrading performance was the prism, due to the polarization independent, reflective metallic coating. Upon completion of the simulations, the effect proved to be small, resulting in negligible RF response variation of the 5-20 GHz bandwidth. The final broadside radiated power output produced by each optical feed integration configuration indicates a 4:1, 5 – 20 GHz, 3-dB operational bandwidth, as presented in Figure 3.8.

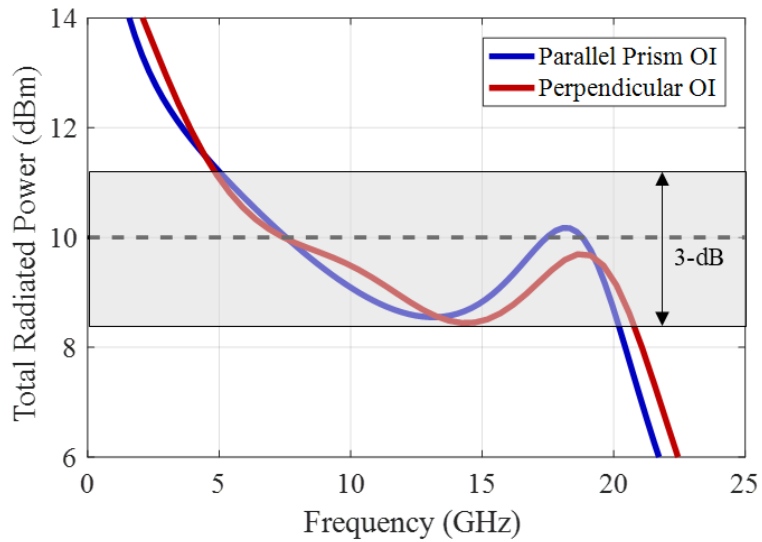


Figure 3.8: Comparison of RF response of an infinite array element fed by a normally incident optical integration and a prism based integration at 20 mA photocurrent. The 50 Ω ideal output power is 10 dBm, indicated by the dotted line.

3.1.6 Beam Steering

Upon completion of the photodiode-coupled CA antenna model, a broad angular beam steering range, i.e. 0-45°, was simulated. Phase applied to the master and slave walls of the periodic boundary conditions in the infinite array model was determined using Equation 2.25 based on the chosen steering angle. As illustrated in Figure 3.9, the approximate 4:1 bandwidth was only achievable with a steering angle up to 30°. Although this is not ideal, the photodiode-coupled CA antenna satisfies design goals of creating an UWB antenna with a broad steering range. Additionally, if the optical alignment system is correctly design, this antenna will also obtain the highly desired low profile and conformal structures necessary for today’s applications.

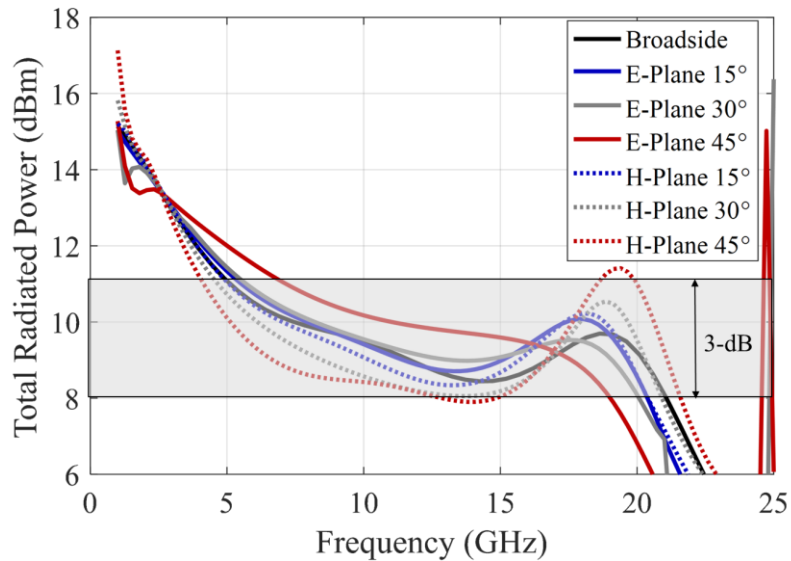


Figure 3.9: Simulated CA beam steering results at 20 mA photocurrent.

3.1.7 Discrete Array Modeling

Although the infinite array model is a convenient, computationally simple simulation method to maximize impedance bandwidth by manipulating the photodiode-coupled dipole unit cell, its accuracy diminishes with decreasing array size. As array size shrinks, finite array edge effects degrade antenna bandwidth. These effects are derived from an inability to uniformly excite the array due to reduced edge-element mutual coupling, causing an active impedance imbalance between outer and inner unit cells. Thus, supplying each lumped port with equal power in an attempt to reproduce uniform excitation will end in inner-outer element discrepancies, and narrowband impedance matching.

Simulation of these finite array edge effects is necessary to determine performance of the smaller array prototypes used to demonstrate beam-steering

capabilities of an optical antenna fed Tx system. Accurate modeling of finite arrays can be accomplished by swapping the infinite array model’s PBC on the planes truncating the dipole substrate with ABCs and extracting real and imaginary active S-parameters from each port. Implementing both modeling parameters enables emulation of a finite antenna surrounded in free space while incorporating mutual coupling effects of each active element.

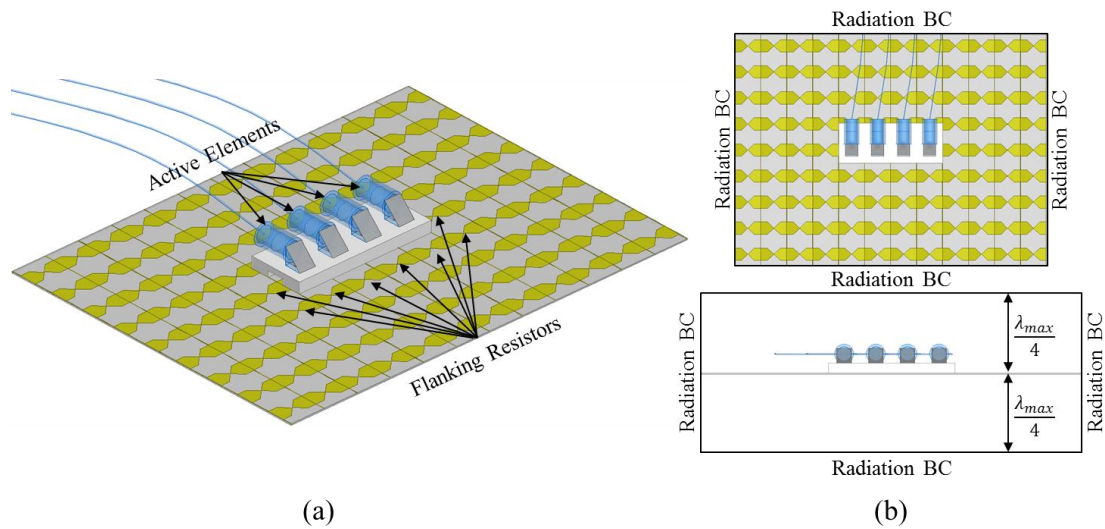


Figure 3.10: (a) 1×4 photodiode-coupled CA antenna with optical integration components, and (b) boundary conditions applied for finite modeling.

In order to sufficiently form and steer a beam, an example 9×12 connected dipole array antenna surrounding a 1×4 active element photodiode-coupled CA array is proposed. This configuration model, along with applied boundary conditions, are illustrated in Figure 3.10 (a) and (b), respectively. Including “dummy” dipoles around the active array reduces finite array edge effects by adding in antenna impedance-matched flanking resistors at dipole inputs to extend RF current distribution outwards.

Farther distribution of the RF current, rather than abrupt cut-off at the 1×4 edges, causes the active array to appear larger and approach the infinite array approximation. Additionally, finite array characteristic mode resonances associated with the half-wavelength and wavelength of the array size in each direction can be shifted to lower frequencies outside of the operational bandwidth [139].

These characteristic resonant effects are illustrated in a dipole surface current distribution plot in Figure 3.11. In Figures 3.11 (a), (c), and (e), in which no flanking resistors are present, the surface current distribution is strongly concentrated within the 1×4 lumped port excited dipoles allowing for potential bandwidth degrading characteristic mode resonances. Although there are traces of surface current in other dipoles, it is minimal incoherent excitation due to surface wave interaction with the surrounding dipole's metallic material. Contrarily, it can be seen in Figures 3.11 (b), (d), and (f) that the current distribution is uniformly spread in phase outwards for coupled-excitation of the surrounding dipoles for the appearance of a larger active element array. Further extension of the surface current is possible by simply extending resistor-populated dipoles outward for "larger" arrays.

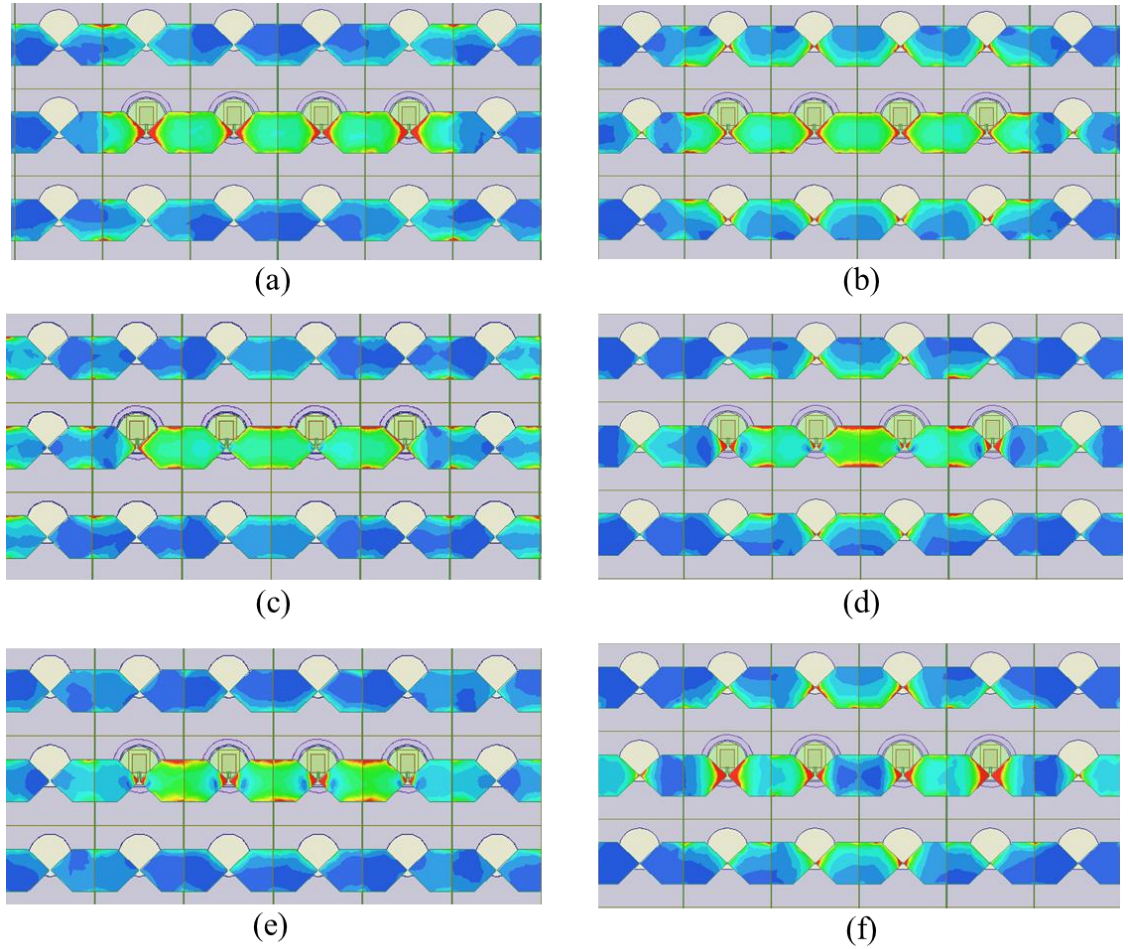


Figure 3.11: Surface current distribution for a discrete 1×4 photodiode CA antenna model at (a) 5 GHz without flanking resistors (FR), (b) 5 GHz with surrounding 75Ω FR, (c) 12 GHz w/o, (d) 12 GHz w/ 75Ω FR, (e) 15 GHz w/o FR, and (f) 15 GHz w/ 75Ω FR.

Preliminary analysis of an example finite photodiode-coupled CA antenna provides valuable insight on expecting bandwidth degradation of the infinite array model results, as well as compensative measures that can be readily introduced into a physical device. Ideally, this model would be thoroughly optimized to meet the same bandwidth and steering range requirements previously mentioned; however, the

computational rigor of accurately simulating this structure drastically increases modeling time, making the design process extremely inefficient. Nonetheless, upon completion of fabricating exemplary photodiode-coupled CA antennas, exact device dimensions will be fully simulated as a finite structure, as it is pertinent to the characterization of the constructed device. It is important to note, that this time-consuming finite array simulation can be circumvented through the use of software packages catered towards finite array structures, but these were not available to the author during the time of this work.

3.2 Fabrication

The final CA design consists of gold dipole elements on a thin 250 μm AlN superstrate, which provides heat-sinking for the photodiodes. At the end of each dipole arm is a DC bias line and a 5 μm gap separating each unit cell for reverse biasing of the photodiodes. This CA antenna design is fabricated in parallel with MUTC photodiodes and AlN sub-mounts used for wirebonding. After antenna and photodiode fabrication, the photodiodes are integrated into the antenna, and fiber alignment spacer/mounts are designed, and printed to link the photodiode-coupled antenna to all optical feed components, *i.e.*, GRIN lens, fiber ferrule, mating sleeve purchased from Thorlabs, Inc, and a 2 mm prism if the low profile feeding is used. Following this process, two separate photodiode-coupled CA antennas were fabricated. The first generation consisted of a one-dimensional, 4-element array with an orthogonal optical integration configuration. In order to preserve the inherent low profile nature of the CA antenna, and improve beamforming capabilities, a second generation design incorporating the prism-based optical integration method was introduced into a one-dimension, 8-element array. Both designs will be concurrently presented throughout the remaining fabrication sections, as

much of the process is carried through from the first generation design to the second. The entire fabrication and optical integration process flow is briefly overviewed in Figure 3.12, and discussed more in depth throughout the remaining sections.

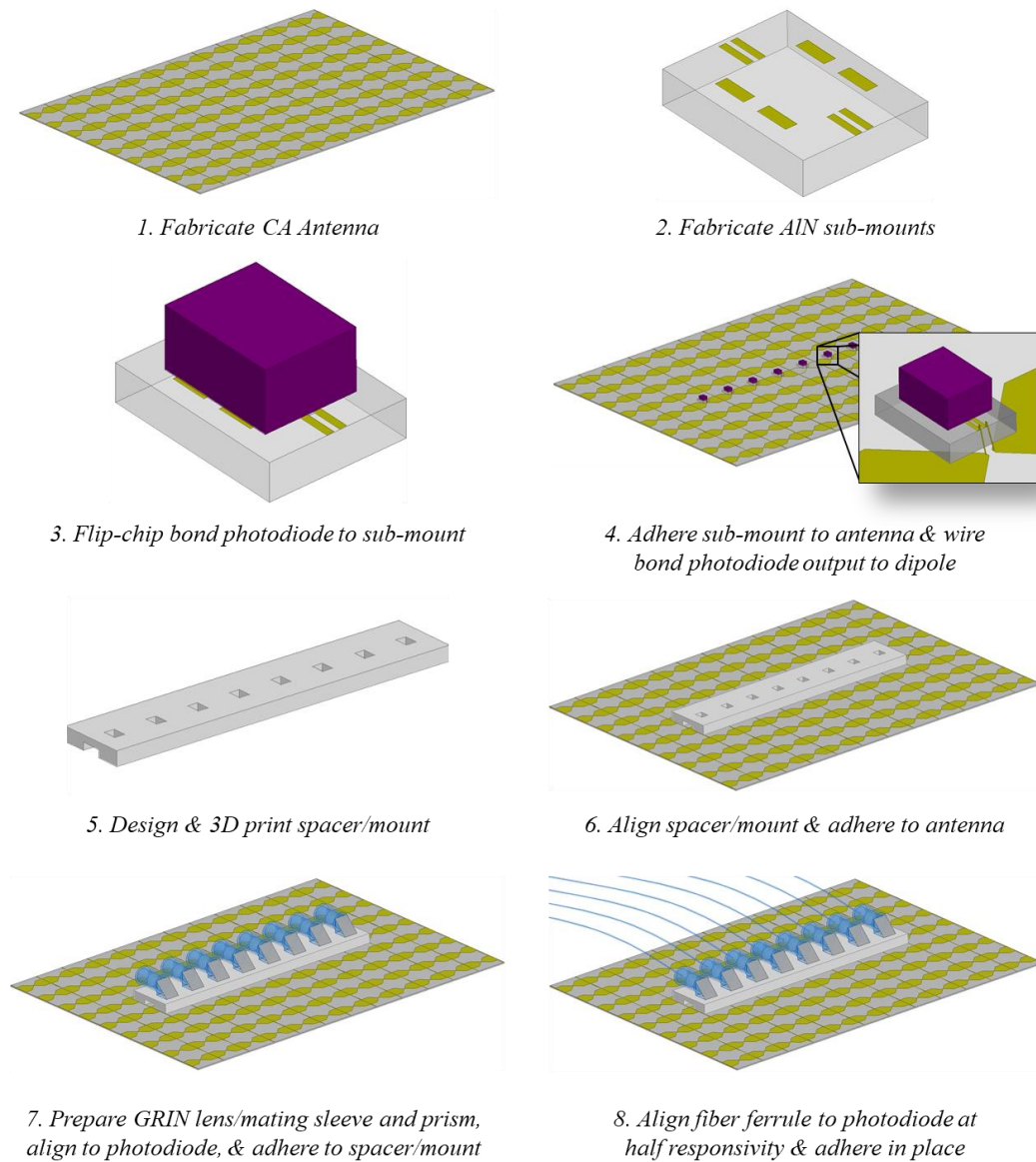


Figure 3.12: Overview of 1×8 photodiode-coupled CA antenna with integration of low profile optical components linked to feed network.

3.2.1 Antenna

The CA antenna is fabricated on a 12 cm × 12 cm, 250 μm thick, AlN substrate possessing a thermal conductivity of 285 W/(m·K) (Maruwa Co., LTD). A seed layer of titanium (Ti) is first deposited to act as a glue-like layer allowing Au to be subsequently deposited. Since each material is common and step coverage is not an issue, deposition of the 20 nm Ti and 50 nm Au seed layer was performed using electron beam evaporation. Next, a photomask consisting of a 12 × 9 array of dipole elements connected to a bias control port was designed to accommodate active arrays up to 8 × 8 with a current distribution dissipation area of non-active elements around the edge. Pattern transfer of this CA antenna and bias feed network is subsequently performed through standard *i*-line photolithography processing. In order to form layers thick enough for Au dipoles to satisfy the skin depth relation, an electroplating process is used to grow a 7 μm thick Au CA antenna. The electroplating processing of this array was accomplished using Techni-Gold 25 ES RTU solution (Technic). Once metallization of the CA antenna pattern is complete, the substrate is diced to an 8 cm × 8 cm square and is ready for photodiode integration.

3.2.2 Optical Integration

The photodiodes integrated into the CA antenna are 34 μm diameter CC-MUTC photodiodes flip-chip bonded to 1 mm × 2 mm, 300 μm thick AlN submounts patterned with CPS outputs. Flip-chip bonded 34 μm diameter CC-MUTC photodiodes are adhered proximal to a central row of adjacent dipoles' inner ports via thermally conductive epoxy (KONA 870FT-LV-DP, Resin Technology Group, LLC). Once secured to the substrate, the CPW output on the photodiode sub-mount was wirebonded to the appropriate dipole arms for electrical connection, as highlighted with the 1 × 8

array in Figure 3.13. In order to ensure a reliable wirebond link from the photodiode to antenna during any jostling or substrate flexion, epoxy was applied around each submount to encase all wirebonds. This robust epoxy-based securing technique was also used on the flexible flat cable (FFC) bias feed connector soldered to the CA antenna bias port.

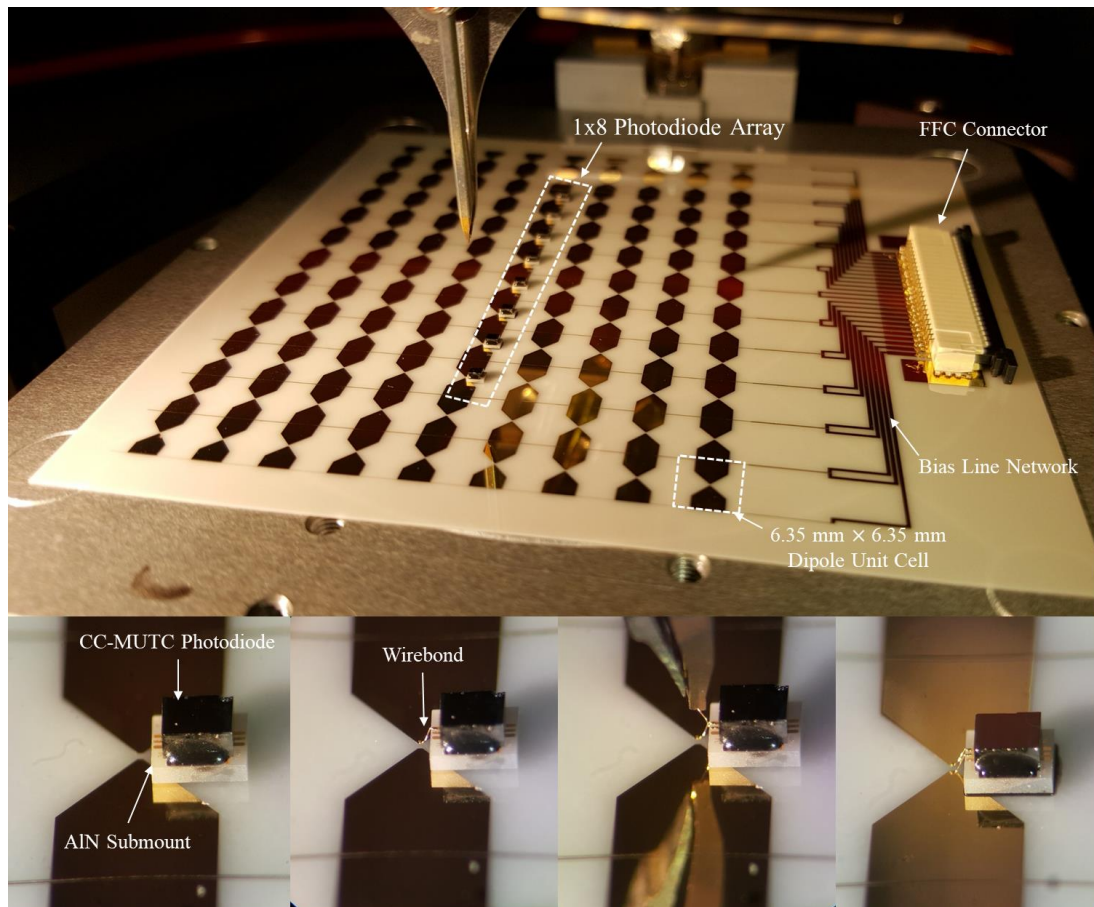


Figure 3.13: Photodiodes thermally and electrically connected to CA antenna.

After securing photodiodes to the CA antenna both electrically and thermally, and verifying correct IV characteristics of each photodiode, the process of coupling a single-mode fiber to the photodiode begins. Optical alignment starts with mounting the antenna substrate containing the four photodiodes, and FFC connector onto a vacuum stage with six degrees of movement freedom. The GRIN lens/mating sleeve unit is set into a 3D-printed clamp positioned over the photodiode currently being aligned. A fiber feed clamp, connected to a separate stage, resides over the sleeve clamp to input the fiber ferrule into the sleeve while retaining the ability to control the spot size by sliding the ferrule up and down. Finally, a FFC links the connector on the antenna to the bias control board, enabling read-out of the DC photocurrent produced during optical-coupling to the photodiode.

3.2.2.1 Orthonormal Optical Fiber Configuration

Next, a low fill-factor 3D printed ABS mount needs to be secured over the array of photodiodes. For the normally incident fiber configuration used in the 1×4 CA antenna, a $25 \text{ mm} \times 25 \text{ mm} \times 6 \text{ mm}$ mount with four sets of circular slots spaced 6.35 mm apart is printed to align over each of the photodiodes; the slots consist of a circle of radius, $r_1 = 1.3 \text{ mm}$, extending up 3 mm from the bottom, and a circle of radius, $r_2 = 1.9 \text{ mm}$, extending down 3 mm from the top side. At the merging point, a ledge forms a set point for the GRIN lens/mating sleeve unit to stabilize during alignment. Placement of the spacer/mount must be done with precision to ensure light from each slot can be coupled to its respected photodiode. Before alignment, the base of the spacer is evenly coated in UV-curable optical adhesive, Norland Optical Adhesive (NOA) 61. Rough positioning over the photodiodes is accomplished by hand, followed by fine tuning with stage translation under the GRIN lens/mating sleeve. Once max responsivity of each

photodiode can be read with the sleeve set at the base of the spacer, the spacer is cured under UV exposure for 2 minutes. At this point the spacer should be firmly in place; however, additional NOA 61 is applied and cured around the outer edge for a more reliable bond to hold against potential strain once the fibers are connected.

With the spacer in place, the GRIN lens/mating sleeve unit is reintroduced with the fiber ferrule into the spacer slots. Stage translation scanning for local maximum photocurrent, indicating max responsivity, through focal point positioning across the photodiode junction determines the location of the GRIN lens/mating sleeve at the ledge of the spacer slot. While holding this local maximum reading, NOA 61 is applied around the sleeve, completely filling vacant slot space, to secure an accurate focus on the 34 μm photodiode. Curing this epoxy requires more precision than a standard flood UV exposure; therefore, two UV fiber-light “wands” are used to uniformly cure the optical adhesive over time in attempt of eliminating uneven solid/liquid NOA 61 barriers causing sleeve and alignment shifting.

Lastly, focal point positioning along the axis passing normal through the photodiode’s junction is adjusted by translating the fiber ferrule vertically within the sleeve. Consistent with the high-power handling theme of the MUTC photodiodes, positioning of the ferrule resolves a focal point vertically off-set from the photodiode absorption region. By offsetting the focal point to produce a half-maximum responsivity, MUTC photodiodes are able to operate at higher maximum RF output power by uniformly illuminating the entire junction to reduce the peak to average optical power across the photodiode. This decreases hot-spot burnout risk to consequently improve longevity and reliability of the device. Upon reaching half-max responsivity, the ferrule is cured to the inside of the sleeve.

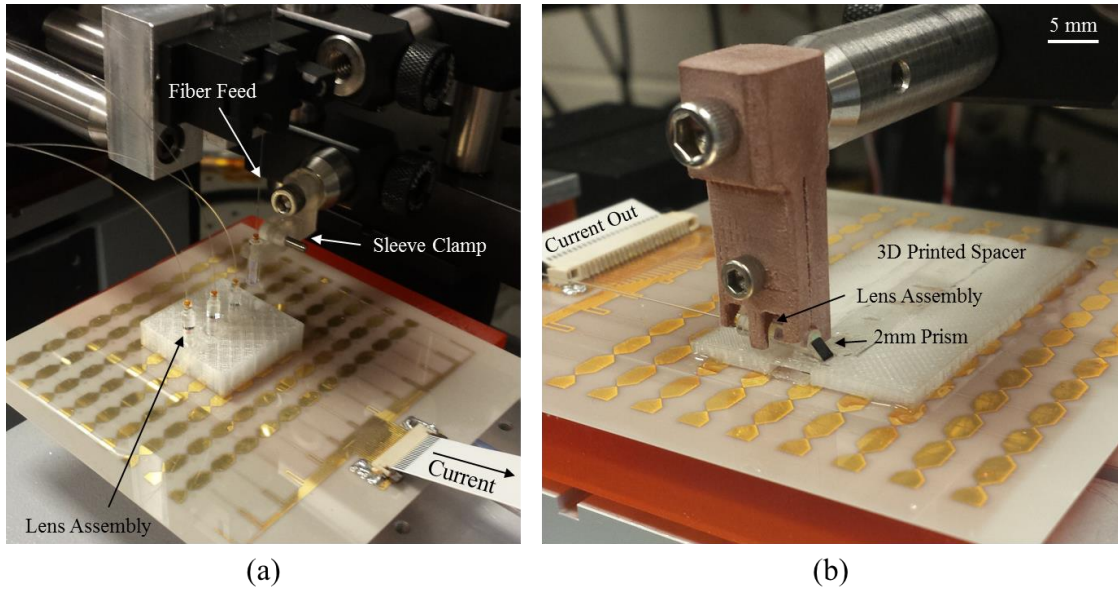


Figure 3.14: Optical alignment setup of the (a) orthonormal optical integration configuration used for the 1×4 CA antenna, and (b) parallel optical integration configuration consisting of a single prism-included GRIN lens assembly and optical fiber through the optical coupling slot of the glass-topped ABS mount. The current supplied by the photodiode is read through probing the white surface mounted flex cable edge of each array.

After performing the same process three more times for each GRIN lens assembly and fiber ferrule, the optical alignment is complete. Before removing the optically-coupled CA antenna from the vacuum stage, final responsivity measurements are recorded determining overall success. Responsivities recorded for each photodiode are present in Table 3.1, where numbers 1-4 correspond to left to right positioning displayed in Figure 3.14 (a).

	PD #1	PD #2	PD #3	PD#4
Initial Max \mathfrak{R} (A/W)	0.70	0.70	0.74	0.70
Packaged \mathfrak{R} (A/W)	0.26	0.29	0.32	0.20

Table 3.1: Comparison of 1×4 CA antenna’s photodiode responsivity before and after optical alignment.

Based on the large discrepancies (<75%) between expected packaging responsivities, *i.e.* PD #1: 0.35, PD #2: 0.35, PD #3: 0.37, and PD #4: 0.35, the optical alignment process needs to be refined in order for ideal responsivity packaging to be maintained over time. Primarily, error in integration stems from the uneven curing between the sleeve and fiber/mount slot inner wall. Although responsivity drift is minimized by balanced curing from the UV “wands,” adhesive hardening is capable of exerting undetected forces on the GRIN lens/mating sleeve due to the sleeve clamp’s temporary support. Removal of the sleeve clamp eliminates cancellation of these forces, allowing the GRIN lens/mating sleeve to physically move, resulting in an optical shift off of the $34 \mu\text{m}$ diameter target. Additionally, factoring in tugging on optical fibers, spacer slipping during curing, and hardened optical adhesive obstructions within the sleeve multiplex potential inaccuracies into a complex and delicate process, diminishing physical tolerances and room for error. If one or two of these issues, most likely spacer/mount slot size and placement accuracy, become avoidable, the presented optical integration will routinely provide accurate coupling at half-maximum responsivity.

3.2.2.2 Parallel Optical Integration Configuration

For the parallel optical integration configuration used in the 1×8 CA antenna, a $5 \text{ cm} \times 3 \text{ cm} \times 2 \text{ mm}$ low fill-factor 3D printed ABS mount ($\epsilon_r \approx 1$) with eight light-coupling slots is aligned to the array of photodiodes. Placed on top of the light-coupling slots is a $100 \text{ }\mu\text{m}$ thick sheet of low IR optical loss quartz glass for protection of the photodiodes from any optical adhesive droplets. Next, construction of each GRIN lens assembly is completed by securing the GRIN lens within a lens sleeve, and subsequently adhering a 2 mm prism to the end of the GRIN lens. Introduction of the GRIN lens assembly with the fiber ferrule initiates a rough alignment to the photodiode by way of focal point positioning on the photodiode junction, and local maximum current readout through the surface mounted flex cable. The setup of this optical alignment process is illustrated in Figure 3.14 (b). Upon locating the photodiode junction, the GRIN lens assembly is adhered to the mount with UV curable NOA 61. Lastly, fine-tuning of the fiber ferrule position within the sleeve intentionally defocuses the beam, in turn reducing photodiode responsivity to approximately 50% of its maximum value. Repetition of this process occurs for alignment of all eight fiber/photodiode pairs. A final responsivity readout for each channel presented values of $0.27 \pm 0.02 \text{ A/W}$, which is slightly lower than the designated 0.35 A/W , 50% maximum responsivity. Overall, this optical feed configuration enabled a profile reduction from 3 cm ($2\lambda_{\text{high}}$) down to approximately 5 mm ($0.33\lambda_{\text{high}}$).

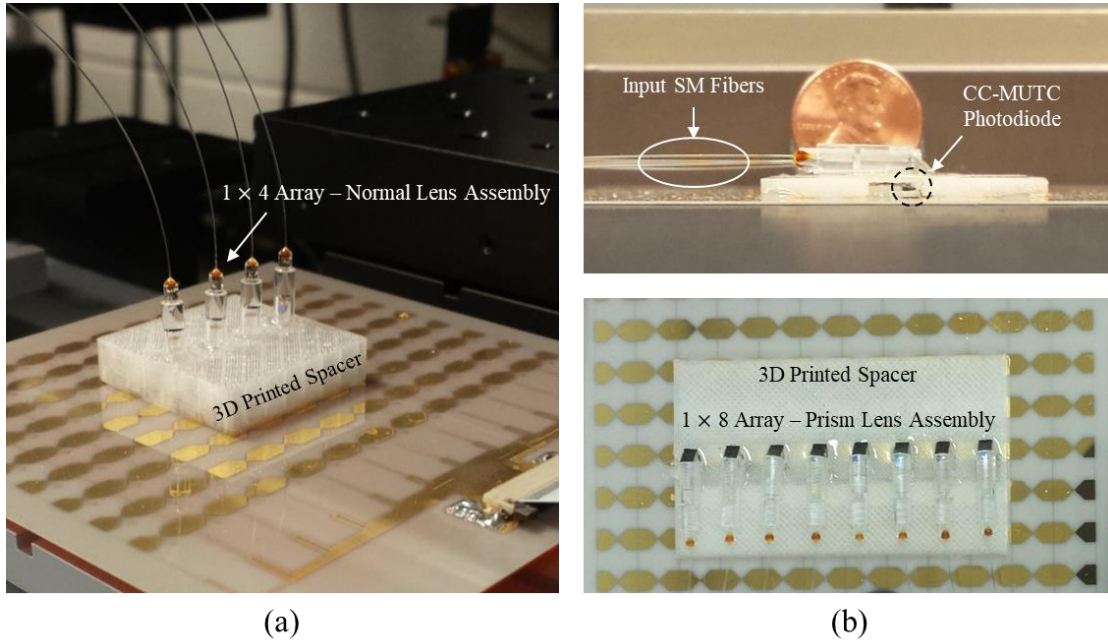


Figure 3.15: (a) 1×4 CA antenna, and (b) low profile 1×8 CA antenna after completing the optical alignment process.

3.2.3 Packaging

After aligning the input fibers to the wirebonded photodiodes, each CA antenna is positioned within a protective housing for characterization and transport. Similar to the spacer/mount, a protective, low fill-factor housing was 3D printed using ABS with a rectangular slot opening for undisturbed antenna radiation. Each housing structure is shown in Figure 3.16. The 1×4 array housing is $16.5 \text{ cm} \times 12.5 \text{ cm} \times 6.5 \text{ cm}$, shown in Figure 3.16 (a), and the 1×8 array housing is $25 \text{ cm} \times 17.5 \text{ cm} \times 1.9 \text{ cm}$, shown in Figure 3.16 (b), and the open backside of each is enclosed by an acrylic sheet. The housings also holds the photodiode biasing control board (green), that doubles as a real

time photocurrent feedback circuit, and the photodiode-coupled single mode fibers, which port through the bottom of the housing to the optical phase feed network.

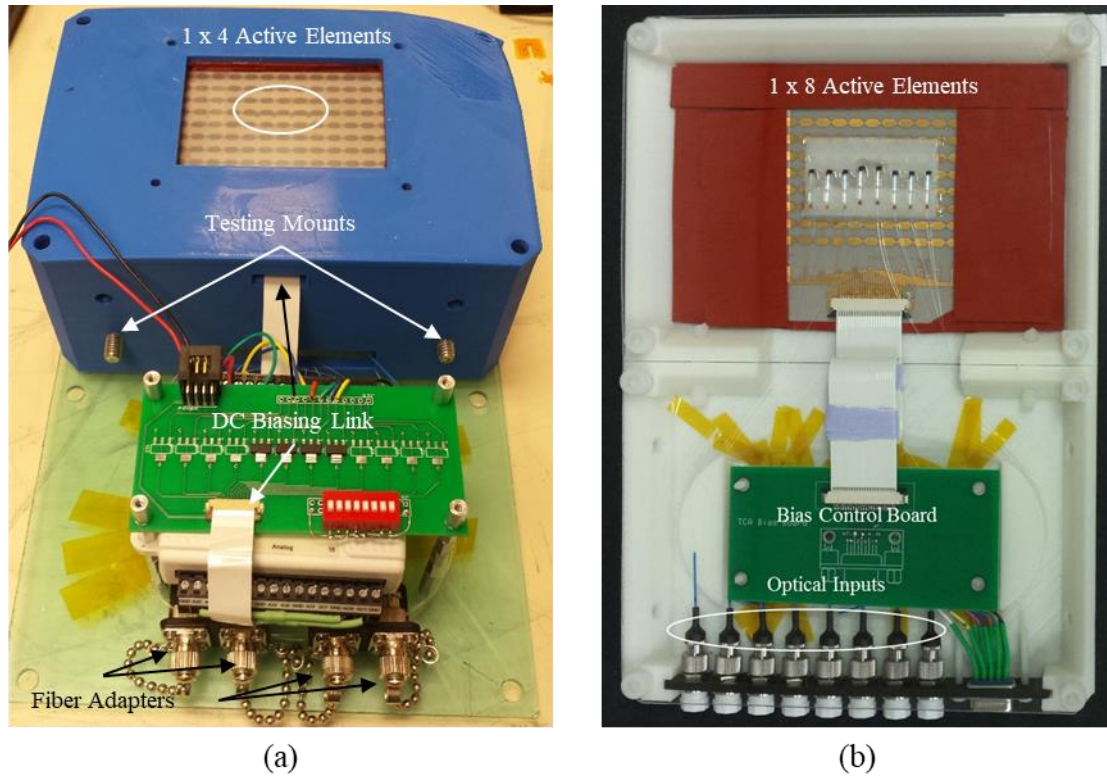


Figure 3.16: Packaged (a) 1×4 CA, and (b) low profile 1×8 CA connected to biasing control boards via FFC cables, and the optical inputs to the feed network.

Chapter 4

TX SYSTEM CHARACTERIZATION

4.1 Experimental Setup

Excitation of the photodiode-coupled CA is accomplished with an optical feed network based on the generation of two coherent, frequency-offset, phase shifted ~ 1550 nm laser signals. As mentioned, providing the photodiodes with phase noise correlated laser signals, offset by the desired RF signal frequency, enables high-fidelity RF beam formation free of the broadening effects of phase drift commonly experienced with heterodyne detection of uncorrelated lasers. Therefore, a TOPS coupled phase feed network is constructed to enable heterodyne detection of phase-controlled coherent signals by the CC-MUTC photodiodes. Signals generated from the TOPS system enter, and are power-balanced by, polarization-maintaining (PM) erbium doped fiber amplifiers before subsequently combining into a PM fiber where the two tones travel in separate polarization modes. These modes are distributed through N equal length channels comprised of lithium niobate (LiNbO_3) phase modulators integrated into an array. At the input of each phase modulator, the fast and slow axes of the PM fiber couple to the transverse-electric (TE) and transverse-magnetic (TM) modes of the z -cut LiNbO_3 waveguide, respectively. Applying a bias voltage to the modulator induces a net phase shift between optical modes due to the electro-optic coefficient imbalance between TM and TE polarizations within the z -cut LiNbO_3 waveguide, i.e., $r_{33} \approx 3r_{13}$, as previously discussed. Thereafter, 45° rotational keys and linear polarizers project the coherent phase-adjusted signals onto the same axis before traveling through constant

power ytterbium erbium doped fiber amplifiers for equalization of optical power heterodyned on to CC-MUTC photodiodes across the CA antenna.

System integration of the TOPS and phase feed network with the 1×8 optically addressed CA is illustrated in Figure 4.1. Also shown is the photonic receiver and processor used to detect the received RF signal power. By utilizing a photonic down-conversion scheme for analysis of received RF power, rather than an electronic spectrum analyzer (ESA), efficiency of phase calibration and other operational procedures is greatly improved with respect to speed and accuracy. The system uses a packaged photodiode located in the receiver processor, with an operational bandwidth of 1 GHz, to directly detect the received signal after down-conversion. A dual Mach-Zehnder modulator (DMZI) biased to single sideband suppressed carrier (SSB-SC) mode modulates a pure tone set at, $\omega_{dm} < 1$ GHz, onto one of the polarized optical modes, ω_2 . In doing so, the other optical mode, ω_1 , is transmitted to the photonic receiver where the received wireless RF signal, $\omega_{RF} = \omega_1 - (\omega_2 - \omega_{dm})$, is modulated onto the optical tone using a null-biased MZI. Selection of the lower sideband produced by this process results in a signal of frequency, $\omega_2 - \omega_{dm}$, which can be subsequently heterodyned with the optical mode, ω_2 , for down-conversion and analysis of the data. Phased array characteristics related to power measurements, i.e., 3-dB bandwidth, maximum EIRP, beamforming and beam steering, are presented here, while performance within a data link is presented elsewhere [140].

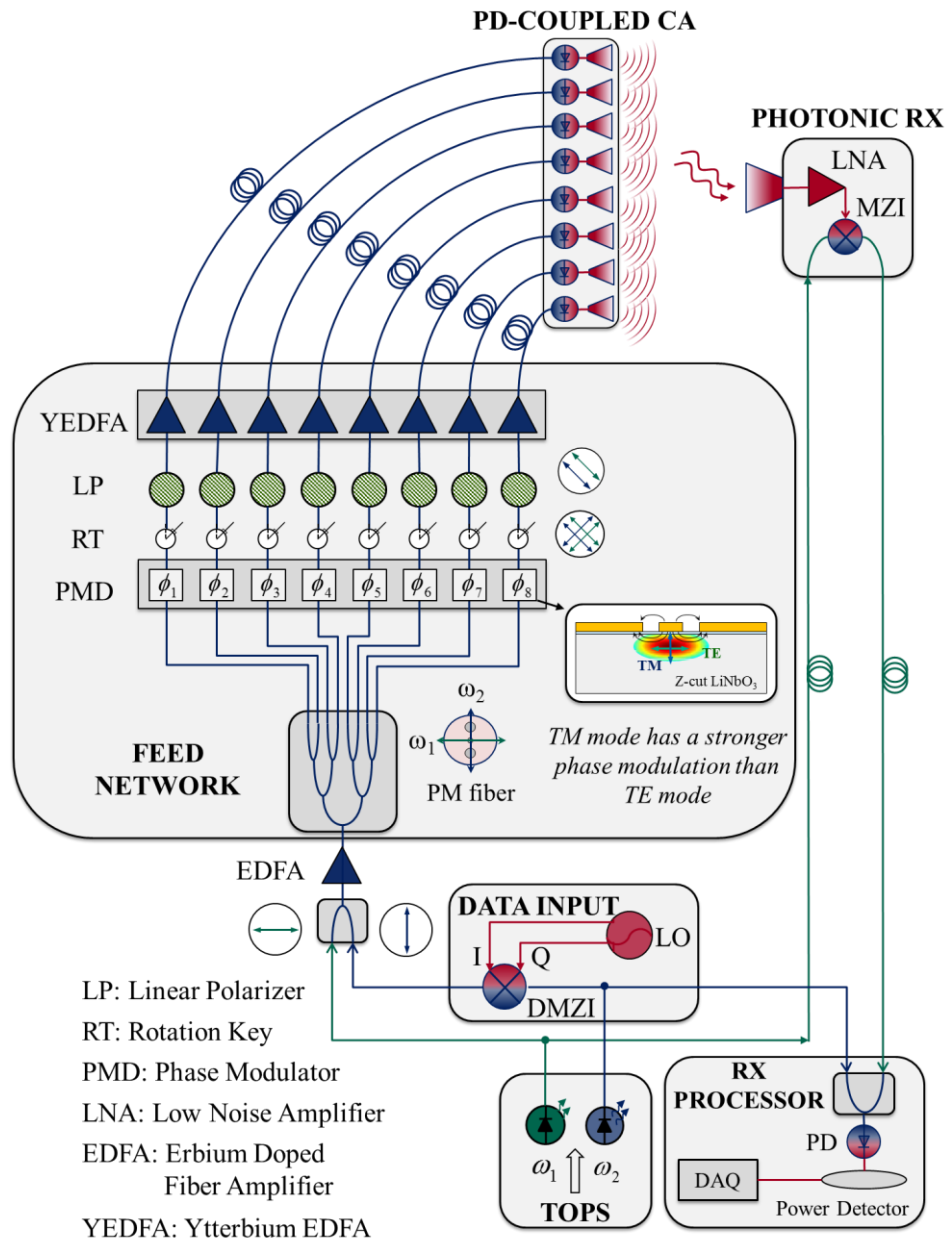


Figure 4.1: Schematic of experimental setup. The schematic includes the two-tone input from the TONS system, optical phase feed network, PD-coupled CA, and photonic receiver unit. Note that the TONS input does not include the sideband injection process for generation of the RF frequency offset optical signals.

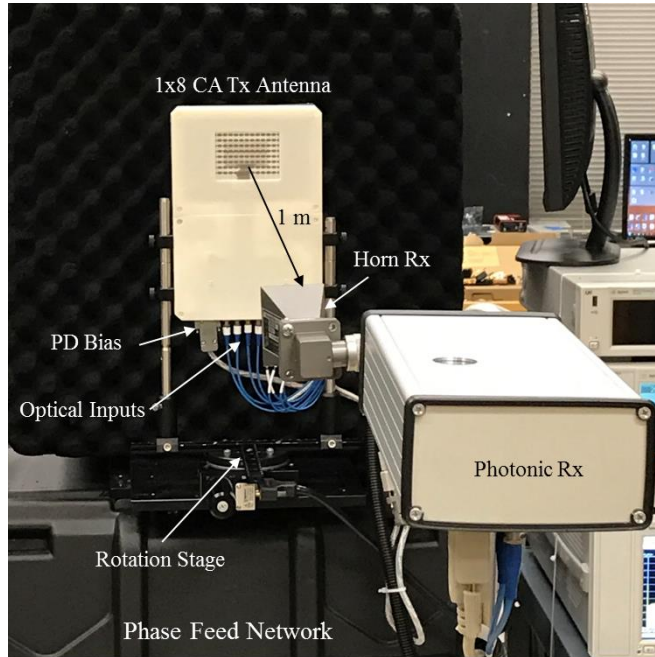


Figure 4.2: Image of experimental setup during 1×8 CA antenna characterization. The packaged 1×8 CA antenna is connected to optical fiber inputs from the phase feed network, and an RS-232 cable for photodiode (PD) biasing before being mounted on a rotation stage. Positioned 1 m away from the 1×8 CA antenna in the broadside direction is the horn-coupled photonic receiver.

Prior to characterizing the array, a phase calibration is necessary to synchronize each channel for effective beamforming and beam steering. To accomplish this, a reference channel is paired with each other channel individually for concurrent and sequential excitation of two elements while all other channels operate in extreme saturation without an applied bias. A bias board used to select on/off states controls channel suppression and excitation of each channel throughout the process. As two channels become isolated from the remainder of the array, a 2π phase sweep induces amplitude modulation at a Nearfield Systems Inc. 4-40 GHz dual ridged waveguide horn antenna, set 1 meter away, due to interference patterns produced from the two channels.

Upon completion of the phase calibration, the resultant phase correlation between all channels allows for high-fidelity beam generation. Over time, thermal variation in the optical fibers, modulators, and photodiodes contributes to minor phase drift; however, these effects remain minimal due to the injection locking setup.

4.2 Characterization and Results

In the following sections, the characterization and results of the two photonic CA antennas are presented. The first section discusses the characterization of the 1×4 photonic CA antenna, which primarily includes 3-dB bandwidth and beamforming performance, analyzed with a more simplistic, and less ideal, experimental setup than the one discussed in the previous sections. The fundamental differences in the setup includes the absence of optical power equalization in YEDFAs immediately prior to the CC-MUTC array, and the absence of the photonic receiver network. Without the final optical power equalization, unequal excitation of CC-MUTC photodiodes within the 1×4 CA can occur due to polarization dependent losses, causing imbalance optical power between ω_1 and ω_2 , that result in degradation of the modulation depths across the array. Based on this effect, the radiation efficiency of the array is lower than expect, as the next section will illustrate. Instead of the photonic receiver, the Nearfield Systems Inc. 4-40 GHz dual ridged waveguide horn antenna is directly coupled to an ESA through a 2.4 mm coaxial cable. This receiver configuration substantially increases the time capturing span required at each frequency and electronically controlled angular position sweep, and is the primary limitation confining the characterization to 3-dB bandwidth and beamforming analysis.

In the second generation design of the low profile, 1×8 photonic CA antenna, these effects were mitigated through reconfiguring the experimental setup to the

described system presented in the previous section. These improvements not only allow for improvement in the radiation efficiency of the array, but enabled more thorough characterization of the 3-dB bandwidth, EIRP, radiation patterns, and beamforming capabilities. As a final note, it is important to mention that in each experimental setup, the specific TOPS integrated into the transmit system was designed towards more efficient high frequency operation; therefore, injection locking at frequencies below 5 GHz was limited and led to characterization from this frequency up through 20 GHz.

4.2.1 1×4 Connected Array Antenna

In order to characterize the far-field response of the beams formed by the 1×4 photonic CA antenna, the dual ridged horn antenna is set up 1 meter way from the array at broadside, similar to the setup shown in Figure 4.2, and the beam formed by the array is electronically steered from -90° to $+90^\circ$. This process is repeated at 1 GHz increments over the design bandwidth of 5 – 20 GHz. Results from this process, at select frequencies, are included in Figure 4.3, where the relative power detected by the receiver is normalized for -60° to $+60^\circ$ steering angles. The angular measure shown is indicative of the direction of phase shifters in the phase feed network, i.e., the angular offset between the electrically steered main lobe position and the stationary receiver horn. Overall, the measured radiation profiles are well matched to simulated data produced in infinite array modeling of the fabricated 1×4 photonic CA antenna, with only a slight discrepancy due to the optical power imbalance occurring across the array of radiating elements created by the aforementioned optical tone power offset, and the unequal photodiode responsivities.

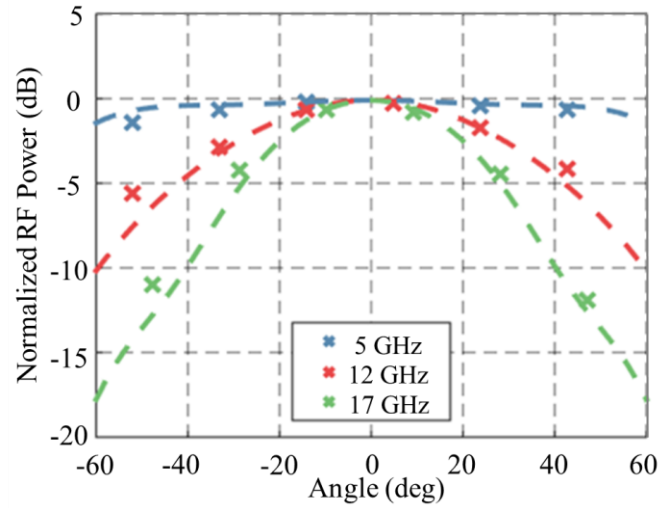


Figure 4.3 Normalization of measured far-field response of the 1×4 photonic CA antenna at various frequencies during electronic steering of a beam -60° to $+60^\circ$ with stationary receiver at 0° [141] © 2017 IEEE.

Bandwidth characterization of the 1×4 photonic CA antenna was completed by measuring received RF power with an ESA, and calculating the transmitted RF power and effective isotropic radiated power (EIRP) with Friis transmission equation:

$$EIRP = P_t + G_t = P_r - G_r - FSPL, \quad (4.1)$$

where P_t is the transmitted RF power, G_t is the transmitter gain, P_r is the received RF power, G_r is the receiver gain, and $FSPL$ is free space path loss. Following this process, bandwidth performance was analyzed at incremental photocurrent levels up to 40 mA per CC-MUTC photodiode, or 120 mA total photocurrent (40 mA photodiode). Due to the limitations in the initial photonic feed network, i.e., the absence of the YEDFA units and the maximum optical input power of the phase modulators being 23 dBm, this total

photocurrent excitation of 120 mA was the peak excitation level of the 1×4 photonic CA antenna. Additionally, during low power testing, mechanical defects in the photodiode bonding reduced the active element count to 3 active elements.

Even with only 3 active elements for high-power testing, the measured 3-dB transmitted RF power bandwidth was determined to be 7 – 17 GHz, 2.38:1, while driven at a total photocurrent of 90 mA, as observed by the results presented in Figure 4.4. Furthermore, comparison with finite simulation results of the fabricated CA antenna, which incorporates edge and photocurrent-frequency dependent transit time effects, indicates the measured frequency response of the 1×3 photonic CA antenna is well aligned with the expected performance. As mentioned, array edge effects produced due to the reduction of the infinite array model to 3 active elements will inevitably result in a more limited 3-dB bandwidth response. However, the drastic roll-off at high-frequency is more indicative of the photocurrent dependent bandwidth of the CC-MUTC devices, where approximately 1 dB efficiency loss is exhibited passed 12 GHz at the presented photocurrent level. This efficiency loss is assumed to be due to transit time limitations, within the photodiode, and is modeled according to Equation 2.10. As observed in Figure 2.9 (a), the bandwidth of the photodiodes drastically improves as the optical input power increases beyond 100 mW, allowing for potential extension of the fabricated photonic CA antennas 3-dB bandwidth by eliminating this efficiency loss. Although an increase in photocurrent enables improvements in operational bandwidth, the overall conversion efficiency of the array will be limited by the aforementioned degradation in modulation efficiency due to optical power imbalanced between the optical tones across the array, and other losses induced by the phase feed network. These

effects account for the offset between the measured RF power and the ideal 50 Ω RF output of 18.3 dBm.

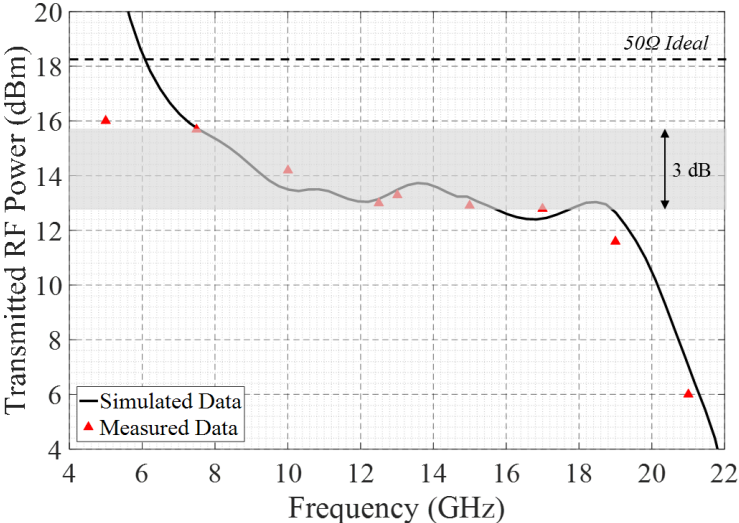


Figure 4.4 Frequency response of the 1×4 photonic CA antenna at 30 mA photocurrent per CC-MUTC photodiode. The ideal 50 Ω RF transmitted power at this photocurrent is approximately 18.3 dBm.

Regardless of the efficiency losses described, the array was characterized to the maximum optical input power allowed by the first generation photonic feed network. At this maximum input, the 1×3 photonic CA antenna was driven by CC-MUTC photodiodes outputting at total photocurrent of 120 mA, or 40 mA photocurrent each. This increase in photocurrent afforded a transmitted RF output power greater than 15 dBm up to 17 GHz. Even though the optical input power maximum for array excitation was reached, the CC-MUTC photodiodes integrated into the antenna were individually analyzed at photocurrents up to 100 mA at 6 V bias to ensure device reliability for future feed networks capable of providing input close to the maximum power handling limit

of the diodes. These tests were performed over several continuous hours, and none of the remaining antenna-coupled photodiodes exhibited thermal induced failure.

4.2.2 1×8 Connected Array Antenna

Using the setup in Figure 4.2, simultaneous characterization of the 3-dB bandwidth, EIRP, and beamforming capabilities of the 1×8 optically addressed CA is achieved through measuring received RF power at the dual ridged waveguide horn antenna connected to the photonic receiver during -90° to $+90^\circ$ beam steering cycles at 1 GHz iterative frequency steps. For each captured electrical steering scan within a 5-20 GHz test range, the received RF power is converted to EIRP using Friis transmission equation, which compensates for the receiver and transmitter antenna gain, and free-space path loss. The receive antenna manufacturer, Nearfield Systems Inc., provided gain values for each frequency, and radiation patterns from finite 1×8 CA antenna simulations provided simulated gain values for the transmitter at each frequency.

Additional compensation for a more accurate EIRP calculation required accounting for losses imposed on the measurement by the photonic receiver and down-conversion link. To accomplish this, a set of standard gain horn antennas with contiguous bandwidth of 5-20 GHz were set at the position of the 1×8 CA prototype, and connected to an Agilent PSG with a 0 dBm RF output. RF power values measured by the photonic receiver were collected at each frequency iteration used in the CA array characterization, and the effect of the photonic receiver link was calculated using the known gain of both transmit and receive horn antennas.

The beam patterns displayed in Figure 4.5 are the normalized far-field of the electrical scan measurements with 7 active elements, due to a nonfunctioning channel within the optical phase feed network. Additionally, one of the photodiodes among the

active elements exhibited 50% photodiode responsivity degradation from the original alignment. Based on these two detriments, the beams formed by the array exhibit less than ideal symmetry and uniformity. Even with 8 fully operational photodiodes of equal responsivity, a small amount of nonuniformity in beam profiles can be expected as a result of unequal photocurrent channels. Nonetheless, the array demonstrated effective beam forming with consistent extinction ratios over 10 dBm throughout the tested band, as exemplified in Figure 4.5, with 11.5 dBm and 12 ± 1 dBm at 8 GHz and 16 GHz, respectively.

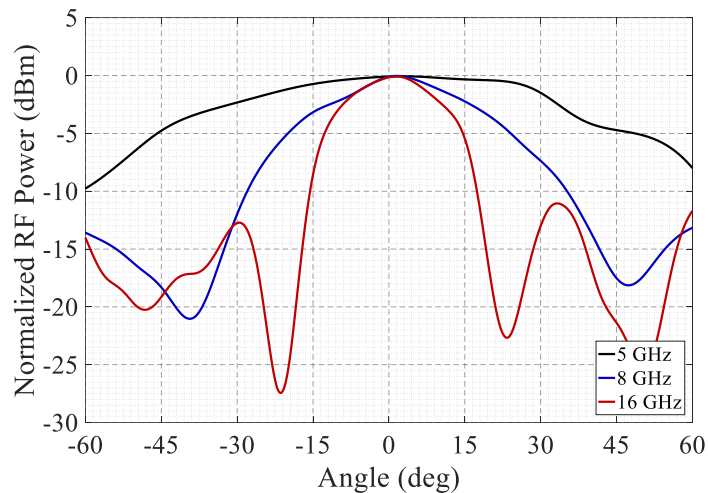


Figure 4.5: Normalization of measured far-field response at various frequencies during electronic steering of a beam -90° to $+90^\circ$ with stationary receiver at 0° . The angle is representative of the directional setting of the phase shifters in the phase feed network, i.e. the angular offset between the electrically steered main lobe position and the stationary receiver horn.

For each frequency-iterative electrical scan, the EIRP at the broadside beam position was extracted to characterize the frequency response of the array. This process

was repeated for incremental increases in optical input power, starting with a total array photocurrent of approximately 45 mA, *i.e.*, roughly 8 mA for each photodiode. As illustrated in Figure 4.6, the 3-dB bandwidth of the transmitted RF power at this optical input is 6-17 GHz, 2.83:1. Since the active array within the CA antenna prototype is much less than what constitutes an infinite array approximation used in our modeled device, the operational bandwidth is expected to degrade slightly due to edge effects. This bandwidth reducing effect is included in the simulation results compared against the measured data, by modeling a finite 1×8 CA in free-space, represented by the solid black line in Figure 4.6. In comparison to HFSS simulations of the finite 1×8 array, the measured transmitted RF power aligns well to the simulated response and is only slightly below the 50Ω ideal output of 8 dBm. The primary discrepancy between the two occurs at higher frequencies, where the decrease in measured transmitted RF power happens at a much more rapid rate than illustrated in the simulated data. Again, this effect is a result of the photocurrent-dependent bandwidth of the MUTC photodiodes, where the photodiode bandwidth is expected to increase at much higher photocurrents [141]. A final measurement was taken at 40 mA per photodiode. At this photocurrent the array generated a maximum EIRP of 27.5 dBm at 13 GHz, as shown in Figure 4.7.

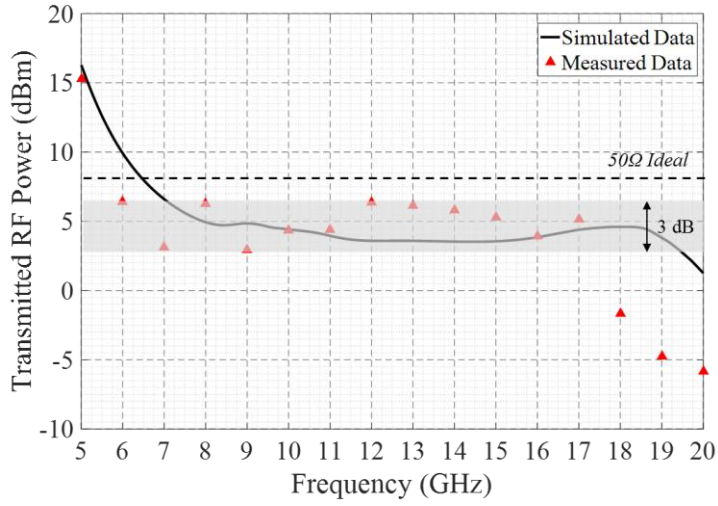


Figure 4.6: Bandwidth characterization of the array at approximately 8 mA photocurrent per diode (45mA total photocurrent). The ideal 50 Ω RF transmitted power at this photocurrent is approximately 8 dBm.

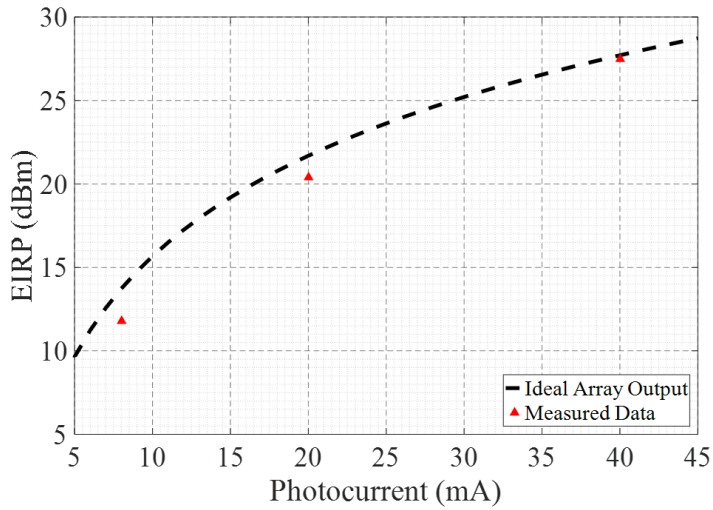


Figure 4.7: EIRP comparison of ideal 50 Ω array output and measured 1x8 CA antenna output for photocurrents of 8 mA, 20 mA, and 40 mA per photodiode at 13 GHz. Measured values approach the ideal as photocurrent is increased.

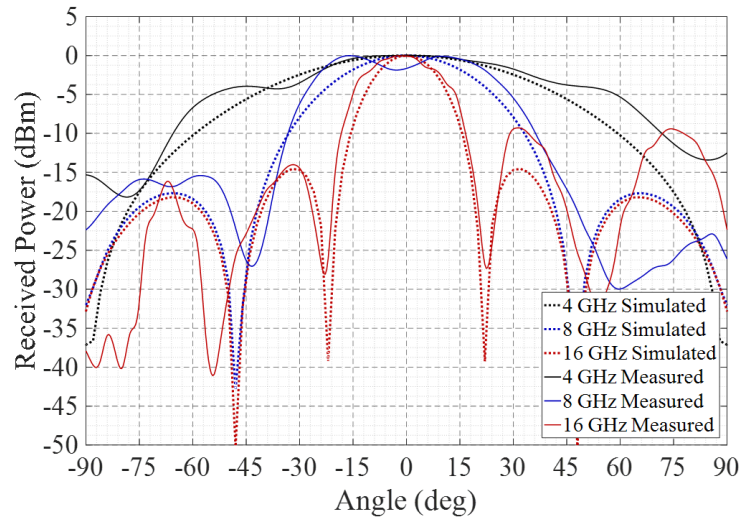


Figure 4.8: Normalization of the measured radiation patterns at various frequencies ranging from 5-20 GHz. The dotted lines represent the simulated results; measured results are overlaid with solid lines of the same color. The angle is representative of the broadside position of the physically rotated phased array transmitter relative to the stationary receiver.

Along with the electrical scans at different operational frequencies, -90° to $+90^\circ$ mechanical broadside rotational scans were conducted, using the rotation stage in Figure 4.2, to capture the E-field radiation pattern of the antenna at each frequency. As shown in Figure 4.8, the measured radiation patterns are in close agreement with the simulated radiation patterns with a slight symmetry offset due to the aforementioned imbalance in optical power excitation across the array. In addition to this, a small rippling effect across the measured radiations patterns, not present in the infinite array simulations, appears due to the amplitude variation between channels and the finite dimensionality of the active array. Even with the presence of these minor discrepancies, each radiation pattern displayed an extinction ratio greater than 9 dBm between the main lobe and first side lobes. Further reduction of these side lobe levels is possible through

implementation of amplitude weighting techniques, similar to those employed in [142]. Due to the low active element count in the array, most of the lower frequencies exhibit large main lobe beam widths. However, while approaching higher operating frequencies, such as 16 GHz, the array demonstrated main lobes with 3-dB beamwidth less than 35° .

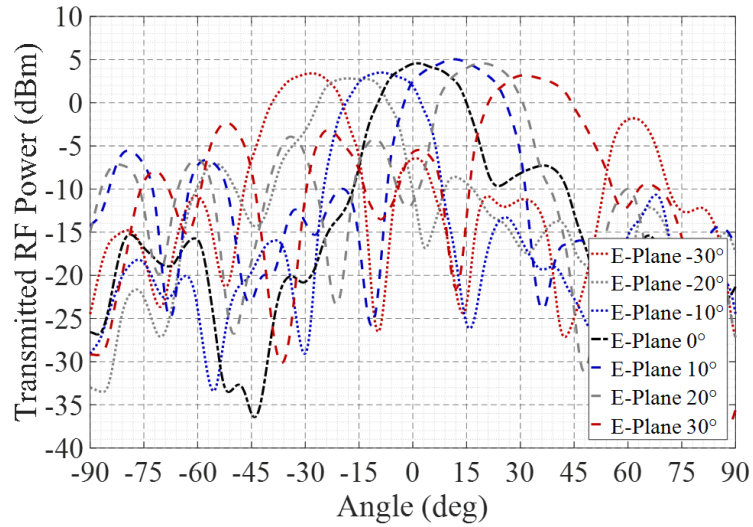


Figure 4.9: Low profile optically addressed 1×8 CA antenna beam steering at 16 GHz as it is excited with a total array photocurrent of 45 mA. Measured transmitted RF powers recorded during -90° to $+90^\circ$ broadside rotational scans with concurrent, increment electrical scans to $\pm 30^\circ$ in 10° increments.

Figure 4.9 exemplifies the beam steering capabilities of the 1×8 optically addressed phased array. Measurements were taken in the same manner as the broadside rotation scans while simultaneously electronically steering the beam from -30° to $+30^\circ$ in 10° increments. As the beam is steered toward larger scan angles, the antenna impedance is reduced according to Equation 2.2, results in the expected decrease in

transmitted RF power. This fundamental effect is evident in the actual responses presented here. Nonetheless, over this steering range the transmitted RF power remained within 3-dB of the broadside peak, which closely matches the $\pm 30^\circ$ 3-dB steering range shown in the infinite array model simulation of the CA antenna, presented in Figure 3.8.

4.3 Conclusion

Throughout Chapters 2 – 4 the fundamental principle and theory-guided design of RF photonic transmit apertures has been presented and implemented to successfully develop optically integrated UWB phased array architectures capable of meeting aforementioned demands. By directly integrating high-power photodiodes into inherently low profile CSA antennas, and coupling this RF photonic transmit aperture with a TOPS and interleaving optical phase feed network, these arrays can be readily deployed into compact, distributed remote units unhindered by base station to cell tower transmission losses. Additionally, the introduction of substrate loading and inductive peaking techniques, rather than lossy matching networks, afford improvements in photodiode response. Thus, through dense population of CC-MUTC photodiodes, supplied with adequate optical input powers, high-fidelity beamforming and beam steering of multiple data encoded beams can be realized over an UWB, using proper modulation techniques.

Initial prototyping of this ideal transmit configuration has been demonstrated with two lower element count CA antennas. Although these arrays were not able to be characterized at high optical input powers, analysis of each provided simulation matching performance, ultimately validating the techniques implemented. Based on this, by improving up the known performance deficiencies such as, optical feed network efficiencies, element count, and photocurrent-bandwidth relations, an RF photonic

transmit aperture possessing wider operational bandwidth, and output powers approaching the 50Ω ideal are realizable. Furthermore, through leveraging miniature right angle optical prisms, the profile of the CA antenna, optics included, was reduced to 0.33λ at the highest operating frequency of 20 GHz for the 1×8 optically addressed phased array. With smaller right angle optical prisms, and lens assembly components, commercially available, higher frequencies photodiodes can be introduced to both push the operation bandwidth further into the mmW regime, and allow for ground plane integration for 3-dB improvements in RF output powers.

Overall, this fundamental RF photonic transmit architecture development is an appealing portion of the overall network required to satisfy the demands of next generation 5G wireless communication deployment. Completion of a *smart*, adaptive RF photonic network relies on construction of a phased array receiver counterpart. More specifically, an RF photonic receiving aperture and processing unit capable of sensing spatial-spectral information of the RF environment, as well as down-conversion of transmitted data sequences. The remainder of this dissertation will focus on the theory, design, and fabrication of an RF photonic receiver capable of providing accurate spatial-spectral mapping of RF sources, which can be relayed to the RF photonic transmit system for user-targeted, data encoded, beam positioning.

Chapter 5

K-SPACE TOMOGRAPHY FUNDAMENTALS

5.1 k-Space Fundamentals

Complete characterization of the RF environment in terms of spatial and spectral components requires proper processing of field distributions over space and time. One non-intuitive method to accomplish this is by considering wave-space, referred to as k-space, rather than physical space as a sensing domain. In this chapter, the mathematical basis of k-space is presented, and through Fourier analysis, it will be shown that this linear-space dual of physical space allows for detection of RF waves without loss of information. Practical system component's view of k-space are subsequently presented in terms of a truncated, visible k-space, and spatial and spectral component extraction. Furthermore, coherent optical processing methods are introduced as an intriguing approach for capturing valuable information from k-space. By carefully constructing an RF photonic receiver aperture, and leveraging coherent optical processing, a k-space tomograph can be developed, and utilized for computational reconstruction of RF signal distributions.

5.1.1 Defining k-Space

To mathematically formulate, and define k-space, it is appropriate to begin describing the concept in terms of Fourier analysis. Thus, consider a complex-valued field $f(\mathbf{r})$ defined throughout volume V , which can be represented by a Fourier transformation:

$$\hat{f}(\mathbf{k}) = \frac{1}{(2\pi)^{3/2}} \iiint_V f(\mathbf{r}) e^{j\mathbf{k}\cdot\mathbf{r}} d^3\mathbf{r}, \quad (5.1)$$

with a corresponding inverse Fourier transformation expressed as

$$f(\mathbf{r}) = \frac{1}{(2\pi)^{3/2}} \iiint \hat{f}(\mathbf{k}) e^{-j\mathbf{k}\cdot\mathbf{r}} d^3\mathbf{k}, \quad (5.2)$$

under some existence conditions [143]. Moreover, by applying Fourier analysis to a time-variable field $f(t, \mathbf{r})$ over a finite range in time and space, the Fourier transformation can be represented as

$$\hat{f}(\omega, \mathbf{k}) = \frac{1}{4\pi^2} \iint f(t, \mathbf{r}) e^{-j(\omega t - \mathbf{k}\cdot\mathbf{r})} dt d^3\mathbf{r}. \quad (5.3)$$

This process can most simply be thought of as a decomposition of the original time-variable field,

$$f(t, \mathbf{r}) = \frac{1}{4\pi^2} \iint \hat{f}(\omega, \mathbf{k}) e^{j(\omega t - \mathbf{k}\cdot\mathbf{r})} d\omega d^3\mathbf{k}, \quad (5.4)$$

into sinusoidal plane waves for a defined ω and \mathbf{k} . In this case, $\hat{f}(\omega, \mathbf{k})$ is the amplitude, ω is the angular (temporal) frequency, and \mathbf{k} is the spatial frequency of a specific sinusoidal plane wave, $e^{-j(\omega t - \mathbf{k}\cdot\mathbf{r})}$, in the planewave decomposition of time-varying field $f(t, \mathbf{r})$. Due to the sinusoidal nature of $e^{-j(\omega t - \mathbf{k}\cdot\mathbf{r})}$, the angular frequency has a reciprocal relation to the temporal period T of field oscillation at \mathbf{r} of

$$\omega = \frac{2\pi}{T}, \quad (5.5)$$

and the spatial frequency vector length has a reciprocal relation to the wavelength λ of the plane wave

$$|\mathbf{k}| = \frac{2\pi}{\lambda}. \quad (5.6)$$

Based on this analysis, it is sufficient to utilize plane wave decomposition amplitudes $\hat{f}(\omega, \mathbf{k})$, in place of original field values, to delineate a time-variable field $f(t, \mathbf{r})$, or vice versa. Furthermore, by analyzing the homogenous form of the wave equation for free-space:

$$\frac{1}{c^2} \frac{\partial^2 f}{\partial t^2} - \nabla^2 f = 0, \quad (5.7)$$

where c is the speed of light in vacuum, and f can take the form of either the electric field \mathbf{E} or the magnetic field \mathbf{B} . It becomes apparent that, for time-variable fields satisfying Equation 5.7, only plane wave decomposition amplitudes $\hat{f}(\omega, \mathbf{k})$ exist for the case

$$\omega^2 = c_0^2 |\mathbf{k}|^2. \quad (5.8)$$

As a result, the information necessary to entirely represent a time-varying field is reduced to obtaining a complex amplitude weighted plane wave's wave-vector, \mathbf{k} , from which the temporal frequency component is calculated using the above relation. Therefore, the sensed RF environment is perceived through the superposition of \mathbf{k} -vectors in vector space, referred to as \mathbf{k} -space. As previously mentioned, this wave-space can be simply interpreted as a linear-space dual of the physical space described in terms of \mathbf{r} , and its depiction, which is referred to as the \mathbf{k} -space representation, is realized through Equation 5.3.

5.1.2 Practical System Considerations

In the above section, it was proven that a time-variable field $f(t, \mathbf{r})$ can be defined in terms of original field values, or plane wave decomposition amplitudes $\hat{f}(\omega, \mathbf{k})$ without loss of information. This flexibility shifts the decision of field analysis

method to application based suitability. For cases requiring multilateration, to calculate time difference of arrival through distributed sensing of the time-varying field in three-dimensional (3D) space, it is more appropriate to formulate the field from $f(t, \mathbf{r})$. In contrast, situations necessitating determination of absolute time of arrival (ToA), angle of arrival (AoA), or distance, e.g., field analysis at a base station, $\hat{f}(\omega, \mathbf{k})$ analysis is oftentimes more fitting. For the spatial-spectral utilization mapping application discussed through this dissertation, the absolute AoA and frequency are of interest; therefore, the k-space representation is apposite.

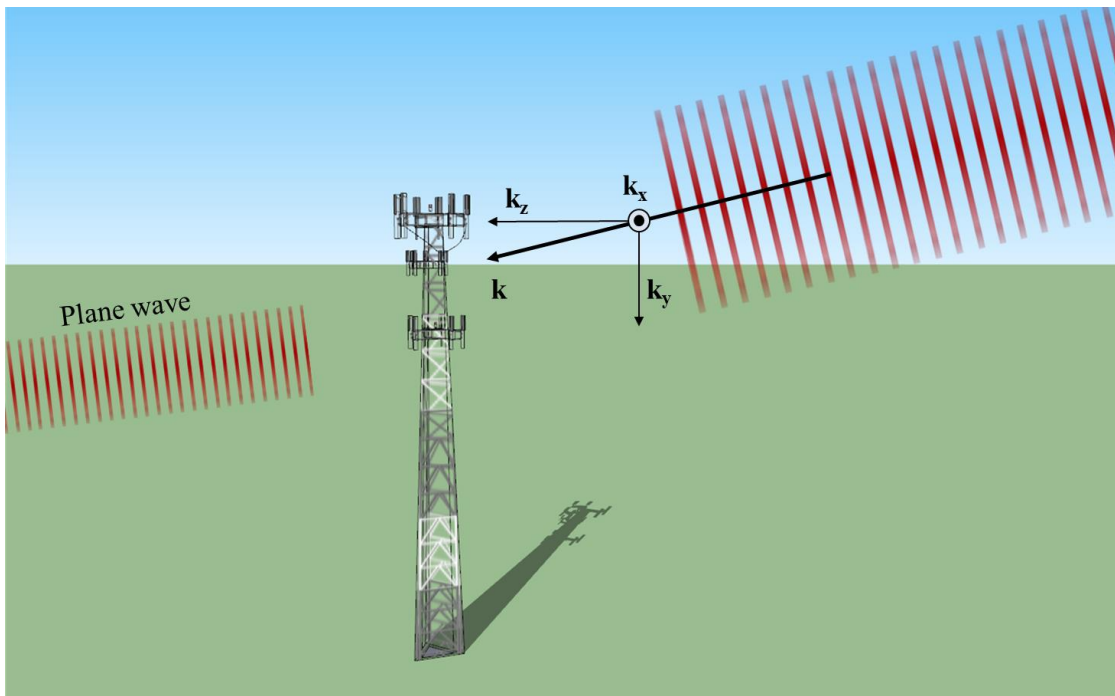


Figure 5.1: Mergence physical space and k-space, as a base station senses the k-space representation of the RF environment.

The concept of k-space sensing is illustrated in Figure 5.1, where incident plane waves are collected by a base station receiver. Assuming adequate processing, each plane wave is decomposed into respective complex amplitude weighted k-vectors, resolved at singular points in k-space. Lengths of each k-vector are subsequently calculated using the relation in Equation 5.8, and low frequency signals are expressed as short k-vectors, i.e., small spatial frequencies, while higher frequency RF waves form longer k-vectors. To more clearly understand this concept, consider a two-dimensional (2D) k-space representation, i.e., azimuthal AoA and frequency, formed by a theoretical omnidirectional antenna with infinite bandwidth, as depicted in Figure 5.2. It is shown that the non-bandlimited receiver effectively “sees” an infinite 2D, Cartesian k-space grid comprised of k-vector components k_x and k_z . By accurately analyzing the incident plane wave propagation vectors, the angular coordinate of the incident plane wave is recovered by

$$\theta = \tan^{-1}\left(\frac{k_x}{k_z}\right), \quad (5.9)$$

and the radial coordinate is obtain through the relation $|\mathbf{k}| = \sqrt{k_x^2 + k_z^2}$, where $k_x = |\mathbf{k}|\sin\theta$ and $k_z = |\mathbf{k}|\cos\theta$. Using these relations, the AoA is simply the value obtained from Equation 5.9, and the temporal frequency is calculated using Equation 5.8.

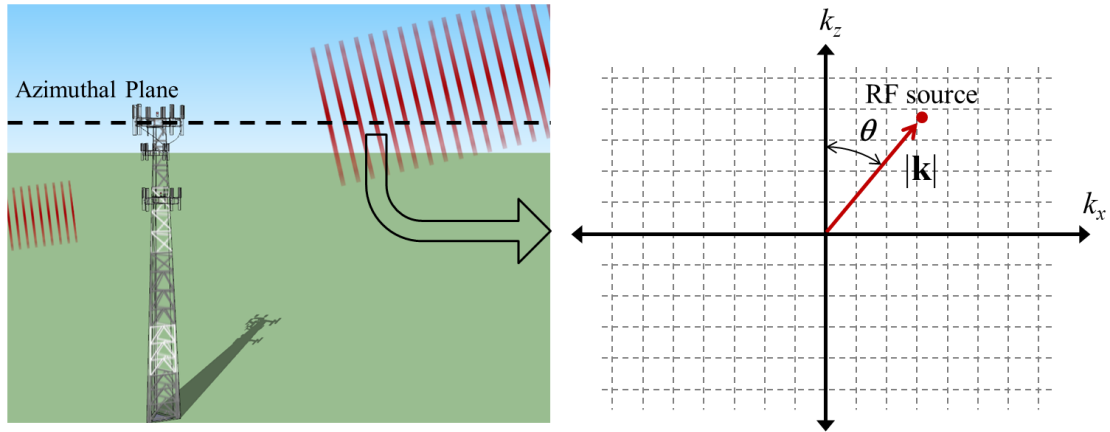


Figure 5.2: Two dimensional k-space representation.

In a practical receiver system, the antenna elements in the RF frontend effectively truncate k-space to a finite region based on bandwidth, field of view (FOV), and gain properties. First, consider an omnidirectional antenna with finite bandwidth. Since the temporal frequency of an incident plane wave is proportional to the length of the wave-vector \mathbf{k} , the truncation of the k-space representation occurs on the radial direction, as exemplified in Figure 5.3(a). It can be seen that the lower and upper limits on the antenna's operational bandwidth correspond to the k-space region constrained between the shortest and longest resolvable k-vectors, respectively. Next, if an antenna with a smaller FOV is integrated into the receiver, the k-space representation is further reduced. In this case, the k-space representation is angularly condensed according to the gain characteristics of the type of antenna. For an antenna with gain independent of frequency, the visible k-space region is truncated at radial lines corresponding to the acceptance region of the selected antenna, as shown in Figure 5.3(b). If the antenna possesses a frequency dependent gain, i.e. an effective size independent of frequency,

the visible k-space region is cut off at lines perpendicular to the antenna plane, as illustrated in Figure 5.3(c).

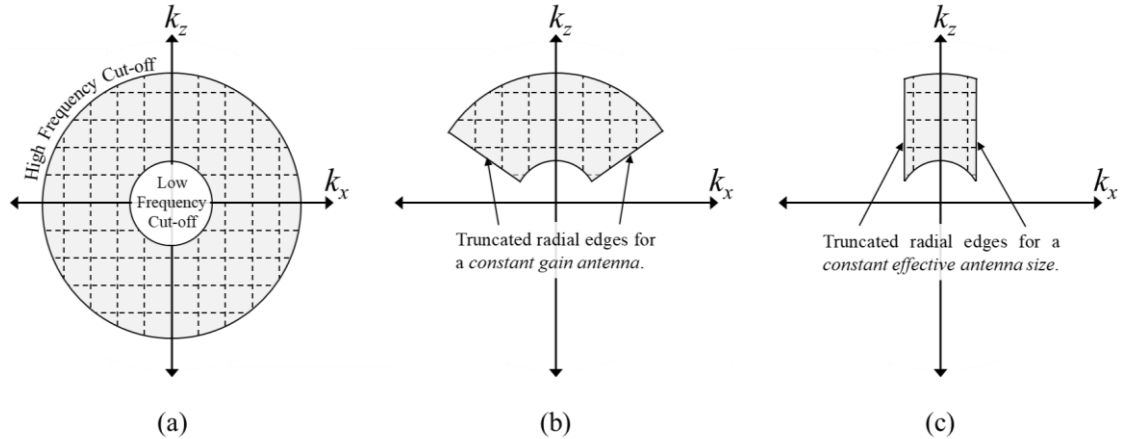


Figure 5.3: Truncated k-space representations for (a) an omnidirectional antenna, (b) a constant gain antenna, and (c) an antenna with a constant effective size.

While antenna selection controls the visible k-space region, an appropriate backend needs to be designed to extract both frequency and AoA of the RF signals contained within the respective region. If a single antenna element is connected to a channelized receiver, the frequency of received signals can be determined by sifting through the operational bandwidth. However, this type of receiver is only capable of providing a general direction of the signal based on the directivity of the integrated antenna, i.e. equal magnitude k-vectors are not separable into exact AoA's. This case is exemplified in Figure 5.4(a), where sources sensed by a constant gain antenna collapse to arcs of constant frequency. Alternatively, if a receiver is designed as a monochromatic imaging system, e.g., a microbolometer focal plane array IR camera, the EM energy is integrated along AoA directions, and frequency is indistinguishable.

An example k-space representation of an ideal achromatic camera is presented in Figure 5.4(b), indicating resolvable points as radial projection lines of constant AoA. Even if the imaging system is adjusted to include a standard color camera, the k-vector magnitudes will be lumped into large regions resolved on constant radial directions, and exact frequency values remain indiscernible.

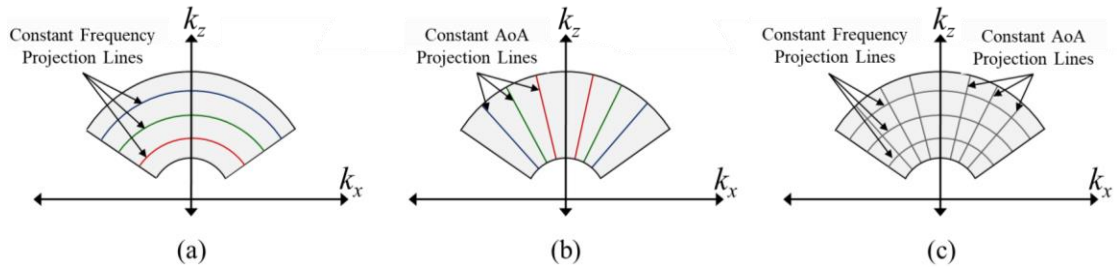


Figure 5.4: Distinguishable k-space regions based on constant lines of projection for (a) a channelized receiver coupled to a constant gain antenna, (b) an achromatic imaging system, and (c) a hypothetical system comprised of an ideal camera coupled to a channelized receiver.

In order to resolve exact frequency and AoA values, the concepts from each receiver backend can be theoretically combined to produce an orthogonal polar grid, as shown in Figure 5.4(c). From the presented receiver architectures, this system could include a channelized receiver coupled to each pixel in an achromatic imager. While this system would enable simultaneous extraction of frequency and AoA information, an unsurmountable amount of data would need to be processed in real-time. Based on this, an alternative method is required. One method for satisfying the requirements for properly sensing k-space is by reconfiguring current passive mmW imaging, and RF imaging receiver technology based on stereoscopic imaging and computed tomography principles. In the subsequent sections, the spatial-spectral processing capabilities

afforded by these concepts are presented for development of a practical k-space imaging receiver.

5.2 RF Photonic Spatial-Spectral Processing

Employing optics as a means of processing radio-frequency (RF) signals is an appealing technique due to its advantages over purely electronic counterparts [54], [57]–[60]. While most methods restrict focus to time-variable signals, RF-photonic coherent processing has demonstrated the capability of obtaining unique spatial information [144]–[154]. This spatial processing technique has been previously demonstrated in passive mmW imagers [145]–[152], [154], as well as an RF imaging receiver [153], and stands as a distinct functionality advantage over all-electronic systems. Although both system configurations acquire spatial information essential to spatial-spectral utilization mapping, the principles linked to proper image formation necessitate the use of identical length fibers to convey up-converted signals of a constrained instantaneous bandwidth to the optical processing unit. Consequently, signals with carrier frequencies distributed over broad bandwidths, or in separate mmW 5G spectral bands [12], and differing angle-of-arrivals (AoA) could produce ambiguous projections onto the detector plane due to squint.

This inherent limitation is removed by intentionally reconfiguring the optical fibers to unequal lengths, effectively coupling a temporal aperture with the system's spatial aperture, i.e., phased array antenna, to create real-time, analog correlations of the received RF signal. As a result, temporal processing, i.e., frequency detection, is afforded, at the cost of misaligned spatial correlations, and a scrambled optical image of the RF environment. Fortunately, both spatial and temporal correlations imposed by

the apertures can be recovered through implementation of a computed tomography (CT) algorithm to reconstruct spatial and spectral characteristics of each incident RF signal.

5.2.1 Spatial Processing

The core of RF photonic spatial processing relies on the up-conversion of incident EM radiation on a phased array receiver system through equal length optical fibers. In a practical system, as illustrated in Figure 5.5, each incident RF wavefront is sampled at discrete spatial positions on an antenna array coupled to electro-optic (EO) modulators for up-conversion to the optical domain. By distributing a common laser source to each modulator, the phase information encoded in cross-correlations between channels is preserved. As a result, the coherent optical up-conversion process generates amplitude-and-phase-encoded optical sidebands, effectively creating an RF-equivalent optical wavefront. Upon filtering out the carrier, and one sideband, these wavefronts can be imaged with a conventional optical system comprised of lenses and camera sensors. Ultimately this allows for real-time spatial mapping of active RF sources, distributed within the FOV of the imager, to different spatial locations on the image plane.

In the following sections the operating principles pertaining to the RF photonic spatial aperture, i.e. up-conversion modules and distributed aperture phased array, and backend optical processor will be discussed with respect to RF image formation. The optical up-conversion process with carrier suppression was originally proposed for mmW imaging applications; therefore, an in-depth analysis of the up-conversion process, and its noise and sensitivity properties are presented in [155], [156]. Nonetheless, a summary of this foundational process is included in the general

mathematical formulation of single-sideband imaging, as it is essential to spatial processing.

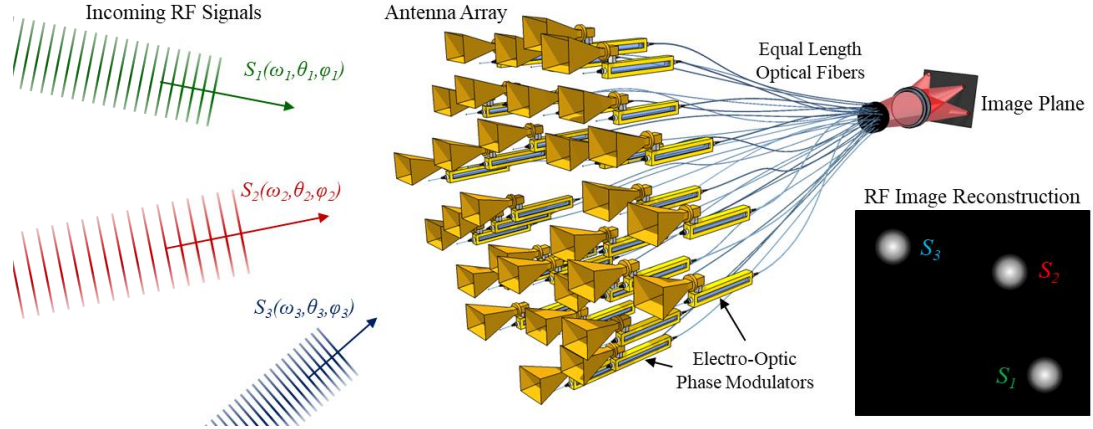


Figure 5.5: Conceptual representation of an imaging receiver.

5.2.1.1 Optical Up-Conversion Process

In order to analyze the spatial information contained within a targeted RF scene, the phase information from incident wavefronts needs to be sampled at discrete spatial positions and preserved throughout the system. Realization of this begins with the optical up-conversion of a RF signal into the optical domain, and is accomplished by integrating an EO phase modulator at the output of each antenna in a distributed phased array to encode the RF signal onto a monochromatic optical signal.

The nonlinear process enabling this conversion is referred to as the linear electro-optic effect, or Pockels effect. By applying a constant or varying electric field to an EO material, the effective refractive index of the noncentrosymmetric media is manipulated through orbital state distortion based on the relation:

$$\Delta n(t) = \frac{1}{2} n_e^3 r_{ij} \vec{E}(t) = \frac{1}{2} n_e^3 r_{ij} \frac{V(t)}{d}, \quad (5.10)$$

where n_e is the effective index of the EO material, r_{ij} is the linear electro-optic coefficient on the j -axis of the media, $E(t)$ is the external electric field equal to the applied voltage, $V(t)$, across the devices electrode distance, d , as a function of time. Consequently, if a monochromatic, linearly polarized optical wave propagates through this media along one of the crystalline axes when the external electric field is applied, the changed effective refractive index induces a net phase change in the optical wave:

$$\Delta\varphi(t) = 2\pi\Delta n(t) \frac{L}{\lambda}, \quad (5.11)$$

where L is the length of the interaction region within the EO material, and λ is the wavelength of the optical wave. As a result, the optical field at the output of the EO phase modulator becomes

$$E_o = E_{opt} e^{j(\omega_o t + \Delta\varphi)}, \quad (5.12)$$

where E_{opt} is the input optical field, and ω_o is the angular frequency of the optical wave.

When the EO phase modulators are coupled to antennas within a distributed phased array aperture to sense RF radiation, the applied voltage is governed by properties of the antenna receiving a sinusoidal signal. In this case, the antenna load is assumed to be $R_L = 50 \Omega$, and perfectly matched with the phase modulator input. Additionally, the incident RF signal is assumed to be a single tone propagating from the far field in free space. From these assumptions, the antenna input voltage can be derived from the power density of the incoming wave,

$$S_i = \vec{E} \times \vec{H} = \frac{1}{2\eta} \left(|E_\theta|^2 + |E_\phi|^2 \right), \quad (5.13)$$

where η is the impedance of free space, and is approximately $120\pi \Omega$. More specifically, the power received is determined by the effective area of the antenna collecting the incident power density, $P_{RF} = S_i A_{eff}$. As shown in [135], [157], the effective area of the receiving antenna is related to the gain and wavelength of design frequency by:

$$A_{eff}(\theta, \varphi) = \frac{\lambda^2}{4\pi} G(\theta, \varphi). \quad (5.14)$$

From the above relations, the received power can be represented as

$$P_{RF} = \frac{1}{2\eta} \left(|E_\theta|^2 + |E_\phi|^2 \right) \cdot \frac{\lambda^2}{4\pi} G(\theta, \varphi), \quad (5.15)$$

and the applied voltage can be formulated according to the relation $P_{RF} = \frac{V_{RF}^2}{R_L}$ as

$$V_{RF} = \frac{\left(|E_\theta|^2 + |E_\phi|^2 \right) \lambda}{2\pi} \cdot \sqrt{\frac{R_L}{120} G(\theta, \varphi)}. \quad (5.16)$$

The RF radiation collected by the receiving antenna is subsequently coupled to the RF input of the EO phase modulator. Based on the sinusoidal nature of the RF signal, the optical field at the output of the EO phase modulator becomes

$$E_o = E_{opt} e^{j \left(\omega_o t + \pi \frac{V_{RF}}{V_\pi} \cos(\Omega t) \right)}, \quad (5.17)$$

where Ω is the angular RF frequency, and V_π is the modulators half-wave voltage defined by:

$$V_{\pi} = \frac{\lambda d}{r_{ij} L n_e^3}. \quad (5.18)$$

As is evident from the relations above, the optical up-conversion preserves both the amplitude and phase information of incident RF signals. Thus, by integrating antenna-coupled EO phase modulators into a distributed phased array system for discrete spatial sampling of RF wavefronts, spatial processing of each signal is afforded, assuming proper transfer of the energy to an optical processing unit. In the next section, the method of RF image reconstruction is presented, and it is explicitly shown that only a single-sideband is required for spatial imaging of RF sources.

5.2.1.2 RF Image Reconstruction

As previously mentioned, by equivalently distributing a monochromatic laser source between each up-conversion module in a distributed aperture array, i.e. antenna-coupled EO phase modulator, the RF wavefront is transduced into an equivalent optical wavefront within optical fibers. The optical carrier and sidebands containing amplitude and phase components of the received RF signal are then conveyed through equal length optical fibers to a lenslet array configured identical in geometry to the antenna elements, scaled based on the optical wavelength. At this point, the optical beams emanate from the lenslet array into free space for channel-to-channel interference, and collectively propagate through a band-pass optical filter for upper-sideband and carrier suppression. From here, the overlapping optical beams containing only the lower-sidebands are projected onto a CCD array, where the resultant interference pattern produces an optical image of the RF signal spatial distribution, as sensed by the RF distributed aperture array.

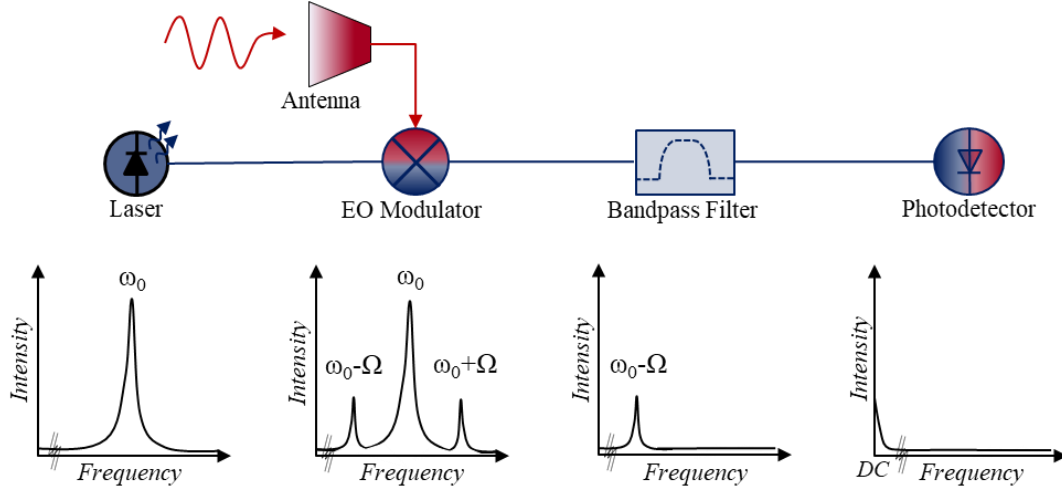


Figure 5.6: Optical up-conversion link and the frequency spectrum through the process.

In order to provide an understanding of this spatial processing, and the transfer for phased information from the RF environment to the CCD array pixels, consider the following process of RF image reconstruction:

$$E_n = \frac{1}{\sqrt{N}} \sum_{m=0}^{M-1} B_m e^{j(\omega t + \theta_{nm} + \varphi_{RF})} + c.c., \quad (5.19)$$

where E_n is the electrical field, in the optical domain, at the n^{th} pixel in the CCD without spectral filtering, B_m is the field amplitude at the output of the m^{th} optical fiber, ω is the optical frequency, θ_{nm} is the phase obtained by the optical beam during free space propagation from m^{th} optical fiber to n^{th} pixel, φ_{RF} is the RF-modulated phase of the optical beam in the m^{th} optical fiber, and $c.c.$ denotes the existence of a complex conjugate term necessary for the electric field to be a real number. As evident by the definitions provided, the system is assumed to have M receiving elements and optical fibers, and N elements in the CCD array. In addition to this, it is assumed that optical

light intensity emanating from each fiber is evenly distributed throughout the CCD array.

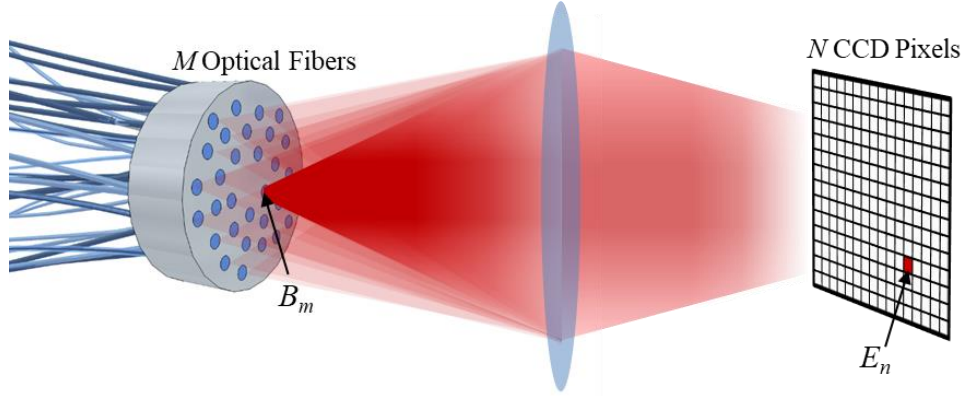


Figure 5.7: Geometrical setup and mapping of RF-encoded optical beam projections between the optical fiber array and CCD camera.

For the EM environment, it is assumed that K point sources are emitting single RF tones incoherently. Concomitant sensing, and optical-upconversion of all sources within the RF scene results in phases encoded within the m^{th} channel of the following form:

$$\varphi_{RF} = \sum_{k=0}^{K-1} S_k \cos(\Omega t + \phi_{km}), \quad (5.20)$$

where S_k are amplitudes of the RF signals scaled by modulation efficiency, antenna collection efficiency, and the distance from the aperture, and ϕ_{km} is the phase obtained during free space propagation from the k^{th} emitter to m^{th} antenna in the array. It is important to note that modulation efficiency across the array is assume to be identical. By substituting Equation 5.20 into Equation 5.19, the electric field at the n^{th} pixel in the CCD array without spectral filtering becomes

$$E_n = \frac{1}{\sqrt{N}} \sum_{m=0}^{M-1} B_m e^{j\left(\omega t + \theta_{nm} + \sum_k S_k \cos(\Omega t + \phi_{km})\right)} + c.c. \quad (5.21)$$

To achieve sufficient filtering, the spectral information in E_n needs to be identified, and more specifically, the specific frequencies present need to be documented. This is accomplished by reducing the exponential RF modulation term to a summation of Bessel functions with the Jacobi-Anger Expansion as follows:

$$e^{j\left(\omega t + \theta_{nm} + \sum_k S_k \cos(\Omega t + \phi_{km})\right)} = e^{j(\omega t + \theta_{nm})} \prod_k e^{j S_k \cos(\Omega t + \phi_{km})}, \quad (5.22)$$

where

$$\begin{aligned} e^{j S_k \cos(\Omega t + \phi_{km})} &= \sum_{\ell=-\infty}^{\infty} j^\ell J_\ell(S_k) e^{j\ell(\Omega t + \phi_{km})} \\ &= -j J_{-1}(S_k) e^{-j(\Omega t + \phi_{km})} + J_0(S_k) + j J_1(S_k) e^{j(\Omega t + \phi_{km})} \\ &= j J_1(S_k) e^{-j(\Omega t + \phi_{km})} + J_0(S_k) + j J_1(S_k) e^{j(\Omega t + \phi_{km})}. \end{aligned} \quad (5.23)$$

In accordance with the optical up-conversion of the RF signal, only terms corresponding to the lowest sidebands are kept. This expression can be further reduced by assuming the imposed RF field has a small amplitude, i.e. $S_k = 1$, to enable Taylor expansion of the Bessel functions of the first kind. Consequently, Equation 5.23 can be concisely described as

$$e^{j S_k \cos(\Omega t + \phi_{km})} = j \frac{S_k}{2} e^{-j(\Omega t + \phi_{km})} + \left(1 - j \frac{S_k^2}{4}\right) + j \frac{S_k}{2} e^{j(\Omega t + \phi_{km})}. \quad (5.24)$$

By substituting this equation into Equation 5.22, and performing simple algebra, the components in the optical beam are realized:

$$\begin{aligned}
e^{j\left(\omega t + \theta_{nm} + \sum_k S_k \cos(\Omega t + \phi_{km})\right)} &= e^{j\theta_{nm}} \left[1 - \frac{1}{4} \sum_{kk'} S_k S_{k'} e^{j(\phi_{km} - \phi_{km'})} \right] e^{j\omega t} + \dots \\
\left[\frac{j}{2} e^{j\theta_{nm}} \sum_k S_k e^{-j\phi_{km}} \right] e^{j(\omega t - \Omega t)} &+ \left[\frac{j}{2} e^{j\theta_{nm}} \sum_k S_k e^{j\phi_{km}} \right] e^{j(\omega t + \Omega t)},
\end{aligned} \tag{5.25}$$

where, on the right-hand-side of the equation, the first term is the carrier, the second term is the lower-sideband, and the third term is the upper-sideband. From here, it is apparent that as the optical beams traverse a band-pass optical filter for upper-sideband and carrier suppression and single sideband detection, the filtered electric field at the CCD array becomes

$$E_n^{LSB} = \frac{j e^{j(\omega - \Omega)t}}{2\sqrt{N}} \sum_{mk} B_m S_k e^{j(\theta_{nm} + \phi_{km})} + c.c. \tag{5.26}$$

At the CCD array, each element senses and integrates the intensity of the electric field over time. As a result, the detected signal at the n^{th} photodetector within the array can be represented as

$$\left\langle \left| E_n^{LSB} \right|^2 \right\rangle = \left\langle 2 \left| \frac{j e^{j(\omega - \Omega)t}}{2\sqrt{N}} \sum_{mk} B_m S_k e^{j(\theta_{nm} + \phi_{km})} \right|^2 \right\rangle. \tag{5.27}$$

To ensure proper image formation, the imaging system requires the optical fiber lengths conveying the RF signals to be equal. This implies that the time delays imposed by the

optical fibers are equivalent across the array. By taking this into consideration, and performing simple algebra, the detected signal becomes

$$\left\langle \left| E_n^{LSB} \right|^2 \right\rangle = \frac{1}{2N} \sum_{mm'} B_m B_{m'}^* e^{j(\theta_{mm} - \theta_{mm'})} \sum_{kk'} S_k S_{k'} \left\langle e^{-j(\phi_{km} - \phi_{k'm'})} \right\rangle. \quad (5.28)$$

While this expression holds based on the linearity of the averaging operation, the averaging of the phase components related to the incoherent emitters requires some consideration.

In a practical system, the averaging process is automatically carried out by setting the integration time of the CCD array to be orders of magnitude larger than the time components associated with the RF carrier frequency and bandwidth. By assuming the incident signals possess a bandwidth of several GHz, the coherence time is on the sub-nanosecond range. Thus, when sensed over the integration time of the CCD array, i.e., several milliseconds, the phase-difference from wavefronts produced at different spatial positions will be a small fraction of this time. As a result, the phase-differences will be averaged at the optical sensors.

With respect to incoherent sources with a finite bandwidth, it is instructive to consider the RF signals phase compared to an ideal sinusoid at the center frequency over large integration times. Throughout these intervals, the phase of the RF wave shifts either ahead or behind the ideal reference. Based on this variation, it becomes apparent that the time change of the phase needs to remain within a specific bounds. At the high end, this phase variation must be below the 2π shift corresponding to the signal's finite bandwidth. At the low end, it must vary fast enough to occupy the entire designated bandwidth. More simply stated, different incoherent sources are represented as imperfect sine waves with phases shifting back and forth independently, with respect to

an ideal sinusoid, where the speed of phase variation is confined within a finite bandwidth.

When the incoherent sources are projected onto an optical sensing element, i.e., a square-law detector, the waves will interfere either constructively or destructively. By integrating over a period much larger than the bandwidth of the received signal, the time averaging process becomes equivalent to averaging over all possible phased differences between the incoherent waves. Consequently, the phase averaging of incoherent sources within Equation 5.28 can be expressed as

$$\left\langle e^{-j(\phi_{km} - \phi_{k'm'})} \right\rangle = \frac{1}{(2\pi)^2} \int_{-\pi}^{\pi} \int_{-\pi}^{\pi} e^{-j(\phi_{km} - \phi_k - \phi_{k'm'} + \phi_{k'})} d\phi_k d\phi_{k'}, \quad (5.29)$$

and solving the integral reduces the average to

$$\left\langle e^{-j(\phi_{km} - \phi_{k'm'})} \right\rangle = e^{-j(\phi_{km} - \phi_{k'm'})} \delta_{kk'}, \quad (5.30)$$

where $\delta_{kk'}$ is the Kronecker delta. By substituting this into Equation 2.28, the average single-sideband intensity detected at the n^{th} pixel of the CCD array becomes

$$\left\langle \left| E_n^{LSB} \right|^2 \right\rangle = \frac{1}{2N} \sum_{mm'} B_m B_m^* e^{j(\theta_{nm} - \theta_{nm'})} \sum_k S_k^2 e^{-j(\phi_{km} - \phi_{k'm'})}, \quad (5.31)$$

which can be reduced to

$$\left\langle |E_n^{LSB}|^2 \right\rangle = \frac{1}{2N} \sum_k \left| \sum_m S_k B_m e^{j(\theta_{nm} - \phi_{km})} \right|^2. \quad (5.32)$$

Based on this expression, it is explicitly shown that distributed aperture up-conversion process enables the capability to image incoherent RF radiation from the information contained on a single-sideband. By preserving the amplitude and phase of each signal throughout the imaging receiver, each signal is spatially mapped to different sectors within the CCD array, ultimately producing real-time spatial processing of the RF scene. Extension of the processing capabilities to afford detection of both spatial and temporal information is realized through modifying specific components within the imaging receiver architecture. In the next section, the process of reconfiguring the system to enable temporal processing is presented.

5.2.2 Temporal Processing

The proposed methodology for obtaining temporal information, in addition to spatial information, through reconfiguration of the imaging receiver stems is derived from two concepts: stereoscopic imaging and chromatic aberration. In stereoscopic imaging, two offset, 2D images are resolved separately for subsequent recombination, and formulation of a 3D depth perception. This process is analogous to the way humans visualize physical 3D space, where our spatially separated eyes project offset 2D images onto the 2D retina, and our brain processes this information to reconstruct the 3D physical environment. By considering the k-space representation from an ideal imaging system in Figure 5.4(b), the application of stereoscopic imaging principles provides a method of viewing k-space in the same way our eyes view the 3D world. More specifically, by obtaining multiple projects of incoming waves on radial directions, the

2D k-space regions presented above, can be resolved from offset 1D k-space images. This process of reconstructing 2D k-space effectively involves separating the frequency components contained on radial lines of constant AoA. In this case, the detrimental effect of squint within the imaging receiver operating over wide bandwidths can be opportunistically leveraged in conjunction with the stereoscopic imaging techniques.

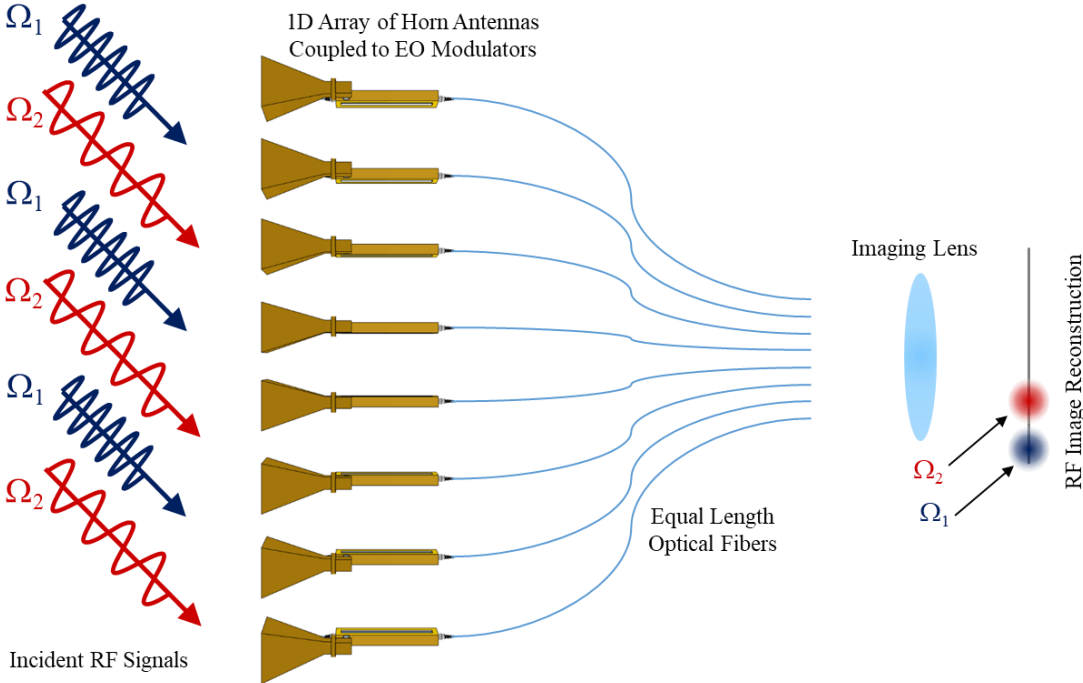


Figure 5.8: Squint effects from the phased array antenna effectively appear as chromatic aberration in the imaging receiver, where incident RF waves with same AoA, but different frequency are reconstructed at different positions in the image plane.

To understand the merging of these concepts, first consider the squint effects within the proposed imaging receiver. While the derivation in the previous section focused on incoherent signals of the same frequency, it is apparent that the discrete

sampling of signals with differing frequency will affect the phase information transfer through the system. This notion defines the deficiency commonly seen in phased arrays, where AoA of incident signals is a function of frequency. As a result, RF wavefronts of different frequencies and same oblique AoA are resolved at different points on the imaging plane of the imaging receiver. This effect is shown in Figure 5.8, with incident signals of frequencies Ω_1 and Ω_2 of the same AoA captured by the distributed phased array antenna. Upon optical up-conversion, and projection onto the imaging plane, an RF image is formed with the sources resolved to different spots.

This principle of squint in the imaging receiver directly transfers to k-space sensing, where the spatial positioning of RF wave-vectors are resolved within the image is determined by the scalar projection onto the imaging axis of the system. Based on this spatial separation principle, it is limited to only distinguishing k-vectors of oblique incidence, as multiple k-vectors of normal incidence will yield the same projection. In addition to this type of scene, it is important to discuss the effects of the presented phenomenon on other k-space distribution cases, shown in Figure 5.9. Similar to the scene presented in Figure 5.8, sources of different frequency and same oblique AoA are resolved to separate points on the imaging plane. In k-space this occurs through the projection of two k-vectors, \mathbf{k}_1 and \mathbf{k}_2 , of different lengths, i.e., different spatial frequencies, from the same AoA onto the imaging axis. Another interesting case is when multiple wave-vectors \mathbf{k}_3 , \mathbf{k}_4 , and \mathbf{k}_5 share the identical scalar projections onto the imaging axis. As a result, particular RF signal distributions are ambiguously reconstructed to the same point in an RF image. From these effects, the k-space region visible from an imaging receiver is simply formulated with resolvable points along lines of constant k_x , assuming a 1D antenna aperture aligned along the x -axis, as illustrated in

Figure 5.10(a). Accordingly, all k -vectors projected onto the same line of constant k_x are imaged onto a single spot during optical reconstruction, where each k_x line is directly mapped to its own position on the imaging plane, as shown in Figure 5.10(b).

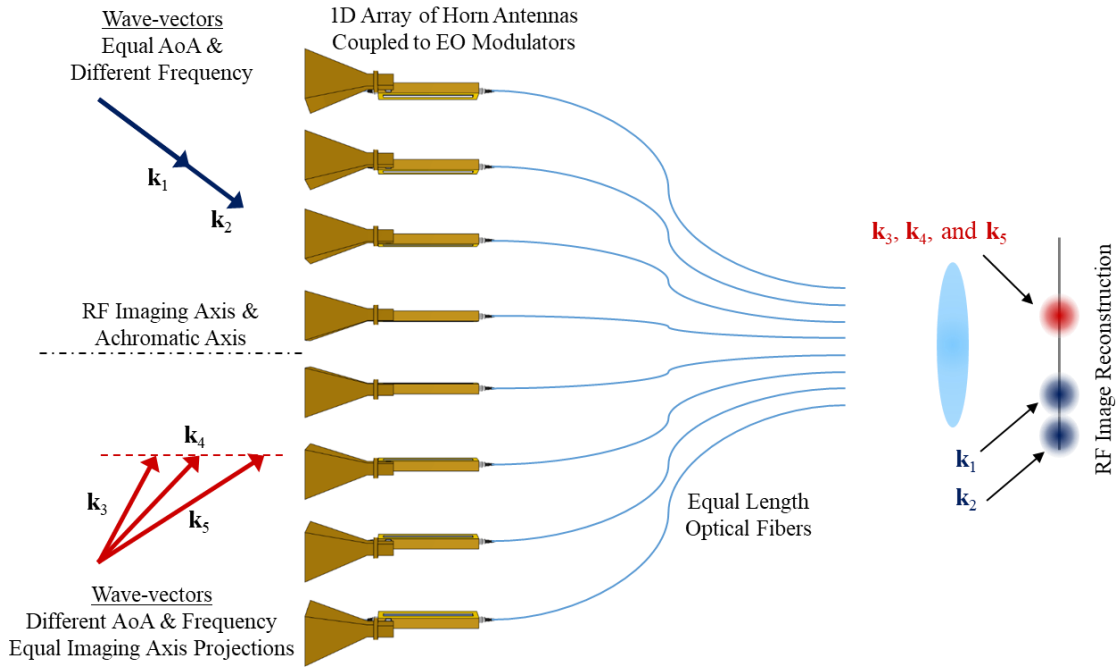


Figure 5.9: Incident RF waves are imaged in k -space by the imaging receiver as projections of 3D wave-vectors onto a 2D image plane of the lens. The chromatic aberration is realized through the scalar projection of each k -vector onto the RF imaging axis.

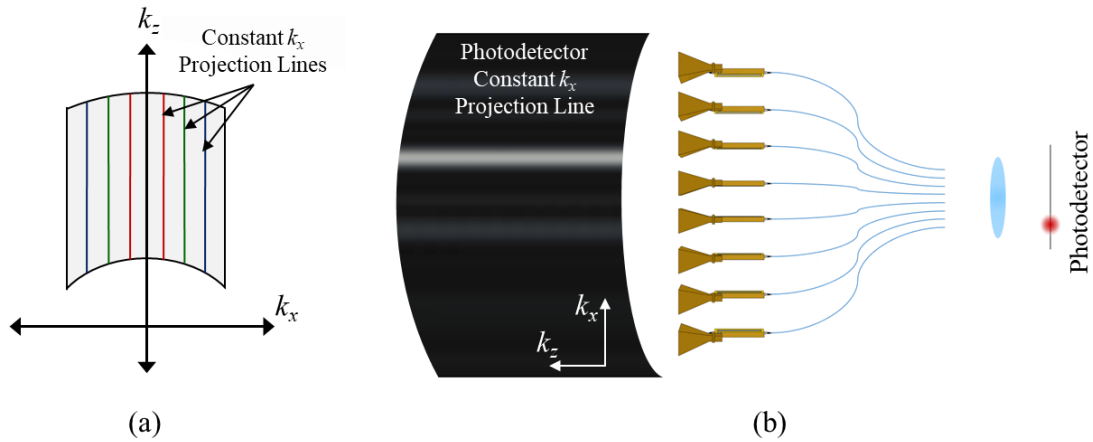


Figure 5.10: (a) The view of k -space from an imaging receiver is based on the system's ability to only sense projections onto the RF imaging axis, collapsing incident RF waves along lines of constant k_x . (b) At the image plane, each pixel corresponds to a particular line of constant k_x projection.

From the descriptions above, it is shown that squint effects inherent to the imaging receiver architecture allow for differentiation of incident wavefronts comprised of different frequencies. The main limiting factor in the current configuration, it is the inability to separate sources incident along the imaging axis. One method of preventing ambiguity for sources of this type is to manipulate the system's components so all sources are incident along one side of this axis. This unconventional approach of deliberately magnifying squint effects can be accomplished in two ways. The first technique is rotating the antennas within the aperture for misalignment of the antenna acceptance angle and the achromatic axis of the lens-based optical processor. The second is maintaining the original antenna positioning, but modifying the optical fiber lengths carrying the RF-encoded optical beams. It will be shown that the latter approach serves as a more feasible approach for simultaneous spatial-spectral processing.

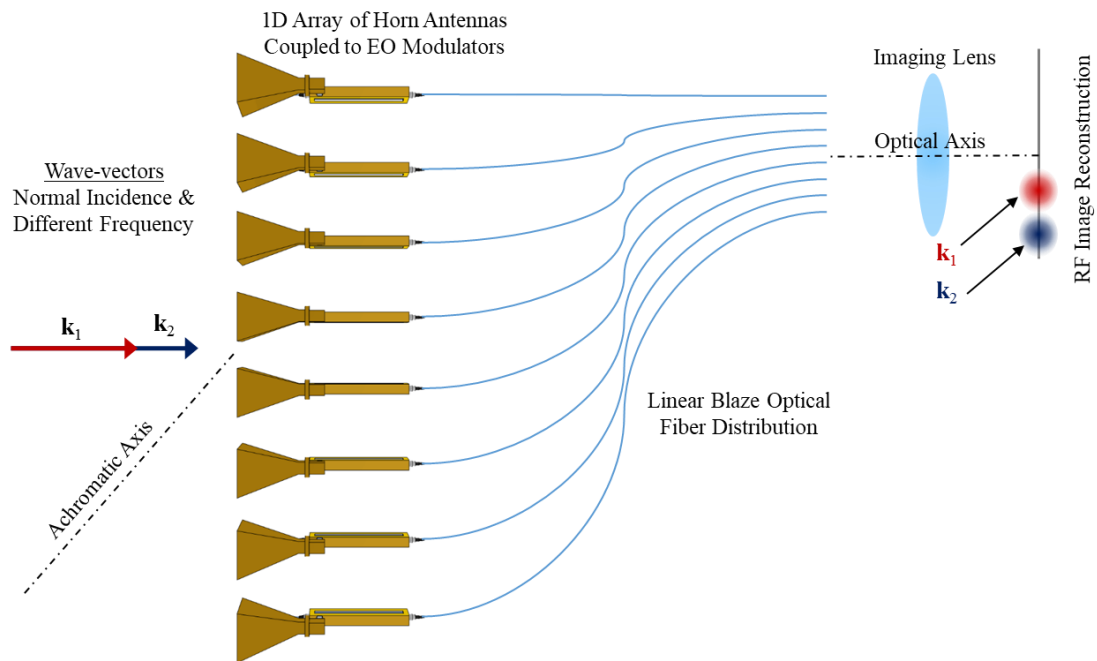


Figure 5.11: Introduction of a linear optical fiber length progression across the array steers the achromatic axis of the imaging receiver.

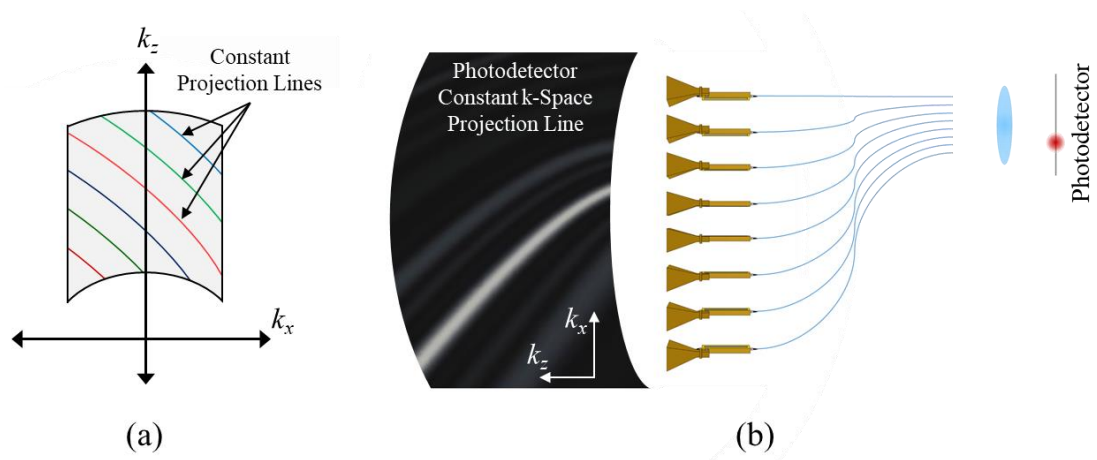


Figure 5.12: (a) The view of k -space from an imaging receiver with a linear optical fiber length distribution distorts projection lines based on achromatic axis tilt. (b) At the image plane, each pixel corresponds to a particular line of constant projection comprised of mixed k_x and k_z values.

To understand the effects of changing the optical fiber lengths, it is most appropriate to begin with a simple linear profile, as illustrated in Figure 5.11. By positioning the fibers in this linear blaze formation, a TTD effectively steers the RF-encoded optical wavefronts, and tilts the achromatic axis. As a result, all incident RF waves experience the effects of squint, regardless of AoA. In k-space, the scalar projection lines are curved according to the change in achromatic axis, as displayed in Figure 5.12. Resolvable k-points will now mix the k_x and k_x components necessary to resolve frequency and AoA of emitters. Thus, a single blazed profile merely shifts the constant projections without eliminating the possibility of unresolvable, degenerate frequency and AoA pairs.

In an effort to circumvent loss of information, the aforementioned principles from stereoscopic imaging can be adopted to reconstruct a 2D scene from two 1D images. Stereoscopic k-space imaging is realized by adding a second imaging receiver, with an optical fiber blaze profile organized in the opposite direction to produce scalar projections in k-space that are curved along two separate achromatic axes. Contrary to conventional stereoscopic imaging of physical space, the apertures sensing the RF environment in k-space can be co-located, as illustrated in Figure 5.13, without changing the projection lines. This is due to the fact that the projections occur based on the fiber length distributions, rather than a physical adjustment in the RF frontend. Furthermore, by splitting the output of each up-conversion module, two optical fiber configurations can be easily construction within a practical system.

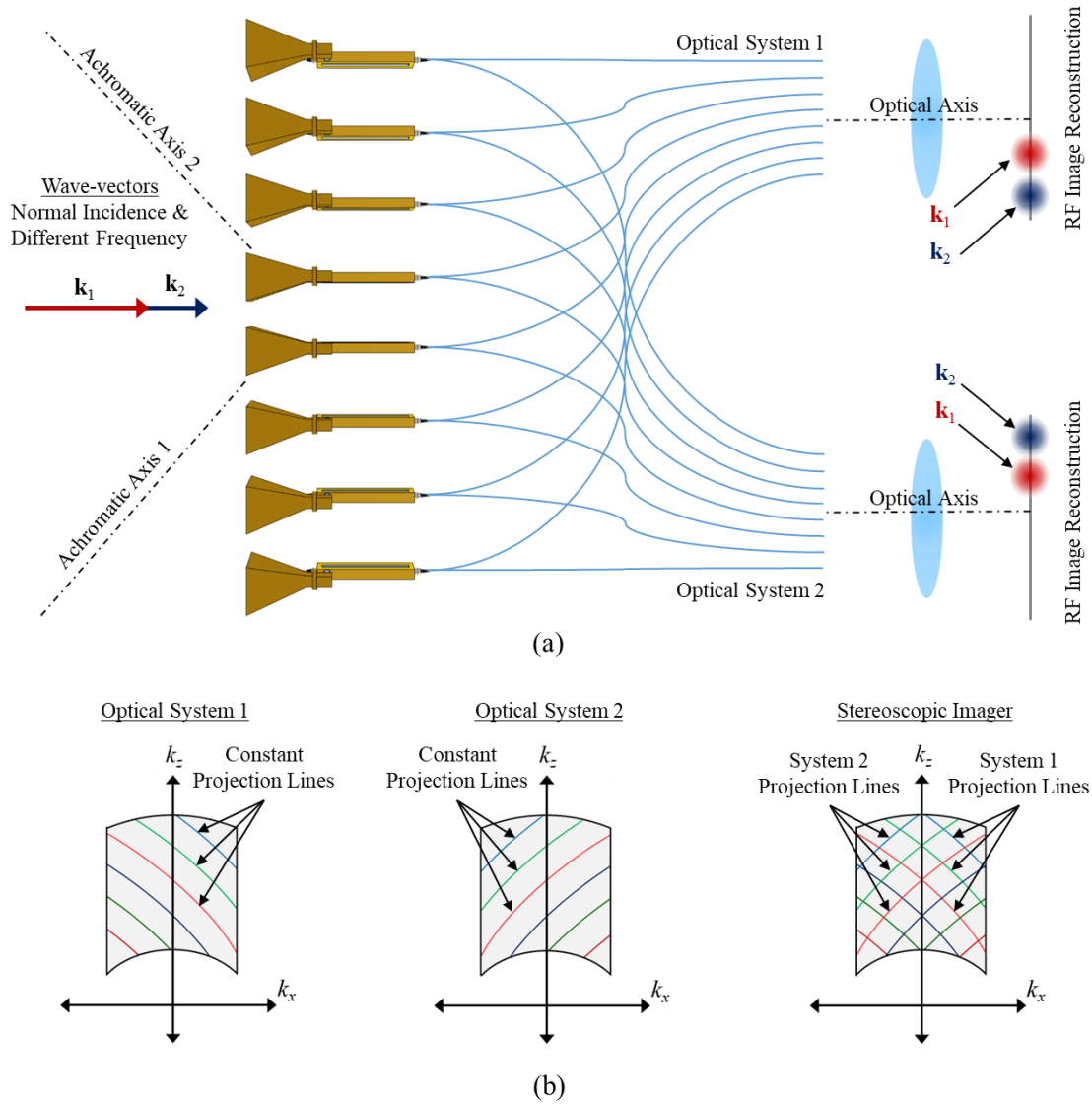


Figure 5.13: (a) Stereoscopic imaging of k -space is created by splitting output from EO modulator into two opposing linear optical fiber length progressions across the array, effectively forming two non-parallel achromatic axes. (b) As a result the distorted projection lines created by each linear progression are combined as one set of non-parallel lines of constant projection.

While a stereoscopic k -space imager will provide enough information to locate both k_x and k_z components of an incident RF plane wave, cases where multiple sources

are present still create the possibility for ambiguous reconstructions. It is possible to improve the accuracy of k-space reconstructions by continuing to add more optical fiber profiles, as each added projection will reduce the risk of degenerate frequency and AoA pairs. However, from the perspective of practical system development, continual addition of more optical fiber profiles diminishes signal-to-noise ratio, and increases cost and complexity. In an effort to avoid these challenges, an imaging receiver can be designed with a single optical fiber behind each up-conversion module, where the length of each is arbitrarily selected, and the reconstruction of spatial-temporal information from k-space relies on computational methods. From this idea, a new imaging modality, referred to as k-space tomography, is developed, and details of this approach is presented in the following section.

5.3 k-Space Tomography

In the previous sections, the mathematical foundation and system considerations essential to spatial-spectral processing were presented. In Section 5.2.1, it was shown that spatial processing is realized by designing an imaging receiver comprised of spatially distributed optical up-conversion modules, and equal length optical fibers conveying RF-equivalent wavefronts for RF image reconstruction within an optical processing unit. To extend the spatial processing, afforded by the distributed phased array, it was shown that differentiating the optical fiber lengths introduces a temporal component crucial to discerning frequency information, in addition to AoA. Furthermore, it was stated that by intentionally differentiating optical fibers to arbitrary lengths, both constituents can be obtained through computational techniques, without risking ambiguous reconstruction of RF signal distributions.

In order to understand the effects arbitrary fiber lengths, and their time delays t_m , have on RF image formation, it convenient to start with a generalized version of Equation 5.32, where the finite size of optical sensing elements and their uneven illumination are accounted for,

$$\left\langle \left| E_n^{LSB}(u) \right|^2 \right\rangle = \frac{1}{2N} \sum_k \left| \sum_m S_k a_m(u) B_m e^{-j(\phi_{km} + \Omega_k t_m)} \right|^2, \quad (5.33)$$

where $\left\langle \left| E_n^{LSB}(u) \right|^2 \right\rangle$ is the areal optical power density of the lower-sideband incident on the CCD array at point u , $a_m(u)$ is the amplitude density of the optical beam propagating out of the m^{th} optical fiber to the n^{th} photodetector at point u . The optical beam emanating from the end of the fiber will be of Gaussian form, leading to amplitude density of the optical field of

$$a_m(\mathbf{u}_n) = \frac{1}{z - jz_0} e^{\frac{j2\pi |\mathbf{u}_n - \mathbf{x}_m|^2}{\lambda 2(z - jz_0)}}, \quad (5.34)$$

where \mathbf{x}_m is the lateral position of the m^{th} fiber in the array, \mathbf{u}_n is the lateral position of the n^{th} photodetector, z is the axial distance from the end of the fiber array to CCD array, λ is the optical wavelength, and z_0 is the Rayleigh distance related to the Gaussian-beam waist,

$$w_0^2 = \frac{z_0 \lambda}{\pi}. \quad (5.35)$$

Assuming z is much larger than z_0 , and $|\mathbf{x}_m|$, based on the optical processing system parameters, the complex Gaussian amplitude can be represented as

$$a_m(u_n) = \frac{1}{z - jz_0} e^{\frac{j2\pi}{\lambda} \frac{|u_n|^2}{2(z - jz_0)}} e^{-\frac{j2\pi}{\lambda} \frac{\mathbf{u}_n \cdot \mathbf{x}_m}{(z - jz_0)}}. \quad (5.36)$$

For RF sources emitting at a distance sufficiently far away from the distributed aperture antenna array, the incident waves are approximately as plane waves. Thus, is the phase obtained during free space propagation from the k^{th} emitter to m^{th} antenna in the array can be represented as $\phi_{km} = \mathbf{K}_k \cdot \mathbf{r}_m$, where \mathbf{K}_k is the wave-vector of the k^{th} emitter, and \mathbf{r}_m is the position of the m^{th} antenna in the array. It can be shown that for incoherent sources, Equation 5.33 is reduced to

$$\left\langle |i_n^{LSB}(u)|^2 \right\rangle = \frac{1}{2N} \sum_k |S_k|^2 \left| \sum_m a_m(u) B_m e^{-j(\mathbf{K}_k \cdot \mathbf{r}_m + \Omega_k t_m)} \right|^2, \quad (5.37)$$

and the power detected by the n^{th} photodetector is obtained by integrating the power density over the photodetector area. For a sufficiently small photodetector, the optical power density remain fairly constant over its size; therefore, the integration can be simplified by multiplying it by the area of the n^{th} photodetector area:

$$P_n = \frac{A}{2N} \sum_k |S_k|^2 \left| \sum_m a_m(u_n) B_m e^{-j(\mathbf{K}_k \cdot \mathbf{r}_m + \Omega_k t_m)} \right|^2. \quad (5.38)$$

By substituting the complex Gaussian amplitude into this equation, and performing some algebra, the power detected by the n^{th} photodetector becomes

$$P_n = \frac{1}{2N} \frac{A}{z^2} e^{-\frac{1}{2} \left| \frac{2\pi}{\lambda} w_0 \frac{\mathbf{u}_n}{z} \right|^2} \sum_k |S_k|^2 \left| \sum_m B_m e^{-j \left(\frac{2\pi}{\lambda} \mathbf{x}_m \cdot \frac{\mathbf{u}_n}{z} + \mathbf{K}_k \cdot \mathbf{r}_m + \Omega_k t_m \right)} \right|^2. \quad (5.39)$$

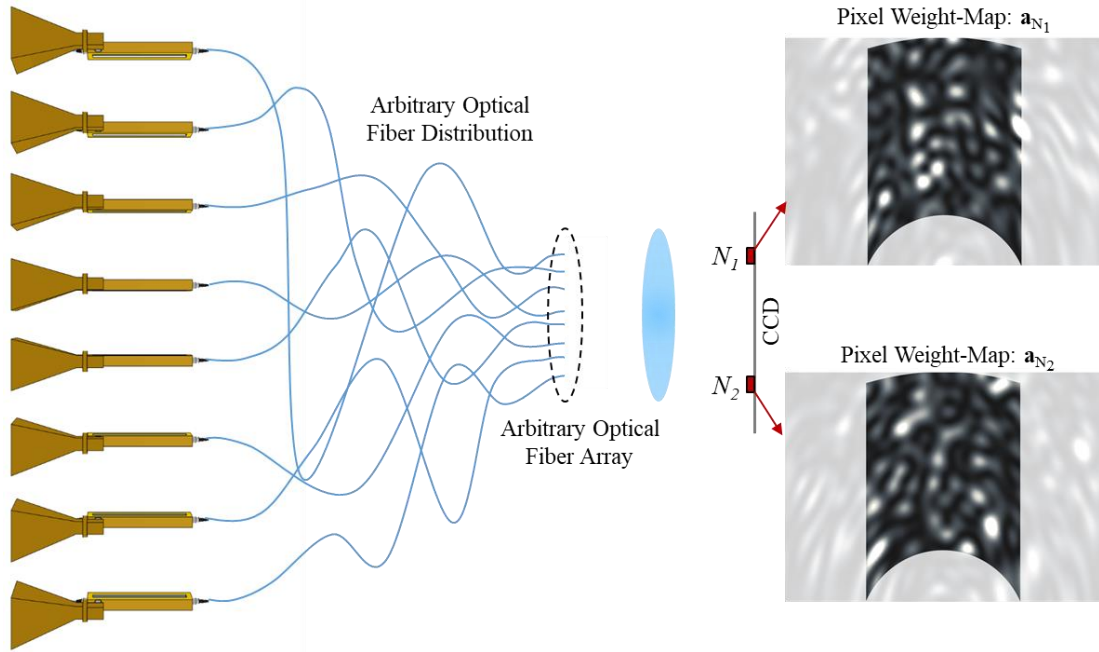


Figure 5.14: Introduction of an arbitrary optical fiber length distribution behind the RF frontend creates a different projection of k-space at each pixel in the CCD camera at the image plane.

This expression, relating the RF power distribution in k-space to the optical power detected at the CCD array, can be more concisely represented as follows:

$$P_n = \sum_k a_{nk} \tilde{S}_k, \quad (5.40)$$

where a_{nk} is a weighting component representing the contribution of the k^{th} plane wave to the n^{th} pixel, and \tilde{S}_k is the power of that k^{th} plane wave in the scene. Alternatively, this linear matrix equation can be formulated based on the dot product operator:

$$P_n = \mathbf{a}_n \cdot \tilde{\mathbf{S}}. \quad (5.41)$$

In correspondence with the previous definitions, \mathbf{a}_n is an amplitude-weighted map of the contributions to the n^{th} pixel of all the plane waves within the systems operational k-space volume i.e., its field of view times operating bandwidth, and \mathbf{S} is the total RF power distribution. Within Equation 5.41, both P_n and \mathbf{a}_n are known values. The entirety of P_n is simply the intensities measured by the individual photodetectors with the CCD array, and \mathbf{a}_n is determined by the antenna array geometry, optical fiber lengths, optical phases applied to optical signals with the fiber, and optical reconstruction setup. By introducing arbitrary fiber lengths, the constant projection lines, previously shown in Figure 5.11 and Figure 5.12, mapped to a specific pixel within the CCD array are scrambled into unique patterns. To illustrate this effect, a weight-map comparison of the original equal length, i.e., the imaging receiver, and arbitrary length optical fiber distributions are presented in Figure 5.14.

The dot product operation in Equation 5.41 consists of multiplying the weight-map of each pixel, \mathbf{a}_n , by each “pixel” in the RF scene, \mathbf{S} , where the summation of products is equal to a single value, P_n , measured at each photodetector. Based on this operation, the linear equation can be further compacted into the linear matrix:

$$\mathbf{P} = \mathbf{A}\mathbf{S}, \quad (5.42)$$

where \mathbf{P} is a detected light intensity vector, and \mathbf{A} is a compilation of amplitude weight-map vectors into a weight-matrix. Since both \mathbf{P} and \mathbf{A} are known through optical intensity measurement and system parameters, respectively, the solution to this linear equation relies on calculation of the RF scene vector, \mathbf{S} . For most cases, the weight-matrix \mathbf{A} will take a rectangular form, resulting in inefficiencies when trying to apply a basic inversion solving method. However, under conditions where \mathbf{A} is suitably diverse,

techniques commonly implemented in real-time computed tomography (CT) applications can be used to reconstruct \mathbf{S} from a known input \mathbf{P} and \mathbf{A} with Equation 5.42. One group of algorithms well-suited for reconstructing an RF scene in k-space from arbitrary projections is the algebraic reconstruction technique (ART) [158]–[163], originally derived from the Kaczmarz method used for solving linear systems of equations [164]. Note that the algorithm terminology commonly uses ART and Kaczmarz method interchangeably.

5.4 Conclusion

In this chapter, the mathematical basis of k-space was presented through Fourier analysis to show this linear-space dual of physical space allows for detection of RF waves without loss of information. From this, practical system considerations were discussed with respect to accurately capturing spatial and spectral components of incident plane waves. To provide spatial processing, a conceptual RF photonic imaging receiver, leveraging spatially coherent optical up-conversion and a lens-based processing unit was presented. Additionally, a mathematical representation of the system was used to verify the transfer of preserved phase information from the distributed aperture antennas to the CCD camera. With respect to spectral processing, optical fiber length dispersion was integrated within each channel for realization of spectral component reconstruction. To optimize these the dispersion properties for unambiguous reconstructions, a technique using arbitrary length optical fibers behind the up-conversion modules was proposed to effectively create a spatio-temporal aperture. From this aperture, information from k-space is spatially and temporally encoded into interference patterns on a CCD camera, which are referred to as k-space tomographs, from which RF power distributions in k-space can be reconstructed using

CT algorithms. Overall, the combination of spatio-temporal aperture with CT algorithms set the foundation for a new imaging modality, referred to as k-space tomography, capable of simultaneously detecting radio waves' frequency and AoA.

Chapter 6

K-SPACE RF IMAGING RECEIVER DESIGN AND FABRICATION

To demonstrate simultaneous detection of radio waves' frequency and AoA for the newly allocated 5G spectrum, a distributed-aperture k-space imaging receiver is designed with an operational bandwidth spanning 26-40 GHz and a 20° FOV by reconstructing a 30-channel 35 GHz passive mmW imaging system [148]–[150], [152], [154]. During the upgrade, the RF frontend components are replaced to broaden the operational bandwidth, and a temporal aperture is designed and installed in place of the original, equal length fiber distributions. To account for these effects, the system is first modeled as an imaging receiver with new RF frontend components, i.e., 26-40 GHz antennas and LNAs, coupled to the original EO phase modulators. The main goal in this design step is to optimize the distributed aperture imaging receiver's PSF based on positioning of the characterized components within the aperture. Following this, a numerical simulation model was developed to characterize performance limitations of the Ka-band k-space imaging receiver's spatial-spectral sensing.

6.1 Distributed-Aperture Imaging Receiver Design

The design of an imaging receiver from the conceptual model, presented in the previous chapter, originates from the development of passive mmW imaging systems. Initially, passive mmW imagers were constructed with a single dish antenna. For this type of imager, the dish antenna is required to span a diameter of several meters to obtain a reasonable diffraction limited angular resolution, defined by the Rayleigh criterion as

$$\theta = 1.22 \frac{\lambda}{D}, \quad (6.1)$$

where λ is the wavelength and D is the aperture diameter. Since further expansion of the dish antenna is an impractical method to improve system resolution, alternative methods have been explored. One method, commonly used in radio astronomy, consists of positioning multiple smaller antennas into a sparse array to effectively synthesize an aperture equivalent to the dish antennas. In this configuration, the maximum resolution is set by the longest baseline, i.e., longest relative spacing, between antennas in a given direction. While this technique affords improvement in angular resolution, the detection of incident radiation is limited due to the sparsity of antennas within the populated area. Moreover, traditional systems experience complications in routing and processing.

However, these problems can be minimized by properly designing a distributed-aperture, and coupling each element to the aforementioned optical up-conversion modules. As a result, the radiation collected can be routed by optical fibers to an optical processing unit, all within a smaller volume. Optical processing of radiation captured at a distributed-aperture array was first demonstrated at microwave frequencies [144]. This method was subsequently improved upon through the introduction of carrier suppression for real-time mmW image reconstruction at a shortwave infrared (SWIR) camera [145], [146], [152]. Not only does this method enable improvements in size and routing through integration of optical fibers and conventional imaging components, but the processing complexity is greatly reduced as well. Typically, digital correlation algorithms, performing discrete spatial Fourier transforms, are utilized to properly reconstruct images. This process requires approximately $N^2/2$ correlations per N channels, leading to a quick increase in computational rigor as more elements are

integrated into the distributed array. Contrarily, optical-based processing condenses the entire correlation engine into a small lens-based system, where the Fourier properties of lenses reconstruct the mmW image from single-sideband information in real-time.

Distributed-aperture mmW imaging based on optical up-conversion and carrier suppression was first demonstrated with a 35 GHz linear 4 element array [150]. In this configuration, the mmW radiation was sampled at the discrete spatial positions, and the complex amplitude of the receive signal was converted to the optical domain through the optical up-conversion process. Preserved amplitude and phase information was subsequently routed through equal length optical fibers to an optically scaled fiber array replica of the antenna array. The optical beams emanating from the fiber array undergo a continuous Fourier transform while propagating the lens-based optical processing unit, where the reconstructed image is captured at a SWIR camera. As a result, incident wavefront directions were analyzed within the angular resolution set by the distance between the outer antenna elements.

To achieve recognizable images, rather than linearly translated 1D interference patterns, the imaging system was scaled to a 2D array. Design of a 2D distributed-aperture imager requires careful consideration of the number of elements and their positioning, as the layout of antennas determines the resolution, alias-free FOV, and the amount of undesired radiation added to the image from a non-ideal point spread function (PSF). The spacing between antenna elements sets the resolution, and alias-free FOV, where the resolution is governed by the longest baseline between elements, as mentioned above, and the alias-free FOV depends on the shortest baseline between elements. Sidelobe levels in the imager's PSF are determined by the format of the antenna configuration, where their minimization is achieved through uniform coverage

of spatial frequencies between the shortest and longest element baselines. Furthermore, the optical fiber array geometry need to be homothetically mapped to the selected antenna positions, i.e., the entire fiber array is arranged as a wavelength scaled version of the distributed antenna array. Therefore, consideration of arbitrary optical fiber arrays, and the diameter of the optical fiber is also required.

One 2D distributed aperture design, commonly used in radio astronomy [165], is the “Y”-array. This array enables relatively uniform coverage of the sampled u - v imaging plane, and is enhanced through the earth’s rotation of the array relative to the imaged object. In snapshot imaging applications, this rotational enhancement is not possible. Therefore, the sidelobes present in the initial PSF introduce undesired information and blurring into the reconstructed images. To achieve better sidelobe suppression, alternative designs, such as the one originally designed by Kogan have been created [166]. This design consists of two concentric circles, and serves a more optimal sampling function for improved u - v distributions. However, fabrication limitations in constructing a homothetically mapped optical fiber array restricted implementation of this design.

As a compromise, two concentric hexagonal patterns replaced the circular antenna arrangements. This configuration provides a u - v coverage comparable to the concentric-circle array, while allowing for optical fibers to be placed into a lattice structure. Ultimately, the design was integrated into a 30-channel mmW imaging system for image reconstruction of passive radiation at 35 GHz [150], [152], [154]. Upon advancements in optical fiber array fabrication, more diverse distributed aperture designs became available [167]. As a result, a five-arm spiral antenna pattern was designed, as a layout with minimal periodicity, to suppress the hex-polar sidelobes

present in the concentric-hexagonal array, as shown in Figure 6.1. A second generation 30-channel, 35 GHz passive mmW imager was subsequently constructed based on the five-spiral design [152], and serves as a platform for the upgrade to a Ka-band k-space imager.

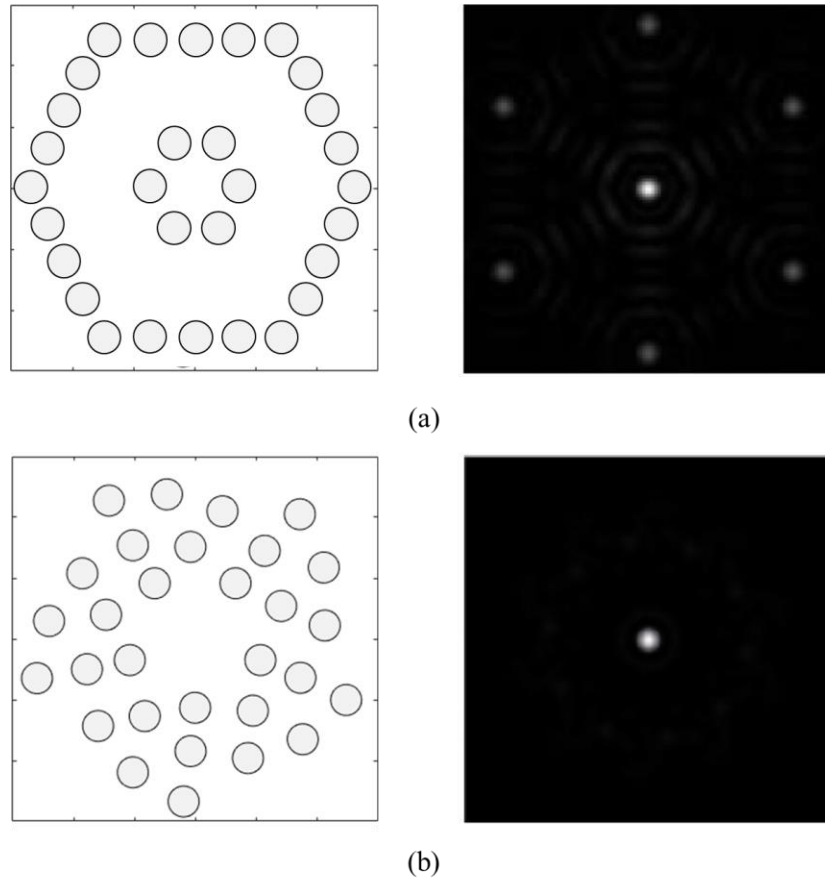


Figure 6.1: Distributed-aperture configurations (left) and corresponding PSF (right) for the (a) concentric hexagonal pattern, and (b) five-arm spiral pattern.

6.1.1 System Architecture

A schematic of the original five-spiral 35 GHz passive mmW imaging system architecture is shown in Figure 6.2. Optical power is generated by a distributed feedback

(DFB) laser (Hewlett Packard 8164A Lightwave Measurement System) emitting at ~ 1550 nm, and is divided into two channels by a 50/50 splitter. The optical power in the main channel is amplified to a constant power 4 W by a PM EDFA purchased from IPG Photonics Inc., and supplied to a 1×32 splitter network prior to being distributed equally among 30 receiver channels in the five-spiral distributed aperture. Each RF fronted channel is comprised of a 35 GHz standard gain rectangular horn antenna coupled to an LNA. These RF modules are connected to 35 GHz EO phase modulators, fabricated by Covega, Inc., through waveguide to coax converters. Incident mmW signals captured at each RF frontend antenna bias the EO phase modulators, and induce a phase shift to impress sidebands onto the optical carrier from the splitter network. Thereafter, the RF-encoded signals are routed through equal length optical fibers to a scaled five-spiral optical fiber array coupled to a microlens array, which collimates the optical beams as they propagate into an optical processor configured as in [151].

At the first stage of the optical processor, the optical beams traverse a Fourier transform lens, placed once focal length from the lenslet array. Thereafter, a small percentage of the carrier is tapped off toward a $4-f$ system, for phase analysis of each channel, while the remaining optical carrier and sideband power is conveyed toward a $6-f$ system for mmW image reconstruction. In the imaging path, a bandpass filter, comprised of four 100 GHz channel spaced optical add-drop multiplexer (OADM) filters, is approximately positioned one focal length from the Fourier transform lens. By setting this dielectric stack filter near the focal length, the optical beam configuration is at its smallest diameter, allowing for suppression of the carrier and upper-sideband without introducing the filter surface into the image. After passing through the filter, the lower-sideband information propagates two focal lengths to a relay lens. This lens

subsequently positions the mmW image onto a CCD array, two more focal lengths away. In the case where all channels contain equal amplitude and phase, the imager's PSF is formed on the CCD camera. Otherwise, the complex amplitude corresponding to the mmW scene will vary in between channels based on Fourier plane sampling from discrete antenna positions within the distributed-aperture. As a result, the incident mmW signals will be coherently processed for scene image reconstruction.

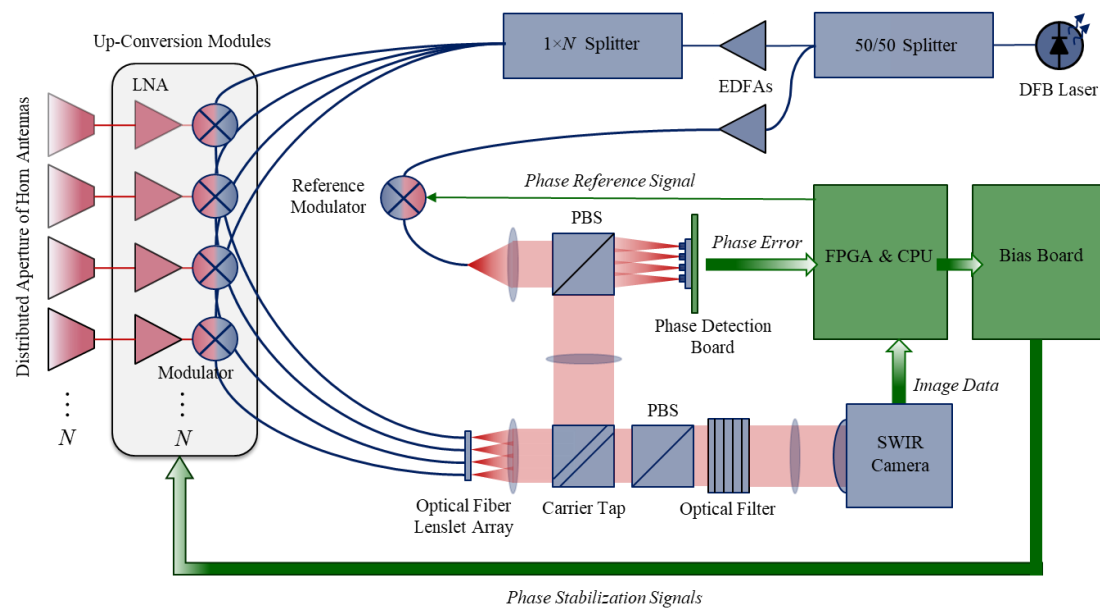


Figure 6.2: Schematic of original 35 GHz passive mmW imager. Blue lines indicate optical signal paths, red lines indicate RF signal paths, thin green lines indicate singular electrical signal paths, thick green lines indicate electrical signal array paths, and red blocks indicate free-space paths.

In the phase analysis portion of the optical processor, the tapped off carrier travels two focal lengths to a relay lens, and is subsequently positioned onto a focal plane array (FPA) comprising detectors organized in the same configuration as the optical fiber array. As shown in Figure 6.2, before the image of the optical source array

is projected onto the phase alignment FPA, the carrier beam configuration propagates through a polarization beam splitter. At this point, the carrier signal in each channel is overlaid with a collimated reference beam originating from the 50/50 splitter in the optical source. Prior to entering the optical processor, the reference optical power is amplified to 1.2 W by a PM EDFA from Calmer Laser, Inc., and input into a reference EO phase modulator. To achieve sufficient phase analysis of the carrier, the reference beam is modulated with saw tooth wave that sweeps the channel phase from 0 to 2π . By routing the modulated optical beam into the optical processor, and mixing it with the channels in the optical source array image, the phase in each channel can be analyzed and calculated using an FPGA, as described in [148], [149], [168]. By obtaining carrier phase information over time for each channel, a bias can be applied to the EO phase modulators in the distributed-aperture up-conversion modules. Consequently, phase variations induced by thermal and vibration effects are mitigated to enable stable mmW image reconstruction at the CCD camera.

6.2 k-Space Imaging Receiver Design

As mentioned, the process of reconfiguring the 35 GHz passive mmW imager to operate as a k-space RF imaging receiver consists of two primary upgrades. The first portion is an RF frontend component replacement for imaging over an operational bandwidth of 26 – 40 GHz. In addition to changing the RF components, distributed-aperture framing and mechanical devices are replaced to account for calibration routines critical in forming the k-space tomography weight-matrix. Upon completion of the new RF frontend, the imaging receiver is able to spatially process incident RF wavefronts; however, it is unable to discern spectral information. To introduce this added processing capability, a temporal aperture is designed and integrated behind the spatial aperture.

Configuration of a temporal aperture consists of organizing an array of arbitrary length optical fibers according to the desired spectral resolution. In the following sections, the design and optimization of both the spatial aperture and temporal aperture are discussed in detail.

6.2.1 Spatial Aperture

The spatial aperture design process began with the selection of RF frontend and up-conversion module components. As mentioned previously, the current system employs 35 GHz standard gain horn antennas, LNAs, EO phase modulators. To achieve operation throughout Ka-band, both the antennas and LNAs are replaced with wideband components. To this end, antipodal linear tapered slot (ALTS) antennas were designed and fabricated at the University of Delaware, and 26 – 40 GHz LNAs were purchased from RF Lambda (RLNA24G40GB). It is important to note that while the Covega, Inc. EO phase modulators possess a 35 GHz 3-dB bandwidth, the roll-off in conversion efficiency is minimal throughout 40 GHz; therefore, upgrading these components is not required.

Prior to integrating each component into the system, all antennas, LNAs and modulators were characterized through calibrated measurements. The bandwidth performance of the ALTS antennas was characterized by measuring the S11 from 26 – 40 GHz, and the results are presented in Figure 6.3. For the LNAs, gain, noise figure (NF), and flat phase response were measured. A sample set of results is shown in Figure 6.4, where the emphasis is placed on the range of values for each figure of merit. One additional component explored throughout these measurements was the ability to flatten out the phase response through a simulated system calibration, and the effect of phase drift with respect to LNA temperature, as extended periods of operation will drastically

change the component response. Each of these effects are included in Figure 6.4 (c) and (d), respectively. The EO phase modulators were characterized in terms of conversion efficiency, which can be easily converted to a half-wave voltage by assuming a 50Ω input impedance. Results of modulator performance are included in Figure 6.5.

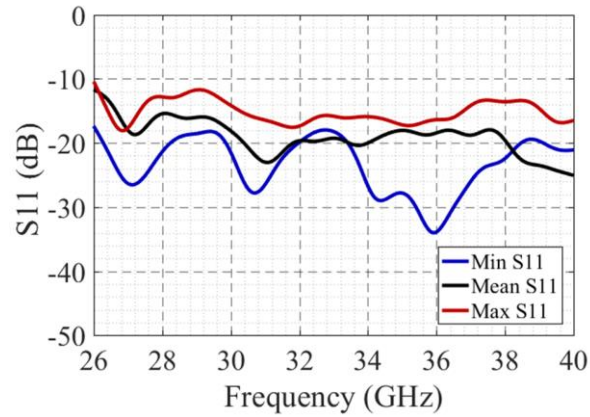


Figure 6.3: ALTS antenna S11 measurements over operational bandwidth.

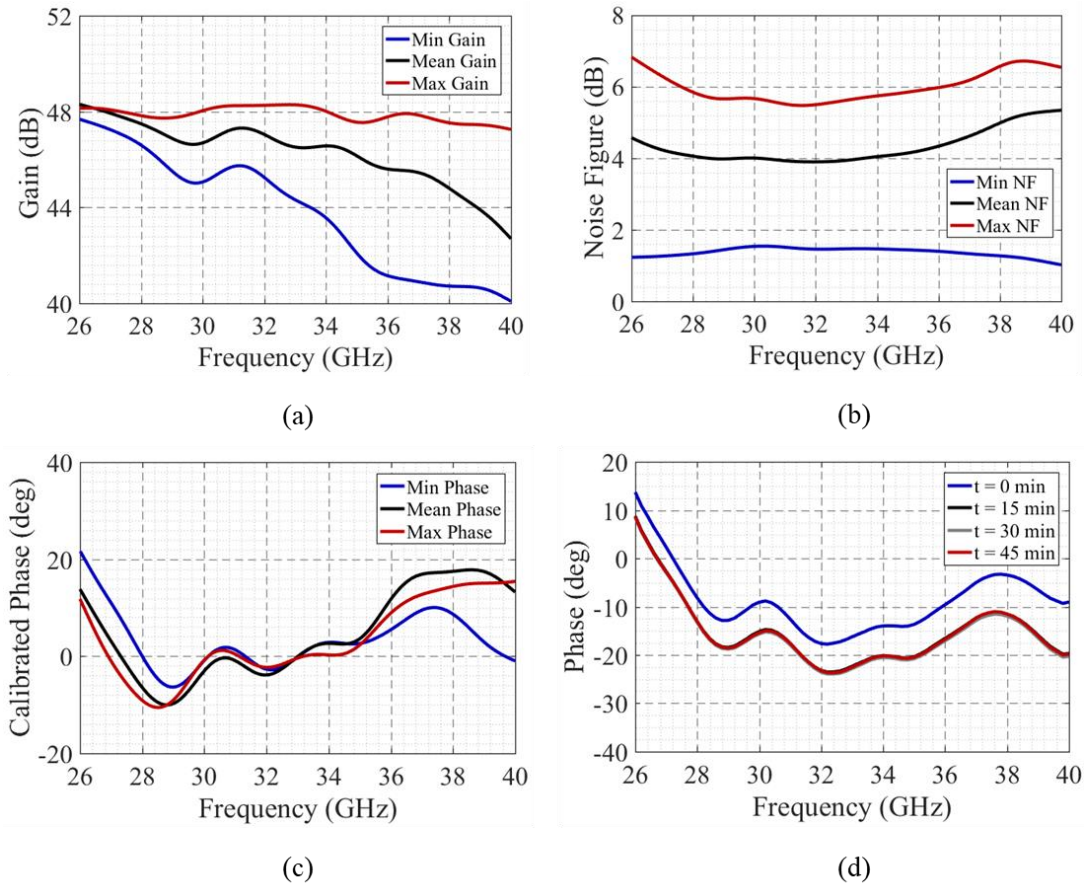


Figure 6.4: Measured RF Lambda LNA (a) gain, (b), noise figure, (c) flat phase response calibrated at 33 GHz, and (d) flat phase response of a single LNA over a time period of 45 min.

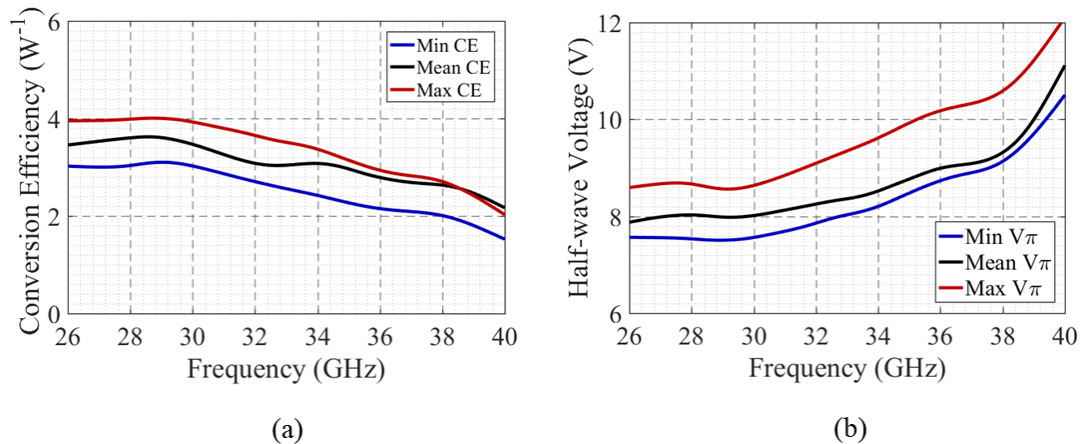


Figure 6.5: Measured Covega, Inc. EO phase modulator (a) conversion efficiency, and converted to (b) half-wave voltage assuming 50Ω impedance.

With all of the necessary components for the RF frontend and upconversion module portion of the upgrade characterized, collective compilation of each device, with its respective performance metrics, can be used for design of the aperture configuration. Typically, the distributed aperture design consists of optimizing the figures of merit mentioned earlier in this Chapter, i.e., the resolution, alias-free FOV, and PSF. However, since the same five-arm spiral module layout is preserved throughout the upgrade, both the shortest and longest baselines are predetermined. Consequently, the resolution and alias-free FOV are limited to each baseline, scaled by the new RF wavelengths. Thus, the priority in spatial aperture optimization revolves around further suppressing sidelobes in the PSF for reduced image clutter. To accomplish this, the LNA and EO phase modulators are strategically placed within the predefined receiver channel positions.

Modeling of the Ka-band imaging receiver's PSF is completed by formulating a numerical simulation based on the mathematics presented in Section 5.1.2.1, and

component scaling of phase and amplitude are accounted for in the same manner as presented in [169]. The approach taken to satisfy the design goal consisted of centralization of the low NF, high gain LNAs and high conversion efficiency (CE) phase modulators within the five spiral aperture. Most of the advantages from this methodology stem from the increase in signal amplitude within the center of the aperture, which is considerably denser than the outer portion. It is important to note that the NF effects in the PSF are minimal. This is due to the fact that noise contributions on the image plane manifest as a Gaussian noise profile from incoherent summation through the optical processor based on kTB . Furthermore, in a practical system, this known image noise structure can be subtracted from the mmW image reconstruction. Aside from pure image formation, other applications, such as signal recovery require high signal-to-noise ratios (SNRs). With this in mind, the central location of the high CE phase modulators acts as a partial apodization, effectively providing a centralized weighting of the LNAs NF contribution to the system's SNR. Further exploitation of this effect can be exhibited through more sophisticated apodization techniques; however, experimental implementation of this is beyond the scope of the spatial-spectral cueing receiver presented through the remainder of this dissertation.

To study the effect of these component configurations, the simulation of the imaging receiver with the new arrangement of LNAs (NF, gain, and phase) and phase modulators (CE) was used to compute the system's PSF. In this modeling, the antenna response across the aperture was assumed to be uniform, and the phases within the LNAs were set based on values obtained from a simulated phase calibration at the bandwidth center frequency of 33 GHz, Figure 6.4(c). The finalized positioning of RF frontend and up-conversion module components, and the computed PSF results, are

presented in Figure 6.6. As evident in Figure 6.6(e), the upgrade RF frontend and organized components provided 15-dB side lobe suppression, a 3-dB improvement in comparison to the previous state of the 35 GHz passive mmW imaging system.

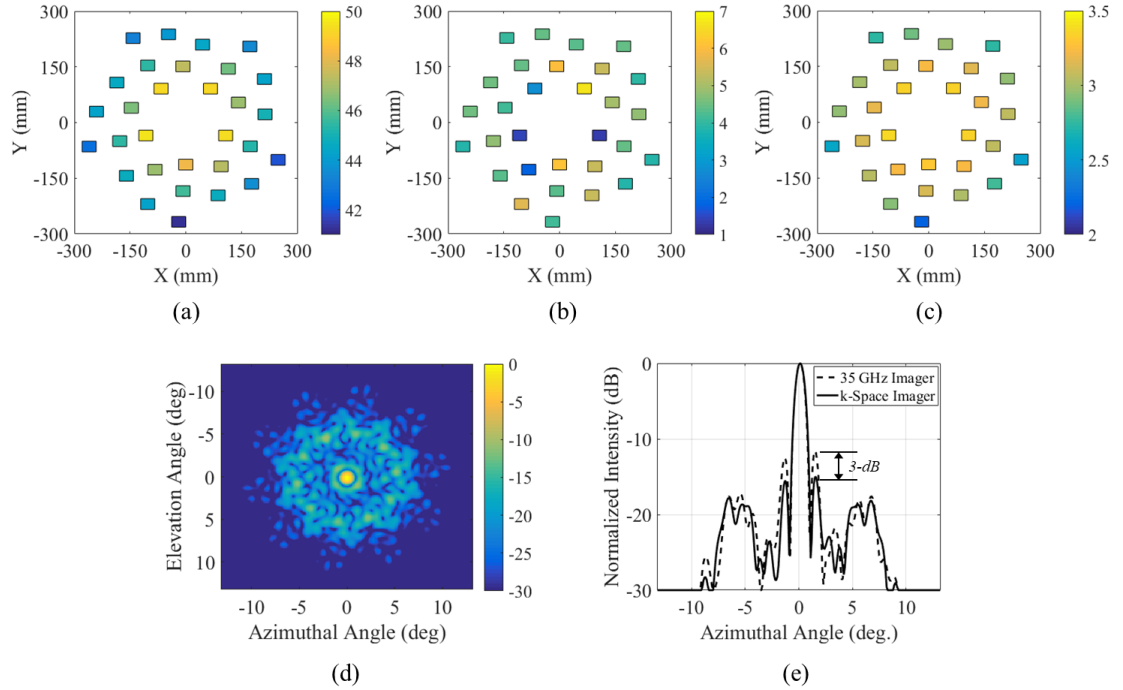


Figure 6.6: Component configuration within the distributed-aperture for (a) LNA gain, (b) LNA NF, and (c) modulator conversion efficiency. The color bar in these three panes represent the measured value for the respective figure of merit. (d) Simulated PSF, and a (e) PSF comparison for the k-space imaging receiver and original passive mmW imager.

6.2.2 Temporal Aperture

The second primary design component in the construction of a k-space imaging receiver is the temporal aperture, comprised of arbitrary optical fiber length, which extends the spatial processing capabilities to include spectral information. Similar to the spatial aperture design, the performance of the temporal aperture is dependent on the

longest and shortest baselines. The longest temporal baseline parameter is analogous to the longest spatial baseline, as it determines the spectral resolution of the system. This effect is realized through the following relation:

$$\Delta f = \frac{c}{2n\Delta L_{\max}}, \quad (6.2)$$

where n is the refractive index of the optical fiber ($n = 1.5$), ΔL_{\max} is the longest baseline of optical fiber length, i.e., difference between the longest optical fiber and shortest optical fiber, c is the speed of light, and Δf is the spectral resolution. Through the same relation, it is apparent that the shortest baseline in the arbitrary optical fiber array sets the minimal resolvable time-pulsed signal. This effect can be thought of as the coherence length of the temporal aperture. Accordingly, time signatures extending below this shortest baseline are not resolvable since signals traversing the arbitrary optical fiber array will not experience the channel-to-channel interference necessary to produce the spatially-and-temporally-encoded k-space tomograph.

In addition to the baselines defined within the temporal aperture, the fill-factor between the shortest and longest optical fiber lengths contributes to the quality of the spectrally resolved information. This optical fiber layout effect is comparable to the spatial configuration in the imaging receiver, where two factors contributed to the overall performance. For the spatial aperture, the PSF is determined by the fill-factor of the receiver channels within the distributed aperture, which contributes to the diffraction efficiency of the imager, and the periodicity of the channel positions contributed to the sidelobes present at the image plane. In reference to the distributed aperture presented here, the arrangement of elements within the total aperture is categorized as sparse, resulting in a decreased diffraction efficiency. Based on this effect, the sparse layout

was optimized through the principle of spatial non-periodicity to mitigate periodic pattern transfer onto the image plane in the form of sidelobes. For the temporal aperture, each of these cases hold for reconstructing spectral information. Ideally, the fill-factor of the temporal aperture would be designed so that the number of channels is equal to the total operational bandwidth, divided by the Nyquist sampling of the spectral resolution. Since the implementation of optical fiber splitters behind the EO phase modulators is relatively simple, this requirement can be obtained with ease. However, if the number of temporal spacing intervals is much larger than the number of channels within the system, the same non-periodic design approaches need to be implemented. Realization of this is, again, analogous to the distributed aperture, where the periodicity of a sparse spatial layout produces spatial sidelobes in the PSF. Thus, optical fiber periodicity manifests as grating lobes, in the spectral component reconstruction.

6.3 Numerical Analysis

To evaluate the k-space reconstruction accuracy in terms of spatial and spectral information extraction, a custom Matlab model was developed. The 2D distributed-aperture k-space imager numerical model was developed to emulate the capture of far-field radiation amplitude and phase information. Each wavefront is subsequently up-converted to an equivalent optical wavefront, and conveyed through an arbitrary optical fiber lengths to a fiber array. The Gaussian beams emanating from the optically scaled distributed optical fiber array traverse through a $2-f$ optical processor system for interferogram projection onto a photodetector array. A graphical representation of the numerical simulation model is presented in Figure 6.7.

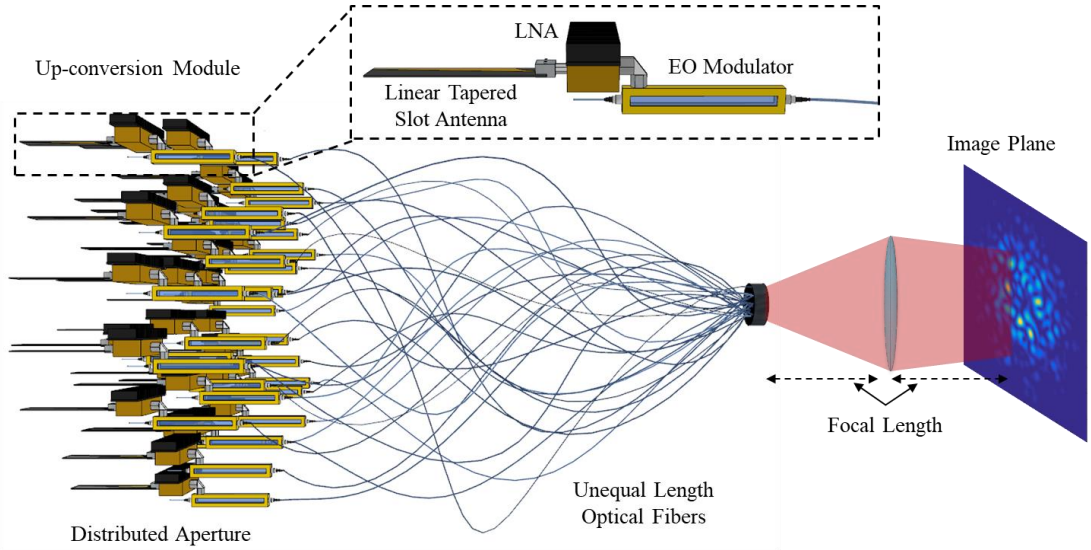


Figure 6.7: Component configuration and PSF response.

In the distributed-aperture simulation model, the modules are positioned in the exact coordinates as the five-arm spiral distributed-aperture, which spans a diameter of 60 cm. The antennas are modeled uniformly across the frontend, and the effective area is calculated from the main lobe solid angle based on the half-power beamwidths [157],

$$\Omega_p \simeq \beta_{xz} \beta_{yz}, \quad (6.3)$$

where β_{xz} and β_{yz} are the half-power beamwidths in radians for the E- and H-plane, respectively. For the ALTS antennas designed for the k-space imaging receiver, the half-power beamwidths are approximately 10° in the E-plane and 14° in the H-plane. Upon capturing the incident wavefronts, the carrier optical power of 40 mW is scaled by the LNA gain and NF, along with the EO modulator conversion efficiency and loss of approximately 3 dB, where each component is positioned according to the configurations presented in Figure 6.6. In addition to this, the phase of the RF-equivalent

optical wavefront is shifted according the LNA phase effects in the calibrated responses presented in Figure 6.4(c).

The temporal aperture is designed with a longest optical fiber baseline of 40 cm, i.e. an equivalent 60 cm free space path length offset, to afford an spectral resolution equivalent to the spatial resolution in k-space. Optical fiber interval spacing over the maximum offset is set to an initial 1.5 cm. To circumvent grating lobe effects, each optical fiber length is randomly shifted by adding a random permutation of millimeter scale adjustments to the 30 optical fibers. A graphical representation of the spatio-temporal aperture, and the corresponding spatio-spectral mapping is shown in Figure 6.8.

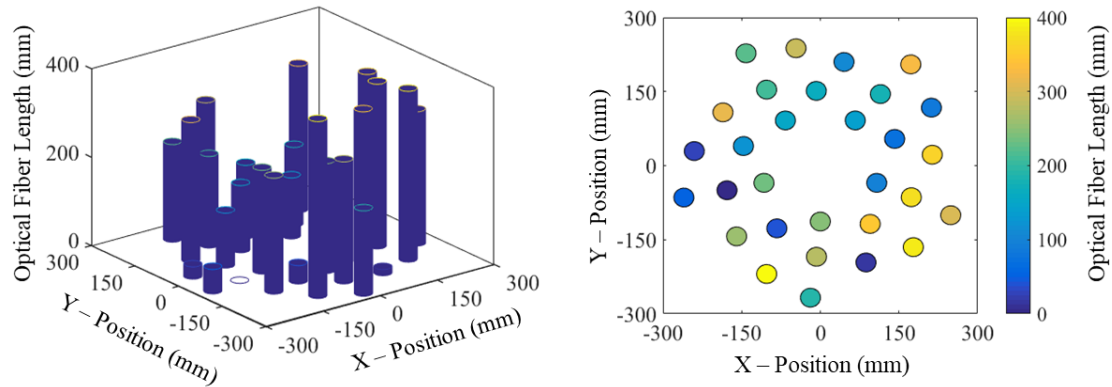


Figure 6.8: Spatio-temporal aperture with arbitrary optical fiber lengths coupled to each receiver channel in the distributed-aperture array.

At the end of the temporal aperture, the optical fiber array is organized based on homothetic mapping, and a dimensional scaling proportional to the wavelength difference between the original passive mmW imager’s operational frequency of 35 GHz, and the optical source frequency of ~ 193 THz. It is important note that it is not

imperative for the fiber array configuration to match the antenna array for k-space application, only for analog imaging. Optical beams emanating from each fiber array position are combined and modeled with a Gaussian beam profile. The collective optical beam propagates one focal length to a Fourier transform lens, which performs the necessary correlation computations between channels. From here, the PSF is calculated, and the k-space tomograph is projected onto the image plane, one focal length away from the lens. Note that throughout the free space optical processor, the loss from lenses and the optical filter, present in the physical system, is set to 2 dB. The CCD is comprised of a 100×100 array of $30 \mu\text{m} \times 30 \mu\text{m}$ pixels. As the optical power density is detected by the camera, it is converted to the photon number arriving at the camera, and evaluated over the integration time τ :

$$n_{ph}(n) = \frac{\langle |E_n^{LSB}(n)|^2 \rangle A \tau}{h\nu}, \quad (6.4)$$

where $\langle |E_n^{LSB}(n)|^2 \rangle$ is the areal optical power density of the lower-sideband on the n^{th} photodetector, A is the area of the photodetector, and $h\nu$ is the photon energy. This photon number is subsequently digitized to ADU counts based on the camera's quantum efficiency, shot noise, and readout noise. Throughout this work, the camera used both in numerical modeling and the experimental system is the 14-bit FLIR SC2500. Thus, the quantum efficiency, shot noise, and readout noise are all set based on this camera's specifications.

6.3.1 Weight-Matrix Formulation

In the previous Chapter, it was stated that the linear matrix equation in Equation 5.42 can be solved based on *a priori* knowledge of system parameters, and the measured

optical intensity. Therefore, the weight-matrix consisting of contributions from each point of k-space to N pixels needs to be acquired before capturing scene wavefronts. To accomplish this, the visible k-space region is sampled at Nyquist of the imager's spatial and temporal resolution to prevent aliasing, and the interferograms produced at the image plane are compiled into the weight-matrix \mathbf{A} . This process is carried out in two stages: 1) construction of sampling nodes in k-space, and 2) calculation and compilation of image plane projections produced from each k-space node.

To formulate the node-based k-space scene, the azimuthal and elevation FOVs are sampled at Nyquist of the highest angular resolution within the operation bandwidth, and the operational bandwidth is sampled at Nyquist of the spectral resolution. Based on the shortest and longest baselines in the spatial aperture, the k-space imager has a FOV of 20° in each direction, and an angular resolution of approximately 0.874° at 40 GHz. Therefore, the angular nodes for the azimuthal and elevation directions are positioned from -10° to $+10^\circ$ at 0.4° intervals. At each angular position, the frequency is sampled over the 26 – 40 GHz operation bandwidth at intervals of 125 MHz, due to 250 MHz spectral resolution set by the maximum free space offset in the temporal aperture. At this point the sampling nodes produce an array of angular and spectral positions in a 3D grid. To convert to k-space, the k_x , k_y , and k_z coordinates for each node are calculated using the relation $2\pi f = c|\mathbf{k}|$ and trigonometric equations. As a result, a 3D polar node grid, representing each sampled k-vector, is formulated, as shown in Figure 6.9.

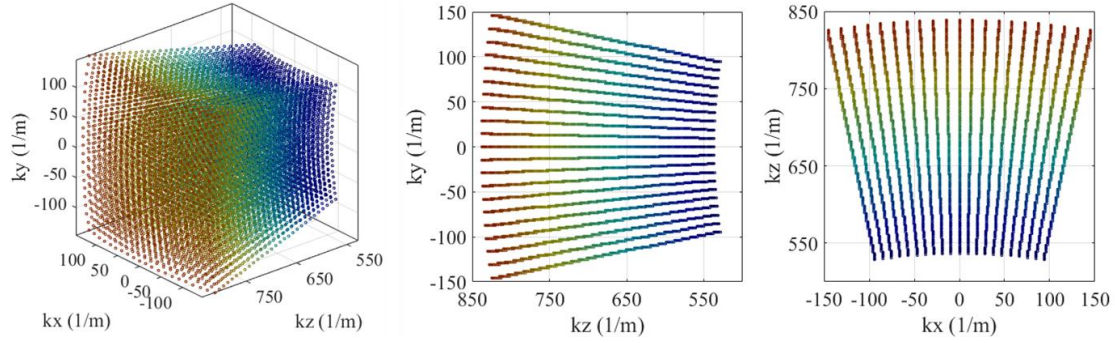


Figure 6.9: Node-based k-space scene used for calibration. Each discrete point represents an AoA/frequency pair that is projected onto the image plane, from which the interferogram is compiled into the weight-matrix.

Once a calibration scene is constructed, the unique PSF produced by each k-vector is calculated individually. Throughout this computation, the 2D interferograms projected onto the 100×100 pixel array are normalized and compiled into a 3D weight-matrix. At this point it is important to address components of the weight-matrix formulation with respect to computational intensiveness and memory management. In the ideal Nyquist sampling case presented, the weight-matrix is constructed for mitigation of aliasing. However, this results in a $100 \times 100 \times 293,913$ matrix, i.e. 2.94×10^9 numerical values. Consequently, proper storage as a double results in 23.51 GB of data. In the experimental system, the FLIR SC2500 contains a 320×256 pixel array, and consequently increases the required memory for the weight-matrix to be 192.62 GB. While storage of this data set is feasible, Matlab's memory allocation restricts computation to RAM, and current desktop CPUs do not possess the necessary RAM to process this amount of data. This problem could be circumvented through the use of external memory algorithms in a different software implementation; however, large latencies in processing would still exist. Thus, since the work presented in this

dissertation is focused on developing an RF photonic aperture to demonstrate spatial-spectral sensing, a large amount of the analysis will be presented in terms of sub-spaces within the visible 3D k-space environment. Nonetheless, adaptations of k-space imaging have been explored to minimize the magnitude of data storage and processing, one of these techniques will be presented in Chapter 8.

6.3.2 k-Space Reconstruction Process

The process of reconstructing k-space scenes for the simulation model consists of building sample RF environments, calculating the image plane response for the respective scene, and reconstructing the amplitude distribution in k-space using the Kaczmarz algorithm. Construction of the sample RF scene consists of generating emitters of different frequencies, AoAs, and amplitudes. In each case, the distribution of emitters depends on the sub-space determined by the weight-matrix format; however, spatial-spectral position does not need to match exact calibration node coordinates. To calculate the image response, the source's frequency and AoA pairs are converted to k-space using the inverse of the process presented in the previous section. This k-space scene vector, \mathbf{S}_i , is subsequently multiplied by the weight-matrix to emulate propagation through the simulated imager, and produce the detected light intensity vector \mathbf{P} .

With both \mathbf{P} and \mathbf{A} calculated, Equation 5.42 and the Kaczmarz method can be used to reconstruct the RF scene vector, \mathbf{S} . The Matlab implementation of the iterative Kaczmarz algorithm used in this process was originally developed in [170], and involves computing

$$x^{k+1} = x^k + \lambda^k \frac{b_i - \langle a_i, x^k \rangle}{\|a_i\|^2} \bar{a}_i, \quad (6.4)$$

for $k = 0, 1, 2, \dots$, where a_i is the i^{th} row of the weigh-matrix A , \bar{a}_i is the complex conjugate of a_i , b is the detected light intensity vector input, k is the number of input iterations, λ is a relaxation parameter ranging between 0 and 2, with a default value of 1, and $i = k \bmod m + 1$, where m is the number of rows in the weight-matrix. Furthermore, x^0 denotes the initial approximation for the RF scene vector, and is selected as an arbitrary complex-valued vector if no input is provided. In addition to these parameters, the algorithm includes an option for non-negativity in the solution. Since the RF sources in k-space are represented by the sources respective amplitude, and the remaining spatio-spectral mapping should approach zero, the non-negativity option is used for reconstruction of \mathbf{S} to improve the rate of convergence. It is important to note that the Kaczmarz method has an algorithm efficiency of $O(n)$; therefore, a change in the iteration input, weight-matrix, and detected light intensity vector will linearly affect the computation time and space.

Once the computation of \mathbf{S} is complete, the output can be compared with the initial input scene. The accuracy of the reconstruction is calculated by comparing the resolved source positions to the expected positions. This comparison can be completed in two different ways. The first method is by calculating the percent difference between the output of the algorithm with the expected amplitude distribution. An alternative method is by detecting the reconstructed RF emitters through implementation of a numerical peak detection algorithm and comparing the peak coordinates with the expected positions. In the latter, the amplitude search range can be tailored according the amplitudes set in the initial simulation scene. In the next section, the numerical

analysis results for reconstruction of various RF signal environments, and metrics corresponding to the algorithm performance are presented.

6.3.3 Numerical Model Characterization

In an effort to assess the 30-element k-space imaging receiver’s ability to resolve RF dense signal environments, a thorough analysis of the Kaczmarz algorithm and system model was performed. First, the effects of increasing signal density in the scene was examined in terms of algorithm convergence. As expected, a gradual increase in the number of signals within the imager FOV results in a significant reduction in the negative convergence slope, which extends to a floor determined by the bit resolution in the processor used. This relationship between signal distribution density and the number of algorithm iterations, shown in Figure 6.10, serves as a baseline for signal vector reconstruction accuracy, and the corresponding processing time.

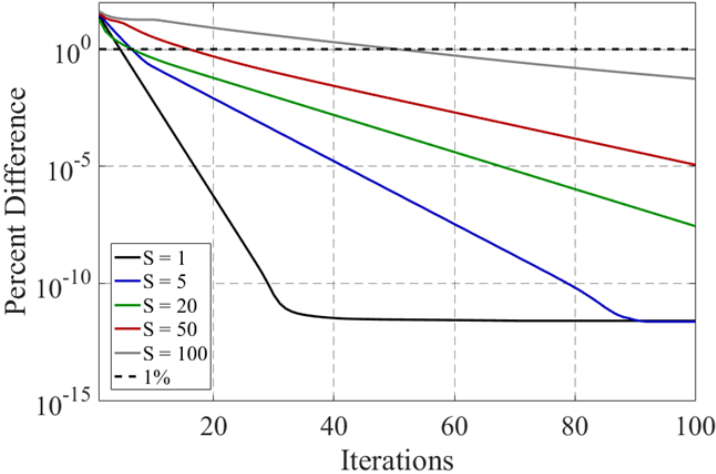


Figure 6.10: Kaczmarz algorithm convergence with respect to signal density in the k-space visible by the receiver. The black dotted line, representing a 1% change between iterations, serves as an empirically defined cut-off for a well reconstructed scene [171] © 2018 IEEE.

By utilizing these relations, the number of iterations required to adequately reconstruct a scene was empirically derived to a cut-off point, indicated by a 1% variation between the previous and current iteration signal vectors. Alternatively, this cut-off point is interpreted as the number of iterations necessary to converge to 99% of the solution. As a result, the processing time can be optimized for various RF scene densities based on the corresponding algorithmic iteration requirement, where the processing time is linearly dependent on the iteration count, due to Kaczmarz algorithms linear efficiency. Furthermore, the algorithm completion time is dependent on the processor unit used to solve the linear matrix equation. At this point, it is important to note that all simulated reconstructions presented were performed using an Intel core i7-4790 processor with 4 cores, a base frequency of 3.6 GHz, and a memory bandwidth of 25.6 GB/s.

6.3.3.1 Two-Dimensional k-Space Reconstructions

To demonstrate the effectiveness of the empirically derived relationship between reconstruction accuracy and algorithm iteration count, 2D k-space scenes were generated with RF emitters randomly distributed throughout the azimuthal plane. Prior to creating simulation environments, the weight-matrix is formulated through Nyquist sampling of the azimuthal 20° FOV at 0.4° intervals, and operational bandwidth of 26 – 40 GHz at 125 MHz intervals. Once compiled, source distributions are generated with RF emitters of equal 10 arbitrary unit (a.u.) amplitudes randomly permuted throughout 2D k-space. The random permutation of sources consists of selecting a frequency and AoA pair, where the possible frequencies span the operational bandwidth at intervals of 100 MHz, and the possible AoAs span the FOV at intervals of 0.1° . This type of source distribution interval selection enables sources to generate k-space tomographs that are

not directly encoded into the weight-matrix, consequently extending the processing beyond a simple matching of existing PSFs. While sources may exist at coordinates misaligned with nodes, the algorithm will compute a solution where the off-grid sources are reconstructed at the nearest Nyquist-sampled spatio-spectral positions. This effect is due to the angular and spectral resolutions defined by the system, and the algorithm being configured to solve the linear matrix equation according the predefined responses compiled from these properties.

In Figure 6.11, each RF source distribution was reconstructed using the iteration cut-offs corresponding to the source density. For each amplitude distribution in k-space, the aforementioned numerical peak detection algorithm was implemented with a 3-dB detection range. The outputs were subsequently compared to the expected positioned, and accuracy was characterized based on whether the measured frequencies and AoAs were resolved within the system resolution. Figures 6.11 (a-c) illustrates the reconstructed k-space distributions for 10-, 25-, and 50-source scenes, respectively. In each case, all emitters randomly positioned in 2D k-space were resolved to a node point within one-half of the resolution for both spatial and spectral components.

For simplicity, the measured/expected comparison is converted from a k-space representation to a frequency and AoA distribution, as shown in Figures 6.11 (d-f). Blue dots represent the reconstructed spatio-spectral positions, and red-outlined circles represent the actual locations, where the center is an exact position and the diameter is the angular resolution. It is important to note that since the longest baselines of the spatial aperture, and the temporal aperture are both 60 cm, the resolution tolerance in k-space is equal. However, when converting to the frequency and AoA distribution the resolution bounds on the exact location distorts the circle. Since the conversion

presented here is merely used for simplistic visual analysis, the geometry of the circle is not distorted, and the diameter is adjusted according to reconstruction results.

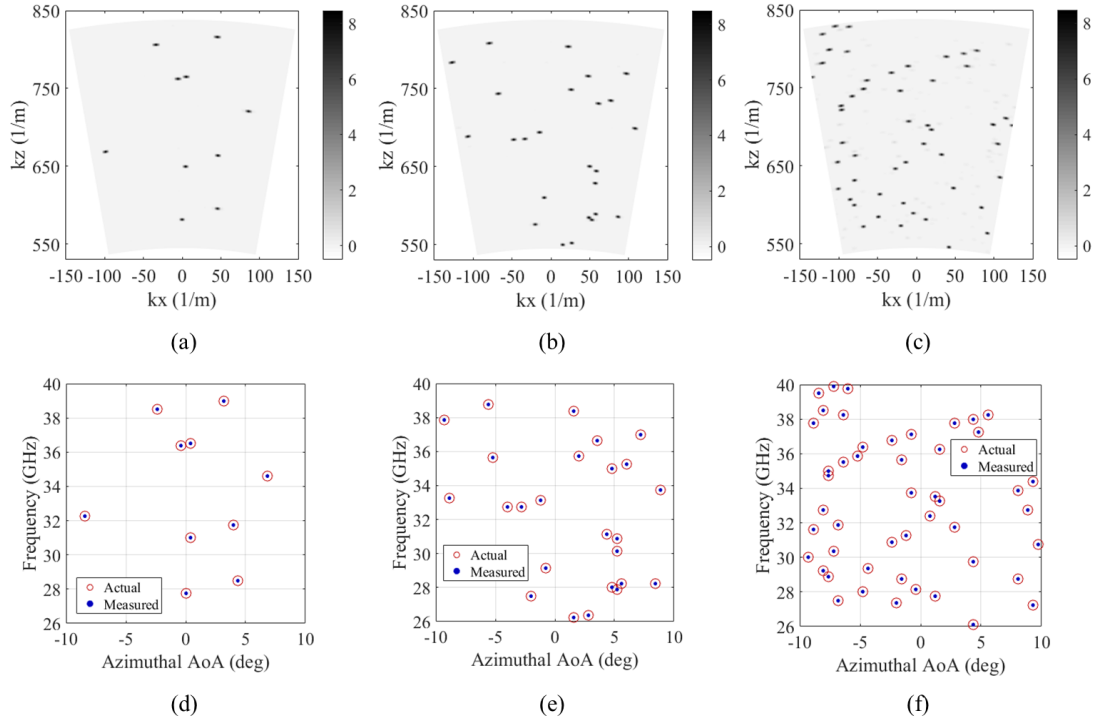


Figure 6.11: Simulated 2D k-space amplitude distribution reconstructions for a (a) 10-source scene, (b) 25-source scene, (c) 50-source scene, and their respective peak detection results in (d-e). Each scene is reconstructed using the required number of iterations.

In Figure 6.12 each RF source distribution was reconstructed using the iteration count based on the cut-off for an environment comprised of 25 RF emitters. Figures 6.12 (a-c) illustrates the reconstructed k-space distributions for 10-, 25-, and 50-source scenes, respectively. During post-processing, the same 3-dB numerical peak detection algorithm was used. For the 10- and 25-emitter distributions, all sources were reconstructed within one-half of the spatio-spectral resolution. Contrarily, the 50-source

scene exhibited errors in the reconstruction process, and resulted in only 80% of the RF sources resolved at expected locations. This is due to the insufficient algorithm iteration input, and demonstrates the importance of tailoring the Kaczmarz algorithm iteration count to the scene densities. In a practical scenario, the scene will not be known, thus a predefined input is not realizable. However, initial reconstructions can be performed at higher iteration counts, at cost of higher frame-to-frame latency, then be adjusted in accordance with the density of the RF environment.

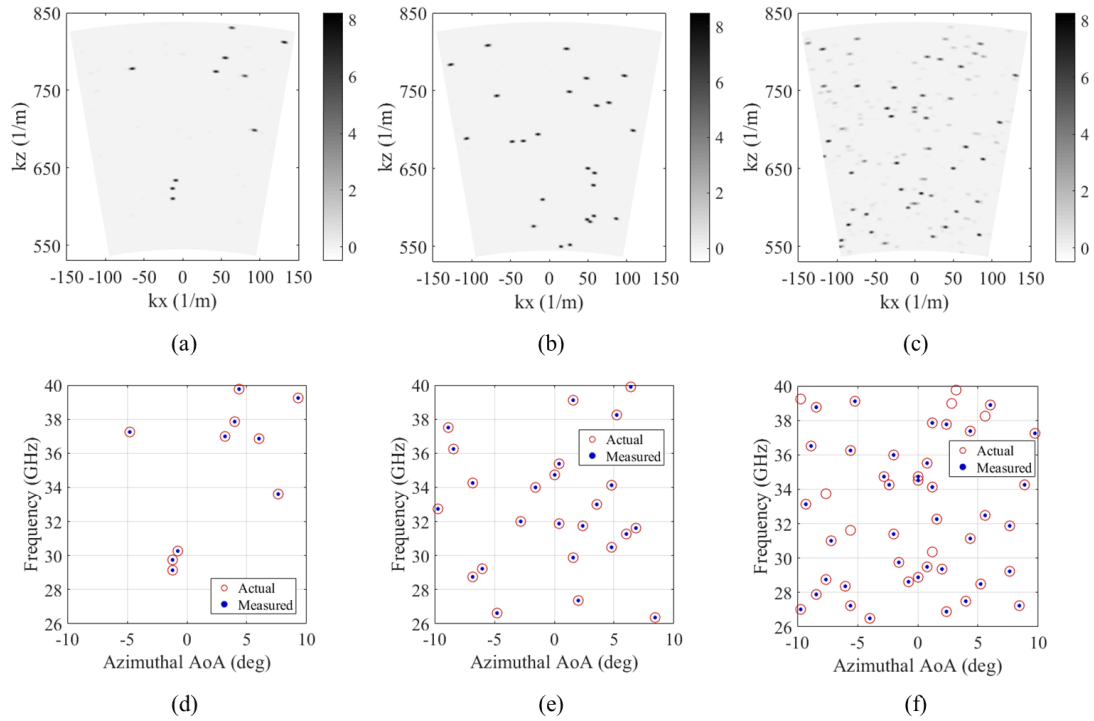


Figure 6.12: Simulated 2D k-space amplitude distribution reconstructions for a (a) 10-source scene, (b) 25-source scene, (c) 50-source scene, and their respective peak detection results in (d-e). Each scene is reconstructed using the required number of iterations for a 25-source scene.

6.3.3.2 Three-Dimensional k-Space Reconstructions

To extend the numerical analysis of the 2D distributed-aperture k-space imager to 3D k-space, without exceeding memory requirements of the aforementioned desktop CPU, an undersampled weight-matrix was constructed. The weight-matrix was formulated by sampling the azimuthal and elevation 20° FOVs at 0.5° intervals, and operational bandwidth of 26 – 40 GHz at 250 MHz intervals. As with the 2D k-space scenes, the scene distributions are generated with RF emitters of equal 10 arbitrary unit (a.u.) amplitudes randomly permuted throughout 3D k-space. These random permutations comprise frequency and AoA pairs, with frequencies span the operational bandwidth at intervals of 200 MHz, and AoAs spanning the FOV at intervals of 0.2° .

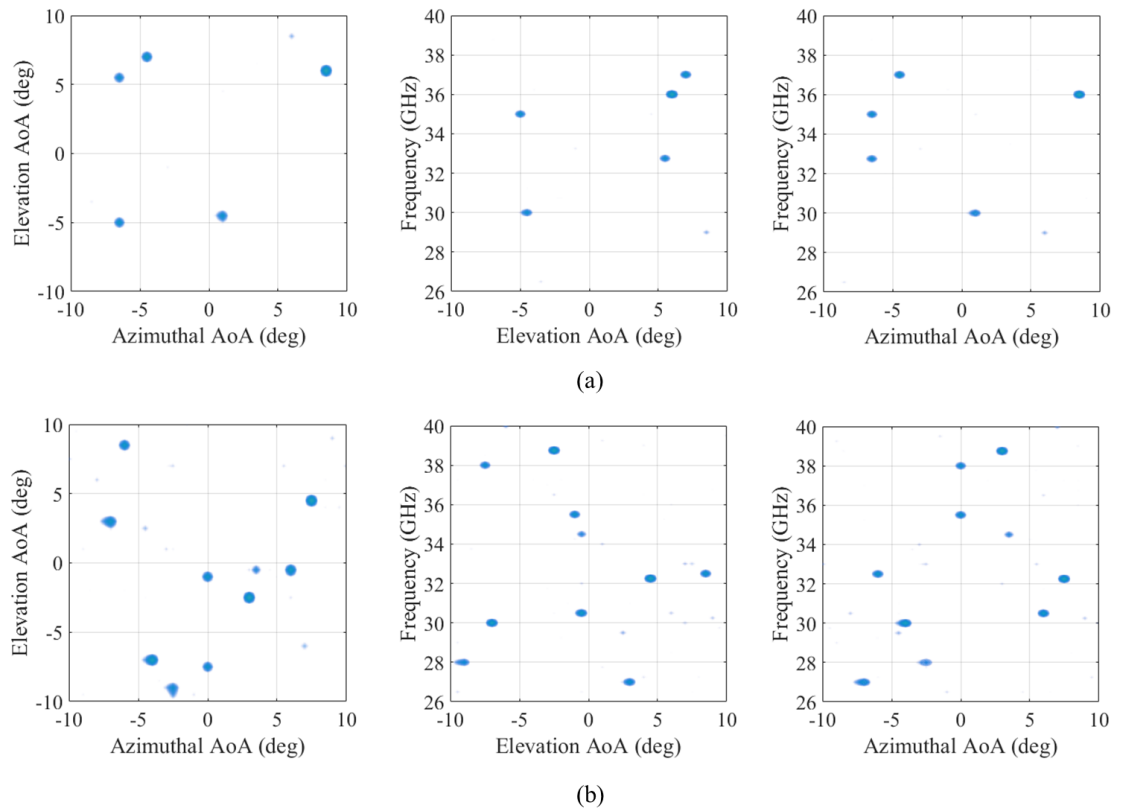


Figure 6.13: Simulated 3D k-space amplitude distribution reconstructions for a (a) 5-source scene, (b) 10-source scene. Each scene is reconstructed using the required number of iterations.

Figure 6.13 exemplifies reconstructed 3D RF source distributions, where Figures 6.13 (a-c) contain cross-sectional views of a 5-source scene, and Figures (d-f) comprise cross-sectional views of a 10-source scene. Both scenes were resolved using the respective iteration cut-offs corresponding to each source density, and reconstructed k-space positions were extracted using the 3-dB numerical peak detection algorithm. The comparison of the measured and expected positions are presented in Tables 6.1 and 6.2 for the 5-source and 10-source scenes, respectively. As evident from the included values, each simulated scene was reconstructed accurately with the measured positions resolved at the nearest sampling node in the weight-matrix.

Source	f_{RF} (GHz)	Az. AoA (deg.)	El. AoA (deg.)
1	36.00 (36.00)	$\theta_{AZ} = 8.5$ (8.4)	$\varphi_{EL} = 6.0$ (6.2)
2	30.00 (30.00)	$\theta_{AZ} = 0.5$ (0.8)	$\varphi_{EL} = -4.5$ (-4.6)
3	32.75 (32.80)	$\theta_{AZ} = -6.5$ (-6.6)	$\varphi_{EL} = 5.5$ (5.4)
4	35.00 (35.00)	$\theta_{AZ} = -6.5$ (-6.4)	$\varphi_{EL} = -5.0$ (-4.8)
5	37.00 (37.00)	$\theta_{AZ} = -4.5$ (-4.6)	$\varphi_{EL} = 7.0$ (7.0)

Table 6.1: Simulated 3D k-space reconstruction results for the 5-source scene. Measured frequency and AoA positions are in plain text and expected positions are in parenthesis.

Source	f_{RF} (GHz)	Az. AoA (deg.)	El. AoA (deg.)
1	32.25 (32.20)	$\theta_{AZ} = -7.5$ (7.4)	$\varphi_{EL} = 4.5$ (4.6)
2	30.00 (30.00)	$\theta_{AZ} = -4.0$ (-4.2)	$\varphi_{EL} = -7.0$ (-7.2)
3	27.00 (27.00)	$\theta_{AZ} = -7.0$ (-7.0)	$\varphi_{EL} = 3.0$ (2.8)
4	35.50 (35.40)	$\theta_{AZ} = 0.0$ (0.2)	$\varphi_{EL} = -1.0$ (-0.8)
5	34.50 (34.40)	$\theta_{AZ} = 3.5$ (3.6)	$\varphi_{EL} = -0.5$ (-0.4)
6	38.00 (38.00)	$\theta_{AZ} = 0.0$ (0.0)	$\varphi_{EL} = -7.5$ (-7.6)
7	39.00 (38.80)	$\theta_{AZ} = 3.0$ (3.2)	$\varphi_{EL} = -2.5$ (-2.4)
8	30.50 (30.60)	$\theta_{AZ} = 6.0$ (6.2)	$\varphi_{EL} = -0.5$ (-0.6)
9	32.50 (32.40)	$\theta_{AZ} = -6.0$ (-6.0)	$\varphi_{EL} = 8.5$ (8.6)
10	28.00 (28.00)	$\theta_{AZ} = -2.5$ (-2.4)	$\varphi_{EL} = -9.0$ (-8.8)

Table 6.2: Simulated 3D k-space reconstruction results for the 10-source scene. Measured frequency and AoA positions are in plain text and expected positions are in parenthesis.

6.4 k-Space Imaging Receiver Fabrication

The final distributed-aperture k-space imaging receiver design consists of the spatio-temporal aperture integrated into the original 35 GHz passive mmW imager system architecture, presented in Section 6.1.1. Throughout the subsequent sections, the process of upgrading the spatial aperture, and fabrication and installation of a temporal aperture will be discussed in detail. Following this, an overview of the completed Ka-band distributed-aperture k-space imaging receiver and its hardware components is provided.

6.4.1 Spatial Aperture

Assembly of the k-space imager’s spatial aperture consists of two processes. The first is installation of the 26 – 40 GHz ALTS antenna fabricated at the University of Delaware, and LNAs purchased from RF Lambda (RLNA24G40GB). The second portion involves restoring the mechanical rotation stages, required for the calibration routine, to an operational state.

6.4.1.1 RF Frontend

To construct the five-arm spiral distributed-aperture based on the simulated spatial aperture, presented in Section 6.2.1, each module in the 35 GHz passive mmW imager is removed and organized based on the integrated EO phase modulator conversion efficiency. The 35 GHz standard gain horn antennas and LNAs are subsequently uninstalled to prepare for installation of the 26 – 40 GHz ALTS antennas and LNAs, a comparison of the old and new RF components is presented in Figure 6.14(a). ALTS antennas coupled to the LNAs, via 2.94 mm coax connectors, are then organized and connected to the EO phase modulators with right angle 2.94 mm coax connectors based on component positions shown in Figures 6.6(a) and (c). In each module, there are a pair of connections linked to a bias distribution board behind the distributed aperture. One is an RF coaxial cable linking a second EO phase modulator port to the bias distribution board for phase feedback; the second is an Ethernet cable, stripped at one end, to provide bias to the LNA. Since the bias links for the EO modulator have been installed previously, the only bias connection adjustments required are soldering the appropriate Ethernet wires to the LNA +12 V and ground pins. Once the RF components and EO modulators have been installed into the up-conversion module housings, shown in Figure 6.14 (c), each one is slotted into their respective spatial position within the distributed-aperture. A comparison of the old and new RF frontends is shown in Figure 6.15.

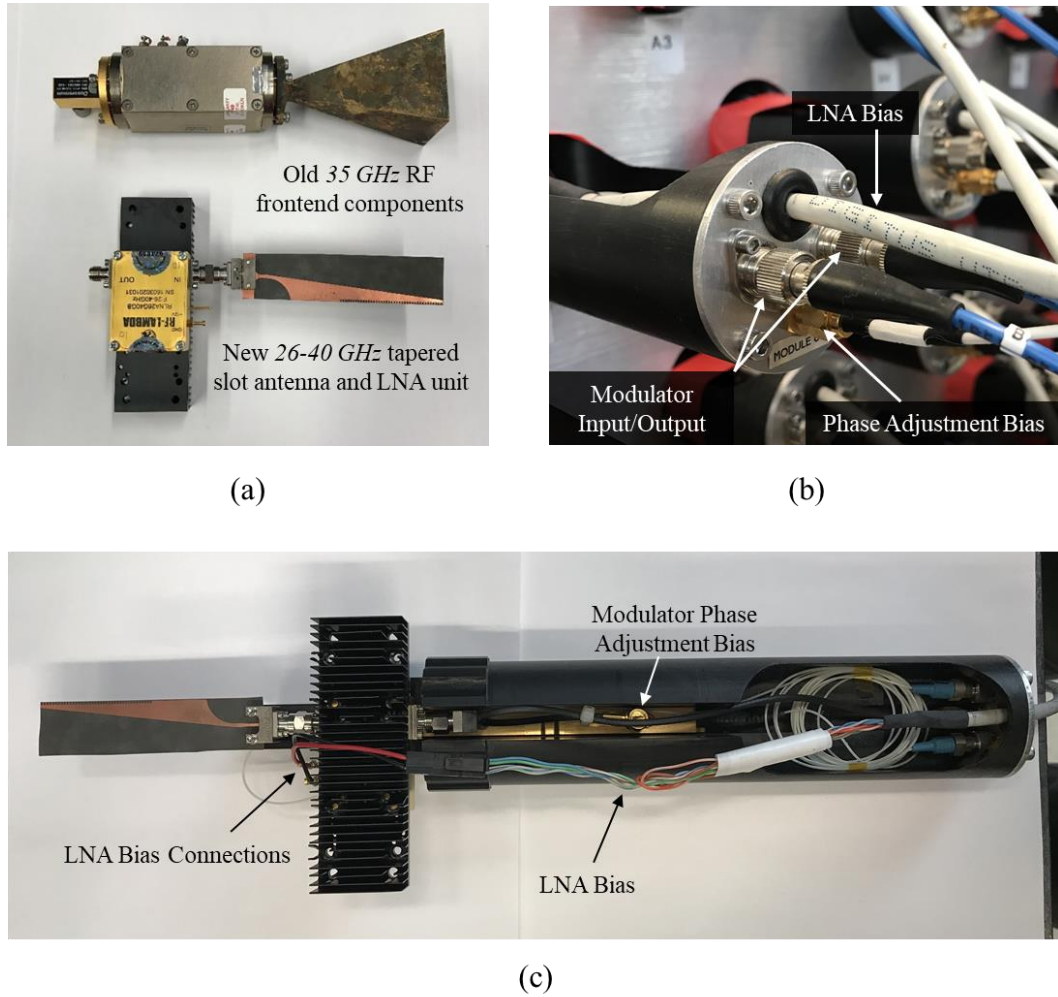
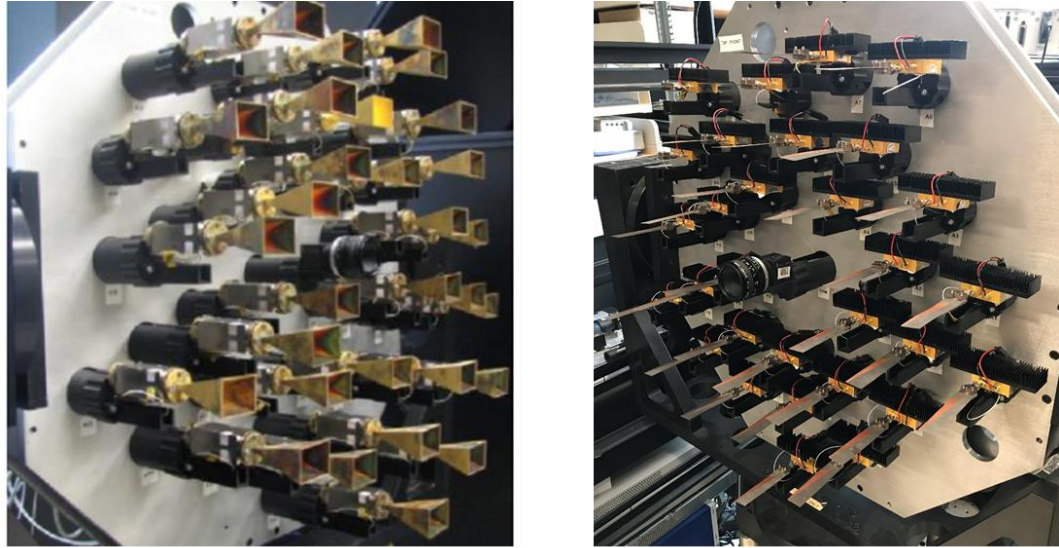


Figure 6.14: (a) Comparison of old and new RF frontend components, and the complete up-conversion module shown in (c) with optical and electrical input highlighted in (b).



(a)

(b)

Figure 6.15: Distributed-aperture RF frontend for the (a) original 35 GHz passive mmW imager, and (b) upgraded 26 – 40 GHz k-space imaging receiver.

Once all of the modules are installed into the distributed-aperture, the positioning, orthogonal to the faceplate, needs to be optimized for mitigation of phase offsets between channels caused by slight inequalities in optical fiber length conveying information to the optical processor. This may seem counterproductive since the ends of the equal length optical fiber array will eventually be connected to an arbitrary optical fiber array of varying lengths, and these inequalities will be encoded into the weight-matrix during the k-space calibration. However, it is important to consider the dual-use capabilities of the k-space imager, where the system performs as both a spatial-spectral cueing sensor and a receiver for down-conversion of signal of interest. With the availability of commercial programmable TTDs, it may be of interest to sense the spatial-spectral information of RF signals then analyze the data of a particular source.

To enable this functionality, the equivalent free-space path lengths in each channel need to be equal for sufficient optical beam steering of the desired wavefront to an optical fiber port, or photodiode, for down-conversion and data analysis. This could be equalization of optical fiber channels could be accomplished by the programmable TTD modules; however, this requires accurate characterization of the small length variations in each fiber, which is difficult to do at optical wavelengths. Consequently, a more suitable approach is to flatten the phase response across the aperture by repositioning the ALTS-coupled up-conversion modules.

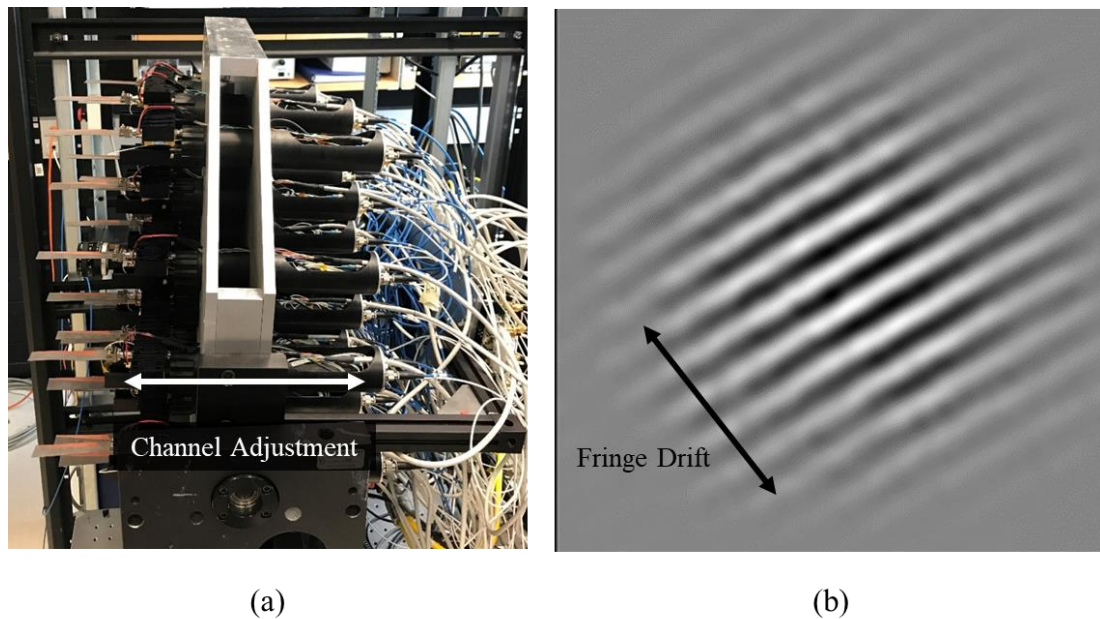


Figure 6.16: (a) Side view of the distributed-aperture, with a white arrow indicating the direction that the up-conversion modules are physically moved, and (b) an example fringe interference pattern produced when two channels are on, the black arrows indicate the fringe drift direction, if the path lengths are not equal.

To accomplish this task, a single Ka-band stand gain horn antenna is placed 3.5 m away from the imaging receiver, so the each element in the distributed-aperture senses the far-field radiation. The antenna is coupled to an RF signal generator and is repetitively swept from 26-40 GHz. As the source frequency is cyclically changing two LNAs within the aperture are turned on, where one channel serves as a reference and the other as a variable. If the free-space equivalent path length between the channels is unequal, the fringe interference pattern, shown in Figure 6.16 (b), will drift across the CCD array as the frequency changes. Equalization of the channel phase offset is accomplished by physically moving the variable channel into or out of the distributed-aperture faceplate, as indicated by Figure 6.16 (a). If the adjustment is properly done, the fringes will no longer drift during the frequency sweep. After all channels are aligned with the original reference channel, the process of upgrading the RF frontend is complete.

6.4.1.2 Mechanical Components

The processes of restoring operation to the mechanical rotation stages from Parker Hannifin Co. began with replacement of the controller and driver hardware, as the previously installed set no longer had the two functional channel ports required to mechanically steer the imager in the azimuthal and elevation directions. To this end, a set of Galil DMC-2030 motion controllers and Aries AR-02AE drivers were repurposed from a mmW imaging scanning cart were retrieved to replace the current National Instruments NI UMI-7774 motion controller, shown in Figure 6.17 (a) and (b), respectively. After applying the require cable connections to the motors, the Galil controllers were connected to the system control CPU for interfacing via RS-232. A communication link was subsequently established by manually installing driver files

into the imager CPU with a manual pointing reference to the controllers. In order to test the new controller and driver hardware, Galil test software was used to send RS-232 commands through the motion controllers to the rotation stages. During this process, it became apparent that the controllers, drivers, and rotation stages were all operational; however, the distributed-aperture and framing exceeded the load limit. Consequently, the steel frame holding the RF fronted needed to be replaced with a significantly lighter, aluminum frame.

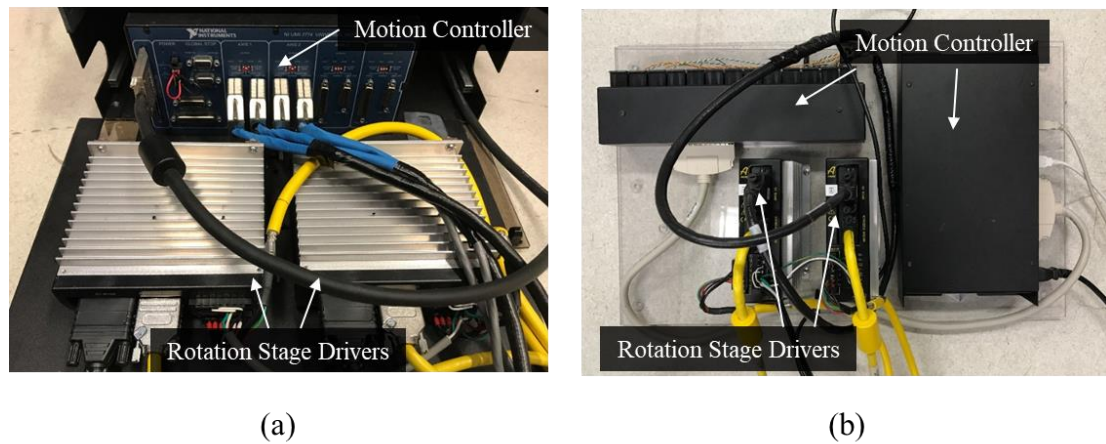


Figure 6.17: (a) Original motion controller and driver setup with a National Instruments NI UMI-7774 Universal Motion Interface and Aries AR-02AE drivers. (b) Updated motion controller and driver setup with a Galil DMC-2030 motion controller and Aries AR-02AE drivers.

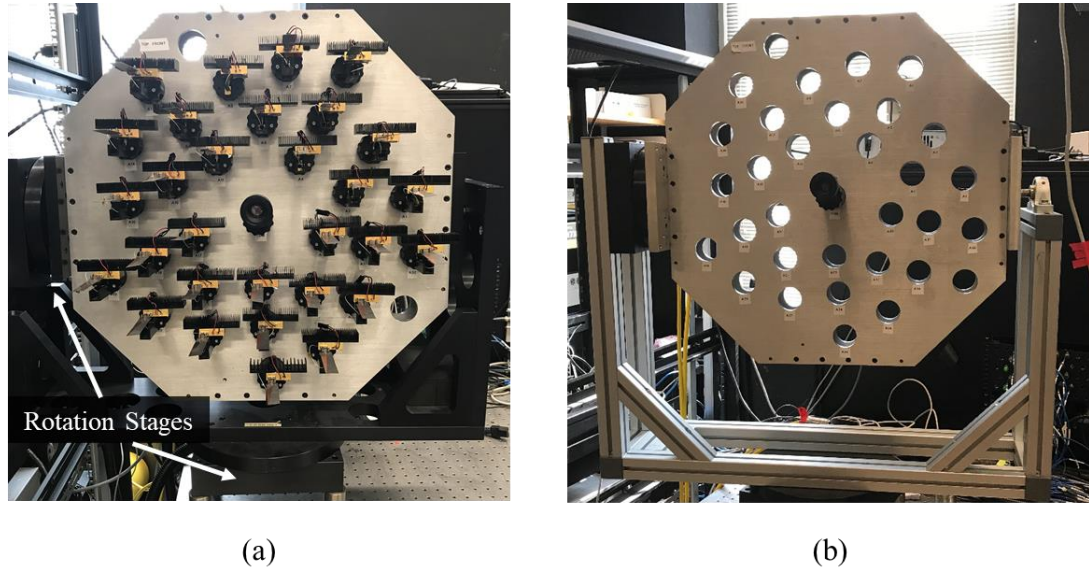


Figure 6.18: (a) Initial distributed-aperture steel framing, and (b) new, lighter, aluminum framing.

After reducing the distributed-aperture load, mechanically steering of the array was enabled. Optimization of mechanical movement to reduce system vibration was accomplished by tuning motor PID parameters, acceleration, velocity, and torque settings. For the k-space imaging calibration routine, an automated raster scan program was developed to cover each angular (x- and y-axis) position in the signal sampling space with a far-field emitter frequency scan from 26-40 GHz at each angular position. This program was subsequently integrated into the imager Labview control software, where the RS-232 commands are sent through a Galil communication library paired with the driver files. Within the code, positional limits are encoded to ensure accuracy in movement bounded in the system's FOV to one-hundredth of a degree. Example positioning is depicted in Figure 6.19 to show start, broadside, and end angular positioning of the mechanically steered array. Once this process concluded, the up-

conversion modules were reinstalled into the frame along with the corresponding optical fibers and RF cable coupled bias board, as illustrated in Figure 6.20.

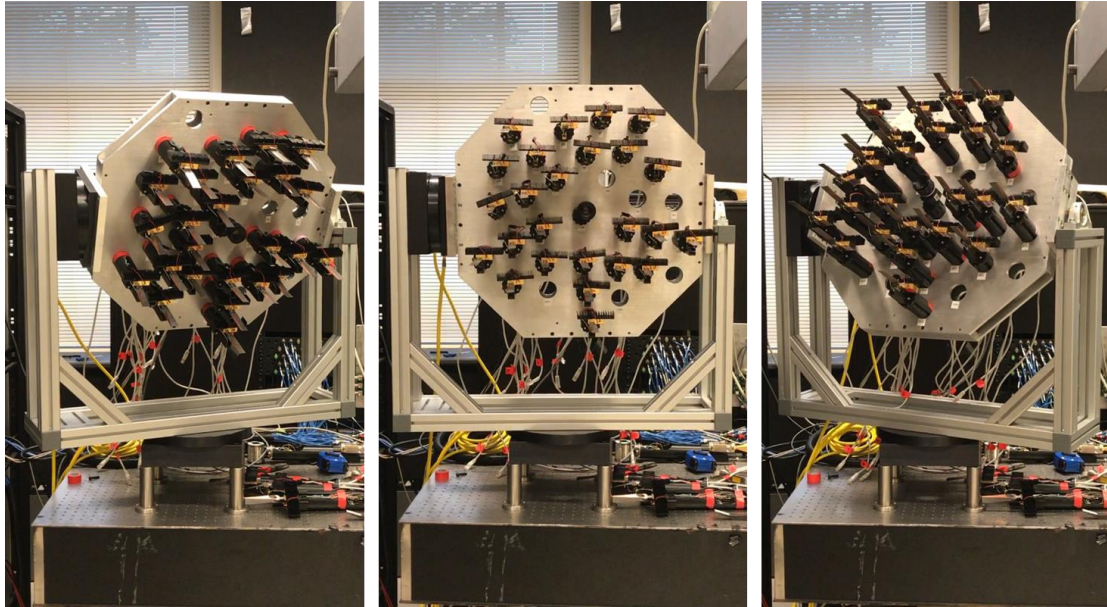


Figure 6.19: Example positions of the mechanically steered distributed-aperture.

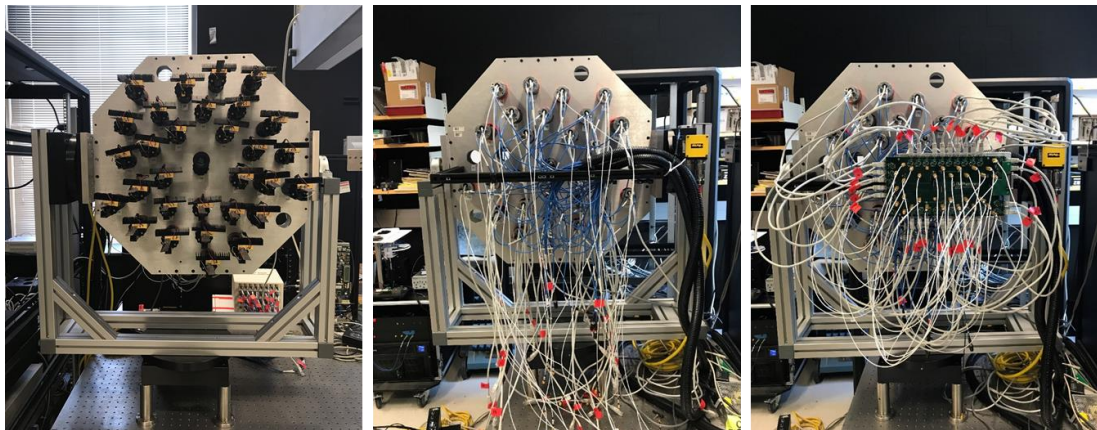


Figure 6.20: Finalized spatial aperture for the Ka-band distributed-aperture k-space imaging receiver.

6.4.2 Temporal Aperture

Fabrication of the fixed temporal aperture consists of constructing 30 different length optical fibers. For the experimental system, the arbitrary optical fiber array presented in Section 6.3 is fabricated, where the longest baseline is 40 cm and the shortest baseline is approximately 1.5 cm. The fabrication process begins with splicing PM connectors to 30 bare PM optical fibers, approximately 2 m in length. To ensure each optical fiber is the appropriate length, the first fiber is measured to a maximum length of 1.5 m for splicing of the second PM connector. The remaining fibers are measured at decreasing lengths in approximate intervals of 1.5 cm and spliced to PM connectors. Prevention of grating lobes in the k-space reconstruction is considered throughout this process, thus the optical fiber cuts are made at different mm-scale offsets from the 1.5 cm increment.

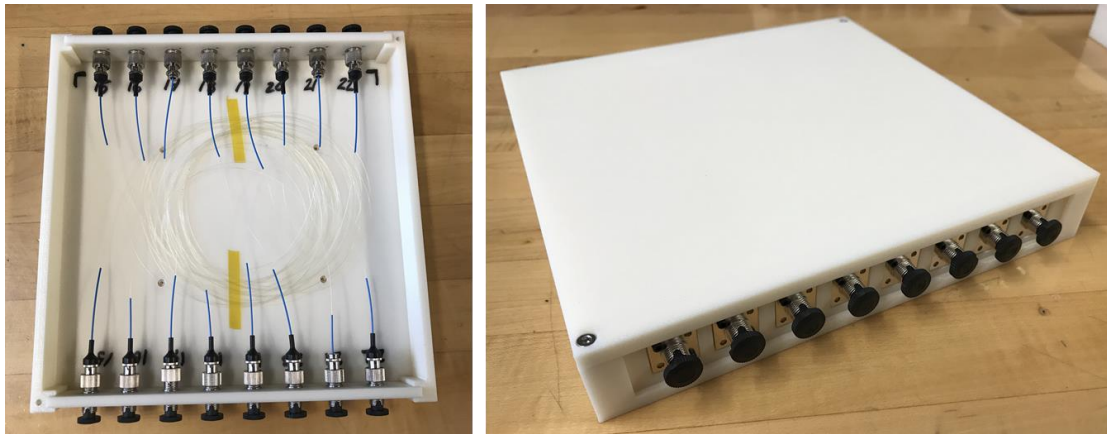


Figure 6.21: One of the four housing populated with temporal aperture channels.

Upon fabricating all of the optical fibers, 20.00 cm \times 20.00 cm \times 3.25 cm 3D printed enclosures were designed to organize and protect the bare fiber. The complete housing set consists of 4 ABS enclosures, each with eight inputs and outputs. Optical

fibers are positioned into the temporal aperture channels in order of ascending lengths to provide simple routing and reconfiguration of the randomly permuted RF fronted channel inputs. An example of one temporal aperture enclosure is displayed in Figure 6.21. After housing assembly concludes, the temporal aperture is installed into the imaging system between the optical fibers connected to the output of the up-conversion modules, and the optical fiber array residing in the optical processor. The spatial and temporal channel mapping was carried out in the same configuration presented in Figure 6.8. During this integration process, channel organization from the distributed aperture to the optical fiber array remains constant, i.e., the inputs and outputs of the temporal aperture are placed at the original connections set for homothetic mapping. The finalized integration of the temporal aperture into the k-space imaging receiver is illustrated in Figure 6.22.

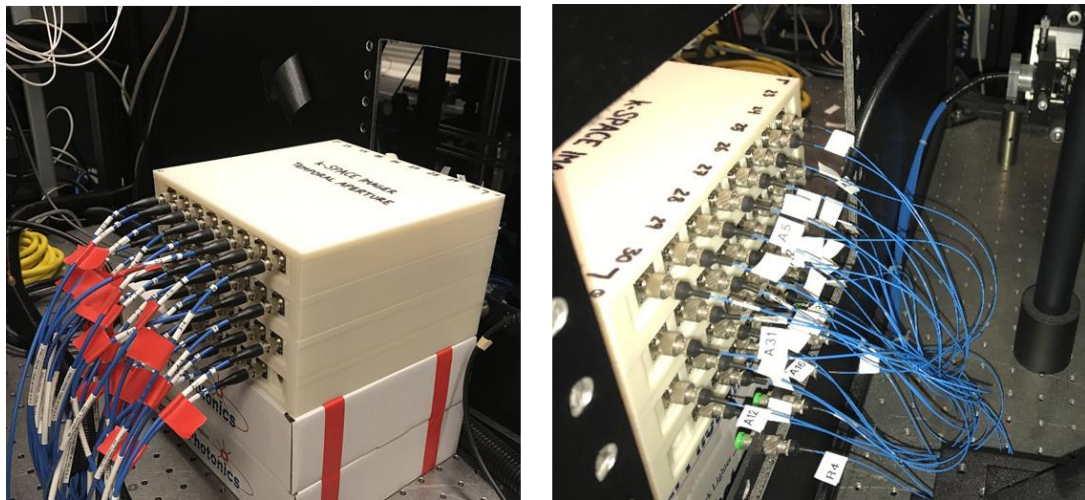


Figure 6.22: Complete temporal aperture, installed into the imaging receiver, with optical fiber inputs from the up-conversion modules and outputs to the optical fiber array.

6.4.3 k-Space Imaging Receiver System

The integration of the spatial and temporal apertures discussed in the previous sections concludes the 30 channel, 2D distributed-aperture k-space imaging receiver construction. Organization of spatial aperture components, comprising ALTS antennas, LNAs, and EO phase modulators, in a five-spiral pattern spanning a diameter of arranged 60 cm, provides an angular resolution ranging from approximately $\theta_{min} = 0.874^\circ$ to $\theta_{max} = 1.345^\circ$ over the operational bandwidth of 26-40 GHz. Behind each up-conversion module is an arbitrary length of optical within the temporal aperture, with a maximum-to-minimum fiber-length difference of 40 cm, equivalent to a 60-cm free-space path offset. Based on these dimensions the system has a spectral resolution of 250 MHz.

The optical source configuration, i.e., DFB laser, EDFAs, and splitter network, control CPU, Agilent N6701A modular power supply, and rotation stage control components are assembled within a 19" equipment rack, shown in Figure 6.23 (a). From the equipment rack, optical outputs from the splitter network connect the common laser source to each EO phase modulator within the array for equal power distribution, and electrical cables are coupled to the two rotation stages in the distributed aperture for azimuthal and elevation axis control. At the output of each modulator, an optical fiber is linked through respective temporal aperture channels to the optical processor, as illustrated in Figure 6.22. Within the optical processor, a small percentage of the carrier is tapped off toward a phase detection board, and the remaining optical carrier and sideband power is conveyed toward a FLIR SC2500 SWIR camera for k-space tomograph collection, all displayed in Figure 6.24. Frames from the 256×320 pixel CCD array are transmitted over an Ethernet cable to the control CPU, and the response captured on the phase detection board are sent to a FPGA driven feedback circuit to

relay corrections to phase variations, related to vibrations and other environmental effects, at the modulators through a bias distribution board, Figure 6.25. In addition to the phase feedback, the bias board simultaneously supplies each LNA bias set in the equipment rack power supply.

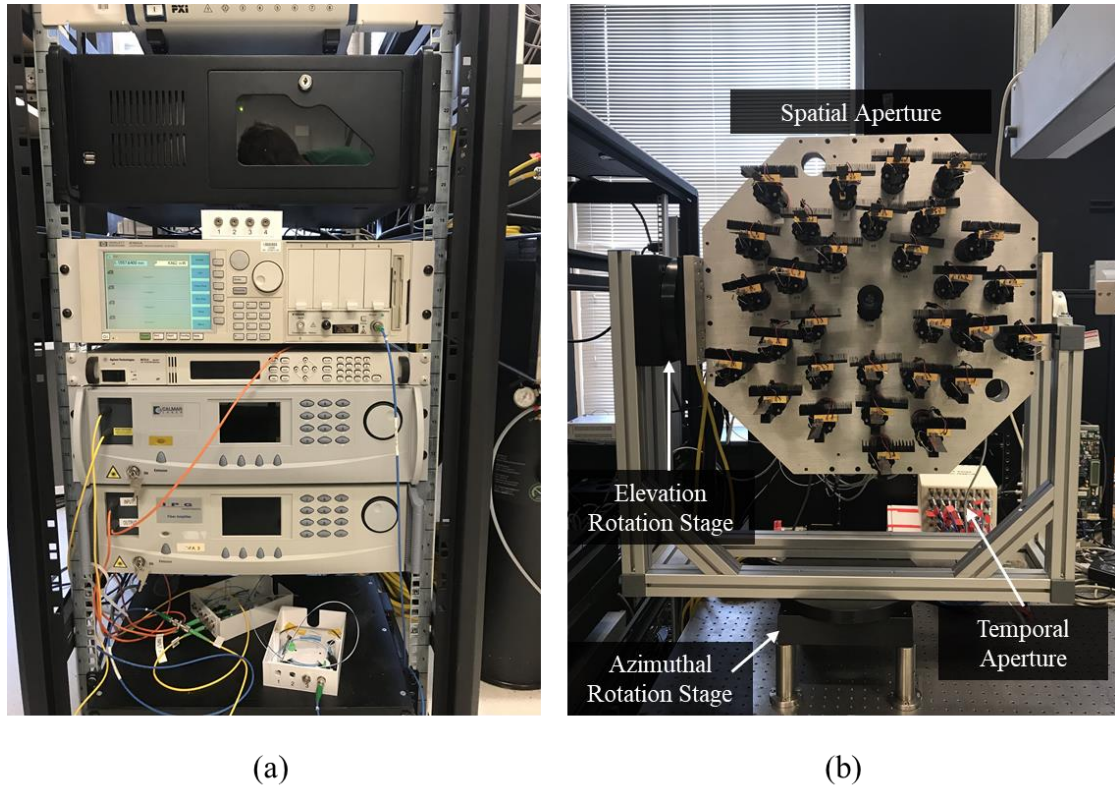


Figure 6.23: (a) 19" equipment rack housing the control CPU (top), DFB laser, power supply, two EDFAs, splitter network, and rotation stage control components (bottom). (b) Distributed-aperture k-space imaging receiver spatio-temporal aperture.

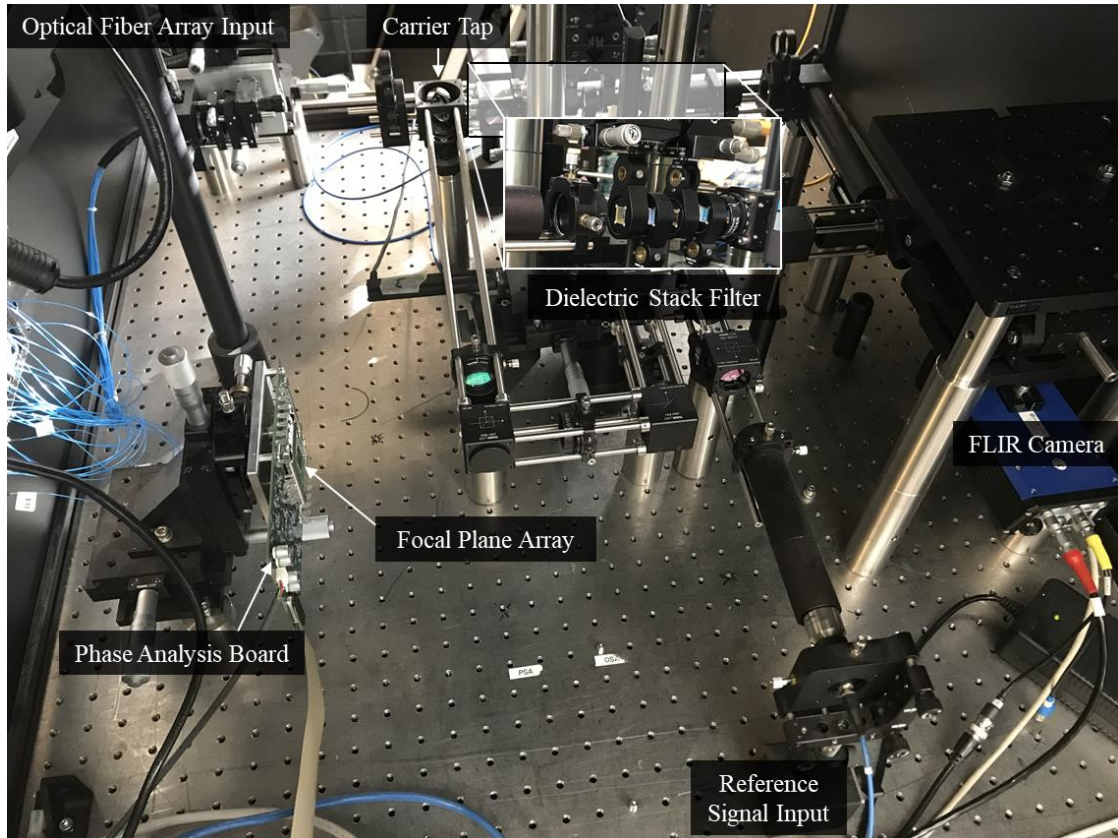


Figure 6.24: Distributed-aperture k-space imaging receiver optical processor.

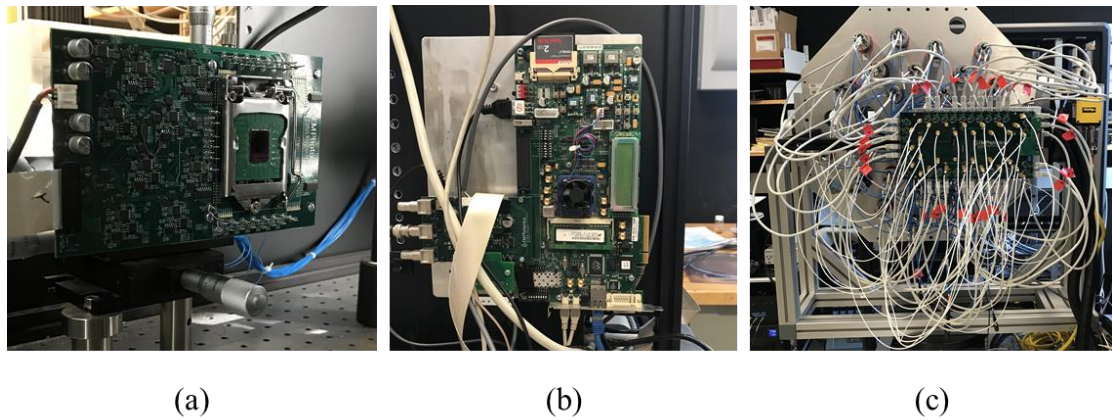


Figure 6.25: (a) Phase alignment FPA board, (b) FPGA used for controlling phase feedback and component biasing, and (c) bias distribution board coupled to each LNA and EO modulator.

In the next two Chapter, this k-space imaging receiver architecture is applied to experimental RF signal distributions for characterization of spatial-spectral sensing capability. More specifically, RF emitters are spectrally located within the newly allocated 5G bands between 28 and 39 GHz to demonstrate the efficacy in passive spatial-spectral utilization mapping for full-dimensional MIMO. Chapter 7 will primarily focus on the accuracy of frequencies and AoA detection for 2D and 3D k-space reconstructions, which is characterized in terms of the resolution tolerance presented throughout this Chapter; and Chapter 8 introduces a new adaptation of k-space tomography through implementation of compressive sensing techniques for reduced latency in experimental reconstructions.

Chapter 7

EXPERIMENTAL SPATIAL-SPECTRAL MAPPING

7.1 System Calibration and Experimental Setup

As mentioned, in order to obtain all of the necessary information required to solve Equation 5.42, the k-space imaging receiver needs to undergo a calibration routine. During this process, the imager's aperture is mechanically rotated to emulate a frequency swept source at each point over a range of azimuth and elevation angles. Throughout this procedure, a normalized CCD camera response from each azimuthal AoA, elevation AoA, and frequency combination is stacked into a 3D weight-matrix \mathbf{A} .

Ideally, the calibration routine would include the entire $\pm 10^\circ$ FOV and 26 – 40 GHz bandwidth. However, proper sampling of the full 3D k-space volume at Nyquist for the system's angular and spectral resolution requires a calibration routine involving compilation of 256 x 320 pixel interferograms from over 290,000 points in k-space. Collection and processing of data at this scale would require an impractical amount of time and computational resources; therefore, the cross configuration, shown in Figure 7.1, was selected as a sampling space to experimental verify 3D k-space reconstruction. It is important to note that k-space tomography is not limited to sub-spaces of the full 3D k-space, as the sparse nature of RF scenes allows for the potential use of compressive sensing and sparse calibration techniques to minimize the impact of the calibration data.

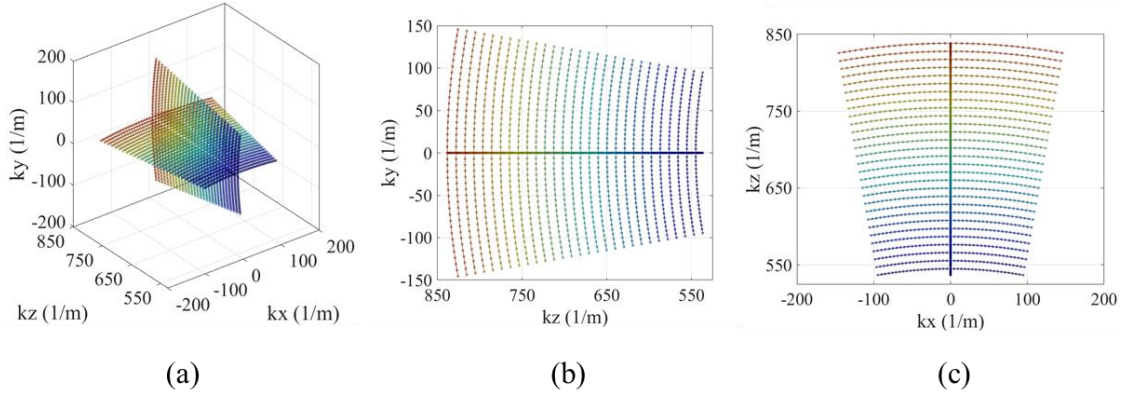


Figure 7.1: (a) Isometric view of \mathbf{k} -space cross configuration. (b) Side view of elevation and frequency sampling points. (c) Top-down view of azimuthal and frequency sampling points.

Calibration of this cross \mathbf{k} -space is accomplished by positioning a calibration source 2 m away at broadside from the RF front end, as illustrated in Figure 7.2, mechanically stepping the antenna array, and electrically sweeping the calibration source frequency. The mechanical stepping was performed in two sequential phases. First, the azimuthal positions between $\pm 10^\circ$ at 0° elevation were sampled at 0.4° increments, i.e., approximately one-half of the angular resolution at the highest frequency. Second, the elevation positions between $\pm 10^\circ$ at 0° azimuth were sampled at 0.4° increments. At each angular position, the calibration source, emitting at 12 dBm, was swept from 26 GHz to 40 GHz in 125 MHz steps, i.e., one-half of the spectral resolution. The interference patterns projected from these spatial-spectral positions onto the 256×320 pixel CCD camera were captured and compiled into the weight-matrix used within the Kaczmarz algorithm for scene reconstructions.

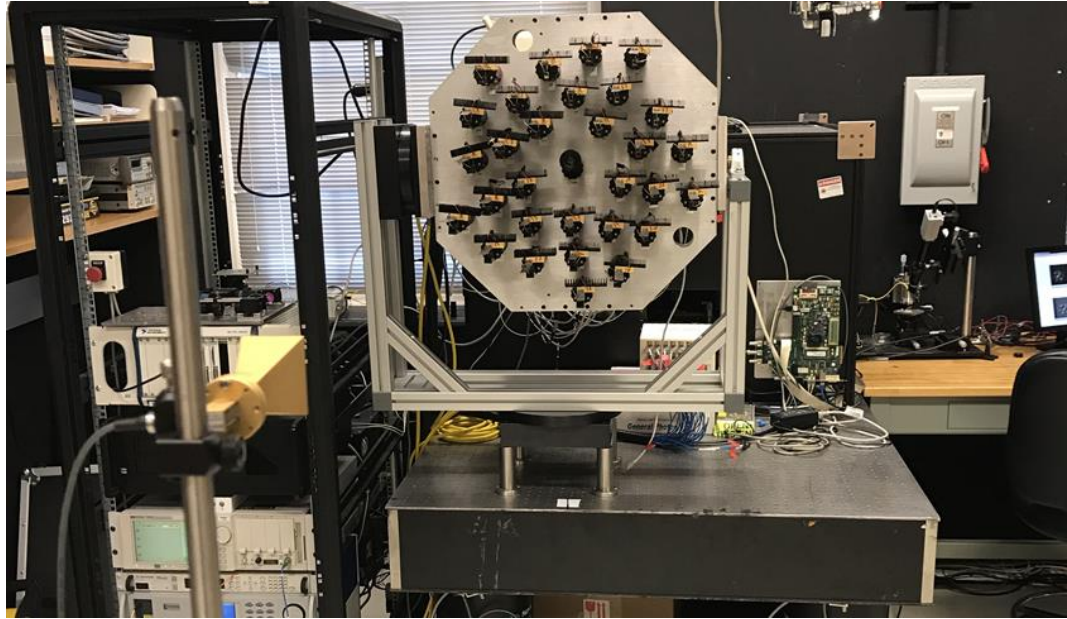


Figure 7.2: Calibration scene depicting broadside positioning of the calibration source at 2 m from the five-spiral distributed-aperture.

Once the calibration routine is completed, RF source scenes consisting of 10 dBm emitters on the azimuthal plane, elevation plane, or both planes simultaneously are set-up, as displayed in Figure 7.3. Although there are a substantial amount of AoA/frequency combinations, the signal distributions organized here are deliberately set to emphasize the combined spatial isolation and frequency detection within new 5G wireless bands. Therefore, all scenes include multiple sources separated in angle and/or frequency, with both horn antennas emitting at 28 GHz, and/or 39 GHz. A variety of such source scenes were arranged for capture of unique interferograms produced by the incident EM waves at the CCD camera. These interferograms were subsequently processed using the Kaczmarz algorithm, along with the weight-matrix for RF amplitude distribution reconstructions.

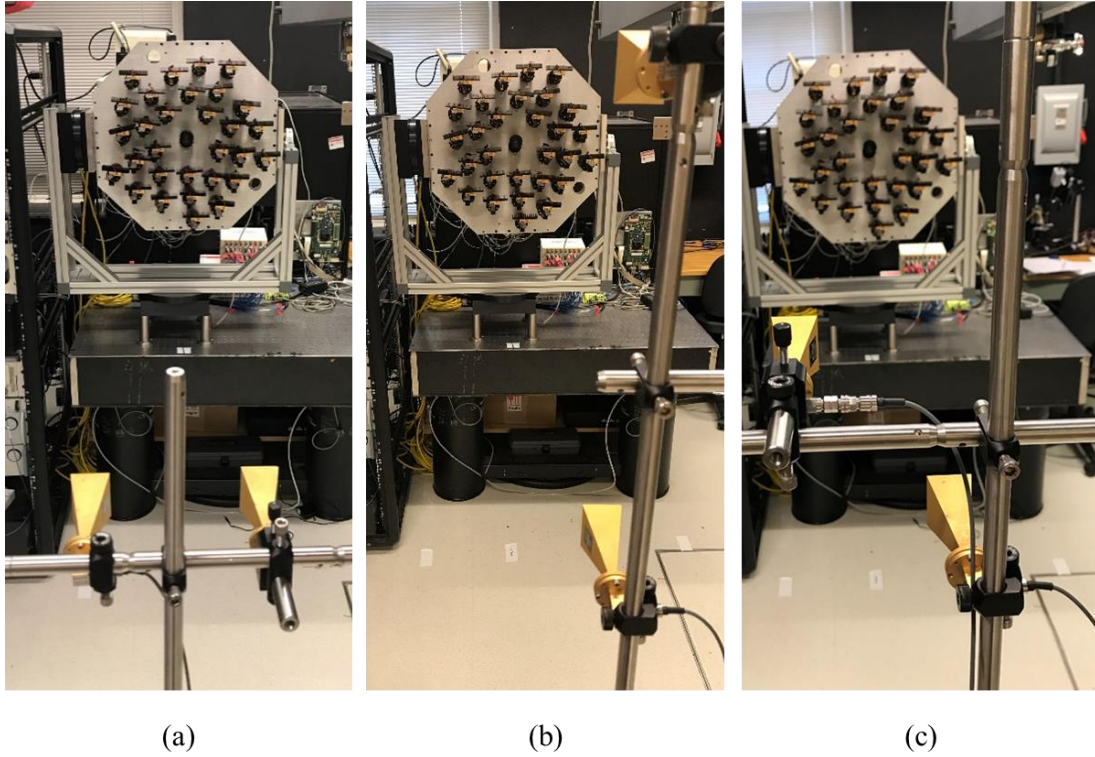


Figure 7.3: Experiment RF scenes consisting of (a) azimuthal only, (b) elevation only, and (c) both angular direction emitter locations.

7.2 Characterization and Results

In the following sections, reconstruction results for dual source RF signal distributions are presented, and characterized based on accuracy of spatial and spectral component extraction within the respective system resolutions. For each case, the RF signals are a constant tone of a particular frequency; therefore, the presented scene reconstructions consist of a k-space amplitude distribution, where signal locations in k-space are represented by a black dot. The black dots can be thought of as the continuous waves' representation in k-space, which is a delta function at a specific k-space coordinate corresponding to the frequency and AoA.

Overlaid onto each k-space amplitude distribution is a black circle. The circles here are placed with the center of the circle representing the exact known position of the source during the experimental measurement, with respect to both frequency and AoA. Furthermore, the diameter of the circle represents the k-space resolution rather than the frequency resolution or the spatial resolution independently. The resolution tolerance can be represented in k-space as a circle due to the spatial and spectral resolutions of the imaging system. The equality of these resolutions in k-space are based on the fact that the physical diameter of the antenna aperture, and the effective free-space path length of the temporal aperture are both 60 cm. Consequently, the circles provide a graphical reference to indicate how accurately the signals (black dots) were reconstructed within the k-space resolution (black circle).

Since the accuracy of the scene reconstructions in k-space are not immediately apparent in terms of frequency and AoA, a numerical peak detection algorithm was used to extract k_x and k_z , or k_y and k_z , coordinate positions of resolved signals. These Polar vectors, corresponding to each peak, are subsequently utilized to convert to AoA and frequency values using trigonometric equations and the relation, $\omega = c|\mathbf{k}|$. The experimental evaluation of the k-space reconstructions in terms of frequency and AoA are included in tables for a simple comparison of measured and expected values, where the measured frequencies and AoAs are present in plain text and the expected positions are included next to the measured values in parenthesis.

Reconstruction performance of the k-space imaging receiver for azimuthal and elevation signal distributions is exemplified in Figure 7.4 and Figure 7.5, respectively, with accuracy in terms of frequency and AoA listed in Table 7.1. Each set of scenes consist of two sources emitting on the same AoA plane, where Figure 7.4 are azimuthal

only reconstructions, and Figure 7.5 are elevation only. For both figures, the camera responses used to solve for the amplitude distribution of delta functions are presented in the left column, while all the resolved scenes are in the right column. It is important to note that the gray-scale colorbar in each pane corresponds to the relative power of a resolved source in arbitrary units. The extension into incorporating both AoA planes is presented in Figures 7.6 and 7.7, for scenes with two 28 GHz sources and two 39 GHz, respectively. As with the 2D k-space distributions, the camera responses used to solve for the amplitude distribution of delta functions are incorporated into each figure, and the accuracy in terms of frequency and AoA listed in Table 7.1

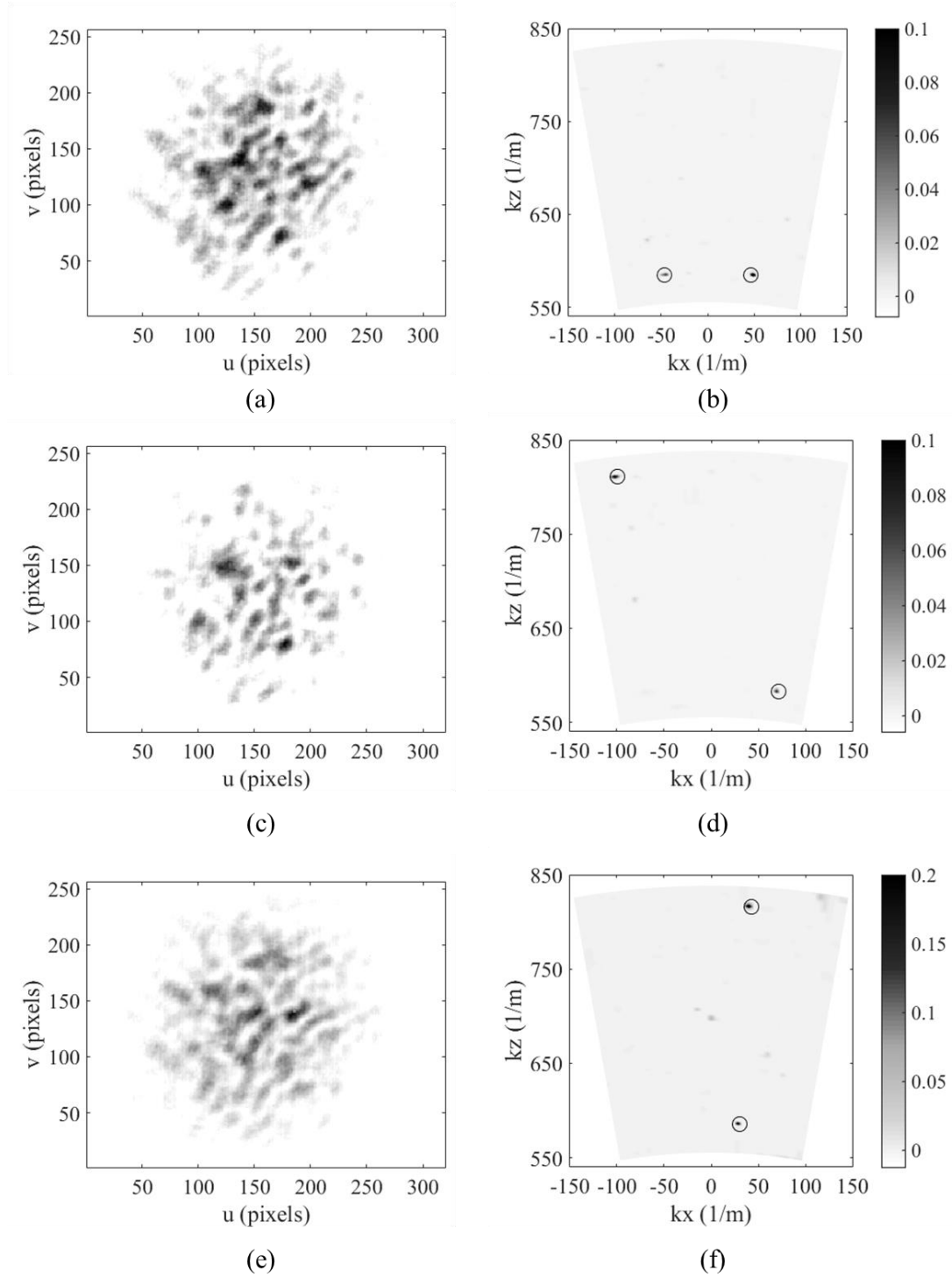


Figure 7.4: Camera responses (left) corresponding to reconstructed amplitude distributions (right) for two emitters in the azimuthal plane.

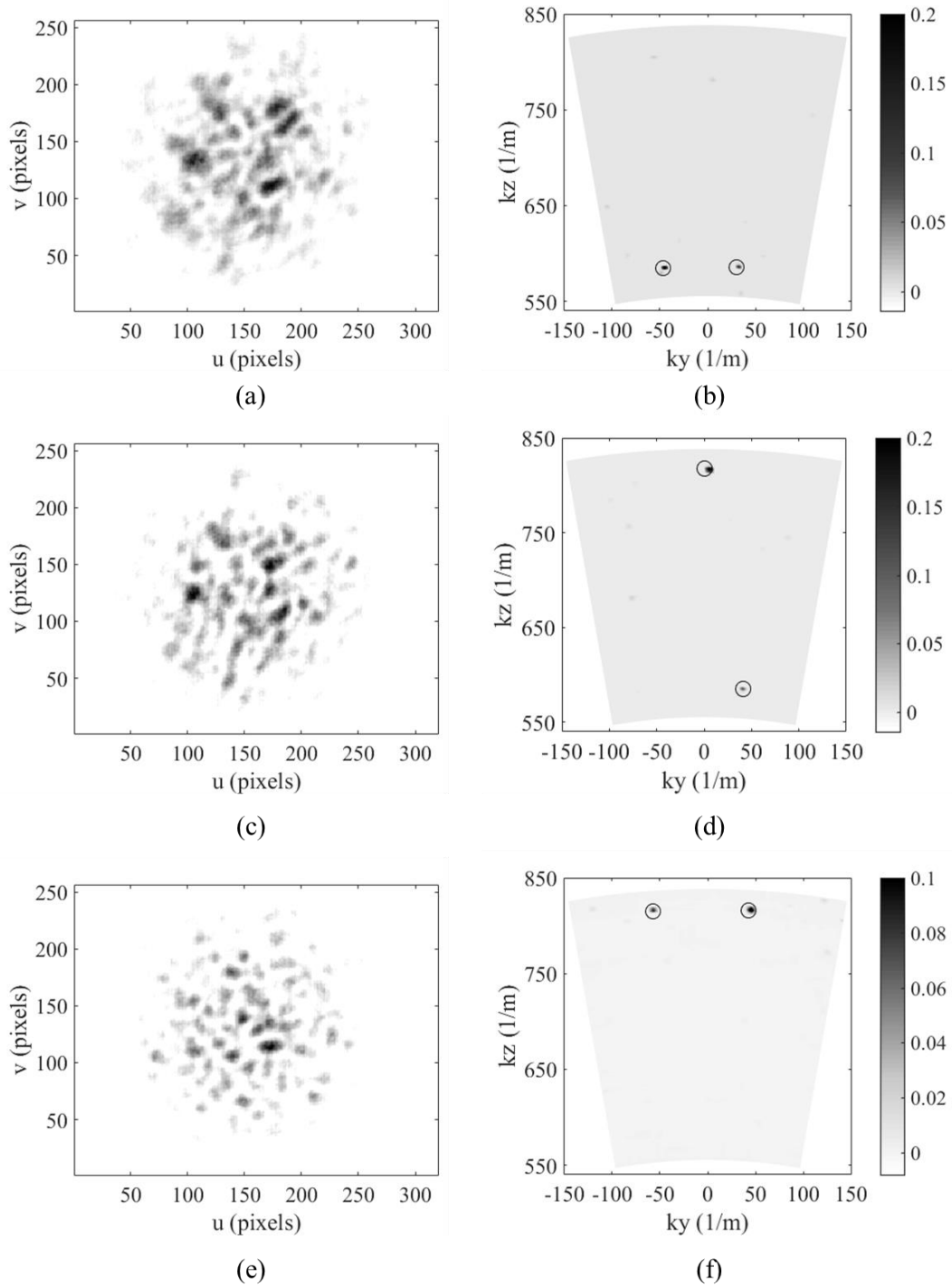


Figure 7.5: Camera responses (left) corresponding to reconstructed amplitude distributions (right) for two emitters in the elevation plane.

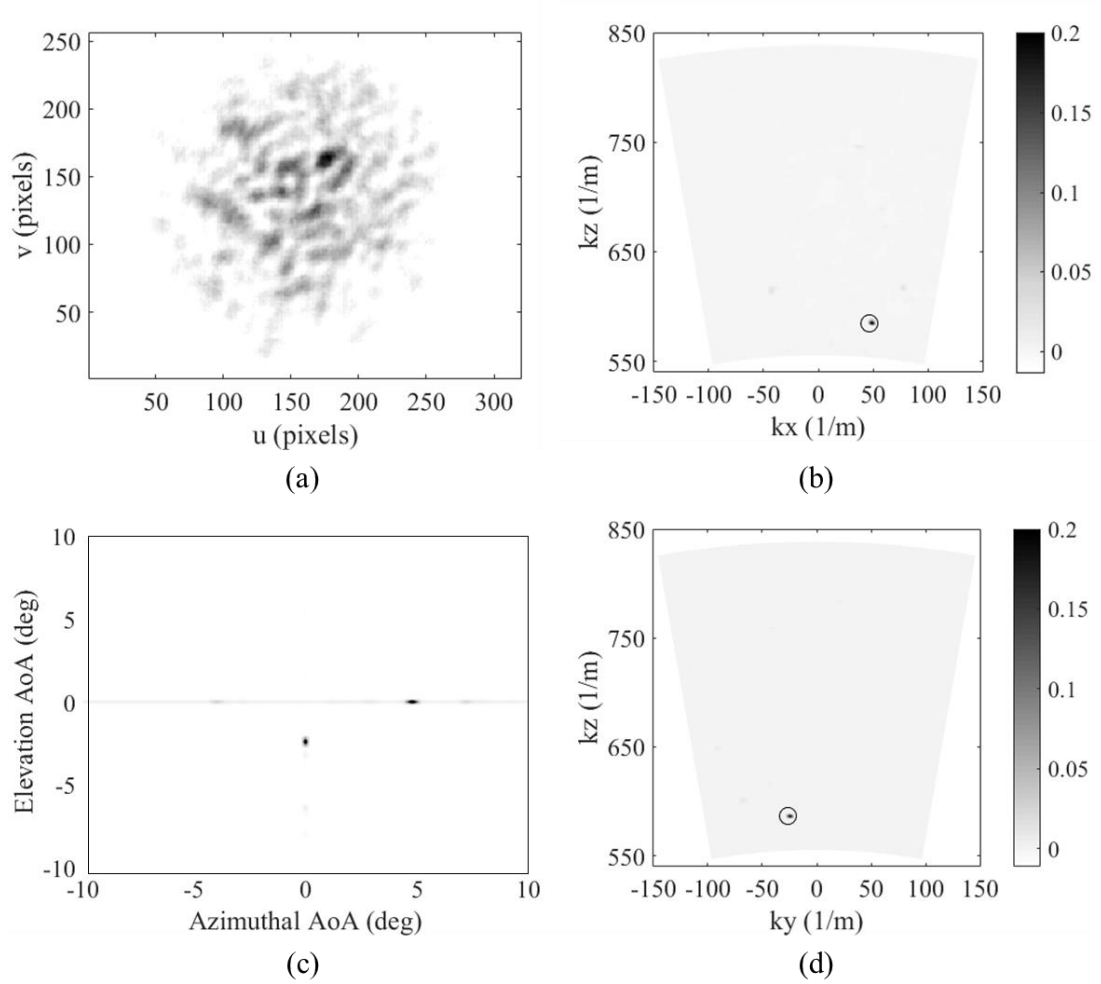


Figure 7.6: (a) Camera response from a source scene comprised of two emitters, one in the azimuthal plane, and one in the elevation plane, with both emitters transmitting at 28 GHz. Corresponding reconstructions for (b) azimuthal plane cross-section, (c) emitter plane cross-section, and (d) elevation plane cross-section.

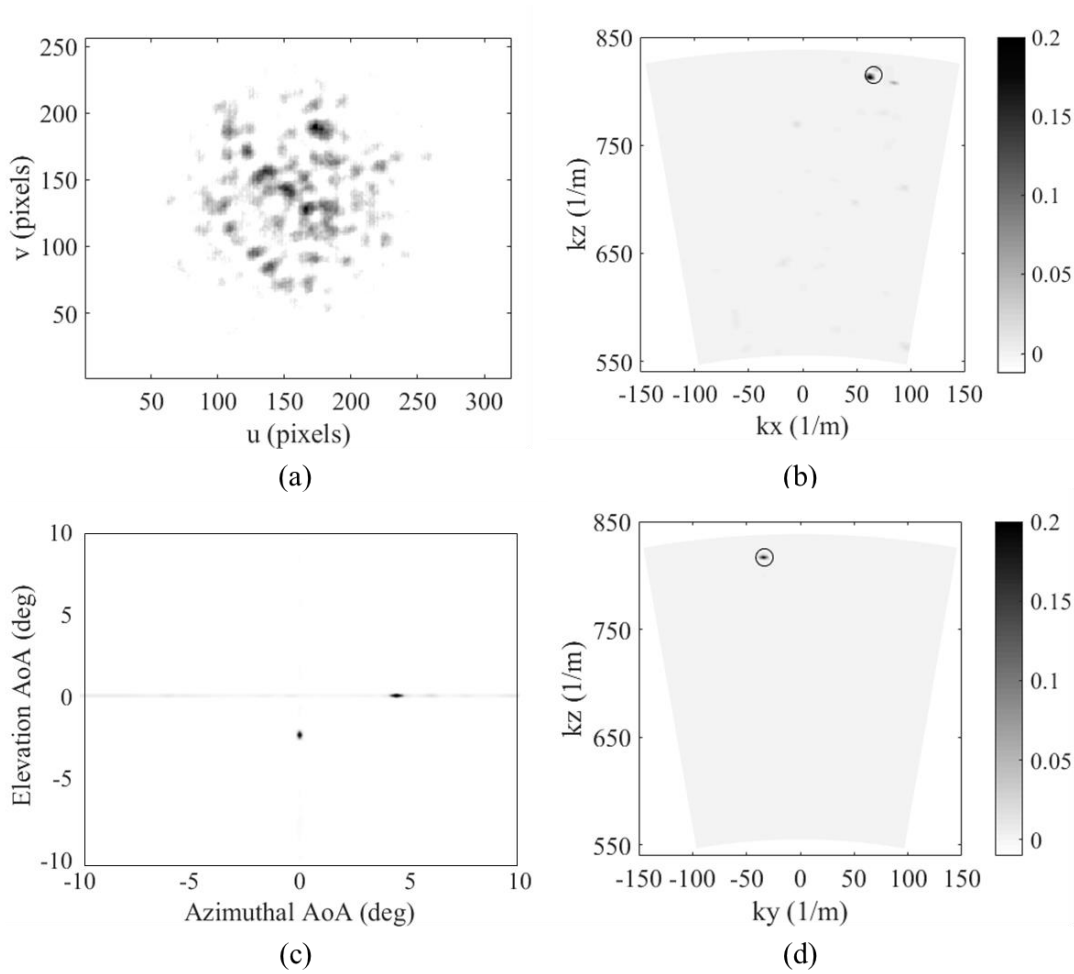


Figure 7.7: (a) Camera response from a source scene comprised of two emitters, one in the azimuthal plane, and one in the elevation plane, with both emitters transmitting at 39 GHz. Corresponding reconstructions for (b) azimuthal plane cross-section, (c) emitter plane cross-section, and (d) elevation plane cross-section.

Source	f_{RF} #1 (GHz)	f_{RF} #2 (GHz)	AoA #1 (deg.)	AoA #2 (deg.)
7.4(b)	28.0 (28.0)	28.0 (28.0)	$\theta_{AZ} = -4.4$ (-4.5)	$\theta_{AZ} = 4.8$ (4.5)
7.4(d)	39.0 (39.0)	28.0 (28.0)	$\theta_{AZ} = -7.2$ (-7.0)	$\theta_{AZ} = 6.8$ (7.0)
7.4(f)	28.0 (28.0)	39.0 (39.0)	$\theta_{AZ} = 2.8$ (3.0)	$\theta_{AZ} = 2.8$ (3.0)
7.5(b)	28.0 (28.0)	28.0 (28.0)	$\varphi_{EL} = -4.4$ (-4.5)	$\varphi_{EL} = 2.8$ (3.0)
7.5(d)	39.0 (39.0)	28.0 (28.0)	$\varphi_{EL} = 0.4$ (0.0)	$\varphi_{EL} = 4.0$ (4.0)
7.5(f)	39.0 (39.0)	39.0 (39.0)	$\varphi_{EL} = -4.0$ (-4.0)	$\varphi_{EL} = 2.8$ (3.0)
7.6	28.0 (28.0)	28.0 (28.0)	$\theta_{AZ} = -2.4$ (-2.5)	$\varphi_{EL} = 4.8$ (5.0)
7.7	39.0 (39.0)	39.0 (39.0)	$\theta_{AZ} = -2.4$ (-2.5)	$\varphi_{EL} = 4.4$ (4.5)

Table 7.1: Experimental k-space reconstruction results. Measured values are presented in plain text, and expected values are presented within parenthesis.

It is evident, based on the figures and the numerical results presented in Table 7.1, that the receiver reliably resolves emitters' AoAs and frequencies, within the system's angular and spectral resolutions, for both AoA directions. Consequently, the system provides capabilities necessary for efficient passive spatial-spectral monitoring of data sectors used in FD-MIMO. However, one key requirement necessary for spatial-spectral utilization mapping for 5G technology is low latency. Since all the experimental reconstructions were completed in a separate post-processing procedure, and the processing times are as high as 16s for a single plane, and 35s for the cross configuration, this need is not satisfied. The primary limiting factor in the current methodology is the large amount of weight-matrix data for each configuration, outlined in Table 7.2. To address this inherent limitation, compressive sensing (CS) techniques are explored in an effort to reduce the weight-matrix, and potentially eliminate the post-processing step. The development of adapting the traditional CS methodology to k-space tomography is presented in the next Chapter.

	Single Plane	Cross-Configuration	Full FOV
k-Points	5,763	11,525	293,913
Numerical Values	4.72×10^8	9.44×10^8	4.72×10^{10}
Memory Required	3.78 GB	7.55 GB	192.61 GB

Table 7.2: Weight-matrix size in terms of k-points, total numerical values, and required memory for three k-space regions. Each value was calculated based on the presented k-space imager resolutions and Nyquist sampling.

Chapter 8

COMPRESSIVE K-SPACE TOMOGRAPHY

Conveniently, due to the sparse nature of RF signals distributed within the field of view (FOV) of the array antenna, compressive sensing (CS) techniques can be leveraged to reconstruct spatial-spectral signal information with reduced latency. As in [171], traditional CS techniques are implemented to opportunistically compress the original k-space tomography problem. The basic notion of what will be referred to as traditional CS, is presented in the next section to set a foundation for compressive k-space tomography to build upon. To quantify the accuracy and latency reduction effects of the new CS application, numerical analysis is performed for various levels of compression, and scene sparsity. Finally, the compressive k-space tomography imaging modality is applied to experimental scenes for passive spatial-spectral utilization mapping at drastically reduced latencies.

8.1 Compressive Sensing

Conventional data acquisition of signals or images is subject to the Shannon/Nyquist sampling theorem that sets the sampling rate required to avoid information loss to be least twice that of the maximum detected frequency. Although particular sampling cases, namely non-naturally bandlimited images, are governed by factors such as spatial and/or temporal resolutions, antialiasing sampling inherently relies on this theorem as well. Consequently, an overabundance of redundant data is stored and processed.

A well-known method, referred to as CS, asserts this data acquisition inefficiency can be overcome through substantial under sampling due to the circumstance that the majority of signals can be categorized as sparse [172]–[175]. This principle of sparsity enables compression since the corresponding signal can be sparsely represented within an appropriate basis. In addition to this signal-related principle, CS requires the method of signal sensing to satisfy a principle of incoherence. By developing an incoherent sensing process, the information in the sparse basis representation is more likely to be preserved during dimensionality reduction. This procedure can be simply interpreted as an efficiently constructed sampling process that indirectly collects information pertaining to content of interest, allowing for computational reconstruction of the entire signal from a small amount of data.

To illustrate this concept, consider a raw signal or image vector, \mathbf{x} , as an $N \times 1$ column vector in \mathbb{R}^N , which can be represented in terms of an orthonormal basis expansion:

$$\mathbf{x} = \sum_{i=1}^N \alpha_i \psi_i = \Psi \boldsymbol{\alpha}, \quad (8.1)$$

where $\{\alpha_i\}$ is an $N \times 1$ column vector of weighting coefficients, $\alpha_i = \langle \mathbf{x}, \psi_i \rangle = \psi_i^T \mathbf{x}$, and $\{\psi_i\}_{i=1}^N$ are $N \times 1$ basis vectors that are assembled as columns in an $N \times N$ basis matrix $\Psi = [\psi_1 | \psi_2 | \dots | \psi_N]$. The signal, \mathbf{x} , is then deemed sparse, if it is comprised of a linear combination of only S basis vectors, and $S \ll N$. Accordingly, the space- or time-domain signal becomes compressible due to the fact that the equivalent Ψ -domain representation, $\boldsymbol{\alpha}$, contains S non-zero coefficients, and $(N - S)$ zero coefficients,

enabling a large fraction of the coefficients to be discarded without loss in signal reconstruction.

This principle that compressible signals can be expressed by S -sparse weighting coefficients is the foundation of transform coding. In this compression method, the entire N -sampled signal is acquired, and the weighting coefficients are subsequently calculated for the identification of the S largest coefficients. After discarding the remaining coefficients, S values and locations are adaptively encoded. Although this method allows for the reconstruction of the sparse signal with minimal losses, its implementation is fundamentally inefficient based on a required knowledge of all N coefficient values and their signal-dependent locations, even though $(N - S)$ are discarded.

Alternatively, CS utilizes a nonadaptive data acquisition mechanism to directly collect a compressed representation of the signal. This process is accomplished through a linear measurement of $M < N$ inner products of the signal, \mathbf{x} , and a set of measurement vectors, $\{\varphi_j\}_{j=1}^M$, to form the condensed representation $y_j = \langle \mathbf{x}, \varphi_j \rangle$. By compiling the signal measurements into an $M \times 1$ vector, \mathbf{y} , measurement vectors into an $M \times N$ measurement matrix, Φ , and substituting in Equation 8.1, the sensing signal can be expressed as

$$\mathbf{y} = \Phi \Psi \boldsymbol{\alpha}, \quad (8.2)$$

where $\Phi \Psi$ is an $M \times N$ matrix.

This process is simply a dimensionality reduction, and inherently results in a loss of information, as recovering \mathbf{x} from \mathbf{y} is ill-posed when $M < N$. However, by properly constructing Φ , the S -sparse signal \mathbf{x} can be recovered from \mathbf{y} measurements with a

reconstruction algorithm. One method of ensuring the problem no longer has an ill-posed solution is to design $\Phi\Psi$ to satisfy the restricted isometry property (RIP).

Unfortunately, both designing the matrix, and verifying that it adheres to the RIP, is a complex problem in itself. Therefore, Φ is commonly formulated as a pseudo-random matrix, allowing incoherence with the basis matrix, Ψ , and a high probability of satisfying the RIP. To this end, the elemental arrangements are often determined by Bernoulli or independent and identically distributed Gaussian distributions [172], [173], [175]. As a result, the pseudo-random measurement matrix can be subsequently utilized, along with the sparsifying basis and measurements made, to recover the $N \times 1$ signal vector.

In the next section, these CS principles and design factors are distinctly adapted to reconstruct sparse k-space scenes. While the methodology used to develop compressive k-space tomography differs in certain aspects, with respect to the general case presented above, the overall principles are unchanged. Therefore, fundamental terminology and component properties remain consistent in cases of similarity.

8.2 Compressive k-Space Tomography

While this current methodology has been successful for various k-space imaging receiver configurations, solving for a scene vector has been restricted to a post-processing routine, due to excessive algorithm completion times. The primary limiting factor here is the large weight-matrix comprised of an assembly of detected light intensity vectors for each point in the visible k-space, where the number of k-points is determined by Nyquist sampling of k-space according to the receiver's spatial and spectral resolutions. To put this limitation into perspective, consider the imaging receiver presented in the previous Chapters, which senses a k-space volume over a 20°

FOV in both azimuthal and elevation directions, and has an operation bandwidth of 14 GHz, i.e., 26 – 40 GHz. Based on the 60 cm aperture diameter, and the temporal apertures' effective 60 cm free-space path offset, the system possesses an angular resolution ranging from approximately $\theta_{min} = 0.874^\circ$ at 40 GHz to $\theta_{max} = 1.345^\circ$ at 26 GHz, and a spectral resolution of 250 MHz. If the entire k-space volume is sampled, formation of the weight matrix entails collecting and processing 256×320 pixel interferograms from over 290,000 k-points, leading to an impractical amount of time and computation resources necessary to reconstruct the k-space RF scene.

To surmount this momentous challenge, the sparse nature of the complex amplitude-weighted distributions can be leveraged in conjunction with CS techniques to reduce the overabundance of data. While the methods imposed to accurately reconstruct a scene vector from a k-space tomograph are fundamentally different from compression in a properly formed image, the manifest sparsity of the sensed RF environment directly transfers to the interference patterns present in both the weight-matrix \mathbf{A} , and detected light intensity vector \mathbf{P} , enabling compression of the corresponding pixel vectors. Realization of such a procedure entails adapting the CS process to accommodate the nature of k-space tomography and the components in the linear Equation 5.42. One key component controlling the modification is the Nyquist sampling of k-space, as properly sampling is pertinent to obtaining an accurate k-space reconstruction. Therefore, compression can only be applied to the pixel vectors in \mathbf{A} and \mathbf{P} . To this end, an incoherent measurement matrix is integrated into Equation 5.42 to reduce the pixel vectors only. By properly constructing a measurement matrix based on the principles discussed above, the length of the pixel vectors within \mathbf{A} and \mathbf{P} can be significantly reduced without losses in resolving the sparse scene.

In order to understand the adaptation of CS for k-space tomography, referred to as compressive k-space tomography, consider the integration of an $M \times N$ measurement matrix Φ in $\mathbb{R}^{M \times N}$ into Equation 5.42 as

$$\Phi \mathbf{P} = \Phi \mathbf{A} \mathbf{S}, \quad (8.3)$$

where the scene vector S is a $K \times 1$ column vector in \mathbb{R}^K , the weight matrix A is an $N \times K$ matrix in $\mathbb{R}^{N \times K}$, and the detected light intensity vector \mathbf{P} is an $N \times 1$ column vector in \mathbb{R}^N . Through a linear measurement of $M < N$ products of the measurement matrix with the weight matrix, and the detected light intensity vector, a condensed representation of Equation 5.42 is formulated as

$$\mathbf{P}_c = \mathbf{A}_c \mathbf{S}, \quad (8.4)$$

where the pixel vector lengths in \mathbf{A} and \mathbf{P} are reduced proportionally to the compression ratio M/N . Adhering to the aforementioned principles discussed, Φ is formulated as a pseudo-random matrix, allowing incoherence with the interferogram encoded pixel vectors in \mathbf{A} and \mathbf{P} . This compressed linear matrix equation can subsequently be solved using the Kaczmarz method to reconstruct the signal vector \mathbf{S} .

8.3 Numerical Analysis

To verify the effectiveness of compressive k-space tomography, the numerical model of the 30-element distributed-aperture k-space imager presented in Chapter 6 was utilized. Prior to characterizing compressive k-space tomography, it is important to formally revisit certain figures of merit and variable parameters pertaining to the Kaczmarz algorithm reconstruction process. The two figures of merit crucial to analyzing the effectiveness of the compressive techniques in the k-space imaging

modality are reconstruction error and time. For the purpose of this study, reconstruction error is defined by the percentage of sources resolved at the expected spatial-spectral positions within a tolerance set by the k-space resolution of the imaging system. In the case that there are less sources resolved than expected, the number of accurately detected sources is divided by number of expected sources and subtracted from the ideal of 1, e.g., 3 accurately resolved sources when 5 are expected equates to a reconstruction error of 0.4. In the case that there are more sources resolved than expected, the number of accurately detected sources is divided by total number of detected sources and subtracted from the ideal of 1, e.g., 5 accurately resolved sources with 10 total resolved equates to a reconstruction error of 0.5. Reconstruction time is simply the algorithm runtime.

One primary variable contributing to both reconstruction accuracy and time is the number of algorithm iterations. As expected, both of these figures of merit depend on the number of iterations; however, the number of iterations required to resolve a scene depends on the scene sparsity, as evident in Figure 6.10. This relation between signal distribution density and the number of required algorithm iterations serves as a baseline for signal vector reconstruction accuracy for a non-compressed system. Here, the number of iterations required to adequately reconstruct a scene was empirically derived to a cut-off point, indicated by a 1% variation between the previous and current iteration signal vectors. Defining this iteration cut-off is essential to properly analyzing effects of compressive k-space tomography due to the fact that, while lower iteration counts improve reconstruction time, less sparse signal distributions will not be resolvable below the non-compressed baseline.

For the compressive k-space tomography numerical analysis, a set of test RF source scenes were constructed, each with a different number of sources ranging from 1 to 30 emitters, i.e., a sparsity of $S = 1$ to $S = 30$, each with equal amplitude. The measurement matrix, Φ , is designed as a standard Gaussian distribution with a mean of zero and variance of one, $N(0,1)$, and the compression ratio, M/N , is swept from 0 to 1. Each set of scene is subsequently reconstructed at different algorithm iteration counts, and reconstruction error and time are calculated for each. The results of this study are presented in Figure 8.1.

In general, the principles discussed above remain consistent throughout the compression process. Reconstruction time scales linearly with respect to both number of iterations, and compression ratio, for each iteration value, as shown in Figure 8.1(a). Additionally, reconstruction error for decreasing sparsity of test scenes aligns with the requirement of increased iteration counts; however, the compression process further increased the iteration requirement when error is compared in Figure 8.1(b-d) to the cutoff point for non-compressed scenarios in Figure 6.10. Although the iteration count needs to be increased for less sparse scenes, each scene still remains compressible. Based on this relation, drastic improvements in reconstruction time are not guaranteed for all sparsity/compression ratio combinations. Nonetheless, the magnitude of data is consistently reduced, and provides a substantial advantage in cases where memory is limited. In the presented numerical analysis, all processing was completed on a standard desktop CPU. Implementation of accelerated hardware, namely an FPGA or GPU, opens potential for further reduction in reconstruction time based on the fact that solving Equation 8.4 primarily consists of linear algebra operations. This consideration aligns

with a concomitant goal of reducing collected data, to eliminate external memory-to-processor data transfer, which is attainable based on the results presented in Figure 8.1.

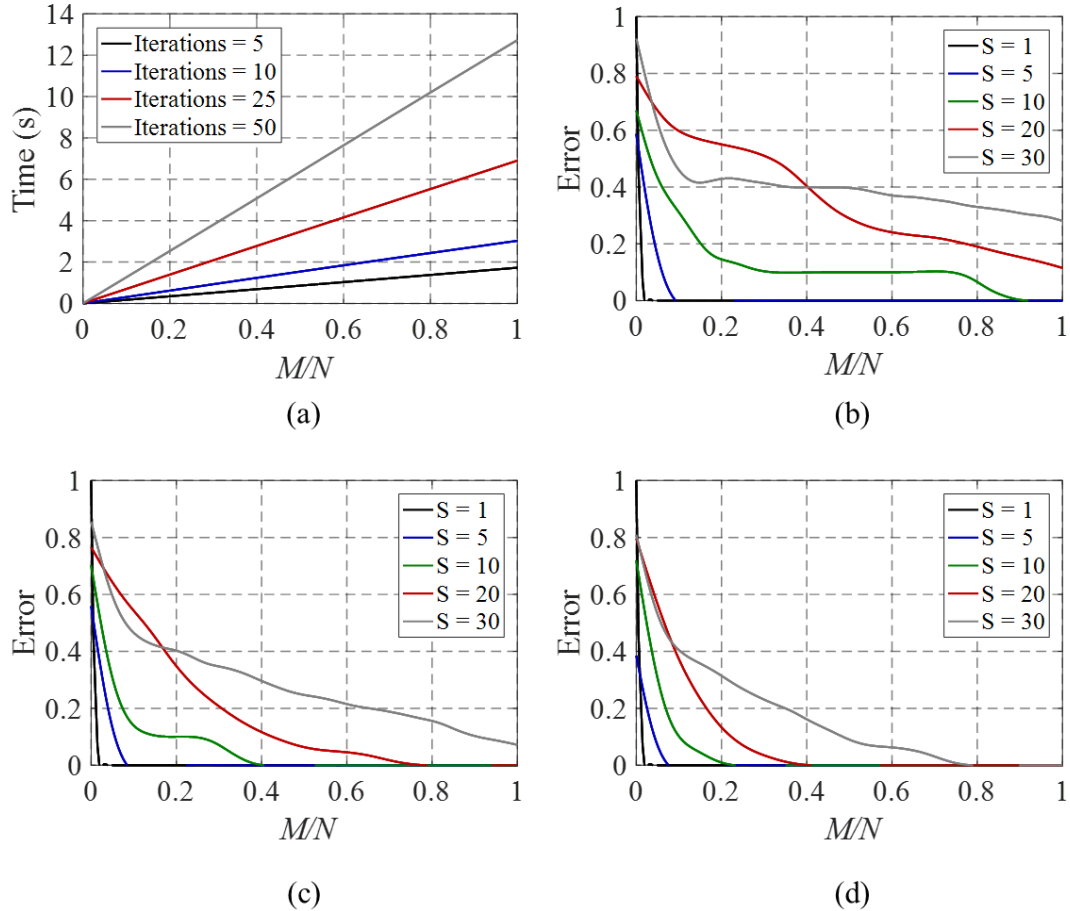


Figure 8.1: Numerical analysis results for compressive k-space tomography in terms of (a) reconstruction time as a function of compression ratio for different algorithm iteration counts, and reconstruction error as a function of compression ratio at different levels of sparsity for algorithm iteration counts of (b) 10 iterations, (c) 25 iterations, and (d) 50 iterations [171] © 2018 IEEE.

Furthermore, in practical operational scenarios, the sparsity of the complex amplitude-weighted distribution in k-space will not be known in advanced. While this may appear as a disadvantage, it actually introduces a level of flexibility in compression ratio and algorithm iteration scaling. To illustrate this flexibility, consider a scene of unknown sparsity. Initial collection and processing of the RF environment can be completed by solving the non-compressed Equation 5.42. In doing so, the scene sparsity will be calculated at the cost of frame-to-frame latency; however, the sparsity value can then be paired with known compressive k-space tomography metrics to readily optimize scalable compression ratios and algorithm iterations. This process provides a way to capitalize on the learned level of sparsity, advantageously reducing reconstruction time and memory requirements without loss of information. Such capability offers a significant benefit in less sparse scenes that prove to be more compressible, and affords remarkable improvements in reconstruction time without detriment to detection accuracy. More specifically, in the cases analyzed here, RF environments with a sparsity of 5 or less preserve an ideal accuracy while decreasing reconstruction times into the hundreds of milliseconds range, and in some cases, into the tens of milliseconds range.

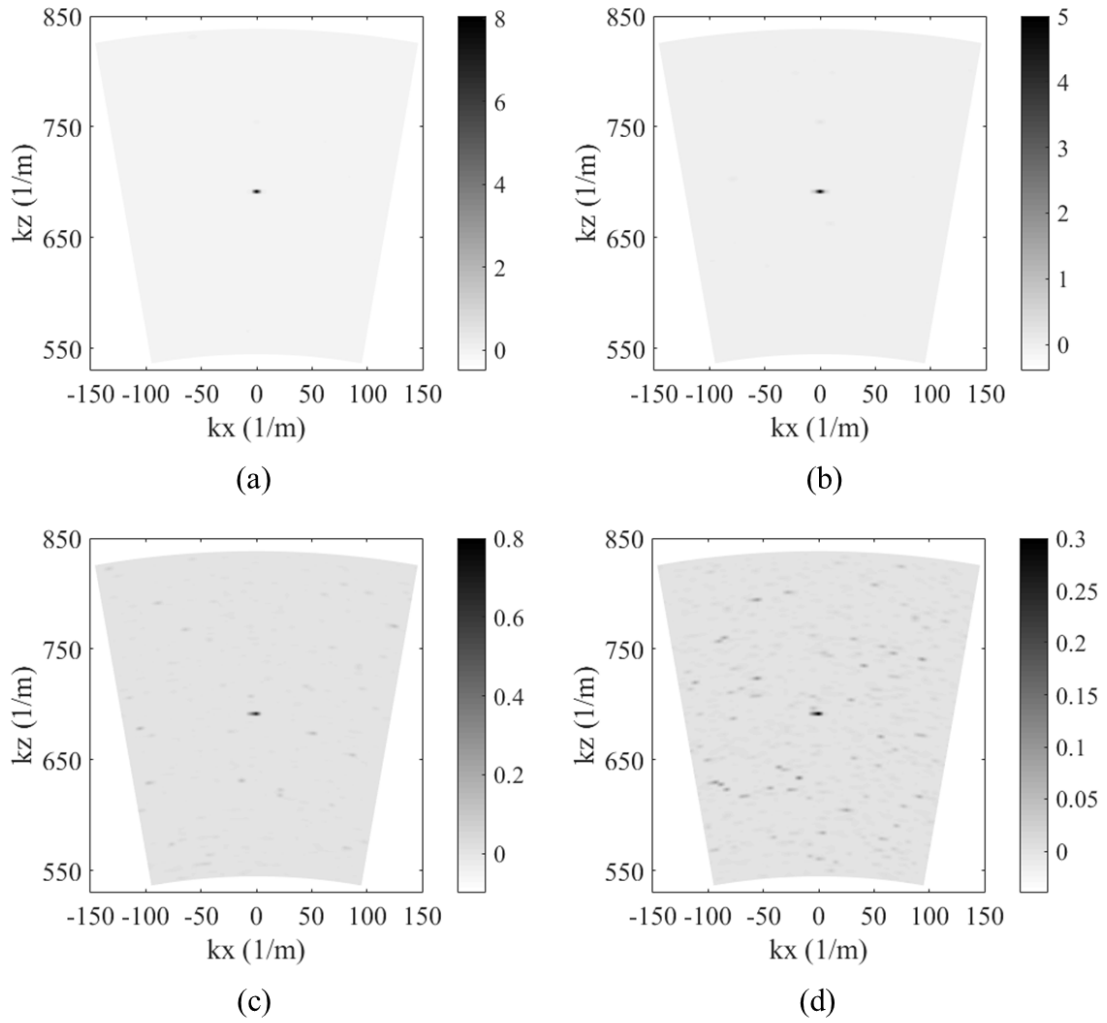


Figure 8.2: Numerical simulation reconstruction for a scene of sparsity $S = 1$, completed with 5 iterations of the Kaczmarz algorithm under different levels of compression. (a) Ideal non-compressed scene reconstruction completed with error = 0, and $t \approx 1.8$ s, (b) compressed scene with $M/N = 0.1$, error = 0, and $t \approx 195$ ms, (c) compressed scene with $M/N = 0.01$, error = 0, and $t \approx 22$ ms, and (d) compressed scene with $M/N = 0.005$, error = 0, and $t \approx 12$ ms. The colorbar in each pane corresponds to the intensity of a resolved source in arbitrary units [171] © 2018 IEEE.

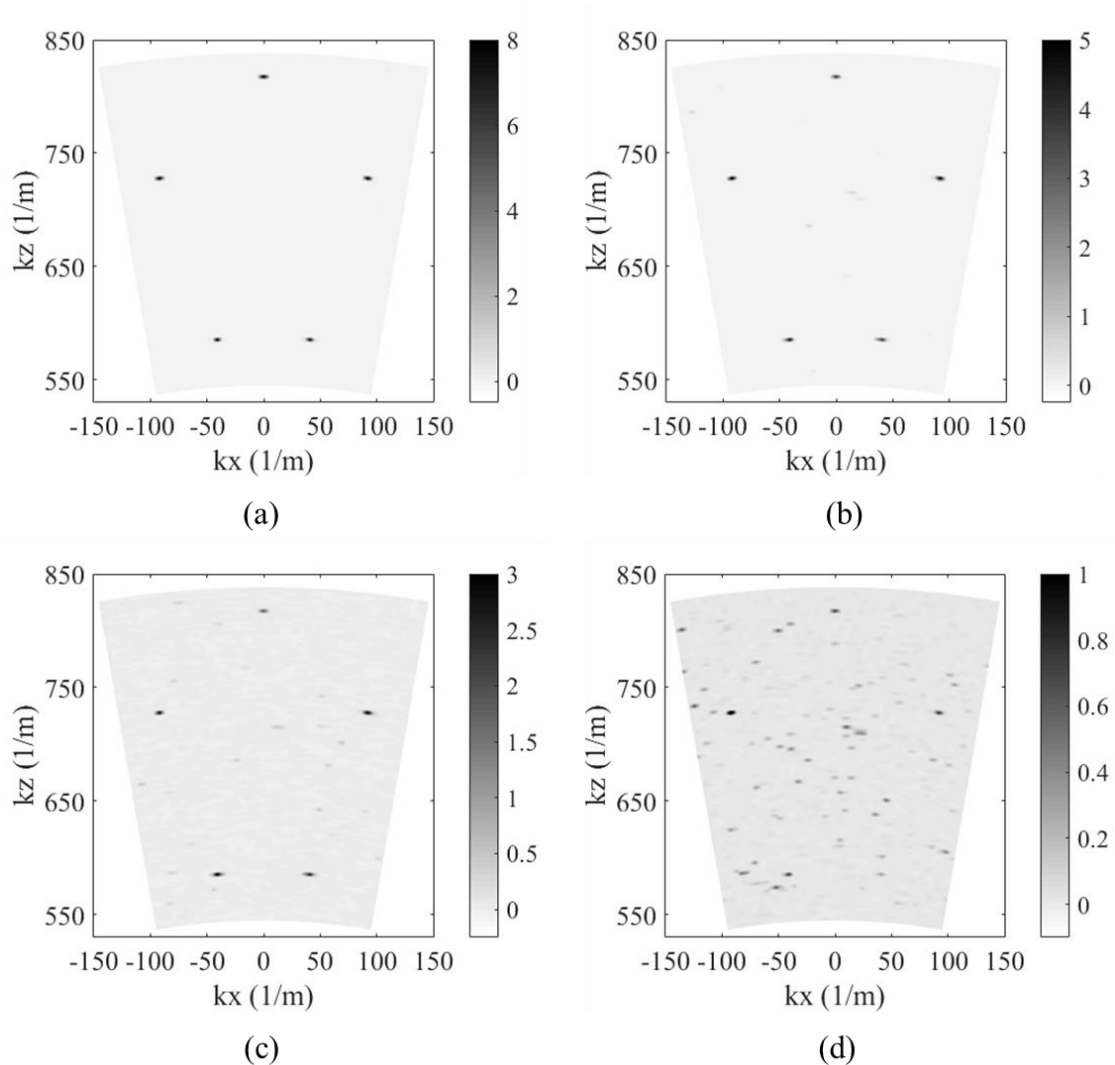


Figure 8.3: Numerical simulation reconstruction for a scene of sparsity $S = 5$, completed with 10 iterations of the Kaczmarz algorithm under different levels of compression. (a) Ideal non-compressed scene reconstruction completed with error = 0, and $t \approx 3.5$ s, (b) compressed scene with $M/N = 0.1$, error = 0, and $t \approx 350$ ms, (c) compressed scene with $M/N = 0.05$, error = 0, and $t \approx 180$ ms, and (d) compressed scene with $M/N = 0.01$, error = 0.5, and $t \approx 40$ ms. The colorbar in each pane corresponds to the intensity of a resolved source in arbitrary units [171] © 2018 IEEE.

Figures 8.2 and 8.3 illustrate these cases through example simulated reconstructions of single- and five-source scenes, respectively. In each figure, an ideal reference is provided in Figure 8.2(a) and Figure 8.3(a), where the non-compressed Equation 5.42 was solved to reconstruct complex amplitude-weighted distributions identical to the original scenes. The remaining reconstructions are solutions obtained through solving the compressed Equation 8.4, at compression ratios ranging from $M/N = 0.1$ to $M/N = 0.005$, with calculated error and time values for each. Accordingly, the single source scene is compressible down to 0.5% of the original size without loss of signal detection accuracy, and consequently results in a memory and reconstruction time decrease of the same percentage. This case defines the lower bound of the simulated model for each parameter as well, where reconstruction time is reduced to approximately 12 ms over the course of 5 iterations. Additionally, the five source scene is compressible to roughly 5% of its original size before suffering from loss of information, affording the equivalent reduction in memory needed, and a reconstruction time down to approximately 180 ms over the course of 10 iterations. Each of which, as mentioned, can be further decreased with optimal processing hardware.

8.4 Experimental Results

To further evaluate the compressive k-space tomography modality, the lessons learned from numerical simulations are applied to reconstructions of experimental source distributions. The system used for the characterization is the same two-dimensional distributed-aperture Ka-band k-space imaging receiver presented in Chapter 6, with the same system components and spatial-spectral resolutions described in the numerical analysis section, except the CCD detector array is 320×256 , rather than 100×100 . Furthermore, the experimental calibration process used to construct the

weight matrix is accomplished in the same manner as described in Chapter 7. The system is configured to sense a “cross” sub-space of k-space comprised of the $\pm 10^\circ$ azimuthal plane at 0° elevation, and the $\pm 10^\circ$ elevation plane at 0° azimuth, throughout an operational bandwidth of 26 – 40 GHz. Each plane is calibrated at Nyquist for the system’s angular and spectral resolution, i.e., 0.4° angular increments over $\pm 10^\circ$ and 125 MHz increments over 26 – 40 GHz at each angular position.

Upon completion of the calibration routine, 10-dBm RF emitters are organized along the azimuthal plane, or elevation plane, at a distance of 2 m from the antenna aperture. To accentuate the capabilities of spatial isolation and frequency detection for the new 5G wireless bands, scenes are organized with two, spatially separated, horn antennas emitting at 28 GHz, and/or 39.5 GHz. For each scene, unique interference patterns produced on the CCD camera are collected, compressed, and subsequently processed using the Kaczmarz algorithm, and calibration weight-matrix. Note, that while some may argue this process can be categorized more closely as transform coding rather than CS, based on the sample-then-compress procedure, the empirical investigation of compression feasibility and limits are more readily analyzed in this manner. In the future, this procedure can be adjusted to a traditional CS process, where a nonadaptive data acquisition process directly collects a compressed representation of the interferograms.

Reconstruction performance of compressive k-space tomography with the distributed aperture system is exemplified in Figure 8.4 and Figure 8.5, where all scenarios were solved using 5 iterations of the Kaczmarz algorithm. As with previous reconstructions, the detected AoA and frequency values for individual scenes are determined by locating k_x and k_z , or k_y , and k_z coordinates with a numerical peak

detection algorithm identifying local maxima within 3-dB of the maximum detected amplitude. Each coordinate position defines a polar vector in k-space that is subsequently converted to Cartesian coordinates, and AoA/frequency pairs with trigonometric equations and the relation $\omega = c|\mathbf{k}|$. Additionally, expected positions are denoted by black circles with a diameter equivalent to the k-space resolution of the imager. It is important to mention that for the spatial and temporal apertures integrated into this system, the resolution is approximately equal for k_x , k_y , and k_z , as the array diameter and temporal aperture's equivalent free-space path offset are both 60 cm.

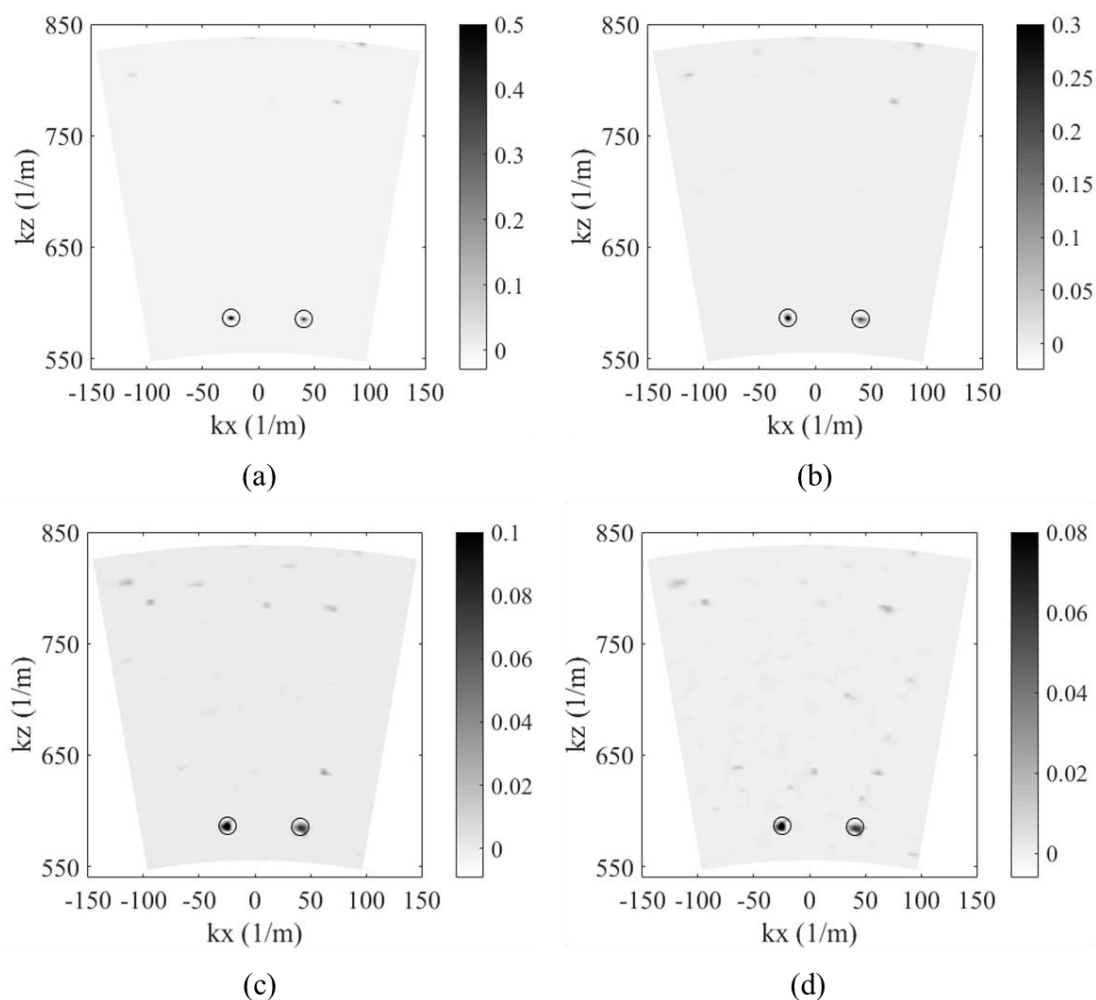


Figure 8.4: Experiment simulation reconstruction for a scene of sparsity, $S = 2$, with two 28 GHz sources positioned along the azimuthal plane at 0° elevation, with one at -2.5° and the other at 4.0° . (a) Ideal non-compressed scene reconstruction with sources at detected 28 GHz, -2.4° and 28 GHz, 4.0° in 17.06 s, (b) compressed scene with $M/N = 0.1$, and sources detected at 28 GHz, -2.4° and 28 GHz, 4.0° in 1.71 s, (c) compressed scene with $M/N = 0.01$, and sources detected at 28 GHz, -2.4° and 28 GHz, 4.0° in 185 ms, and (d) compressed scene with $M/N = 0.005$, and sources detected at 28 GHz, -2.4° and 28 GHz, 4.0° in 99 ms. Black dots are the reconstructed source in k-space, and circle centers indicate actual position of the emitter. The colorbar in each pane corresponds to the intensity of a resolved source in arbitrary units [171] © 2018 IEEE.

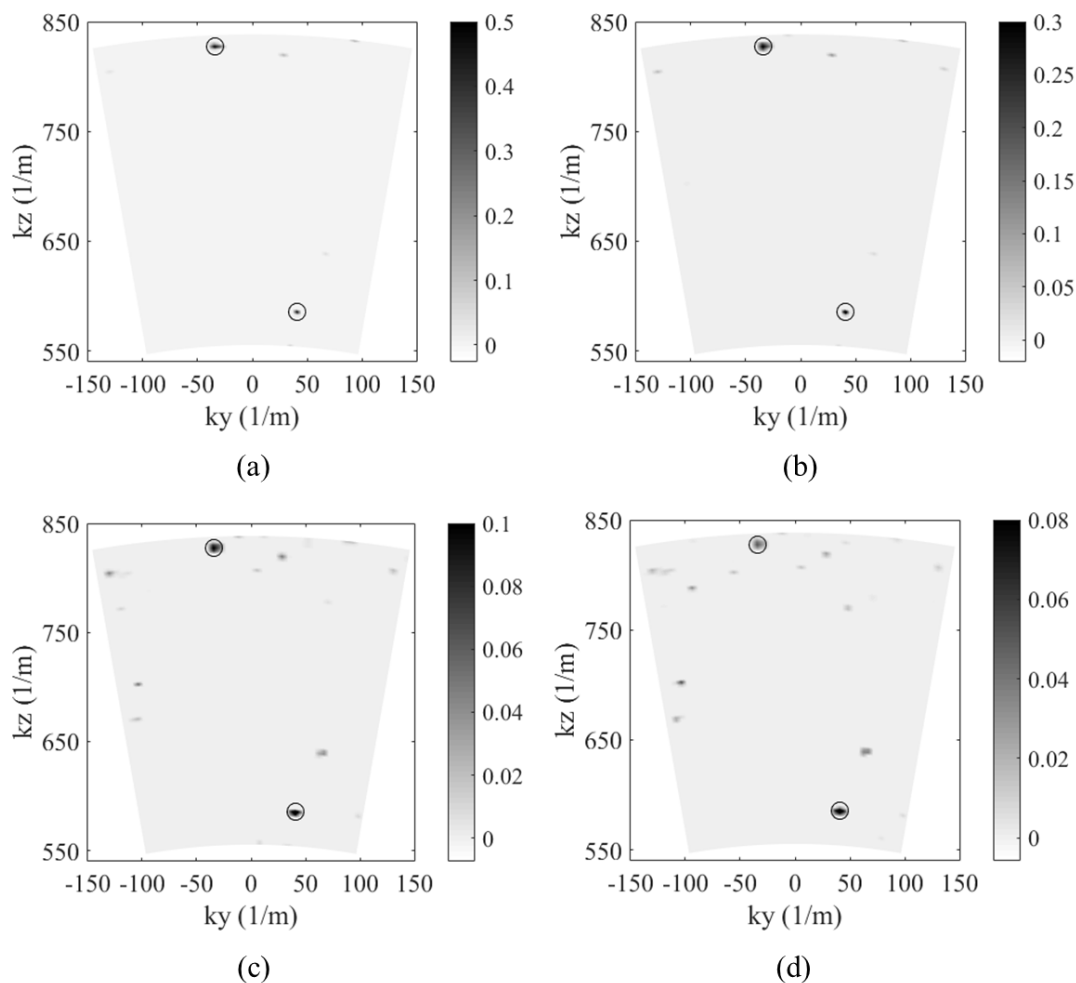


Figure 8.5: Experiment simulation reconstruction for a scene of sparsity, $S = 2$, with one 39.5 GHz source positioned at -2.5° along the elevation plane at 0° azimuth, and one 28 GHz source positioned at 4.0° along the elevation plane at 0° azimuth. (a) Ideal non-compressed scene reconstruction with sources at detected 39.5 GHz, -2.4° and 28 GHz, 4.0° in 17.62 s, (b) compressed scene with $M/N = 0.1$, and sources detected at 39.5 GHz, -2.4° and 28 GHz, 4.0° in 1.91 s, (c) compressed scene with $M/N = 0.01$, and sources detected at 39.5 GHz, -2.4° and 28 GHz, 4.0° in 181 ms, and (d) compressed scene with $M/N = 0.005$, and sources detected at 39.5 GHz, -2.4° and 28 GHz, 4.0° in 105 ms. Black dots are the reconstructed source in k-space, and circle centers indicate actual position of the emitter. The colorbar in each pane corresponds to the intensity of a resolved source in arbitrary units [171] © 2018 IEEE.

Figure 8.4 comprises reconstructions for a scene consisting of two 28 GHz sources positioned along the azimuthal plane at 0° elevation, with one at -2.5° and the other at 4.0° . In Figure 8.4(a), a non-compressed scene reconstruction is provided as a reference, and was resolved in 17.06 s. The remaining figures, Figure 8.4(b-d) are reconstructions performed with an applied measurement matrix with a standard Gaussian distribution $\mathcal{N}(0,1)$, and compression ratios of $N/M = 0.1$, $N/M = 0.01$, and $N/M = 0.005$, respectively. In all cases, the signals were accurately resolved, and calculated to be emitting at 28 GHz, with AoAs of -2.4° and 4° . In the most compressed state, prior to inaccuracies in detection, the reconstruction was completed in 99 ms, affording an improvement in reconstruction time by a factor of approximately 172.

Figure 8.5 comprises reconstructions for a scene consisting of one 39.5 GHz source positioned at -2.5° along the elevation plane at 0° azimuth, and one 28 GHz source positioned at 4.0° along the elevation plane at 0° azimuth. As before, Figure 8.5 (a), a non-compressed scene reconstruction is provided as a reference, and was resolved in 17.62 s. The remaining figures, Figure 8.5(b-d) are reconstructions performed with the same measurement matrix, and compression ratios of $N/M = 0.1$, $N/M = 0.01$, and $N/M = 0.005$, respectively. These signals also were accurately resolved, and calculated to be emitting at 39.5 GHz with an AoA of -2.4° and 28 GHz with an AoA of 4.0° . In the most compressed state, the reconstruction was completed in 105 ms, affording an improvement in reconstruction time by a factor of approximately 167.

8.5 Conclusion

The traditional CS methodology was adapted to the newly developed imaging modality, k-space tomography. Numerical analysis was utilized to show that the inherently sparse nature of the complex amplitude-weighted distributions enables the

use of a standard Gaussian measurement matrix to reduce the overabundance of data without loss of information. In doing so, relations between compression ratio and reconstruction time, and compression ratio and reconstruction error were determined for scenes of different sparsity with respect to increasing Kaczmarz algorithm iteration counts. These relations were subsequently applied to experimental RF source distributions to validate compressive k-space tomography for spatial-spectral utilization mapping, within newly allocated 5G bands, between 28 and 40 GHz. Application of this method resulted in accurate scene reconstructions with data reductions greater than a factor of 100, and greater than 200 for the known equal-amplitude signal environments. Consequently, reconstruction time was simultaneously reduced by a factor of over 165 in the most compressed states. It is expected that these significant improvements can be used to extend the reduced reconstruction time even further through the implementation of accelerated hardware components. Overall, compressive k-space tomography serves as an appealing technology for imaging spatial-spectral utilization at reduced latencies.

Chapter 9

CONCLUSION

9.1 Summary

With wireless communication networks set to undergo a new phase of transformation during the deployment of 5G wireless technology, system design considerations have been drastically reconfigured. More specifically, the adaptation of MIMO technology for mmW frequency operation in UDNs at a massive scale shifts focus to multi-beam phased array systems as a critical component in the development process. As a result, next generation phased array and beamforming network designs will need to be highly integrated, fast scanning apertures capable of dynamically supporting multiple users. Furthermore, these units must be able to monitor user-space with fine phase resolution for low latency beam channel optimization. To satisfy these requirements, the research presented here leveraged RF photonics to enable the development of two novel aperture designs.

The first RF photonic aperture consisted of a highly integrated photodiode-coupled phased array transmit antenna. In Chapter 2, existing electronic UWB phased array antenna technology, and the corresponding fundamental limitations in coaxial cable feeding were discussed. The method of optical excitation was subsequently described through recent developments in high-power CC-MUTC photodiodes, along with a wideband RF photonic source and analog phase network. By integrating this technology with a properly designed connect-array antenna, the inherent light weight,

low profile, and EMI immune optical fibers allow remote deployment of UWB, wide-scanning phased arrays.

Throughout Chapters 3 and 4, two novel photodiode-integrated CA antennas for an operational bandwidth of 5 – 20 GHz were discussed in detail [141], [176]. The CA was designed in an infinite model configuration using full-wave simulations that included all relevant antenna and optical components, and was accompanied by a photodiode circuit model. From the infinite array design, two photodiode-integrated CA antennas were fabricated and characterized. The first wideband, optically-fed CA antenna, was excited with 4 high-power CC-MUTC photodiodes. Calibrated measurements of this array indicated the 3-dB bandwidth of 7 – 17 GHz, or 2.4:1, and compared favorably to the CA antenna model. In addition to this, broadside beam forming was demonstrated at EIRPs greater than 15 dBm over this bandwidth. The second design was 1-D CA antenna array consisting of eight photodiode-coupled active dipole elements. Introduction of a miniature optical prism into the fiber optic feed enabled an efficient 90° coupling to a high-power CC-MUTC photodiode integrated directly at the feed point of the CA antenna elements, and significantly reduced the array profile. The experimentally verified array achieved effective beamforming and beam steering over a 3-dB bandwidth of 6–17 GHz, as well as a peak effective isotropic radiated power of 27.5 dBm at 13 GHz.

The second RF photonic aperture was a receiver comprised of a distributed-aperture phased array coupled to an optical fiber, temporal aperture for imaging of k-space. In Chapter 5, the term k-space and the spatial-spectral processing fundamentals were described. More specifically, the analog spatially coherent optical up-conversion process that preserves amplitude and phase information of incident wavefronts was

presented in depth, and further discussed in terms of RF image reconstruction. This was followed by novel temporal processing components, and the development of the new imaging modality, k-space tomography, for passive high phase resolution spatial-spectral utilization mapping of user-space.

In Chapters 6 and 7, a novel 2D distributed-aperture k-space imaging system was designed and fabricated to enable a full-dimensional reconstruction of RF emitters operating within the newly allocated 5G bands between 28 and 40 GHz [177]. Furthermore, experimental results demonstrate that azimuthal and elevation AoAs, along with frequency, can be simultaneously determined for multiple emitters at accuracies defined by the system's resolution parameters. Consequently, the system provides capabilities necessary for efficient passive spatial-spectral monitoring of data sectors used in MIMO.

In Chapter 8, the traditional CS methodology was adapted to k-space tomography to enable low latency spatial-spectral mapping [171]. Numerical analysis was utilized to show that the inherently sparse nature of the complex amplitude-weighted distributions allows the use of a standard Gaussian measurement matrix to reduce the overabundance of data without loss of information. In doing so, relations between compression ratio and reconstruction time, and compression ratio and reconstruction error were determined for scenes of different sparsity with respect to increasing Kaczmarz algorithm iteration counts. These relations were subsequently applied to experimental RF source distributions to validate compressive k-space tomography for spatial-spectral utilization mapping. Application of this method resulted in accurate scene reconstructions with data reductions greater than a factor of 100, and greater than 200 for the known equal-amplitude signal environments.

Consequently, reconstruction time was simultaneously reduced by a factor of over 165 in the most compressed states. Overall, compressive k-space tomography serves as an appealing technology for imaging spatial-spectral utilization at reduced latencies.

The original contributions as a result of this work are more concisely presented as follows:

- Design, fabrication, and demonstration of first ever CC-MUTC integrated CA antenna
- Design, fabrication, and demonstration of low-profile optical feeding technique for CC-MUTC integrated CA antenna
- 2D distributed-aperture k-space imaging receiver numerical model
- Design and fabrication of first ever 2D distributed-aperture k-space imaging receiver
- First ever demonstration of 3D k-space tomographic reconstruction
- Formulation of compressive k-space tomography
- First ever demonstration of numerical and experimental compressive k-space tomographic reconstruction

Peer Reviewed Journal Publications:

1. **D. D. Ross**, J. Murakowski, C. J. Ryan, G. J. Schneider, and D. W. Prather, "Compressive k-Space Tomography," in *Journal of Lightwave Technology*, vol. PP, no. 99, pp. 1–9, 2018.
2. **D. D. Ross**, C. J. Ryan, G. J. Schneider, J. Murakowski and D. W. Prather, "Passive Three-Dimensional Spatial-Spectral Analysis Based on k-Space Tomography," in *IEEE Photonics Technology Letters*, vol. PP, no. 99, pp. 1-1.
3. M. R. Konkol, **D. D. Ross**, S. Shi, C. E. Harrity, A. A. Wright, C. A. Schuetz, and D. W. Prather, "Photonic Tightly Coupled Array," in *IEEE Transactions on Microwave Theory and Techniques*, vol. PP, no. 99, pp. 1-9.

4. D.W. Prather, S. Shi, G. J. Schneider, P. Yao, C. Schuetz, J. Murakowski, J. C. Deroba, F. Wang, M. R. Konkol, and **D. D. Ross**, "Optically-Upconverted, Spatially-Coherent Phased Array Antenna Feed Networks for Beam-Space MIMO in 5G Cellular Communications," in *IEEE Transactions on Antennas and Propagation*, vol. 65, no. 12, pp. 6432-6443, Dec. 2017.
5. **D. D. Ross**; M. R. Konkol; S. Shi; C. E. Harrity; A. A. Wright; C. A. Schuetz; D. W. Prather, "Low-Profile, High-Power Optically Addressed Phased Array Antenna," in *Journal of Lightwave Technology*, vol. 35, no. 18, pp. 3894-3900, Sept. 15 2017.
6. M. R. Konkol, **D. D. Ross**, K. P. Shreve, C. E. Harrity, S. Shi, C. A. Schuetz, and D. W. Prather, "High-Power, Aperture Coupled Photonic Antenna," in *IEEE Photonics Technology Letters*, vol. 29, no. 14, pp. 1207-1210, July 15 2017.
7. M. R. Konkol, **D. D. Ross**, S. Shi, C. E. Harrity, A. A. Wright, C. A. Schuetz, and D. W. Prather, " High-Power Photodiode-Integrated-Connected Array Antenna," in *Journal of Lightwave Technology*, vol. 35, no. 10, pp. 2010-2016, May 15 2017.
8. D. L. K. Eng, S. T. Kozacik, I. V. Kosilkin, J. P. Wilson, **D. D. Ross**, S. Shi, L. Dalton, B. C. Olbricht, and D. W. Prather, "Simple Fabrication and Processing of an All-Polymer Electrooptic Modulator," in *IEEE Journal of Selected Topics in Quantum Electronics*, vol. 19, no. 6, pp. 190-195, Nov.-Dec. 2013.

Conference Publications and Presentations:

1. **D. D. Ross**, J. Murakowski, G. J. Schneider, S. Shi, C. A. Schuetz, and D. W. Prather, "RF Imaging Receiver Based on k-Space Tomography," *2017 IEEE Avionics and Vehicle Fiber-Optics and Photonics Conference (AVFOP)*, New Orleans, LA, 2017, pp. 9-10.
2. **D. D. Ross**, M. R. Konkol, S. Shi and D. W. Prather, "Integrated photodiode feeds for conformal UWB phased array antenna," *2016 IEEE International Topical Meeting on Microwave Photonics (MWP)*, Long Beach, CA, 2016, pp. 215-216. **(Invited)**
3. D. W. Prather, J. Murakowski, G. J. Schneider, S. Shi, C. Schuetz and **D. D. Ross**, "k-Space tomography for spatial-spectral monitoring in cellular networks," *2017 IEEE MTT-S International Microwave Symposium (IMS)*, Honolulu, HI, 2017, pp. 1162-1164.
4. **D. D. Ross**, M. R. Konkol, C. E. Harrity, S. Shi, P. Yao, C. A. Schuetz, and D. W. Prather, "Integrated photodiode feeds for conformal UWB phased array

antenna," *2016 IEEE International Topical Meeting on Microwave Photonics (MWP)*, Long Beach, CA, 2016, pp. 215-216. **(Invited)**

5. **D. D. Ross**, M. R. Konkol, S. Shi and D. W. Prather, "Optically Addressed Ultra-Wideband Connected Array Antenna," *2016 International Workshop on Antenna Technology (iWAT)*, Cocoa Beach, FL, 2016, pp. 207-210. (Invited)
6. D. L. K. Eng, S. T. Kozacik, J. P. Wilson, **D. D. Ross**, S. Shi, B. C. Olbricht, and D. W. Prather, "Simply fabricated all polymer electro-optic modulator," *2013 IEEE Photonics Conference*, Bellevue, WA, 2013, pp. 30-31.
7. B. C. Olbricht, D. L. K. Eng, S.T. Kozacik, **D.D. Ross**, and D. W. Prather; "Processing of organic electro-optic materials: solution-phase assisted reorientation of chromophores." Proc. SPIE 8622, Organic Photonic Materials and Devices XV, 86220U (March 6, 2013).

9.2 Future Work

Since the development of spatially-coherent RF photonic phased arrays is a relatively new discipline there is vast potential for implementation into wireless communications applications. Consequently, several intriguing research avenues exist for each RF photonic aperture.

9.2.1 RF Photonic Transmit Apertures

For the transmit side, there are three primary areas the author thinks should be investigated. The first two relate to the phased array antenna design, while the third deals with reconfiguring the phase feed network.

9.2.1.1 mmW Photonic Phased Arrays

Both the CA antennas presented within this dissertation, as well as the photodiode-coupled TCA [178] and aperture coupled patch antenna [179] developed throughout this research, have collectively focused on operating between approximately 5 – 22 GHz. Based on the newly allocated 5G bands, for this technique to truly be considered for next generation wireless networks, it is imperative to demonstrate the

capabilities at higher frequencies. From the antennas mentioned, there are two routes that contain reasonable paths toward sufficient mmW operation within the continually reiterated requirements. The first is to introduced a dual, or stack patch configuration to cover multiple 5G operational bandwidths. Between the demonstration of 33 dBm EIRP at 22 GHz in [179], and the coplanar patch antenna demonstration of 22 dBm at 60 GHz [122], CC-MUTC integration into a dual-band is reasonable and valuable to the field. The second route involves the TCA. From the literature review of TCAs in Chapter two, it is evident that this type of antenna serves as the most appealing device in terms of operational bandwidth, scan angle, and SWaP. If properly designed, a high-element count mmW photonic TCA should be able to achieve a 6:1 bandwidth, i.e., operated through all 5G bands between 10 – 60 GHz. Furthermore, the low-profile optical integration approach utilized in [176], can be easily implemented at these higher frequencies without the use of custom parts.

9.2.1.2 Scalable Integration

Currently, the largest active-element photonic CA antenna demonstrated was an 8-element 1D array. For practical implementation, based on 5G demands, the number of active elements needs to be orders of magnitude larger. The primary limiting factor at the moment, is the single element integration process, where each component was positioned by hand. Thus, to expand active element counts, this process needs to be replaced. An alternative method may entail fabricating all of the CC-MUTC photodiodes in the respective TCA antenna input grid, and flip-chip bonding the entire substrate to the AlN antenna.

In order for this method to be effective, the dielectric constant of the photodiode substrate must be reduced. This can be accomplished in two ways: 1) thin the CC-

MUTC photodiodes, which are based on an InP platform with a dielectric constant of $\epsilon_r = 12.5$, or 2) introduce a different thermally conductive material as the antenna substrate, i.e. diamond has a dielectric constant of $\epsilon_r = 5.7$. While a substrate integration process improves the scalability, it is only half of the problem, as optical fibers still need to be aligned to each photodiode. Consequently, a substrate-based optical alignment array needs to accompany the photodiode array in the form of a photonic lightwave circuit, or simple V-groove array.

9.2.1.3 Photonic Feed Network

Throughout this dissertation, the RF photonic transmit aperture was coupled to an analog phase feed network. While photonic techniques offer different capabilities in comparison to purely electronic counterparts, the active analog phase shifting network shares the same limitations as presented in Chapter 1. To increase the number of beams produced by the presented architecture, the number of TOPS or phase modulators needs to be increased which is extremely expensive. However, there is an alternative approach that closely resemble the hybrid multi-beam systems previously mentioned.

That is to create a transmit architecture similar to the receiver's optical processor unit. This would entail digital encoding of in-phase and quadrature information onto the mmW carrier within N optical fiber feed channels, which would be truncated at a fiber array. The amplitude and phase information within each channel subsequently emanates out of each fiber, through a lens, and is collected at another fiber array to be conveyed to the antenna elements. In this configuration, only one, small lens is required for beamforming, and only one TOPS is needed. Furthermore, the number of DACs is depended on the number of occupants in the spatial-spectral region, and the number of

antennas is approximately the number of data feeds, but is not required to be the same in all cases.

9.2.2 RF Photonic Receive Apertures

Due to the bulk of k-space tomography development residing within the past two years, there are a substantial amount of research possibilities. However, the author will instead focus on the two most important areas for exploration.

9.2.2.1 Sparse Calibration

As mentioned, faithful k-space reconstructions require calibrating the system with known sources, sampled at Nyquist of the resolution limit set by the physical size of the aperture and the fiber-length dispersion. Consequently, probing the entire k-space through mechanical AoA sweeping with concurrent electronic frequency sweeping of the source is a cumbersome and time-consuming process. However, there are indications that a reduced number of judiciously chosen calibration points may suffice to produce the full weight matrix. One method of accomplishing this task may be leveraging machine learning algorithms to compute a calibration matrix based on *a priori* knowledge of the system response.

9.2.2.2 Accelerated Processing Hardware

In a practical system, unique interference patterns encoded with spatial-spectral data from the user-space needs to be processed at a low latency. Recent development of compressive k-space tomography have enables substantial reduction in data sized and processing time; however, the processing time still remains in the hundreds of milliseconds range. In most cases, further accelerating this processing requires integrating expensive hardware for accelerated processing. Conversely, in this case, the

data processing is comprised of almost entirely linear matrix operations, making processing units such as FPGAs and GPUs ideal candidates to aid progress towards real-time spatial-spectral monitoring. Furthermore, large reduction in data size enables the entire weight-matrix to be stored in the accelerated processing unit to maximize the computing efficiency by eliminating the need for external memory transfer. Based on existing GPU technology, it is expected that the processing time can be reduced by over a factor of 10, resulting in millisecond scale latencies.

REFERENCES

- [1] M. I. Skolnik, *Radar Handbook, Third Edition*. McGraw-Hill Education, 2008.
- [2] R. M. Page, “The Early History of Radar,” *Proceedings of the IRE*, vol. 50, no. 5, pp. 1232–1236, May 1962.
- [3] C. A. Fowler, “Old Radar Types Never Die; They just Phased Array or ... 55 Years of Trying to Avoid Mechanical Scan,” *IEEE Aerospace and Electronic Systems Magazine*, vol. 13, no. 9, p. 24A–24L, Sep. 1998.
- [4] J. L. Allen, “Phased Array Radar Studies, 1 July 1961 to 1 January 1963,” *MIT Lincoln Laboratories, Tech. Rep. 299*, Feb. 1963.
- [5] J. L. Allen, “Phased Array Radar Studies, 1 January 1963 to 1 July 1964,” *MIT Lincoln Laboratories, Tech. Rep. 381*, Mar. 1965.
- [6] G. C. Tavik *et al.*, “The advanced multifunction RF concept,” *IEEE Transactions on Microwave Theory and Techniques*, vol. 53, no. 3, pp. 1009–1020, Mar. 2005.
- [7] “MACOM - Phased Array Antennas & The Roadmap to 5G Wireless.” [Online]. Available: <https://www.macom.com/blog/phased-array-antennas--the-roadm>. [Accessed: 08-Mar-2018].
- [8] T. S. Rappaport, *Wireless Communications: Principles and Practice*, 2 edition. Upper Saddle River, N.J: Prentice Hall, 2002.
- [9] F. Hillebrand, “The creation of standards for global mobile communication: GSM and UMTS standardization from 1982 to 2000,” *IEEE Wireless Communications*, vol. 20, no. 5, pp. 24–33, Oct. 2013.
- [10] A. Osseiran *et al.*, “Scenarios for 5G mobile and wireless communications: the vision of the METIS project,” *IEEE Communications Magazine*, vol. 52, no. 5, pp. 26–35, May 2014.
- [11] S. Chen and J. Zhao, “The requirements, challenges, and technologies for 5G of terrestrial mobile telecommunication,” *IEEE Communications Magazine*, vol. 52, no. 5, pp. 36–43, May 2014.
- [12] “Forging Our 5G Future,” *Federal Communications Commission*, 15-Sep-2016. [Online]. Available: <https://www.fcc.gov/5G>. [Accessed: 08-Mar-2018].
- [13] E. G. Larsson, O. Edfors, F. Tufvesson, and T. L. Marzetta, “Massive MIMO for next generation wireless systems,” *IEEE Communications Magazine*, vol. 52, no. 2, pp. 186–195, Feb. 2014.
- [14] J. Brady, N. Behdad, and A. M. Sayeed, “Beam-space MIMO for Millimeter-Wave Communications: System Architecture, Modeling, Analysis, and Measurements,” *IEEE Transactions on Antennas and Propagation*, vol. 61, no. 7, pp. 3814–3827, Jul. 2013.

- [15] “Webinar: Analog Beamforming—What is it and How Does it Impact Phased-Array Radar and 5G? - pSemi.” [Online]. Available: <http://www.psemi.com/newsroom/psemi-university/265032-webinar-analog-beamforming-what-is-it-and-how-does-it-impact-phased-array-radar-and-5g>. [Accessed: 08-Mar-2018].
- [16] D. Parker and D. C. Zimmermann, “Phased arrays - part 1: theory and architectures,” *IEEE Transactions on Microwave Theory and Techniques*, vol. 50, no. 3, pp. 678–687, Mar. 2002.
- [17] G. W. Kant, P. D. Patel, S. J. Wijnholds, M. Ruiter, and E. van der Wal, “EMBRACE: A Multi-Beam 20,000-Element Radio Astronomical Phased Array Antenna Demonstrator,” *IEEE Transactions on Antennas and Propagation*, vol. 59, no. 6, pp. 1990–2003, Jun. 2011.
- [18] M. Sayginer and G. M. Rebeiz, “An Eight-Element 2 #x2013;16-GHz Programmable Phased Array Receiver With One, Two, or Four Simultaneous Beams in SiGe BiCMOS,” *IEEE Transactions on Microwave Theory and Techniques*, vol. 64, no. 12, pp. 4585–4597, Dec. 2016.
- [19] D. Parker and D. C. Zimmermann, “Phased arrays-part II: implementations, applications, and future trends,” *IEEE Transactions on Microwave Theory and Techniques*, vol. 50, no. 3, pp. 688–698, Mar. 2002.
- [20] S.-S. Jeon, Y. Wang, Y. Qian, and T. Itoh, “A novel smart antenna system implementation for broad-band wireless communications,” *IEEE Transactions on Antennas and Propagation*, vol. 50, no. 5, pp. 600–606, May 2002.
- [21] E. Lier and R. Melcher, “A Modular and Lightweight Multibeam Active Phased Receiving Array for Satellite Applications: Design and Ground Testing,” *IEEE Antennas and Propagation Magazine*, vol. 51, no. 1, pp. 80–90, Feb. 2009.
- [22] W. Aerts, P. Delmotte, and G. A. E. Vandenbosch, “Conceptual Study of Analog Baseband Beam Forming: Design and Measurement of an Eight-by-Eight Phased Array,” *IEEE Transactions on Antennas and Propagation*, vol. 57, no. 6, pp. 1667–1672, Jun. 2009.
- [23] J. Schoebel, J. Schueuer, R. Caspary, J. Schmitz, and M. Jung, “A true-time-delay phase shifter system for ultra-wideband applications,” in *German Microwave Conference*, 2008, pp. 1–4.
- [24] P. Chen, W. Hong, H. Zhang, J. Chen, H. Tang, and Z. Chen, “Virtual Phase Shifter Array and Its Application on Ku Band Mobile Satellite Reception,” *IEEE Transactions on Antennas and Propagation*, vol. 63, no. 4, pp. 1408–1416, Apr. 2015.
- [25] A. Natarajan, A. Komijani, X. Guan, A. Babakhani, and A. Hajimiri, “A 77-GHz Phased-Array Transceiver With On-Chip Antennas in Silicon: Transmitter and Local LO-Path Phase Shifting,” *IEEE Journal of Solid-State Circuits*, vol. 41, no. 12, pp. 2807–2819, Dec. 2006.
- [26] H. Hashemi, X. Guan, A. Komijani, and A. Hajimiri, “A 24-GHz SiGe phased-array receiver-LO phase-shifting approach,” *IEEE Transactions on Microwave Theory and Techniques*, vol. 53, no. 2, pp. 614–626, Feb. 2005.

- [27] J. Litva and T. K. Lo, *Digital Beamforming in Wireless Communications*, 1st ed. Norwood, MA, USA: Artech House, Inc., 1996.
- [28] H. Steyskal, "Digital beamforming antennas - An introduction," *Microwave Journal*, vol. 30, p. 107, Jan. 1987.
- [29] C. Fulton, M. Yeary, D. Thompson, J. Lake, and A. Mitchell, "Digital Phased Arrays: Challenges and Opportunities," *Proceedings of the IEEE*, vol. 104, no. 3, pp. 487–503, Mar. 2016.
- [30] L. Zhang, A. Natarajan, and H. Krishnaswamy, "Scalable Spatial Notch Suppression in Spatio-Spectral-Filtering MIMO Receiver Arrays for Digital Beamforming," *IEEE Journal of Solid-State Circuits*, vol. 51, no. 12, pp. 3152–3166, Dec. 2016.
- [31] P. Xingdong, H. Wei, Y. Tianyang, and L. Linsheng, "Design and implementation of an active multibeam antenna system with 64 RF channels and 256 antenna elements for massive MIMO application in 5G wireless communications," *China Communications*, vol. 11, no. 11, pp. 16–23, Nov. 2014.
- [32] W. Hong *et al.*, "Multibeam Antenna Technologies for 5G Wireless Communications," *IEEE Transactions on Antennas and Propagation*, vol. 65, no. 12, pp. 6231–6249, Dec. 2017.
- [33] O. E. Ayach, S. Rajagopal, S. Abu-Surra, Z. Pi, and R. W. Heath, "Spatially Sparse Precoding in Millimeter Wave MIMO Systems," *IEEE Transactions on Wireless Communications*, vol. 13, no. 3, pp. 1499–1513, Mar. 2014.
- [34] S. Han, C. I I, Z. Xu, and C. Rowell, "Large-scale antenna systems with hybrid analog and digital beamforming for millimeter wave 5G," *IEEE Communications Magazine*, vol. 53, no. 1, pp. 186–194, Jan. 2015.
- [35] T. E. Bogale, L. B. Le, A. Haghighat, and L. Vandendorpe, "On the Number of RF Chains and Phase Shifters, and Scheduling Design With Hybrid Analog #x2013;Digital Beamforming," *IEEE Transactions on Wireless Communications*, vol. 15, no. 5, pp. 3311–3326, May 2016.
- [36] J. Lee and R. Carlise, "A coma-corrected multibeam shaped lens antenna, part II: Experiments," *IEEE Transactions on Antennas and Propagation*, vol. 31, no. 1, pp. 216–220, Jan. 1983.
- [37] A. L. Peebles, "A dielectric bifocal lens for multibeam antenna applications," *IEEE Transactions on Antennas and Propagation*, vol. 36, no. 5, pp. 599–606, May 1988.
- [38] X. Wu, G. V. Eleftheriades, and T. E. van Deventer-Perkins, "Design and characterization of single- and multiple-beam mm-wave circularly polarized substrate lens antennas for wireless communications," *IEEE Transactions on Microwave Theory and Techniques*, vol. 49, no. 3, pp. 431–441, Mar. 2001.
- [39] T. Maruyama, K. Yamamori, and Y. Kuwahara, "Design of Multibeam Dielectric Lens Antennas by Multi-objective Optimization," in *2008 38th European Microwave Conference*, 2008, pp. 527–530.
- [40] Z. Briqech, A. R. Sebak, and T. A. Denidni, "Wide-Scan MSC-AFTSA Array-Fed Grooved Spherical Lens Antenna for Millimeter-Wave MIMO Applications,"

- IEEE Transactions on Antennas and Propagation*, vol. 64, no. 7, pp. 2971–2980, Jul. 2016.
- [41] R. K. Luneburg and M. Herzberger, *Mathematical Theory of Optics*. University of California Press, 1964.
- [42] L. C. Gunderson and G. T. Holmes, “Microwave Luneburg Lens,” *Appl. Opt.*, *AO*, vol. 7, no. 5, pp. 801–804, May 1968.
- [43] “AT&T Deploying Giant Ball to Boost Capacity at SXSW,” *Wireless Week*, 13-Mar-2015. [Online]. Available: <https://www.wirelessweek.com/news/2015/03/t-deploying-giant-ball-boost-capacity-sxsw>. [Accessed: 08-Mar-2018].
- [44] W. Rotman and P. Franchi, “Cylindrical microwave lens antenna for wideband scanning applications,” in *1980 Antennas and Propagation Society International Symposium*, 1980, vol. 18, pp. 564–567.
- [45] W. Rotman and R. Turner, “Wide-angle microwave lens for line source applications,” *IEEE Transactions on Antennas and Propagation*, vol. 11, no. 6, pp. 623–632, Nov. 1963.
- [46] Y. Gao, M. Khaliel, and T. Kaiser, “Wideband hybrid analog-digital beamforming massive MIMO systems based on Rotman lens,” in *2016 IEEE International Conference on Communication Systems (ICCS)*, 2016, pp. 1–6.
- [47] Y. Gao, M. Khaliel, F. Zheng, and T. Kaiser, “Rotman Lens Based Hybrid Analog #8211;Digital Beamforming in Massive MIMO Systems: Array Architectures, Beam Selection Algorithms and Experiments,” *IEEE Transactions on Vehicular Technology*, vol. 66, no. 10, pp. 9134–9148, Oct. 2017.
- [48] L. C. Godara, “Application of antenna arrays to mobile communications. II. Beam-forming and direction-of-arrival considerations,” *Proceedings of the IEEE*, vol. 85, no. 8, pp. 1195–1245, Aug. 1997.
- [49] R. Schmidt, “Multiple emitter location and signal parameter estimation,” *IEEE Transactions on Antennas and Propagation*, vol. 34, no. 3, pp. 276–280, Mar. 1986.
- [50] X. Zhang, L. Xu, L. Xu, and D. Xu, “Direction of Departure (DOD) and Direction of Arrival (DOA) Estimation in MIMO Radar with Reduced-Dimension MUSIC,” *IEEE Communications Letters*, vol. 14, no. 12, pp. 1161–1163, Dec. 2010.
- [51] R. K. Mohan, C. Harrington, T. Sharpe, Z. W. Barber, and W. R. Babbitt, “Broadband multi-emitter signal analysis and direction finding using a dual-port interferometric photonic spectrum analyzer based on spatial-spectral materials,” in *2013 IEEE International Topical Meeting on Microwave Photonics (MWP)*, 2013, pp. 241–244.
- [52] S. Pan, J. Fu, and J. Yao, “Photonic approach to the simultaneous measurement of the frequency, amplitude, pulse width, and time of arrival of a microwave signal,” *Opt. Lett.*, *OL*, vol. 37, no. 1, pp. 7–9, Jan. 2012.
- [53] J. Capmany and D. Novak, “Microwave photonics combines two worlds,” *Nature Photonics*, vol. 1, no. 6, pp. 319–330, Jun. 2007.
- [54] A. J. Seeds and K. J. Williams, “Microwave Photonics,” *Journal of Lightwave Technology*, vol. 24, no. 12, pp. 4628–4641, Dec. 2006.

- [55] V. J. Urick, K. J. Williams, and J. D. McKinney, *Fundamentals of Microwave Photonics*, 1 edition. Hoboken, New Jersey: Wiley, 2015.
- [56] J. Yao, "Microwave Photonics," *Journal of Lightwave Technology*, vol. 27, no. 3, pp. 314–335, Feb. 2009.
- [57] Z. Jia, J. Yu, G. Ellinas, and G.-K. Chang, "Key Enabling Technologies for Optical–Wireless Networks: Optical Millimeter-Wave Generation, Wavelength Reuse, and Architecture," *J. Lightwave Technol., JLT*, vol. 25, no. 11, pp. 3452–3471, Nov. 2007.
- [58] R. A. Minasian, "Photonic signal processing of microwave signals," *IEEE Transactions on Microwave Theory and Techniques*, vol. 54, no. 2, pp. 832–846, Feb. 2006.
- [59] D. Novak *et al.*, "Radio-Over-Fiber Technologies for Emerging Wireless Systems," *IEEE Journal of Quantum Electronics*, vol. 52, no. 1, pp. 1–11, Jan. 2016.
- [60] J. A. Nanzer, A. Wichman, J. Klamkin, T. P. McKenna, and T. R. C. Jr, "Millimeter-Wave Photonics for Communications and Phased Arrays," *Fiber and Integrated Optics*, vol. 34, no. 4, pp. 159–174, Jul. 2015.
- [61] X. J. Meng, T. Chau, D. T. K. Tong, and M. C. Wu, "Suppression of second harmonic distortion in directly modulated distributed feedback lasers by external light injection," *Electronics Letters*, vol. 34, no. 21, pp. 2040–2041, Oct. 1998.
- [62] K. J. Williams, R. D. Esman, R. B. Wilson, and J. D. Kulick, "Differences in p-side and n-side illuminated p-i-n photodiode nonlinearities," *IEEE Photonics Technology Letters*, vol. 10, no. 1, pp. 132–134, Jan. 1998.
- [63] N. Dagli, "Wide-bandwidth lasers and modulators for RF photonics," *IEEE Transactions on Microwave Theory and Techniques*, vol. 47, no. 7, pp. 1151–1171, Jul. 1999.
- [64] K. Kato, "Ultrawide-band/high-frequency photodetectors," *IEEE Transactions on Microwave Theory Techniques*, vol. 47, pp. 1265–1281, Jul. 1999.
- [65] M. S. Islam *et al.*, "Velocity-matched distributed photodetectors and balanced photodetectors with p-i-n photodiodes," *IEEE Transactions on Microwave Theory and Techniques*, vol. 49, no. 10, pp. 1914–1920, Oct. 2001.
- [66] I. I. I. Charles H. Cox, "Analog Optical Links: Theory and Practice," *Cambridge Core*, Apr-2004. [Online]. Available: [/core/books/analog-optical-links/8176E8D9AAFBAAEA4A0183FD169522E4A](#). [Accessed: 08-Mar-2018].
- [67] V. J. Urick *et al.*, "Photodiode linearity requirements for radio-frequency photonics and demonstration of increased performance using photodiode arrays," in *2008 International Topical Meeting on Microwave Photonics jointly held with the 2008 Asia-Pacific Microwave Photonics Conference*, 2008, pp. 86–89.
- [68] N. J. Gomes *et al.*, "Radio-over-fiber transport for the support of wireless broadband services [Invited]," *J. Opt. Netw., JON*, vol. 8, no. 2, pp. 156–178, Feb. 2009.
- [69] A. Ng'oma *et al.*, "Performance of a Multi-Gb/s 60 GHz Radio Over Fiber System Employing a Directly Modulated Optically Injection-Locked VCSEL," *Journal of Lightwave Technology*, vol. 28, no. 16, pp. 2436–2444, Aug. 2010.

- [70] G. K. Chang and C. Liu, "1-100GHz microwave photonics link technologies for next-generation WiFi and 5G wireless communications," in *2013 IEEE International Topical Meeting on Microwave Photonics (MWP)*, 2013, pp. 5–8.
- [71] T. Kurniawan, A. Nirmalathas, C. Lim, D. Novak, and R. Waterhouse, "Performance analysis of optimized millimeter-wave fiber radio links," *IEEE Transactions on Microwave Theory and Techniques*, vol. 54, no. 2, pp. 921–928, Feb. 2006.
- [72] A. Nirmalathas, P. A. Gamage, C. Lim, D. Novak, and R. Waterhouse, "Digitized Radio-Over-Fiber Technologies for Converged Optical Wireless Access Network," *Journal of Lightwave Technology*, vol. 28, no. 16, pp. 2366–2375, Aug. 2010.
- [73] Z. Ahmed, D. Novak, and H. F. Liu, "SCM millimeter-wave (37 GHz) optical transport system for distribution of video and data signals," in *Proceedings of Optical Fiber Communication Conference* (, 1997, pp. 337–338.
- [74] M. Weiß, M. Huchard, A. Stohr, B. Charbonnier, S. Fedderwitz, and D. S. Jager, "60-GHz Photonic Millimeter-Wave Link for Short- to Medium-Range Wireless Transmission Up to 12.5 Gb/s," *Journal of Lightwave Technology*, vol. 26, no. 15, pp. 2424–2429, Aug. 2008.
- [75] J. A. Nanzer, P. T. Callahan, M. L. Dennis, T. R. Clark, D. Novak, and R. B. Waterhouse, "Millimeter-Wave Wireless Communication Using Dual-Wavelength Photonic Signal Generation and Photonic Upconversion," *IEEE Transactions on Microwave Theory and Techniques*, vol. 59, no. 12, pp. 3522–3530, Dec. 2011.
- [76] D. Pilz and W. Menzel, "Folded reflectarray antenna," *Electronics Letters*, vol. 34, no. 9, pp. 832–833, Apr. 1998.
- [77] D. Novak and R. Waterhouse, "Advanced radio over fiber network technologies," *Opt. Express, OE*, vol. 21, no. 19, pp. 23001–23006, Sep. 2013.
- [78] T. P. McKenna, J. A. Nanzer, and T. R. Clark, "Experimental Demonstration of Photonic Millimeter-Wave System for High Capacity Point-to-Point Wireless Communications," *Journal of Lightwave Technology*, vol. 32, no. 20, pp. 3588–3594, Oct. 2014.
- [79] W. Ng, A. A. Walston, G. L. Tangonan, J. J. Lee, I. L. Newberg, and N. Bernstein, "The first demonstration of an optically steered microwave phased array antenna using true-time-delay," *Journal of Lightwave Technology*, vol. 9, no. 9, pp. 1124–1131, Sep. 1991.
- [80] M. Tur, "True time delay photonic beamforming: A review," in *2009 IEEE International Conference on Microwaves, Communications, Antennas and Electronics Systems*, 2009, pp. 1–2.
- [81] I. Aldaya, G. Campuzano, G. Castañón, and A. Aragón-Zavala, "A Tutorial on Optical Feeding of Millimeter-Wave Phased Array Antennas for Communication Applications," *International Journal of Antennas and Propagation*, 2015. [Online]. Available: <https://www.hindawi.com/journals/ijap/2015/264812/>. [Accessed: 08-Mar-2018].

- [82] A. Hirata, T. Minotani, and T. Nagatsuma, "A 120-GHz Microstrip Antenna Monolithically Integrated with a Photodiode on Si," *Jpn. J. Appl. Phys.*, vol. 41, no. 3R, p. 1390, Mar. 2002.
- [83] X. Xie *et al.*, "Improved power conversion efficiency in high-performance photodiodes by flip-chip bonding on diamond," *Optica*, vol. 1, no. 6, p. 429, Dec. 2014.
- [84] X. Xie *et al.*, "Photonic Generation of High-Power Pulsed Microwave Signals," *Journal of Lightwave Technology*, vol. 33, no. 18, pp. 3808–3814, Sep. 2015.
- [85] Q. Zhou, A. S. Cross, A. Beling, Y. Fu, Z. Lu, and J. C. Campbell, "High-Power V-Band InGaAs/InP Photodiodes," *IEEE Photonics Technology Letters*, vol. 25, no. 10, pp. 907–909, May 2013.
- [86] D. A. Tulchinsky, J. B. Boos, D. Park, P. G. Goetz, W. S. Rabinovich, and K. J. Williams, "High-Current Photodetectors as Efficient, Linear, and High-Power RF Output Stages," *Journal of Lightwave Technology*, vol. 26, no. 4, pp. 408–416, Feb. 2008.
- [87] C. Hemmi, R. T. Dover, F. German, and A. Vespa, "Multifunction wide-band array design," *IEEE Transactions on Antennas and Propagation*, vol. 47, no. 3, pp. 425–431, Mar. 1999.
- [88] H. Holter, T.-H. Chio, and D. H. Schaubert, "Experimental results of 144-element dual-polarized endfire tapered-slot phased arrays," *IEEE Transactions on Antennas and Propagation*, vol. 48, no. 11, pp. 1707–1718, Nov. 2000.
- [89] R. W. Kindt and W. R. Pickles, "Ultrawideband All-Metal Flared-Notch Array Radiator," *IEEE Transactions on Antennas and Propagation*, vol. 58, no. 11, pp. 3568–3575, Nov. 2010.
- [90] J. J. Lee *et al.*, "Photonic wideband array antennas," *IEEE Transactions on Antennas and Propagation*, vol. 43, no. 9, pp. 966–982, Sep. 1995.
- [91] J. J. Lee, S. Livingston, and R. Koenig, "A low-profile wide-band (5:1) dual-pol array," *IEEE Antennas and Wireless Propagation Letters*, vol. 2, no. 1, pp. 46–49, 2003.
- [92] J. J. Lee, S. Livingston, and R. Koenig, "Performance of a wideband (3-14 GHz) dual-pol array," in *IEEE Antennas and Propagation Society International Symposium, 2004*, 2004, vol. 1, p. 551–554 Vol.1.
- [93] J. G. Maloney, B. N. Baker, R. T. Lee, G. N. Kiesel, and J. J. Acree, "Wide scan, integrated printed circuit board, fragmented aperture array antennas," in *2011 IEEE International Symposium on Antennas and Propagation (APSURSI)*, 2011, pp. 1965–1968.
- [94] M. Jones and J. Rawnick, "A New Approach to Broadband Array Design using Tightly Coupled Elements," in *IEEE Military Communications Conference, 2007. MILCOM 2007*, 2007, pp. 1–7.
- [95] W. F. Moulder, K. Sertel, and J. L. Volakis, "Superstrate-Enhanced Ultrawideband Tightly Coupled Array With Resistive FSS," *IEEE Transactions on Antennas and Propagation*, vol. 60, no. 9, pp. 4166–4172, Sep. 2012.

- [96] A. Neto and J. J. Lee, “‘Infinite Bandwidth’ long slot array antenna,” *IEEE Antennas and Wireless Propagation Letters*, vol. 4, pp. 75–78, 2005.
- [97] D. Cavallo, A. Neto, G. Gerini, and G. Toso, “Scanning performance of wide band connected arrays of dipoles,” in *2009 3rd European Conference on Antennas and Propagation*, 2009, pp. 1222–1224.
- [98] I. Tzanidis, K. Sertel, and J. L. Volakis, “UWB Low-Profile Tightly Coupled Dipole Array With Integrated Balun and Edge Terminations,” *IEEE Transactions on Antennas and Propagation*, vol. 61, no. 6, pp. 3017–3025, Jun. 2013.
- [99] H. A. Wheeler, “The Radiation Resistance of an Antenna in an Infinite Array or Waveguide,” *Proceedings of the IRE*, vol. 36, no. 4, pp. 478–487, Apr. 1948.
- [100] H. Wheeler, “Simple relations derived from a phased-array antenna made of an infinite current sheet,” *IEEE Transactions on Antennas and Propagation*, vol. 13, no. 4, pp. 506–514, Jul. 1965.
- [101] B. A. Munk, *Finite Antenna Arrays and FSS*, 1 edition. Piscataway, N.J.: Hoboken, N.J: Wiley-IEEE Press, 2003.
- [102] E. A. Alwan, K. Sertel, and J. L. Volakis, “Circuit model based optimization of ultra-wideband arrays,” in *2012 IEEE Antennas and Propagation Society International Symposium (APSURSI)*, 2012, pp. 1–2.
- [103] R. C. Hansen, “Linear connected arrays [coupled dipole arrays],” *IEEE Antennas and Wireless Propagation Letters*, vol. 3, no. 1, pp. 154–156, Dec. 2004.
- [104] B. A. Munk, “Broadband Wire Arrays,” in *Finite Antenna Arrays and FSS*, John Wiley & Sons, Inc., 2003, pp. 181–213.
- [105] R. C. Hansen, *Phased Array Antennas*, 2 edition. Hoboken, N.J: Wiley-Interscience, 2009.
- [106] J. P. Doane, K. Sertel, and J. L. Volakis, “A 6.3:1 bandwidth scanning Tightly Coupled Dipole Array with co-designed compact balun,” in *Proceedings of the 2012 IEEE International Symposium on Antennas and Propagation*, 2012, pp. 1–2.
- [107] D. K. Papantonis and J. L. Volakis, “Dual-Polarized Tightly Coupled Array With Substrate Loading,” *IEEE Antennas and Wireless Propagation Letters*, vol. 15, pp. 325–328, 2016.
- [108] S. S. Holland, D. H. Schaubert, and M. N. Vouvakis, “A 7-21 GHz Dual-Polarized Planar Ultrawideband Modular Antenna (PUMA) Array,” *IEEE Transactions on Antennas and Propagation*, vol. 60, no. 10, pp. 4589–4600, Oct. 2012.
- [109] I. Tzanidis, K. Sertel, and J. L. Volakis, “Interwoven Spiral Array (ISPA) With a 10:1 Bandwidth on a Ground Plane,” *IEEE Antennas and Wireless Propagation Letters*, vol. 10, pp. 115–118, 2011.
- [110] T. Durham, A. Jones, G. Gothard, and S. Ortiz, “Dual polarization antenna array with inter-element coupling and associated methods,” US20070132643 A1, 14-Jun-2007.
- [111] J. A. Kasemodel, C. C. Chen, and J. L. Volakis, “Wideband Planar Array With Integrated Feed and Matching Network for Wide-Angle Scanning,” *IEEE*

- Transactions on Antennas and Propagation*, vol. 61, no. 9, pp. 4528–4537, Sep. 2013.
- [112] S. S. Holland and M. N. Vouvakis, “The Planar Ultrawideband Modular Antenna (PUMA) Array,” *IEEE Transactions on Antennas and Propagation*, vol. 60, no. 1, pp. 130–140, Jan. 2012.
- [113] M. Y. Lee, J. T. Logan, R. W. Kindt, and M. N. Vouvakis, “Simplified design of 6:1 PUMA arrays,” in *2015 IEEE International Symposium on Antennas and Propagation USNC/URSI National Radio Science Meeting*, 2015, pp. 2515–2516.
- [114] S. March, “A Wideband Stripline Hybrid Ring (Correspondence),” *IEEE Transactions on Microwave Theory and Techniques*, vol. 16, no. 6, pp. 361–361, Jun. 1968.
- [115] J. A. Kasemodel, C. C. Chen, and J. L. Volakis, “Broadband planar wide-scan array employing tightly coupled elements and integrated balun,” in *2010 IEEE International Symposium on Phased Array Systems and Technology (ARRAY)*, 2010, pp. 467–472.
- [116] J. A. Kasemodel, C. C. Chen, and J. L. Volakis, “Low-cost, planar and wideband phased array with integrated balun and matching network for wide-angle scanning,” in *2010 IEEE Antennas and Propagation Society International Symposium (APSURSI)*, 2010, pp. 1–4.
- [117] T. Xia, S. Yang, and Z. Nie, “Design of a Tapered Balun for Broadband Arrays With Closely Spaced Elements,” *IEEE Antennas and Wireless Propagation Letters*, vol. 8, pp. 1291–1294, 2009.
- [118] T. H. Maiman, “Stimulated Optical Radiation in Ruby,” *Nature*, vol. 187, no. 4736, pp. 493–494, Aug. 1960.
- [119] T. Miya, Y. Terunuma, T. Hosaka, and T. Miyashita, “Ultimate low-loss single-mode fibre at 1.55 μm ,” *Electronics Letters*, vol. 15, no. 4, pp. 106–108, Feb. 1979.
- [120] R. J. Mears, L. Reekie, I. M. Jauncey, and D. N. Payne, “Low-noise erbium-doped fibre amplifier operating at 1.54 μm ,” *Electronics Letters*, vol. 23, no. 19, pp. 1026–1028, Sep. 1987.
- [121] H. Ito, F. Nakajima, T. Furuta, and T. Ishibashi, “Continuous THz-wave generation using antenna-integrated uni-travelling-carrier photodiodes,” *Semicond. Sci. Technol.*, vol. 20, no. 7, p. S191, 2005.
- [122] K. Li *et al.*, “High-Power Photodiode Integrated With Coplanar Patch Antenna for 60-GHz Applications,” *IEEE Photonics Technology Letters*, vol. 27, no. 6, pp. 650–653, Mar. 2015.
- [123] S. Shi *et al.*, “Ultrawideband Optically Fed Tightly Coupled Phased Array,” *Journal of Lightwave Technology*, vol. 33, no. 23, pp. 4781–4790, Dec. 2015.
- [124] Z. Li, H. Pan, H. Chen, A. Beling, and J. C. Campbell, “High-Saturation-Current Modified Uni-Travelling-Carrier Photodiode With Cliff Layer,” *IEEE Journal of Quantum Electronics*, vol. 46, no. 5, pp. 626–632, May 2010.
- [125] Z. Li *et al.*, “High-power high-linearity flip-chip bonded modified uni-travelling carrier photodiode,” *Optics Express*, vol. 19, no. 26, p. B385, Dec. 2011.

- [126] H. Ito, S. Kodama, Y. Muramoto, T. Furuta, T. Nagatsuma, and T. Ishibashi, "High-speed and high-output InP-InGaAs unitraveling-carrier photodiodes," *IEEE Journal of Selected Topics in Quantum Electronics*, vol. 10, no. 4, pp. 709–727, Jul. 2004.
- [127] Z. Li, "High-power photodiodes," University of Virginia, 2011.
- [128] "Physics of Semiconductor Devices, 3rd Edition," *Wiley.com*. [Online]. Available: <https://www.wiley.com/en-us/Physics+of+Semiconductor+Devices%2C+3rd+Edition-p-9780471143239>. [Accessed: 08-Mar-2018].
- [129] Q. Zhou, A. Cross, Y. Fu, A. Beling, and J. C. Campbell, "High-power high-bandwidth flip-chip bonded modified uni-traveling carrier photodiodes," in *IEEE Photonics Conference 2012*, 2012, pp. 306–307.
- [130] G. J. Schneider, J. A. Murakowski, C. A. Schuetz, S. Shi, and D. W. Prather, "Radiofrequency signal-generation system with over seven octaves of continuous tuning," *Nat Photon*, vol. 7, no. 2, pp. 118–122, Feb. 2013.
- [131] J. Bai *et al.*, "Optically Driven Ultrawideband Phased Array With an Optical Interleaving Feed Network," *IEEE Antennas and Wireless Propagation Letters*, vol. 13, pp. 47–50, 2014.
- [132] J. Macario *et al.*, "Full spectrum millimeter-wave modulation," *Optics Express*, vol. 20, no. 21, p. 23623, Oct. 2012.
- [133] G. Mur, "Absorbing Boundary Conditions for the Finite-Difference Approximation of the Time-Domain Electromagnetic-Field Equations," *IEEE Transactions on Electromagnetic Compatibility*, vol. EMC-23, no. 4, pp. 377–382, Nov. 1981.
- [134] J. H. Harris, "Sintered aluminum nitride ceramics for high-power electronic applications," *JOM*, vol. 50, no. 6, pp. 56–60, Jun. 1998.
- [135] C. A. Balanis, *Antenna Theory: Analysis and Design, 3rd Edition*, 3 edition. Hoboken, NJ: Wiley-Interscience, 2005.
- [136] K. Li, X. Xie, Q. Zhou, A. Beling, and J. C. Campbell, "High Power 20-GHz Photodiodes With Resonant Microwave Circuits," *IEEE Photonics Technology Letters*, vol. 26, no. 13, pp. 1303–1306, Jul. 2014.
- [137] A. Novack *et al.*, "Germanium photodetector with 60 GHz bandwidth using inductive gain peaking," *Opt. Express, OE*, vol. 21, no. 23, pp. 28387–28393, Nov. 2013.
- [138] P. I. Deffenbaugh, R. C. Rumpf, and K. H. Church, "Broadband Microwave Frequency Characterization of 3-D Printed Materials," *IEEE Transactions on Components, Packaging and Manufacturing Technology*, vol. 3, no. 12, pp. 2147–2155, Dec. 2013.
- [139] R. Harrington and J. Mautz, "Theory of characteristic modes for conducting bodies," *IEEE Transactions on Antennas and Propagation*, vol. 19, no. 5, pp. 622–628, Sep. 1971.
- [140] D. W. Prather *et al.*, "Optically Upconverted, Spatially Coherent Phased-Array-Antenna Feed Networks for Beam-Space MIMO in 5G Cellular Communications,"

- IEEE Transactions on Antennas and Propagation*, vol. 65, no. 12, pp. 6432–6443, Dec. 2017.
- [141] M. R. Konkol *et al.*, “High-Power Photodiode-Integrated-Connected Array Antenna,” *Journal of Lightwave Technology*, vol. 35, no. 10, pp. 2010–2016, May 2017.
- [142] A. W. Doery, “Catalog of window taper functions for sidelobe control,” Sandia National Laboratories, SAND2017-6042, 2017.
- [143] J. W. Goodman, *Introduction to Fourier Optics*, 3 edition. Englewood, Colo: W. H. Freeman, 2004.
- [144] P. M. Blanchard, A. H. Greenaway, A. R. Harvey, and K. Webster, “Coherent optical beam forming with passive millimeter-wave arrays,” *Journal of Lightwave Technology*, vol. 17, no. 3, pp. 418–425, Mar. 1999.
- [145] C. Schuetz *et al.*, “Realization of a video-rate distributed aperture millimeter-wave imaging system using optical upconversion,” in *Passive and Active Millimeter-Wave Imaging XVI*, 2013, vol. 8715, p. 87150I.
- [146] R. D. Martin *et al.*, “Video rate passive millimeter-wave imager utilizing optical upconversion with improved size, weight, and power,” in *Passive and Active Millimeter-Wave Imaging XVIII*, 2015, vol. 9462, p. 946209.
- [147] C. A. Schuetz *et al.*, “Sparse aperture millimeter-wave imaging using optical detection and correlation techniques,” in *Passive Millimeter-Wave Imaging Technology X*, 2007, vol. 6548, p. 65480B.
- [148] C. A. Schuetz, R. D. Martin, D. W. Prather, and T. E. Dillon, “Method for controlling the phase of optical carriers in millimeter wave imaging systems using optical upconversion,” US7965435B2, 21-Jun-2011.
- [149] R. D. Martin, C. A. Schuetz, D. W. Prather, and T. E. Dillon, “Controlling the phase of optical carriers,” US8159737B2, 17-Apr-2012.
- [150] R. Martin *et al.*, “Design and performance of a distributed aperture millimeter-wave imaging system using optical upconversion,” in *Passive Millimeter-Wave Imaging Technology XII*, 2009, vol. 7309, p. 730908.
- [151] T. E. Dillon *et al.*, “Optical configuration of an upconverted millimeter-wave distributed aperture imaging system,” in *Millimetre Wave and Terahertz Sensors and Technology II*, 2009, vol. 7485, p. 74850G.
- [152] D. G. Mackrides, C. A. Schuetz, R. D. Martin, T. E. Dillon, P. Yao, and D. W. Prather, “Progress toward a video-rate, passive millimeter-wave imager for brownout mitigation,” in *Passive Millimeter-Wave Imaging Technology XIV*, 2011, vol. 8022, p. 802203.
- [153] C. Schuetz, J. Murakowski, G. Schneider, S. Shi, and D. Prather, “Phased-arrayradio frequency receiver,” 9525489.
- [154] T. E. Dillon, C. A. Schuetz, R. D. Martin, S. Shi, D. G. Mackrides, and D. W. Prather, “Passive millimeter wave imaging using a distributed aperture and optical upconversion,” in *Millimetre Wave and Terahertz Sensors and Technology III*, 2010, vol. 7837, p. 78370H.

- [155] C. A. Schuetz, J. Murakowski, G. J. Schneider, and D. W. Prather, "Radiometric Millimeter-wave detection via optical upconversion and carrier suppression," *IEEE Transactions on Microwave Theory and Techniques*, vol. 53, no. 5, pp. 1732–1738, May 2005.
- [156] C. A. Schuetz, "Optical techniques for millimeter -wave detection and imaging," Ph.D., University of Delaware, United States -- Delaware, 2007.
- [157] F. T. Ulaby, R. K. Moore, and A. K. Fung, *Microwave remote sensing: active and passive*. Reading, Mass.: Addison-Wesley Pub. Co., Advanced Book Program/World Science Division, 1981.
- [158] R. Gordon, R. Bender, and G. T. Herman, "Algebraic Reconstruction Techniques (ART) for three-dimensional electron microscopy and X-ray photography," *Journal of Theoretical Biology*, vol. 29, no. 3, pp. 471–481, Dec. 1970.
- [159] P. Gilbert, "Iterative methods for the three-dimensional reconstruction of an object from projections," *Journal of Theoretical Biology*, vol. 36, no. 1, pp. 105–117, Jul. 1972.
- [160] R. Gordon and G. Herman, "Three-Dimensional Reconstruction from Projections: A Review of Algorithms," in *International Review of Cytology*, vol. 38, G. H. Bourne, J. F. Danielli, and K. W. Jeon, Eds. Academic Press, 1974, pp. 111–151.
- [161] J. G. Colsher, "Iterative three-dimensional image reconstruction from tomographic projections," *Computer Graphics and Image Processing*, vol. 6, no. 6, pp. 513–537, Dec. 1977.
- [162] Y. Censor, "Finite series-expansion reconstruction methods," *Proceedings of the IEEE*, vol. 71, no. 3, pp. 409–419, Mar. 1983.
- [163] A. Kak and M. Slaney, *Principles of Computerized Tomographic Imaging*. Society for Industrial and Applied Mathematics, 2001.
- [164] S. KACZMARZ, "Approximate solution of systems of linear equations†," *International Journal of Control*, vol. 57, no. 6, pp. 1269–1271, Jun. 1993.
- [165] A. R. Thompson, J. Moran, and G. W. S. Jr, *Interferometry and Synthesis in Radio Astronomy*, 3rd ed. Springer International Publishing, 2017.
- [166] L. Kogan, "Optimizing a large array configuration to minimize the sidelobes," *IEEE Transactions on Antennas and Propagation*, vol. 48, no. 7, pp. 1075–1078, Jul. 2000.
- [167] T. Dillon, "Grayscale lithography with applications to chip-scale optical interconnects," Ph.D., University of Delaware, United States -- Delaware, 2009.
- [168] J. L. Bonnett, "Development and implementation of an FPGA-based control system for a passive, distributed aperture millimeter-wave imaging system," M.S., University of Delaware, United States -- Delaware, 2015.
- [169] S. Shi *et al.*, "System modeling of passive millimeter wave imager based on optical up-conversion," in *Physics and Simulation of Optoelectronic Devices XX*, 2012, vol. 8255, p. 82551O.

- [170] P. C. Hansen and M. Saxild-Hansen, "AIR Tools — A MATLAB package of algebraic iterative reconstruction methods," *Journal of Computational and Applied Mathematics*, vol. 236, no. 8, pp. 2167–2178, Feb. 2012.
- [171] D. D. Ross, J. Murakowski, C. J. Ryan, G. J. Schneider, and D. W. Prather, "Compressive k-Space Tomography," *Journal of Lightwave Technology*, vol. PP, no. 99, pp. 1–8, 2018.
- [172] D. L. Donoho, "Compressed sensing," *IEEE Transactions on Information Theory*, vol. 52, no. 4, pp. 1289–1306, Apr. 2006.
- [173] E. J. Candes and M. B. Wakin, "An Introduction To Compressive Sampling," *IEEE Signal Processing Magazine*, vol. 25, no. 2, pp. 21–30, Mar. 2008.
- [174] R. G. Baraniuk, "Compressive Sensing [Lecture Notes]," *IEEE Signal Processing Magazine*, vol. 24, no. 4, pp. 118–121, Jul. 2007.
- [175] M. F. Duarte *et al.*, "Single-pixel imaging via compressive sampling," *IEEE Signal Processing Magazine*, vol. 25, no. 2, pp. 83–91, Mar. 2008.
- [176] D. D. Ross *et al.*, "Low-Profile High-Power Optically Addressed Phased Array Antenna," *Journal of Lightwave Technology*, vol. 35, no. 18, pp. 3894–3900, Sep. 2017.
- [177] D. D. Ross, C. J. Ryan, G. J. Schneider, J. Murakowski, and D. W. Prather, "Passive Three-Dimensional Spatial-Spectral Analysis Based on k-Space Tomography," in *IEEE Photonics Technology Letters*, vol. 30, no. 9, pp. 817–820, May 1, 2018.
- [178] M. R. Konkol *et al.*, "Photonic Tightly Coupled Array," *IEEE Transactions on Microwave Theory and Techniques*, vol. PP, no. 99, pp. 1–9, 2018.
- [179] M. R. Konkol *et al.*, "High-Power, Aperture Coupled Photonic Antenna," *IEEE Photonics Technology Letters*, vol. 29, no. 14, pp. 1207–1210, Jul. 2017.